JAERI-Review
2003-004

NUCLEAR ENERGY SYSTEM DEPARTMENT ANNUAL REPORT
(APRIL 1, 2001- MARCH 31,2002)

March 2003

Department of Nuclear Energy System

日本原子力研究所
Japan Atomic Energy Research Institute

本レポートは、日本原子力研究所が不定期に公刊している研究報告書です。
入手の問合わせは、日本原子力研究所研究情報部研究情報課（〒319-1195 茨城県那珂郡東海村）あて、お申し越し下さい。なお、このほかに財団法人原子力弘済会資料センター（〒319-1195 茨城県那珂郡東海村日本原子力研究所内）で複写による実費頒布を行っております。

This report is issued irregularly.
Inquiries about availability of the reports should be addressed to Research Information Division, Department of Intellectual Resources, Japan Atomic Energy Research Institute, Tokai-mura, Naka-gun, Ibaraki-ken 〒319-1195, Japan.

編集兼発行　日本原子力研究所

JAERI－Review 2003-004

Nuclear Energy System Department Annual Report

(April 1, 2001 – March 31, 2002)

Department of Nuclear Energy System

Tokai Research Establishment
Japan Atomic Energy Research Institute
Tokai-mura, Naka-gun, Ibaraki-ken

(Received January 17, 2003)

This report summarizes the research and development activities in the Department of Nuclear Energy System during the fiscal year of 2001 (April 1, 2001 - March 31, 2002).

The Department has been organized from April 1998. The main research activity is aimed to build the basis of the development of future nuclear energy systems. The research activities of the Department cover basic nuclear data evaluation, conceptual design of a reduced-moderation water reactor, reactor physics experiments and development of the reactor analysis codes, experiment and analysis of thermal-hydrodynamics, energy system analysis and assessment, development of advanced materials for a reactor, lifetime reliability assessment on structural material, development of advanced nuclear fuel, design of a marine reactor and the research for a nuclear ship system. The maintenance and operation of reactor engineering facilities belonging to the Department are undertaken.

The activities of the research committees to which the Department takes a role of secretariat are also summarized in this report.

Keywords: Nuclear Energy System Department Annual Report, Nuclear Data, Advanced Reactor, Reactor Physics, Thermal-hydraulics, Energy System Analysis, Advanced Material, Advanced Nuclear Fuel, Marine Reactor

---

JAERI－Review 2003-004

平成１３年度エネルギーシステム研究部年報

日本原子力研究所東海研究所
エネルギーシステム研究部

（2003年 1月 17日受理）

本報告書は、平成１３年度におけるエネルギーシステム研究部の研究活動状況をとりまとめたものである。

エネルギーシステム研究部は、平成 10 年度より新たに編成された部であり、将来型炉等新たなエネルギーシステムを視野に入れた基礎基盤的な研究を進めている。平成13年度のエネルギーシステム研究部の研究分野は、核データの評価、低減速スペクトル炉の概念設計研究、炉物理実験及び炉特性解析コードの開発、伝熱流動実験及び解析、原子力エネルギーの経済性評価、原子炉用新材料の開発及び経年挙動の研究、新型燃料の研究、舶用炉及び原子力船システムの研究等に亘っている。この他、エネルギーシステム研究部の各種炉工学施設の維持・管理も行っている。

本報告では、エネルギーシステム研究部が運営を担当する研究委員会の活動報告もとりまとめられている。

東海研究所：〒319-1195　茨城県那珂郡東海村白方白根２－４

Contents

Preface ····· 1
1. Nuclear Data ····· 5
1.1 Development of Japanese Evaluated Nuclear Data Library Version 3 Revision-3, JENDL-3.3 ····· 6
1.2 Nuclear Data Evaluation and Compilation for JENDL Intermediate Energy Files in 2001 ····· 9
1.3 Re-evaluation of Nuclear Data for ^{242m}Am, ^{243}Am, ^{99}Tc and ^{140}Ce ····· 12
1.4 Evaluation of Neutron-induced Reactions on ^{236}Pu for JENDL-3.3 ····· 15
1.5 Calculation of Fission Reaction in the Framework of QMD+SDM ····· 18
1.6 Evaluation and Compilation of Nuclear Structure and Decay Data in 2001 ·· 21
1.7 Compilation of JENDL FP Decay Data File 2000 ····· 23
2. Reactor Physics ····· 26
2.1 Adjustment of Total Delayed Neutron Yields of ^{235}U, ^{238}U and ^{239}Pu in JENDL-3.2 Using Benchmark Experiments on Effective Delayed Neutron Fraction β eff ····· 27
2.2 Burn-up Calculation Benchmark for LWR Next Generation Fuels ····· 30
2.3 Application of Acceleration Methods to a Prism Geometry Nodal Diffusion Code MOSRA-Prism ····· 33
2.4 Determination of Reactivity and Source Intensity Based on the Maximum Likelihood Method ····· 35
2.5 Measurement of Void Reactivity Effect in Light Water Moderator Lattices by Subcritical Bubbling Method ····· 38
2.6 Benchmark Test for JENDL-3.3 Library by Analyses of FCA Cores ····· 41
3. Advanced Reactor System Studies ····· 44
3.1 Study on High Conversion Ratio BWR Type RMWR Core ····· 45
3.2 Study on High Burn-up BWR Type RMWR Core ····· 48
3.3 Study on ABWR Compatible RMWR Core ····· 51
3.4 Study on PWR Type RMWR Core ····· 54
3.5 Optimization a Seed-blanket Type RMWR Fuel Assembly ····· 57
3.6 Study on Dynamical Response Characteristics of RMWR Core ····· 60
3.7 TRAC-BF1 Simulation of Geysering Experiments for Start-up Analysis of BWR Type RMWR with Natural Circulation Core Cooling ····· 63
3.8 Analysis of MOX Fuel Behavior in RMWR by FEMAXI-RM Code ····· 66
3.9 Study on Economical Reprocessing Process Relevant for RMWR ····· 69
3.10 Smart Software Integration for Intelligent Monitoring Systems ····· 72
4. Thermal and Fluid Engineering ····· 75

4.1 Critical Power Experiments of Tight-lattice Bundle for BWR-type Reduced Moderation Water Reactor ····· 76
4.2 Subchannel Analysis of CHF Experiments for Tight Lattice Core with COBRA-TF ····· 79
4.3 Development of the Neutron Radiography 3D CT (NR3DCT) for Measuring the Void Fraction Distribution in Tight-lattice Bundle ····· 82
4.4 Development of Mechanistic Boiling Transition Model-Installation of Boundary Fitting Coordinate Function- ····· 84
4.5 Development of Algorithm for Reduction of Numerical Diffusion against Interface Tracking Method ····· 87
4.6 Numerical Simulation of the Slug Flow using Interface Tracking Method ··· 90
4.7 Experimental Verification of Effectiveness of a Pressure Suppression System in ITER ····· 92
4.8 Analysis of Thermal-hydraulic Characteristics in a Fusion Experimental Reactor during In-vessel LOCA by a Modified TRAC-PF1 Code ····· 95
4.9 Numerical Analysis on Direct-contact Condensation of Vapor Injected into Low-temperature Water ····· 98
4.10 Numerical Simulations of Air Ingress and Dust Mobilization Behavior in a Fusion Reactor during a Loss-of-vacuum Event ····· 101
5. Energy System Analysis and Assessment ····· 104
5.1 Nuclear Power and Its Fuel Cycle Scenario in Japan-Roles of Reduced-moderation Water Reactors- ····· 105
5.2 A Study on the Plutonium Recycling Characteristics of Reduced Moderation Water Reactors ····· 108
5.3 Possible Impacts of Nuclear Phase-out in Japan – Preliminary Study by the Integrated Energy and Macroeconomic Model ····· 111
5.4 A Review of Risk and Externality Studies on Electric Power Generation ···· 114
6. Reactor Structural Materials ····· 117
6.1 Water Temperature Dependence of IASCC Susceptibility of 316LN-IG ···· 118
6.2 AFM Evaluation for Corrosion Behavior of Ion Irradiated Stainless Steel ··· 121
6.3 Present Status of SSRT Facility for In-situ Observation in High Temperature Water of Irradiated Materials ····· 124
6.4 Development of In-pile and Out-of-pile Uniaxial Constant Loading SCC Test Technique in High Temperature Water ····· 127
6.5 Description Method for Knowledge Extracted from Data-Free-Way ····· 130
7. Research on Advanced Materials for Light Water Reactors and Reprocessing Plants ····· 133
7.1 Development of Advanced Fuel Cladding Materials Applied for Ultra-high Burnup Light Water Reactors ····· 134
7.2 Improvement of Micro-cracking Susceptibility in Welding Fully Austenitic Stainless Steel ····· 137

7.3 Effect of Triple Ion Beam Irradiation on Microstructural Evolution of High Chromium Austenitic Stainless Steel ····· 140
7.4 Effect of Triple Ion Beam Irradiation on Mechanical Properties of High Chromium Austenitic Stainless Steel ····· 143
7.5 SCC Susceptibility of High Chromium Austenitic Stainless Steels for High Burnup Cladding Material ····· 146
7.6 Evaluation of the Advanced Cladding Materials for the Ultra High-burn Fuels ····· 149
7.7 Extraction of Mechanical Properties from Load-depth Curve by Using Spherical Indenter and Inverse Analysis ····· 151
7.8 Fatigue Strength Reduction Factor of T-joint Weld with Incomplete Penetration ····· 154
7.9 Operation and In-service Inspection of Demonstration Testing Equipments for Acid Recovery Evaporator and Dissolver ····· 157
7.10 Effects of a Heat-transfer on Corrosion of Zirconium in a Boiling Nitric Acid Solution ····· 160
7.11 Thermodynamic Study on Redox Reactions of Boiling Nitric Acid Solutions 164
7.12 Corrosion of Type 304L Stainless Steel in Simulated Acid Recovery Evaporator Solution ····· 167
7.13 Corrosion Fatigue of Refractory Metals in Boiling Nitric Acid ····· 170
8. Research on Advanced Transuranium Bearing Fuels ····· 173
8.1 Post Irradiation Examination of Nitride and Carbide Fuel Pins for Fast Reactor ····· 174
8.2 Investigation of Vaporization Behavior of Hyper-stoichiometric Uranium Dioxide by Knudsen Effusion Mass Spectrometry ····· 177
8.3 Anodic Dissolution of UN in LiCl-KCl Eutectic Melts ····· 180
8.4 Behaviors of Uranium and Plutonium at Simultaneous Recoveries into Liquid Cadmium Cathodes ····· 183
8.5 Post-irradiation Examination of Rock-like Oxide Fuels (4) –Ceramography and EPMA– ····· 186
8.6 Fabrication of Macro Grain Dispersed Type Rock-like Oxide Fuels ····· 189
8.7 Experimental Procedure of Leach Test for Irradiated Rock-like Oxide (ROX) Fuels ····· 192
8.8 Improvement of Power Distribution of Plutonium Rock-like Oxide Fuel Partial Loading PWR Core ····· 195
9. Research on Small Reactor for Dispersive Energy Supply System ····· 198
9.1 Study on Very Small Reactor for Heat Supply –Possibility of Deep Underground Siting : Examination of Static Stability for a Cave– ····· 199
9.2 Study on Very Small Reactor for Heat Supply- Evaluation of Economy - ···· 202
9.3 Design Study on Very Small Reactor for Small Grid Electricity Supply ···· 204

9.4 Development of Control Rod Drive Mechanism for Very Small Reactor-Back-up Mechanism with Passive Reactor Shut-down System- ····· 207
10. Facility Operation and Techniques Development ····· 210
10.1 Operation Report of Heat Transfer Fluid Flow Test Facility ····· 211
10.2 Operation Report of FCA ····· 212
10.3 Operation Report of TCA ····· 213
10.4 Maintenance Work Report of VHTRC ····· 214
11. Activities of the Research Committee ····· 215
11.1 Activities of Japanese Nuclear Data Committee ····· 216
11.2 Activities of the Research Committee on Reactor Physics ····· 220
Publication List ····· 221
Appendix I Department of Nuclear Energy System Organization Chart ····· 233
Appendix II Engineering Facilities Related to the Department ····· 235

Preface

The research activities of the Department of Nuclear Energy System, Japan Atomic Energy Research Institute, during the fiscal year 2001 (April 1, 2001 – March 31, 2002) are presented in this report. The Department is expected to develop an advanced nuclear energy system and to establish the related fundamental technologies for the system. The research activities cover such field as reactor physics, thermal-hydraulics, material science including research for advanced fuel and R&D for nuclear ship.

The total number of permanent staff working in the Department as of March 31, 2002 was 116 including the clerical service staff. The Department was funded from JAERI expenditure amounting to about 1.3 billion yen for FY 2001, excluding nuclear fuel cost and personnel expense. About 653 million yen was provided by the research contracts with external organizations; Science and Technology Agency (STA) for demonstration of reliability of new materials used in nuclear fuel reprocessing plant, Japan Nuclear Cycle Development Institute (JNC) for improvement of the evaluated nuclear data library for minor actinides, the Institute of Applied Energy for the development of the Reduced Moderation Water Reactor with passive safety equipment, the Institute of research and innovation (IRI) for research on IASCC data preparation for maintenance rule of aging BWR plants, and Mitsubishi Research Institute Inc. (MRI) for investigation of the development and research on cladding materials. The Department has served as the secretariat of Japanese Nuclear Data Center Committee, the Research Committee on Reactor Physics and the Research Committee on Marine Reactors.

The research activities have been conducted in nine research groups with the support of one division.

Nuclear Data Center

Research activities for nuclear data evaluations are devoted to the developments of JENDL (Japanese Evaluated Nuclear Data Libraries, including Special Purpose Files as well as General Purpose File) needed in nuclear energy applications, radiation applications, medical applications, and/or fundamental researches. A new version of JENDL-3.3 has been released to users this May after eight years endurable evaluation work and data confirmation work through benchmark test in cooperation with JNDC (Japanese Nuclear Data Committee). Total of 337 nuclides data are released on WEB site at JAERI Nuclear Data Center (http: //wwwndc.tokai.jaeri.go.jp).

This center acts as a National Data Center by disseminating the nuclear data to Japanese customers, contacting foreign or international centers to exchange the nuclear data information, and

coordinating international collaborations to enhance Research and Developments of nuclear data. To coordinate the development of JENDL, this center also acts as a secretariat of Japanese Nuclear Data Committee (JNDC). We held an International Conference on Nuclear Data for Science and Technology (ND2001) on 7-12 October 2001 in Tsukuba City attended total of 375 researchers. Proceedings has been published as a Supplement 2 Journal of Nuclear Science and Technology (2002).

Research Group for Energy System Assessment

In the assessment of nuclear energy systems, the role of reduced-moderation water reactors (RMWRs) was analyzed by developing long-term scenarios of nuclear power and its fuel cycle in Japan. Also, a database was developed on the isotope ratio of discharged fuel when plutonium from various sources is recycled to RMWRs or FBRs. In the study on the role of nuclear energy, a preliminary analysis was made on the economic impacts of nuclear phase-out by using an energy-economy interaction model. In addition, as an initial step of risk assessment on energy sources, an extensive review was made on existing studies relevant to risk and/or externality of energy systems.

Research Group for Advanced Reactor System

Main research activities of this group are the studies of reduced-moderation water reactor (RMWR), which include core and system design studies, safety analysis of MOX fuel rod for RMWR and investigation on simplified MOX reprocessing technology. Another research areas are development of anomaly detection system of nuclear power plants based on neural networks and new software integration methodology.

Research Group for Reactor Physics

Research field of this group covers very wide range of fundamental studies on reactor physics. Main areas are development of calculation code systems, reactor physics experiments using critical assemblies FCA and TCA and non-destructive assay of TRU content in radioactive waste package. The code development work has been continued for high speed and high accuracy Monte Carlo codes and nodal codes to construct a comprehensive code system for reactor core design including thermal-hydraulics, core management and kinetics. The experimental studies have been concentrated on the reduced-moderation water reactors and accelerator-driven sub-critical systems.

Research Group for Thermal and Fluid Engineering

Critical heat flux experiments for a reduced-moderation water reactor were performed using a

7-rod bundle test apparatus. A constant pressure thermal-hydraulic test facility was constructed in order to investigate the fluid mixing characteristics in a tight-lattice core. A boundary-fitted coordinate method was added into the ACE-3D code for two-phase flow analyses in complicated flow channels. Moreover, a newly mechanistic two-phase flow analysis code was developed to predict the boiling transition phenomenon in a fuel assembly.

Research Group for Reactor Structural Materials

This research group carries out irradiation assisted stress corrosion cracking (IASCC) study and development of material performance database. The group has aimed at clarifying the IASCC mechanism in in-core structural materials like stainless steels, at developing the method of evaluation and prediction of IASCC behavior, and at developing the countermeasures to IASCC. The group has also aimed at constructing the material database networking system.

Research Group for Compatible Materials

The chemical composition and production process of a candidate Fe-Cr-Ni alloy applied to the advanced LWR claddings was optimized. The degradation mechanism of cladding was analyzed with based on the effect of O and H formed by the low energy plasma excitation. On the reprocessing materials, the life prediction model for heat transfer tubes made of type 304ULC steel in acid recovery evaporators was established. The resistance to SCC of heat transfer components made of Zr in nitric acid was evaluated as a function of the corrosion potential.

Research Group for Advanced Fuel

Activities of the research group are focused on R&D on advanced fuels containing transuranium elements, which could contribute to realize flexible fuel cycle system in future. Rock-like oxide fuel has been developed for burning excess plutonium in existing LWRs, followed by direct disposal of spent fuel as a short-term subject. As a long-term subject, nitride fuel has been developed for transmutation of long-lived minor actinides and future fast reactors, being coupled with pyrochemical reprocessing by molten salt electrorefining.

Research Group of Small Reactor for Dispersive Energy Supply System

Two concepts of small reactor systems for dispersive energy supply have been studied by taking over the results of the nuclear ship research activities, which had been so far conducted; The one is a district heat supply system with a small light water reactor to be sited at deep underground, and the other is one for small grid electricity supply system. Thermal power of both the reactors is

100 MW. In the former study, static and dynamic stabilities of the underground caves installing the reactor system were confirmed analytically, and economics of the heat supply system were evaluated. In the latter study, the reactor core is designed for a long life cycle of operation until refueling. A concept of passive reactor shut down system for in case of an anomaly, which is a key technology common for both reactors, has been studied.

Reactor Engineering Facility Operation Division

This division operated three large-scale engineering facilities; FCA, TCA and Heat Transfer Fluid Flow Test Facilities in accordance with each experiment program and maintained in the monthly or the annual inspection. Consequently safety operations of these facilities were achieved and contributed sufficiently to the execution of each experimental study. Furthemore the maintenance work and decommissioning for VHTRC was carried out.

The Department is involved in the following project-oriented program in JAERI;

(1) Design Studies of Advanced Reactors,

(2) Engineering Research for a Fusion Reactor.

The activities of the Department in FY 2001 have contributed to the essential progress in the field of engineering.

Takamichi Iwamura,
Director,
Department of Nuclear Energy System
December 6, 2002

1. Nuclear Data

Both projects of JENDL-3.3 General Purpose File and JENDL Special Purpose Files have been progressed significantly with the cooperation of JNDC (Japanese Nuclear Data Committee) during this period. As a result for general purpose file, a new version of JENDL-3.3 was released to the users on May 2002 through our homepage (http://wwwndc.tokai.jaeri.go.jp/jendl/j33/j33.html). For the special purpose file, JENDL FP Decay Data File 2000 (JENDL/FPD-00) was also published.

As to the JENDL-3.3 General Purpose File, after several repeats of the extensive re-evaluation work for major actinides and minor actinides as well as light and medium mass nuclides including new data measurements for Er-isotopes and also data modification work through the benchmark tests performed in these 5 years, all data has been fixed and the final version was released as JENDL-3.3. Almost all of the feedback information from user's as well as integral tests results has been reflected to the new evaluations. Total of 337 nuclides in the incident energy region from 10^{-5} eV to 20MeV are released.

As to the Intermediate Energy File, which is inevitable for the Accelerator Driven System (ADS) in the nuclear transmutation technology, many efforts are made for the file developments for JENDL High Energy File, JENDL PKA/KERMA File and JENDL Photonuclear Data File. The evaluation work for the neutron and proton files up to 3GeV has been progressed. In connection with this high energy file, calculation of fission reactions in the framework of QMD+SDM (Quantum Molecular Dynamics plus Statistical Decay Model) was made and global tendency of fission neutrons with energy (from 10MeV to 10 GeV) was obtained.

Re-evaluation work for Am-242m, Am-243 and Pu-236 have been made to substitute for JENDL-3.3 and JENDL Actinides File. Also re-evaluation works for Tc-99 and Ce-140 as one of the most important fission products have been made. These evaluations are especially made in the needs from high burn-up applications for advanced nuclear reactors.

Mass chain evaluation has been continued within the framework of the international cooperation for the ENSDF File. The evaluation result for mass chain A=128 was published as the year of 2001/2002 out of 12 Japanese responsible mass chains (i.e., 118-129). FP Decay Data File project has been also completed and released as JENDL FP Decay Data File 2000 including the decay data of 1087 unstable fission product nuclides whose mass number covers from 66 to 172. Out line of evaluations as well as contents of data libraries are described.

1.1 Development of Japanese Evaluated Nuclear Data Library Version 3 Revision-3, JENDL-3.3

K. Shibata, T. Nakagawa, O. Iwamoto, J. Katakura, T. Fukahori, S. Chiba,
A. Hasegawa, H. Takano
(*e-mail:* shibata@ndc.tokai.jaer.go.jp)

The second revision of JENDL-3 (JENDL-3.2)[1] was released in 1994. Since then, the data have been used in various application fields. However, some problems of the library were pointed out by comparing with differential and integral measurements. The evaluation work for JENDL-3.3 started in 1997 to solve the problems of JENDL-3.2. The evaluation and compilation were completed in March 2002, and the library was officially released as JENDL-3.3, which provides the neutron-induced reaction data for 337 nuclides in the incident energy region from 10^{-5} eV to 20 MeV.

As for medium-heavy nuclides, resolved resonance parameters were revised for V, ^{46,48,49,50}Ti, ^{50,52,53,54}Cr, ^{54,56}Fe, ^{58}Ni, ^{59}Co, ^{99}Ru, and ^{186}W by examining experimental data. We kept a policy of isotopic evaluation without producing elemental data files. There are only 2 elemental data files in JENDL-3.3: carbon and vanadium. For many nuclides, reaction cross sections such as (n,2n) were re-evaluated by using nuclear model calculations. Angle-dependent neutron emission spectra were taken from JENDL Fusion File 99 (JENDL/F-99)[2]. The data on erbium and mercury isotopes were newly evaluated for JENDL-3.3; erbium is a candidate material for a burnable poison, and mercury is used for a spallation target. Concerning erbium, we considered the capture cross sections newly measured by the Tokyo Institute of Technology group[3]. The number of nuclides which contain gamma-ray production data increased from 66 to 114 by using nuclear model calculations.

Nuclear data for several important heavy nuclides, Th, U, and Pu isotopes, were extensively re-evaluated for JENDL-3.3. The objective of the current revision was to solve a problem of effective multiplication factors (k_{eff}) overestimated by JENDL-3.2. According to the benchmark analyses with the JENDL-3.2 data, this problem was remarkable for thermal reactor cores with UO_2 fuel, although the prediction of k_{eff} for fast reactor cores was quite acceptable. The resolved resonance parameters of ^{235}U and the prompt fission neutron spectra for ^{235}U were revised in order to solve this problem. In Fig. 1.1.1, the presently evaluated thermal fission neutron spectrum of ^{235}U is illustrated relative to that of JENDL-3.2. Furthermore, fission cross sections of major actinides were updated[4] above several tens of keV by considering recent measurements.

As for minor actinides, the data of ^{237}Np, ^{236}Pu, ^{238}Pu, Am and Cm isotopes were revised, and those of ^{235}Np, ^{237}Pu, ^{244}Pu, ^{246}Pu, ^{240}Cm and ^{237}Bk were newly evaluated. Evaluation of important minor actinide data was made under the International Science and Technology Center projects. These results were reviewed and widely adopted for JENDL-3.3.

The previous library JENDL-3.2 contains covariance data only for ^{55}Mn, although we were requested to prepare covariances for the nuclides which were required to evaluate the characteristics of fast reactors. In order to meet the needs, covariance data were evaluated for selected nuclides in JENDL-3.2, and they were made available as the JENDL-3.2 Covariance File[5]. These covariance data were obtained from measurements or nuclear model calculations which the evaluated mean data were based on. Most of the covariance data were also adopted in JENDL-3.3 with a slight modification. The simultaneous evaluation[4] yielded the covariance matrices for the fission cross sections of ^{233,235,238}U and ^{239,240,241}Pu in the energy region above several tens of keV. The matrices represent not only the correlation of individual fission cross sections between different incident energies but also that of a fission cross sections with another fission cross section, e.g., ^{235}U(n,f) vs. ^{239}Pu(n,f). In JENDL-3.3, covariances are included for 20 nuclides.

Benchmark problems were selected to examine the reliability of the JENDL-3.3 data for reactor and shielding applications. Effective multiplication factors, k_{eff}, were calculated[6] for thermal and fast neutron cores by using a continuous energy Monte Carlo code MVP. The calculations were performed with a statistical uncertainty of 0.02% in k_{eff} values. Figure 1.1.2 shows the result obtained for U-fuel thermal cores. It is found from the figure that the JENDL-3.3 calculations are in good agreement with the measurements at highly enriched U fuel cores of STACY, TRACY and JRR-4, which is due to the modifications of the fission neutron spectrum and thermal fission cross sections of ^{235}U.

References:

1) T. Nakagawa et al.: J. Nucl. Sci. Technol., 32, 1259 (1995).
2) S. Chiba et al.: J. Nucl. Sci. Technol., 39, 187 (2002).
3) A.K.M. Harun-ar-Rashid et al.: J. Nucl. Sci. Technol., 37, 421 (2000).
4) T. Kawano et al.: J. Nucl. Sci. Technol., 37, 327 (2000).
5) K. Shibata et al.: J. Nucl. Sci. Technol., Suppl. 2, 40 (2002).
6) H. Takano et al.: J. Nucl. Sci. Technol., Suppl. 2, 847 (2002).

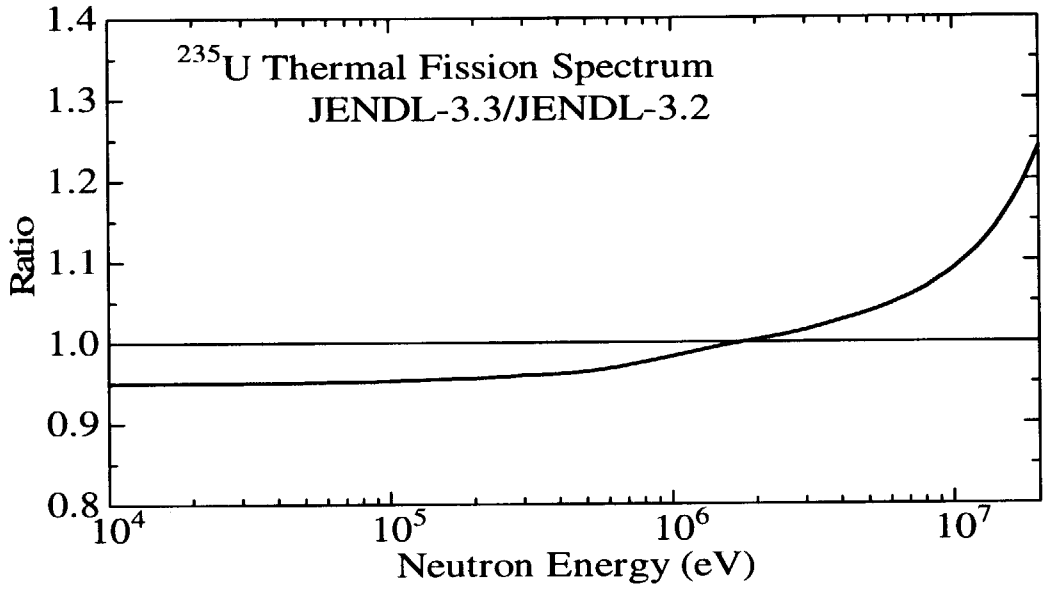

Fig. 1.1.1 Ratio of ^{235}U thermal fission spectra in JENDL-3.3 to those in JENDL-3.2

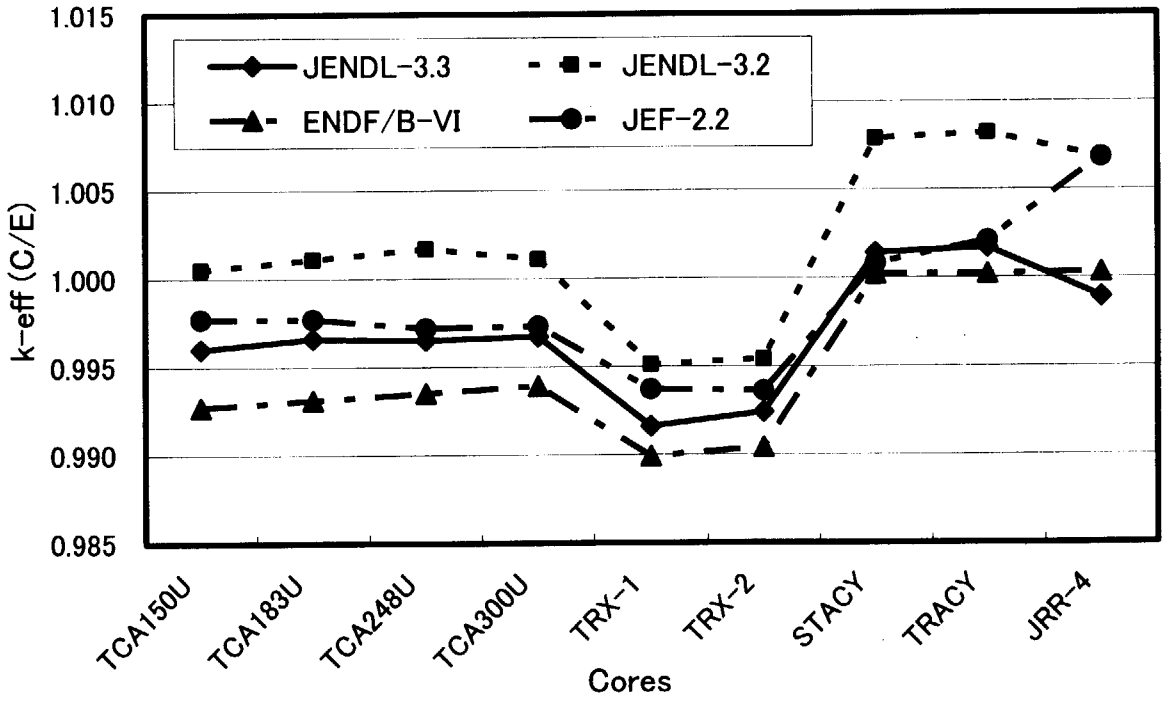

Fig. 1.1.2 C/E values of effective multiplication factors (k_{eff})
for U-fueled thermal-neutron cores

1.2 Nuclear Data Evaluation and Compilation for JENDL Intermediate Energy Files in 2001

T. Fukahori and Japanese Nuclear Data Committee (High Energy Nuclear Data Evaluation WG)
(*E-mail*: fukahori@ndc.tokai.jaeri.go.jp)

The JAERI Nuclear Data Center has been cotinuing evaluation work in cooperation with Japanese Nuclear Data Committee (JNDC) to produce files related intermediate energy, which are JENDL High Energy File, JENDL PKA/KERMA File and JENDL Photonuclear Data File.

The JENDL High Energy File includes nuclear data for proton- and neutron-induced reactions. Below 20 MeV, the data of JENDL-3.3 are adopted. The neutron file for IFMIF[1] in the energy range up to 50 MeV has been merged with files below 20 MeV. The evaluation work for the neutron and proton files energy range up to 3 GeV is performed for the second-priority 42 nuclei by mainly using the "quick-GNASH system"[2], JQMD code[3] and NMTC/JAM code[4]. The target isotopes included in the JENDL High Energy File are summarized in Table 1.2.1 as well as priorities and status. In year 2001, evaluation of over 40 nuclides for proton- and neutron induced reactions has been done, including important actinide nuclides of ^{235}U and ^{238}U. For an example of evaluated results, neutron induced fission cross section of ^{238}U is shown in Fig. 1.2.1 as well as experimental data and GNASH calculation.

The JENDL Photonuclear Data File is being developed for gamma-ray induced reaction data up to 140 MeV. The photon absorption cross section is evaluated with the giant dipole resonance model and quasi-deuteron model, and the decaying processes are estimated with the statistical model with preequilibrium correction by using MCPHOTO[5] and ALICE-F[6] codes. Evaluated results for the 26 target nuclides were compared with the other photonuclear data files evaluated at Los Alamos, Beijing, Moscow and Obninsk as well as experimental data. The evaluated results were compiled in ENDF-6 format and that preliminary review was performed. The work until year 2001 was summarized in Ref. 7).

The JENDL PKA/KERMA File is generated to supply primary knock-on atom (PKA)

spectra, damage energy spectra, DPA (displacement per atom) cross sections and kerma factors by neutron-induced reactions in the energy region up to 50 MeV. A processing code system, ESPERANT[8] was developed to calculate above quantities from evaluated nuclear data file by using effective single particle emission approximation (ESPEA). For light mass nuclei, SCINFUL/DDX code, which considers break-up reactions with PKA spectra, is used as well as EXIFON code which can calculate with correction of preequilibrium process. The work was summarized in Ref. 9).

References

1) K. Noda: Proc. of 1994 Symposium on Nuclear Data, Tokai, Japan, Nov. 17-18, 1994, JAERI-Conf 95-008, p.112 (1995).
2) M.B. Chadwick and P.G. Young: Phys. Rev., **C47**, 2255 (1993).
3) K. Niita and S. Chiba: "JQMD: Quantum Molecular Dynamics and Statistical Decay Model Code", private communication.
4) K. Niita: "NMTC/JAM Code", private communication.
5) N. Kishida and H. Kadotani: private communication.
6) T. Fukahori: Proc. Specialists' Meeting on High Energy Nuclear Data, Tokai, Ibaraki, Oct. 3-4, 1991, JAERI-M 92-039, p.114 (1992).
7) N. Kishida, et al.: "Present Status of JENDL Photonuclear Data File", J. Nucl. Sci. Technol., **Sup. 2**, 56 (2002).
8) T. Fukahori, et al.: Proc. of the Third Specialists' Meeting on Nuclear Data for Fission Reactors, Tokai, Japan, Nov. 29-30, 1995, JAERI-Conf 96-005, p.130 (1996).
9) T. Fukahori, et al.; "JENDL PKA/KERMA File for IFMIF Project", Proc. the Tenth International Symposium on Reactor Dosimetry, Sep.12-17, 1999, Osaka, Japan, *Reactor Dosimetry: Radiation Metrology and Assessment, ASTM STP 1398*, pp.591, Jhon G. Williams, David W. Vehar, Frank H. Ruddy, and David M Gilliam, Eds., American Society for Testing and Materials, West Conshohocken, PA, 2001.

Table 1.2.1 Isotopes included in neutron and proton file up to 3 GeV and their priorities and status

Priorities	Evaluation Finished (Under Compilation)	Under Evaluation	Planning
1st priority (40 nuclides)	H-1, C-12, N-14, O-16, Al-27, Cr-50,52-54, Fe-56, Cu-63,65, W-180,182-184,186, Hg-196,198-202,204, Pb-208, Bi-209, U-235,238	Fe-54,57,58, Ni-58,60-62, Au-197, Pb-204,206,207	Ni-64
2nd priority (45 nuclides)	Si-28-30, K-39,41, Ca-40,42-44,46,48, Ti-46-50, Mn-55, Zr-90-92,94,96, Nb-93, Pu-238-242	H-2, Mg-24-26, V-51, Co-59,	Be-9, B-10,11, Mo-92,94-98,100, Ta-181
3rd priority (37 nuclides)	Zn-64,66-68,70, Np-237, Am-241,242,242m,	C-13, F-19, Na-23, Cl-35,37, Ar-35,38,40, Ga-69,71, Ge-70,72-74,76, As-75, Y-89,	Li-6,7, Th-232, U-233,234,236, Am-243, Cm-243-246

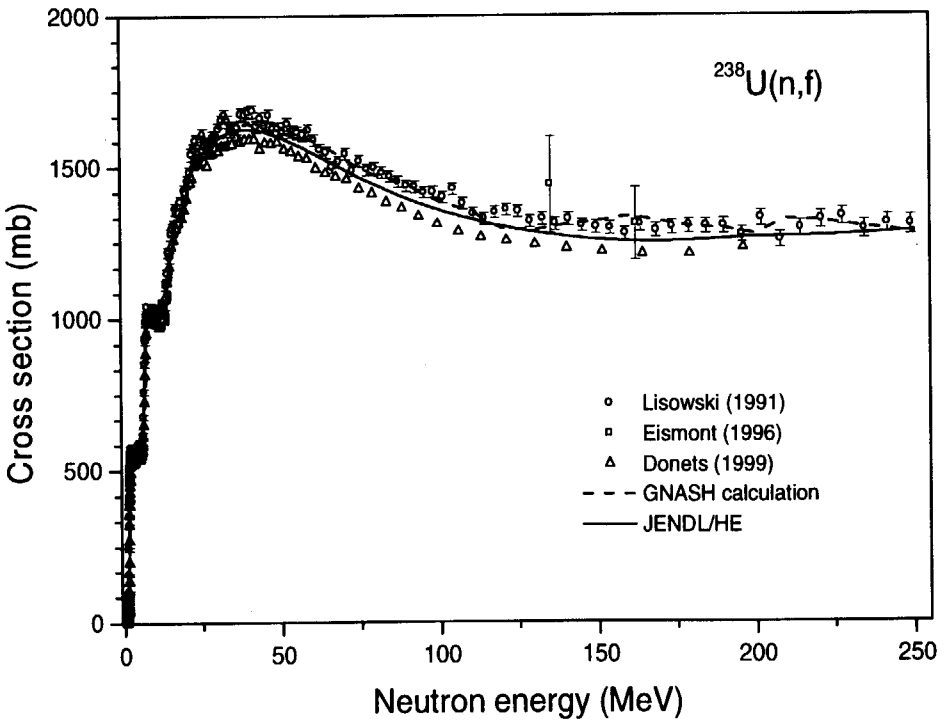

Fig. 1.2.1 Evaluated result (solid line) of ^{238}U(n,f) cross section with experimental (symbols) data and GNASH calculated result (dashed line)

1.3 Re-evaluation of Nuclear Data for ^{242m}Am, ^{243}Am, ^{99}Tc and ^{140}Ce

T. Nakagawa, O. Iwamoto and A. Hasegawa
(*E-mail*: nakagawa@ndc.tokai.jaeri.go.jp)

Nuclear data given in JENDL-3.2 on the neutron-induced reactions with ^{242m}Am, ^{243}Am, ^{99}Tc and ^{140}Ce were revised. These nuclides are important minor actinides and fission product nuclides.

For the data of ^{242m}Am and ^{243}Am, the data were revised on the basis of recent evaluation made by Maslov et al.[1,2] Their data were adopted for the resonance parameters, the total, capture, inelastic scattering, (n,2n) and (n,3n) reaction cross sections after slight modification if needed. The data of JENDL-3.2 were adopted for the fission cross sections. The number of prompt neutrons and energy spectra were also based on Maslov's evaluation whereas the data of delayed neutrons were different from their data.

For the data of ^{99}Tc and ^{140}Ce, the basic model parameters such as the optical potential and level scheme were revised from JENDL-3.2 evaluation. Figure 1.3.1 shows the total cross section of ^{99}Tc in the MeV region. The present calculation from the new parameters is in good agreement with experimental data. The resonance parameters of ^{99}Tc were also revised by adopting recent analysis made by Gunsing et al.[3] after a small modification. The capture cross section was calculated with the statistical model. As shown in Fig. 1.3.2, the present result is in good agreement with the recent measurements by Kobayashi et al.[4] For ^{140}Ce, the resonance parameters were slightly modified so as to reproduce well the capture cross section measured by Harnood et al.[5] Figure 1.3.3 shows the capture cross section of ^{140}Ce. As a result of this modification, Maxwellian averaged capture cross section around kT=30 keV important for the astrophysics was improved to agree with experimental data. The inelastic scattering cross sections were calculated with the new model parameters for the both nuclides. Concerning other threshold reaction cross sections, JENDL-3.2 data were adopted in principle except the ^{99}Tc(n,nα) reaction cross section which was renormalized to the experimental data of Ikeda et al.[6]

Present results were adopted in JENDL-3.3 which were compiled in the ENDF-6 format, and released in May, 2002.

References

1) V.M. Maslov, E.Sh. Sukhovitskij, Yu.V. Porodzinskij and G.B. Morogovskij: "Evaluation of Neutron Data for Americium-242m," INDC(BLR)-7 (1997).

2) V.M. Maslov, E.Sh. Sukhovitskij, Yu.V. Porodzinskij, A.B. Klepatskij and G.B. Morogovskij: "Evaluation of Neutron Data for Americium-243," INDC(BLR)-006 (1996).

3) F. Gunsing, A. Lepretre, C. Mounier, C. Raepsaet, A. Brusegan and E. Macavero: Phys., Rev., **C61**, 054608 (2000).

4) K. Kobayashi, S. Lee, S. Yamamoto, T. Yoshimoto, Y. Fujita, G. Kim, Y. Lee and J. Chang: Proc. International Conf. Nucl. Data Sci. Technol., Tsukuba, Japan, Oct. 7 – 12, 2001, Vol. 1, p.214 (2002).

5) S. Harnood, M. Igashira, T. Matsumoto, S. Mizuno and T. Ohsaki: J. Nucl. Sci. Eng., **37**, 740 (2000).

6) Y. Ikeda, E.T. Cheng, C. Konno and H. Maekawa: Nucl. Sci. Eng., **116**, 28 (1994).

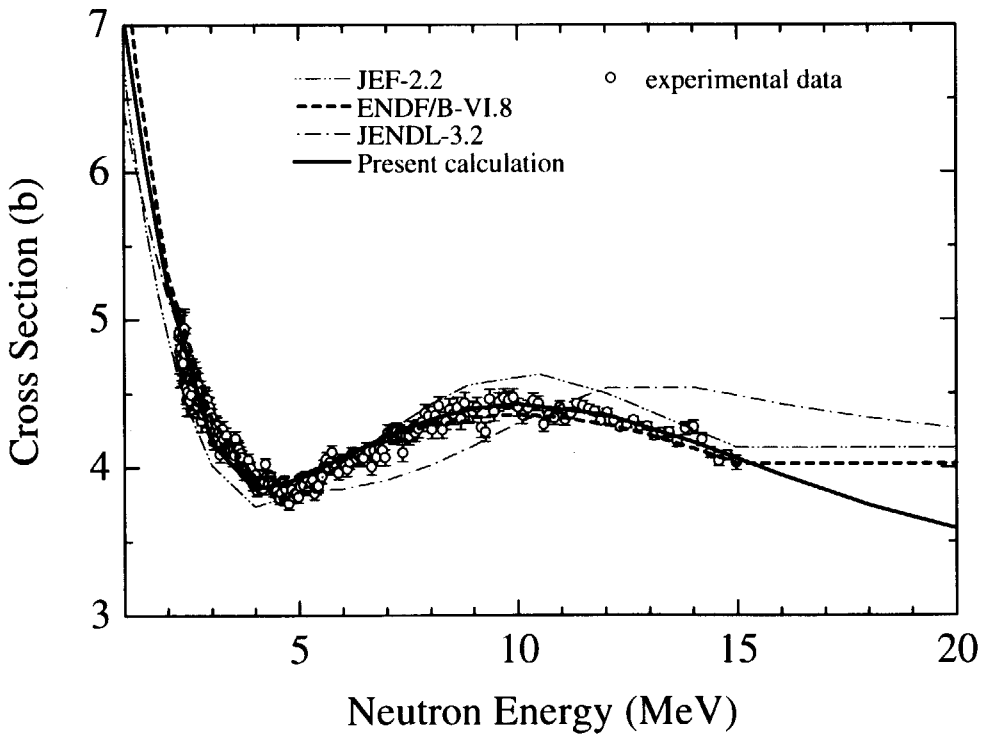

Fig. 1.3.1 Total cross section of ^{99}Tc (MeV region)

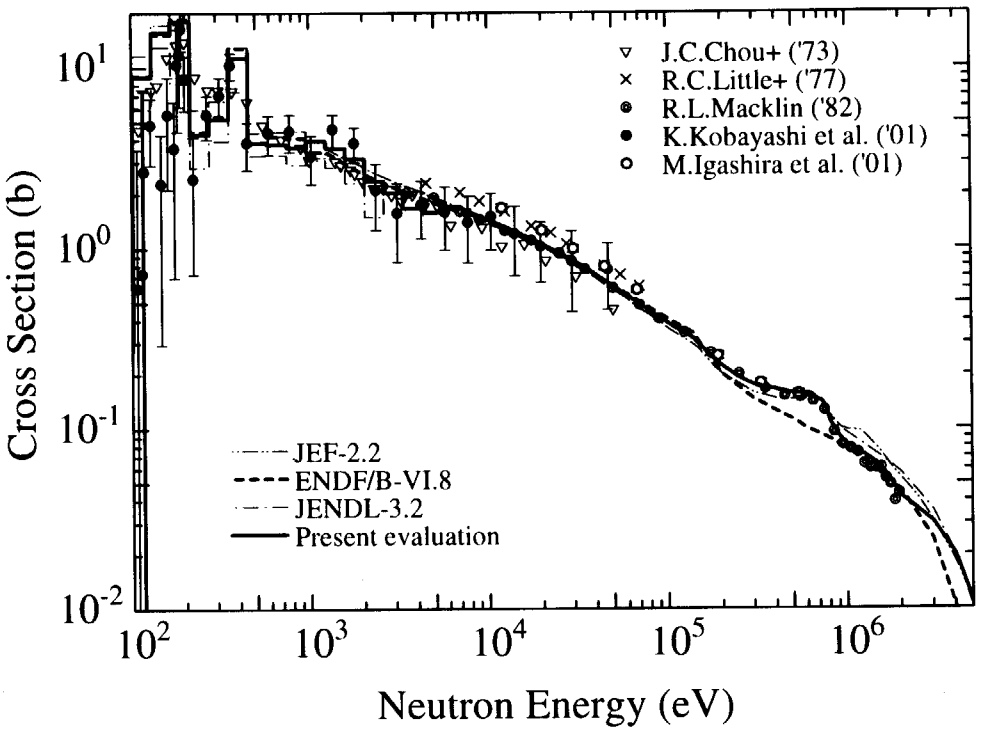

Fig. 1.3.2 Capture cross section of ^{99}Tc

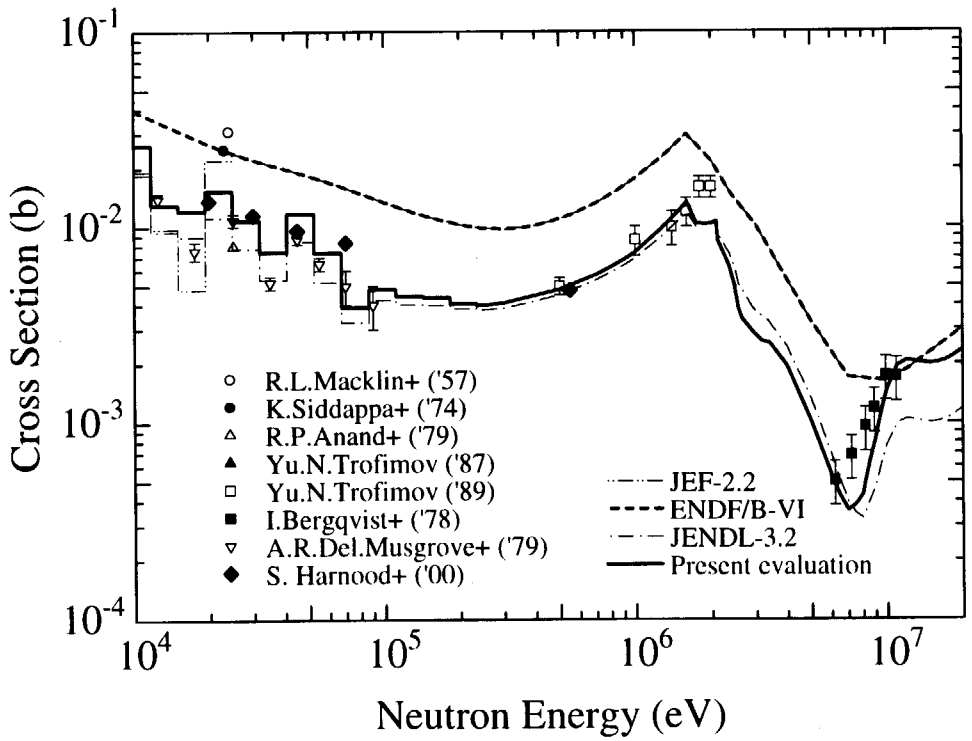

Fig. 1.3.3 Capture cross section of ^{140}Ce

1.4 Evaluation of Neutron-induced Reactions on ^{236}Pu for JENDL-3.3

O. Iwamoto and T. Nakagawa

(*E-mail:* iwamoto@ndc.tokai.jaeri.go.jp)

Cross sections and energy-angular distributions of emitted neutrons were evaluated for the neutron-incident reactions on ^{236}Pu in the incident energy range of 10 eV to 20 MeV by using a statistical model combined with a coupled channel optical model. The calculated results were compiled to the latest evaluated nuclear data library JENDL-3.3 in the ENDF-6 format. The unresolved resonance region is assumed to be from 10 eV to 30 keV, and the averaged resonance parameters were obtained to reproduce the calculated cross sections. Maxwell temperatures for fission neutron spectra were estimated from a systematics with a correction for prefission neutrons. Details of the present work are written in the reference.[1)]

The coupled channel (CC) method with a deformed optical potential was used to estimate transmission coefficients of the neutron channel in the Hauser-Feshbach statistical model, and also to calculate total, elastic scattering and direct-inelastic cross sections. For the CC calculation, the coupled channel optical model code OPTMAN[2)] was used in the rigid rotor option. Four discrete levels in the ground state rotational band were included in the calculation. The optical model potential parameters were taken from a recent study for ^{238}U.[3)]

Neutron and γ-ray emissions and fission were taken into account as decay channels in the statistical model calculation. The statistical model calculation was performed by the code GNASH.[4)] Preequilibrium processes were taken into account using the exciton model. The Fermi gas level density formula given by Gilbert and Cameron[5)] was used. A cumulative plot calculated with the obtained level density parameters for ^{237}Pu is shown in Fig. 1.4.1 with known excited levels. The fission transmission coefficient was calculated by assuming double parabolic fission barrier.

The result of fission cross section is shown in Fig. 1.4.2 with available experimental data[6)-9)] in the experimental nuclear reaction data library EXFOR and evaluated data.

The present result reproduces the experimental data at 10 to 100 eV and above 1 MeV well.

References

1) O. Iwamoto, T. Nakagwa: "*Evaluation of Neutron-induced Reactions on ^{236}Pu for JENDL-3.3*", JAERI-Research 2002-013 (2002)

2) E. Sh. Sukhovitskiĭ, Y. V. Porodzinskiĭ, O. Iwamoto, S. Chiba, K. Shibata: "*Programs OPTMAN and SHEMMAN version 5 (1998)*", JAERI-Data/Code 98-019 (1998)

3) E. Sh. Sukhovitskiĭ, O. Iwamoto, S. Chiba, T. Fukahori: J. Nucl. Sci. Technol., **37**, 120 (2000)

4) P. G. Young, E. D. Arthur, M. B. Chadwick: "*Proceedings of the Workshop Nuclear Reaction Data and Nuclear Reactors - Physics, Design and Safety - *", Trieste, Vol. 1, p. 227 (1998) World Scientific

5) A. Gilbert, A. G. W. Cameron: Canadican J. Phys. **43**, 1446 (1965)

6) E. A. Gromova, S. S. Kovalenko, Yu. A. Selitskii, A. M. Fridkin, V. B. Funshtein, V. A. Yakovlev, S. V. Antipov, P. E. Vorotnikov, B. M. Gokhberg, V. V. Danichev, V. N. Dement'ev, V. S. Zenkevich, S. A. Isakov: Sov. Atom. Ener. **68**, 223 (1990) EXFOR 41064

7) P. E. Vorotnikov, B. M. Gokheerg, E. A. Gromova, S. S. Kovalenko, Yu. A. Selitskiy, A. M. Fridkin, V. B. Funshtein, V. A. Yakovlev: "*Proceedings of 1st. Int. Conf. on Neutron Physics*", Kiev, 14-18 Sep 1987, Vol. 3, 76 (1987) EXFOR 40992

8) B. N. Belyaev, E. A. Gromova, V. N. Dement'ev, V. S. Zenkevich, A. V. Lovtsyus, Yu. A. Selitskii, A. M. Fridkin, V. B. Funshtein, V. A. Yakovlev: Sov. Atom. Ener. **68**, 332 (1990) EXFOR 41093

9) J. E. Gindler, J. Gray Jr., J. R. Huizenga: Phys. Rev. **115**, 1271 (1959) EXFOR 13572

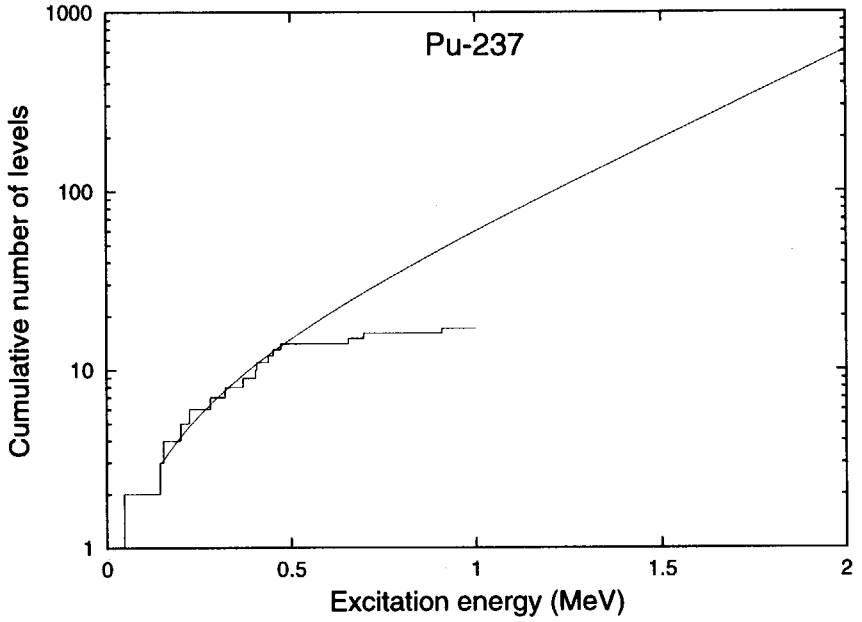

Fig. 1.4.1 Cumulative plot of level density and experimental levels for ^{237}Pu. Smoothed line is given by level density formula and staircase plot by experimental levels.

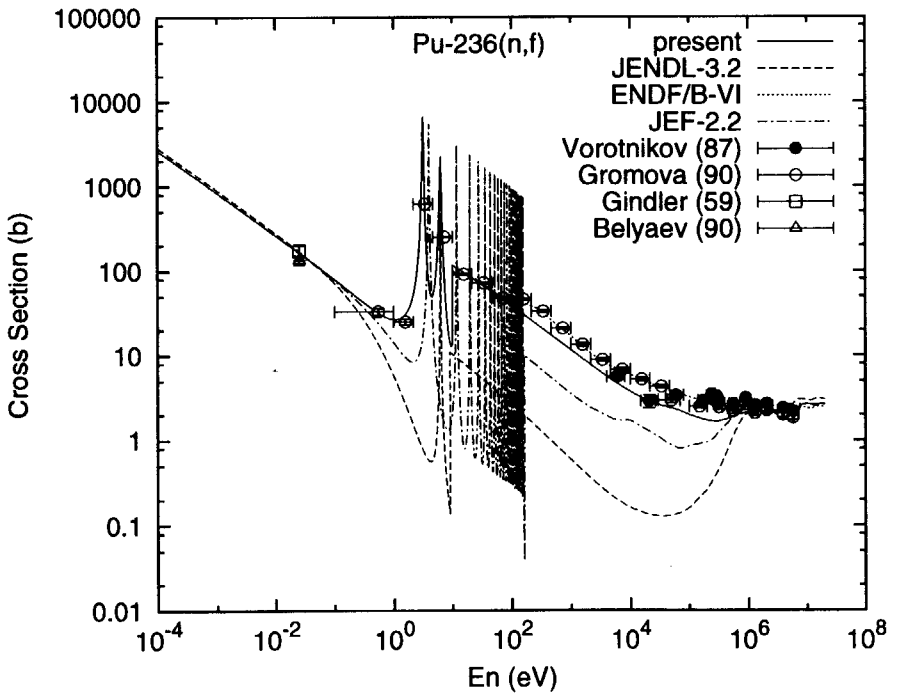

Fig. 1.4.2 Comparison of fission cross section

1.5 Calculation of Fission Reaction in the Framework of QMD + SDM

O. Iwamoto, Jian RONG*, T. Fukahori and S. Chiba

(*E-mail:* iwamoto@ndc.tokai.jaeri.go.jp)

Various quantities related to fission reaction induced by nucleon are calculated using the Quantum Molecular Dynamics (QMD) plus Statistical Decay Model (SDM) in the energy range 10 MeV to 10 GeV.

The QMD, which was originally developed to analyse medium energy heavy ion nuclear reaction, is useful to analyse such a process as many nucleons are involved in the reaction, because the QMD treats the dynamics of all nucleons explicitly. Recently, the QMD incorporated with SDM, (QMD + SDM), was successfully applied to analyse both the energy-angular distribution of emitted nucleons and the production cross section for the fragments, from medium-heavy nucleus induced by nucleon in the energy range from 100 MeV to several GeV.[1),2)]

The fragment mass distribution was calculated for ^{208}Pb at 1.6-GeV proton incident energy, and is shown in Fig. 1.5.1 with experimental data by Gloris *et al.*[3)] The calculated result reproduces the experimental mass distribution well. Two flat regions in the fragment distribution can be seen around A=100 and 180. In the larger mass region, the fragments are mainly produced by emitting light particles without fission. On the other hand, the fragments in the smaller mass region are produced by the fission process. The left hand peak is constructed primarily by the evaporated light particles in the SDM stage ($\sim$ 60%) and secondarily in the QMD ($\sim$ 40%). Around A=100 the calculated result shows rather flat tendency than the experimental value.

Figure 1.5.2 shows fission neutron energy spectrum χ calculated by QMD + SDM for ^{238}U induced by neutron at 500 MeV (left) and 2 GeV (right). The spectra are obtained by selecting fission events from all events. The fission spectrum is shown by decomposing into the components classified by their origin from which the neutron is emitted (QMD, pre-fission SDM or post-fission SDM). The neutrons emitted from QMD

*An STA Fellow during, August, 2000 - July, 2001

stage, which can be considered as direct or pre-equilibrium process, is shown by thin solid line. This spectrum shows the broad distribution up to the incident neutron energy with quasi elastic peak at the upper end of spectrum, which can be seen in inserted figure for E_n=500 MeV. The spectra of neutron from SDM stage show evaporation shape. In the figure the spectra are decomposed into pre-fission (doted line) and post-fission (dot-dashed line) components. The incident energy dependence of the evaporation spectra can be seen. The increase of incident energy causes the spectrum harder especially for pre-fission neutron. The results fitted by Maxwellian distributions are also shown by the smooth line for E_n=2 GeV in Fig. 1.5.2. The spectrum for pre-fission neutron can be fitted by a single Maxwellian but post-fission neuron spectrum cannot be fitted by a single Maxwellian. In the figure the curve fitted by sum of two Maxwellian distributions is shown for the post-fission neutron spectrum. This means pre-fission nucleus emitting neutron has the almost same temperature. After fission the temperature of the nucleus (fission products) decreases with emitting particles.

The details of the present work are shown in reference.[4)]

References

1) K. Niita, S. Chiba, T. Maruyama, T. Maruyama, H. Takada, T. Fukahori, Y. Nakahara, A. Iwamoto: *Phys. Rev.* **C52**, 2620 (1995).

2) S. Chiba, O. Iwamoto, T. Fukahori, K. Niita, T. Maruyama, T. Maruyama, A. Iwamoto: *Phys. Rev.* **C54**, 285 (1996).

3) M. Gloris, R. Michel, U. Herpers, F. Sudbrock, D. Filges: *Nucl. Instr. and Meth.* **B113**, 429 (1996).

4) O. Iwamoto, J. Rong, T. Fukahori, S. Chiba: *"Proceedings of the International Conference on Nuclear Data for Science and Technology"*, *J. Nucl. Sci. Technol.* **Suppl. 2**, 128 (2002).

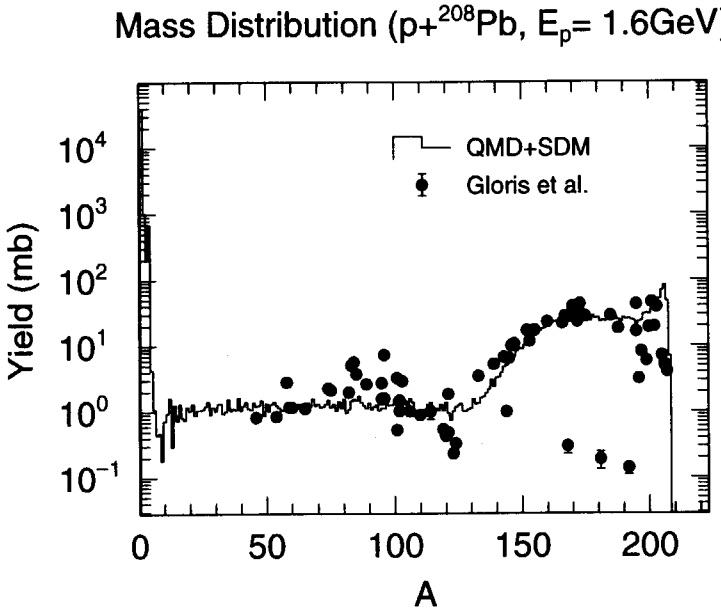

Fig. 1.5.1 Mass distribution for p+^{208}Pb at 1.6 GeV. Line shows calculated results of QMD + SDM and closed circle means experimental data of Gloris *et al.*[3] for ^{208}Pb.

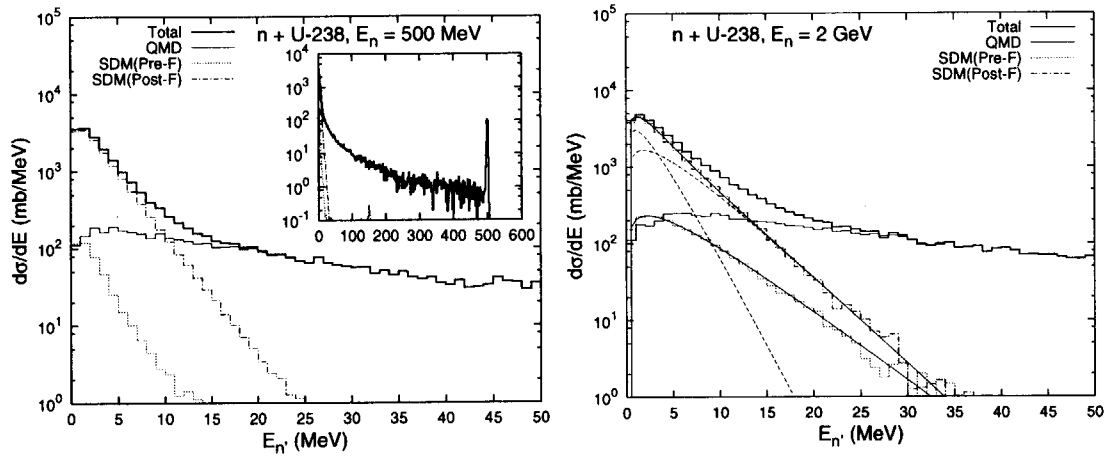

Fig. 1.5.2 Fission neutron energy spectrum for n+^{238}U by QMD + SDM calculation at the incident neutron energy 500 MeV (left) and 1 GeV (right). The staircase plots show calculated results by QMD + SDM and smoothed lines show results fitted by Maxwellian distribution (dashed lines in the lower figure show single Maxwellian components). Thick solid line shows total neutron spectrum with fission event. Thin solid line is for neutron from QMD process. Doted line and dot-dashed line shows neutron emitted from pre-fission nucleus and fission product in SDM precess, respectively.

1.6 Evaluation and Compilation of Nuclear Structure and Decay Data in 2001

J. Katakura and ENSDF Group*
(*E-mail*: katakura@ndc.tokai.jaeri.go.jp)

The international network on nuclear structure and decay data evaluation aims at complete and continuous nuclear structure and decay data evaluation of all mass chains. The evaluated data are compiled as ENSDF (Evaluated Nuclear Struccture Data File) file. The data file is maintained and distributed by National Nuclear Data Center, Brookhaven National Laboratory (BNL), U.S.A. As a member of the network, Japanese group, whose data evaluation center is Nuclear Data Center, Japan Atomic Energy Research Institute, has responsibility for evaluating 12 mass chains with A=118-129.

In the fiscal year of 2001 (from April 2001 to March 2002), the evaluations of A=128 mass chain was published in Nuclear Data Sheets [1]. The evaluation includes all experimental data available after the last evaluations performed in 1983. The published data sets of A=128 are listed in table 1.6.1. These data sets are evaluated based on the all available measured data relating to A=128 mass. Each data set excepting "Adopted Levels, Gammas" or "Adopted Levels" data sets is the evaluated data set from the same kind of measurements categolized in the name of the data set. The "Adopted Levels, Gammas" or "Adopted Levels" data sets are compiled from the each data set in the same nuclide.

The new data from the last evaluation of other mass chains to which Japanese group has the responsibility are reviewed and being prepared for update of the last mass chain evaluation.

References:

1) M. Kanbe, K. Kitao: Nucl. Data Sheets, **94**, 227 (2001)

*Members are H. Iimura, M. Oshima, S. Ohya, J. Katakura, M. Kanbe, K. Kitao and Y. Tendow

Table 1.6.1 Evaluated data sets of A=128

Nuclide	Data Type	Nuclide	Data Type
^{128}Ag	Adopted Levels	^{128}I	^{127}I(d,p) ^{128}Te(p,nγ) ^{128}Te(^{3}He,t) IAS ^{129}I(d,t)
^{128}Cd	Adopted Levels, Gammas ^{128}Ag β^- Decay		
^{128}In	Adopted Levels, Gammas ^{128}Cd β^- Decay	^{128}Xe	Adopted Levels, Gammas ^{128}I β^- Decay (24.99 min) ^{128}Cs ε Decay (3.62 min) ^{125}Te(α,nγ),^{126}Te(α,2nγ) ^{126}Te(^{3}He,n) Coulomb Excitation (HI,xnγ)
^{128}Sn	Adopted Levels, Gammas ^{128}In β^- Decay (0.84 s) ^{128}In β^- Decay (0.72 s) ^{128}Sn IT Decay (6.5 s) ^{129}In β^-n Decay (0.610 s) ^{129}In β^-n Decay (1.23 s)		
^{128}Sb	Adopted Levels, Gammas ^{128}Sn β^- Decay (59.07 min) ^{128}Sb IT Decay (10.4 min)	^{128}Cs	Adopted Levels, Gammas ^{128}Ba ε Decay ^{120}Sn(^{11}B,3nγ)
^{128}Te	Adopted Levels, Gammas ^{128}Sb β^- Decay (9.01 h) ^{128}Sb β^- Decay (10.4 min) ^{128}I ε Decay ^{126}Te(t,p) ^{128}Te(γ,γ') ^{128}Te(n,n'γ) ^{128}Te(p,p') ^{128}Te(d,d') ^{128}Te(α,α') Coulomb Excitation ^{130}Te(p,t) ^{130}Te(^{64}Ni,X)	^{128}Ba	Adopted Levels, Gammas ^{128}La ε Decay (< 1.4 min) ^{128}La ε Decay (5.23 min) (HI,xnγ)
		128La	Adopted Levels, Gammas ^{128}Cs ε Decay (HI,xnγ)
		^{128}Ce	Adopted Levels, Gammas ^{128}Pr ε Decay (HI,xnγ)
		128Pr	Adopted Levels, Gammas ^{128}Nd ε Decay ^{94}Mo(^{40}Ca,αpnγ)
^{128}I	Adopted Levels, Gammas ^{127}I(n,γ) E=thermal: Secondary ^{127}I(n,γ) E=thermal: Primary	^{128}Nd	Adopted Levels, Gammas ^{92}Mo(^{40}Ca,2p2nγ)
		^{128}Pm	Adopted Levels

1.7 Compilation of JENDL FP Decay Data File 2000

J. Katakura, T. Yoshida, K. Oyamatsu and T. Tachibana
(*E-mail*: katakura@ndc.tokai.jaeri.go.jp)

JENDL FP Decay Data File 2000 (JENDL/FPD-00) has been compiled as a special purpose file of JENDL files [1, 2]. The JENDL/FPD-00 file includes the decay data of 1087 unstable fission product nuclides whose mass number covers from 66 to 172. The characteristic of the file is summarised on Table 1.7.1. As seen in this table, the JENDL/FPD-00 file adopts theoretically estimated average decay energy and spectrum data when there are no or incompletely measured data.

Table 1.7.1 Summary of JENDL FP Decay Data File 2000

No. of Nuclides	Data Type, Comments
1087	Unstable nuclides or states
197	First isomeric states
8	Second isomeric states
1087	Average gamma decay energy values
506	Measured (From ENSDF)
581	Theoretically estimated
1087	Average beta decay energy values
544	Measured
543	Theoretically estimated
1053	Gamma ray spectra
496	Measured spectrum only
431	Theoretically estimated spectrum only
126	Measured + Estimated
899	Beta ray spectra
374	Measured spectrum only
432	Theoretically estimated spectrum only
93	Measured + Estimated

The decay heat and spectrum calculations using the JENDL/FPD-00 file are able to reproduce the measured data of various kinds of fissionable nuclides. Examples of the decay heat and spectrum comparisons are shown in Figs. 1.7.1 through 1.7.3.

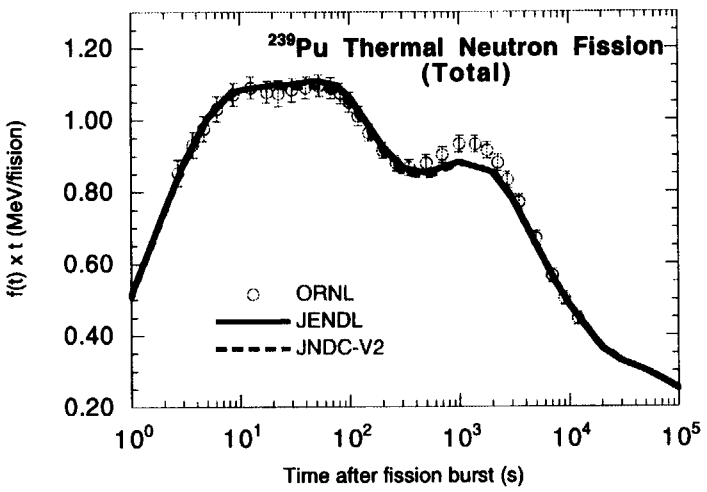

Fig. 1.7.1 FP decay heat of ^{239}Pu thermal neutron fission.

As seen in these figures, the JENDL/FPD-00 file can reproduce well the measured values of decay heat and aggregate beta- and gaama-ray spectra of fission product nuclides.

References:

1) T. Katakura, T. Yoshida, K. Oyamatsu and T. Tachibana: J. Nucl. Sci. Technol., **38**, 470 (2001).

2) T. Katakura, T. Yoshida, K. Oyamatsu and T. Tachibana: JAERI 1343 (2001).

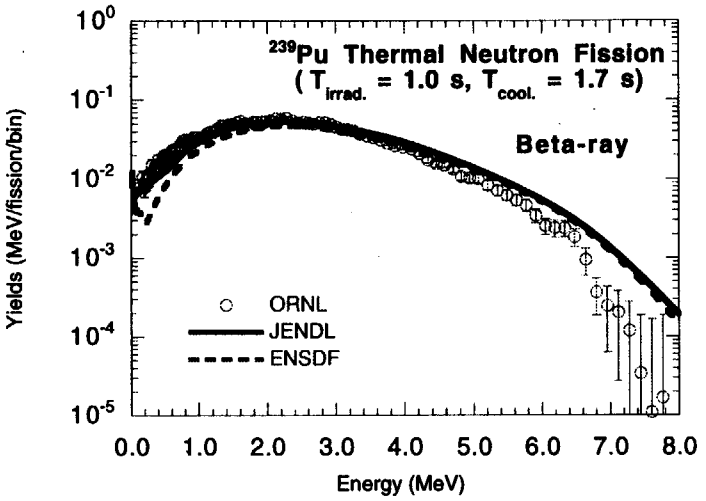

Fig. 1.7.2 Aggregate FP beta-ray spectrum after ^{239}Pu thermal neutron fission.

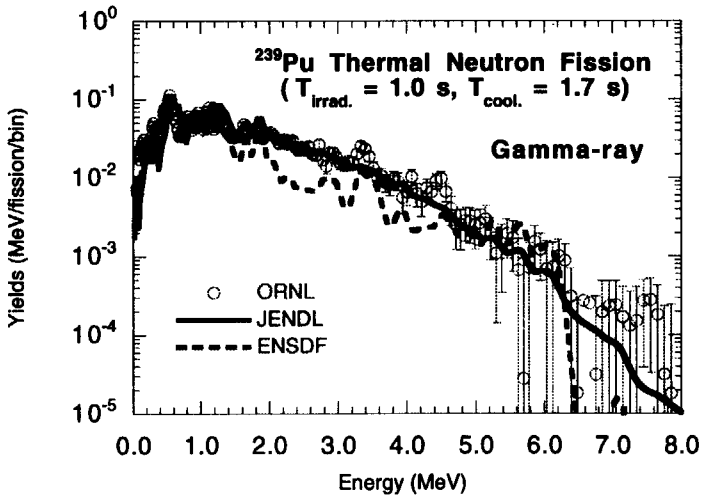

Fig. 1.7.3 Aggregate FP gamma-ray spectrum after ^{239}Pu thermal neutron fission.

2. Reactor Physics

In order to increase accuracy of total delayed neutron yields of ^{235}U, ^{238}U and ^{239}Pu, the cross section adjustment method has been applied for the JENDL-3.2 delayed neutron yield data of these nuclides by using the β_{eff} benchmark experiments performed at two fast critical facilities, FCA and MASURCA, and a thermal critical facility TCA. Notable reduction by a factor of 3~4 has been obtained for the variance of calculated β_{eff} by using the adjusted delayed neutron data.

For the investigation of calculation accuracy for LWR next generation fuels, the Research Committee on Reactor Physics organized by JAERI has proposed "Reactor Physics Benchmark Suites for LWR next generation fuels". Twelve organizations have participated in the benchmark analyses with different codes and cross section libraries.

A prototype version of a three-dimensional diffusion code MOSRA-Prism has been developed on the basis of the polynomial expansion nodal method to analyze hexagonal cores in the reduced-moderation light water reactors. Effectiveness of acceleration methods has been studied for the present code.

A new method has been developed to obtain added reactivity and neutron source intensity by analyzing a transient neutron flux in a subcritical core with an external neutron source. In the new method named the IK-ML method, a set of reactivity and neutron source intensity is determined so that the likelihood may be maximum. The present method can take into account statistical errors in flux measurements, and has been successfully applied to an analysis of the rod drop experiment carried out at the FCA.

To develop a measurement method of void reactivity applicable to tight lattice cores, a real-void formation method using a bubbler at a subcritical state was examined at the the TCA, and the method was proved to give the reactivity value in good agreement with those obtained by a conventional method using mock-up materials of moderator void.

The benchmark test has been carried out on the FCA critical experiments to validate the main revised data in JENDL-3.3: (1) elastic scattering cross section of C, (2) resonance parameters of structural materials and (3) fission and capture cross section of ^{235}U. Criticalities of nine different FCA assemblies have been analyzed by using the MVP continuous energy Monte Carlo code.

2.1 Adjustment of Total Delayed Neutron Yields of ^{235}U, ^{238}U and ^{239}Pu in JENDL-3.2 Using Benchmark Experiments on Effective Delayed Neutron Fraction β_{eff}

T. Sakurai and S. Okajima
(*E-mail* : sakurai@tru.tokai.jaeri.go.jp)

Total delayed neutron yields ν_d of ^{235}U, ^{238}U and ^{239}Pu are the most important nuclear data for the calculation of effective delayed neutron fraction β_{eff}. There are, however, large discrepancies of the yields between major evaluated nuclear data libraries. The cross section adjustment method was applied for the JENDL-3.2 delayed neutron yields of ^{235}U, ^{238}U and ^{239}Pu[1] by using the β_{eff} benchmark experiments performed at two cores fueled with uranium and three cores fueled with plutonium in two fast critical facilities, MASURCA of CEA and FCA of JAERI, and a core fueled with uranium in TCA of JAERI [2－4].

The adjustment was carried out on the yields given at several energy points in the file. The energy dependence of yield between these energy points, which has been given by a linear interpolation in the file, was taken into account in a sensitivity analysis for the adjustment. The uncertainties of both delayed neutron yields and other nuclear data, such as neutron cross sections used for the β_{eff} calculation, were taken into consideration in the adjustment. These uncertainties were based on the JENDL-3.2 covariance file[5], where no correlations were given between the delayed neutron yields of three nuclides and the other nuclear data. The delayed neutron yields of three nuclides therefore were assumed to be statistically independent of the cross sections and the adjustment was made solely for the yields.

As the result of the adjustment, the yields of ^{238}U were uniformly decreased by about 3% below 7 MeV. Figure 2.1.1(a) compares the adjusted yield with those in three major evaluated nuclear data files of the JENDL-3.2, ENDF-B/VI and JEF-2.2. The original yield of JENDL-3.2 takes a value of 0.0481 below 3.5 MeV. The yield of JEF-2.2 and that of JENDL-3.2 take the identical value. The yield of ENDF-B/VI takes a value of 0.044 below 4 MeV. The yield of Tuttle's evaluation, which has been widely used in nuclear industry, takes a value of 0.0439 which is very close to that of ENDF/B-VI below 4 MeV. The discrepancy of about 9% is found for the yields between (a) JENDL-3.2 and JEF-2.2 (0.0481) and (b) ENDF/B-VI and Tuttle (about 0.044). The adjustment resulted in a yield value of 0.0466 below 3.5 MeV, which is close to a mean of (a) and (b). For ^{239}Pu, an increase of yield by 1~2.6% is observed below 1MeV. Figure 2.1.1(b) compares the adjusted yield with those in three nuclear data files. The adjusted yield is close to that of ENDF/B-VI below 1 MeV. For ^{235}U, the change of yield is less than 1%.

Figure 2.1.2 compares the uncertainties(variances) of calculated β_{eff} between before and after the adjustment. Breakdowns of the variances in sources of uncertainty are also shown in this figure. Notable reductions by a factor of 3~4 are observed for the variances after the adjustment. This reduction was brought by both (a)the reduction of uncertainties of yields and (b)negative correlations of yields between different nuclides which were introduced by the

adjustment.

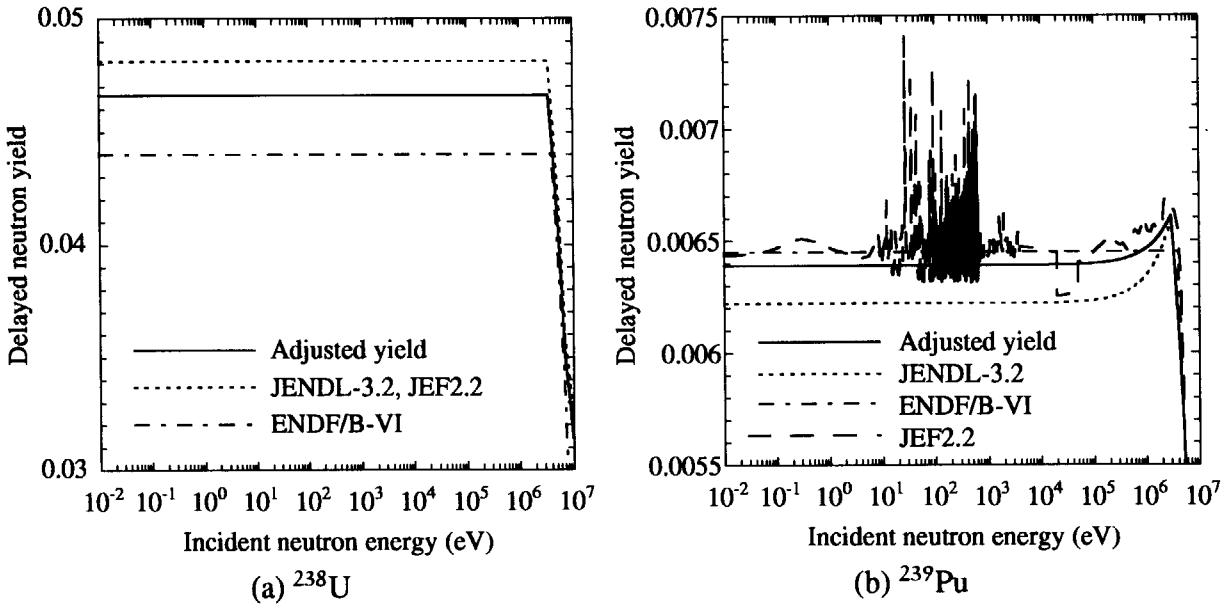

Fig.2.1.1 Comparison of adjusted delayed neutron yield with evaluated ones in JENDL-3.2, ENDF/B-VI and JEF-2.2 for ^{238}U and ^{239}Pu

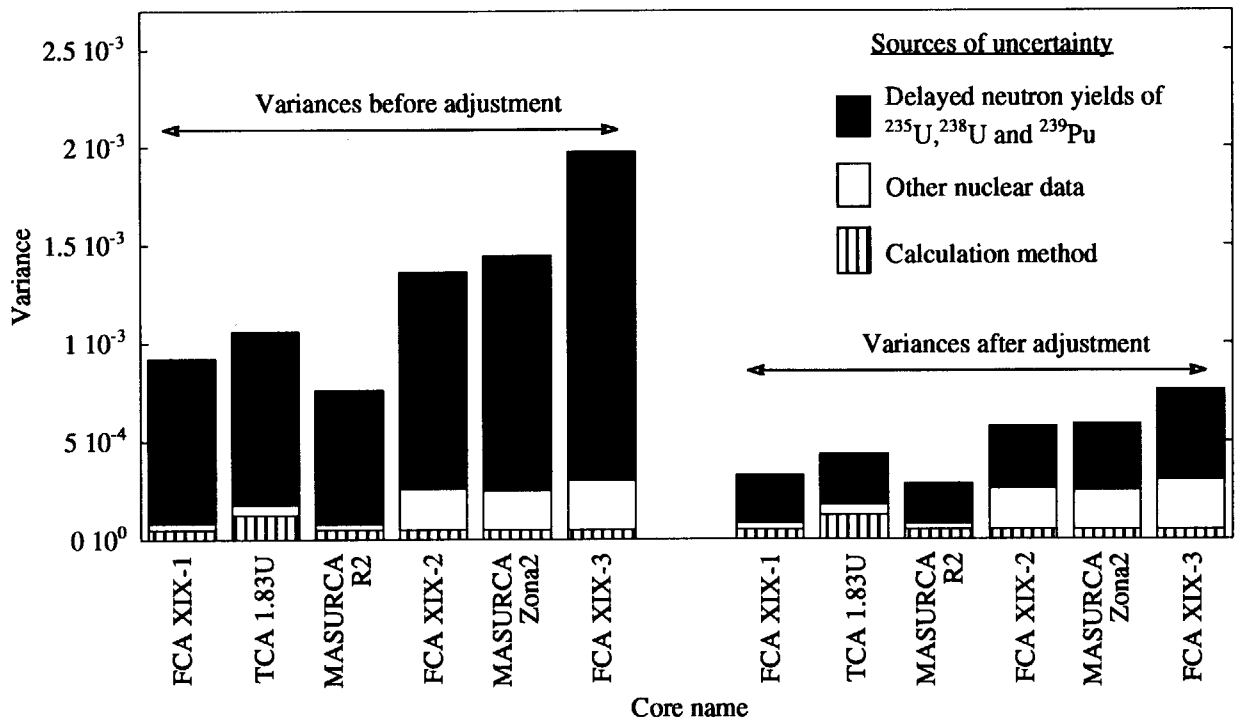

Fig.2.1.2 Comparison of uncertainty(variance) of calculated β_{eff} between before and after adjustment

Table 2.1.1 C/E values of β_{eff}

	MASURCA cores		FCA cores			TCA core
Item	R2	Zona2	XIX-1	XIX-2	XIX-3	1.83U
Fuel	Enriched uranium	MOX	Enriched uranium	Plutonium, Natural uranium	Plutonium	Enriched uranium
Fuel enrichment	30%	25%	93%	23%	(92% fiss -ile Pu)	2.6%
C/E before adjustment	1.016	1.019	1.003	1.010	0.978	1.024
C/E after adjustment	1.003	1.012	0.994	1.002	0.990	1.012

Table 2.1.1 compares the C/E values of β_{eff} between before and after the adjustment. The adjusted yields improved the agreement of β_{eff} between experiment and calculation. The present adjustment study made a large contribution for the evaluation of delayed neutron yields for JENDL-3.3 [6].

References

1) T. Sakurai and S. Okajima, "Adjustment of Total Delayed Neutron Yields of ^{235}U, ^{238}U and ^{239}Pu in JENDL-3.2 Using Benchmark Experiments on Effective Delayed Neutron Fraction β_{eff}", *J. Nucl. Sci. Technol.* **39**, pp.19-30 (2002).
2) T. Sakurai and S. Okajima, "Analysis of benchmark experiments of effective delayed neutron fraction β_{eff} at FCA", *Progress in Nuclear Energy*, **35** , pp.209-225 (1999).
3) P. Bertrand, *et al.*, "BERNICE -Interlaboratory comparison of β_{eff} measurement techniques at MASURCA", *Proc. Int. Conf. on the Physics of Reactors, Physor 96*, Mito, Japan, pp.E-190-E-199 (1996).
4) K. Nakajima, "Re-evaluation of the effective delayed neutron fraction measured by the substitution technique for a light water moderated low-enriched uranium core", *J. Nucl. Sci. Technol.* **38**, pp.1120-1125 (2001).
5) K. Shibata, *et al.*, "JENDL-3.2 Covariance File", *J. Nucl. Sci. Technol.*, Supplement 2, pp.40-43 (2002).
6) T. Yoshida, *et al.*, "Evaluation of Delayed Neutron Data for JENDL-3.3", *Int. Conf. on Nuclear Data for Science and Technology*, Tsukuba, Japan, pp.136-139 (2001).

2.2 Burn-up Calculation Benchmark for LWR Next Generation Fuels

K. Okumura, H. Unesaki[*1], T. Kitada[*2] and E. Saji[*3]
E-mail : okumura@mike.tokai.jaeri.go.jp

In order to investigate the calculation accuracy of the nuclear characteristics of LWR next generation fuels, the Research Committee on Reactor Physics organized by Japan Atomic Energy Research Institute has proposed "Reactor Physics Benchmark Suites for LWR Next Generation Fuels". [1] The next generation fuels aim at very high discharged burn-up of about 70GWd/t in PWR or BWR with UO_2 or MOX fuels whose fissile enrichments may exceed the Japanese regulatory limitations for the current LWR fuels such as 5wt% ^{235}U.

The benchmark problems consist of UO_2 fuel and MOX fuel problems, each of which has a pin cell configuration, a PWR assembly configuration (17x17) and a BWR assembly configuration (9x9-7 for UO_2 or 10x10-9 for MOX). In a pin cell configuration, the basic nuclear parameters such as an infinite multiplication factor, temperature and void reactivities and various isotopic concentrations as functions of burn-up are required to be evaluated. The isotopes to be evaluated were selected from the viewpoint of the back-end requirement as well as the reactivity point of view. In the assembly configurations, the important characteristics that can be investigated only in an assembly calculation, such as a power peaking factor and the effect of burnable poison (Gadolinia) on the reactivity coefficients or burn-up change in an infinite multiplication factor, are required to be evaluated.

As shown in Table 2.2.1, twelve organizations have participated in the benchmark analysis with different codes and libraries. Until now, 14 solutions and about 5 solutions have been submitted to the pin cell problems and the assembly problems, respectively. As a sample of the benchmark results, comparison of the k-infinities in the BWR assembly problem (UO_2) is shown in Fig.2.2.1. Other detailed results can bee seen in Ref.2.

From the comparison of the benchmark results, the following conclusions and future subjects have been drawn:

- The differences among the benchmark results are somewhat large for the k-infinities at

---

[*1] Kyoto University Research Reactor Institute, [*2] Osaka University,
[*3] Secretariat of the Nuclear Safety Commission

BOL in the MOX-pin cell and MOX-PWR problems. A reference experimental data is desired for high Pu content fuels (about 17 wt% as total Pu) with typical Pu isotope vector discharged from LWRs.

- For the PWR-UO_2 and BWR-UO_2/-MOX problems with Gadolinia, overall burn-up behavior of k-infinities shows fairly good agreements among participants' results.
- Spreads for void, Doppler and Hot-to-Cold reactivities in the UO_2 problems show a tendency to become larger as burn-up increases, whereas the spreads in the MOX problems are large from BOL.
- Local peaking factors show good agreements within ±1% for both of the PWR and BWR assembly problems.
- Difference more than 20% is observed at 70GWd/t for the atomic number densities of nuclides ^{237}Np, ^{238}Pu, ^{242}Am, ^{243}Am, ^{245}Cm, ^{152}Sm, and ^{155}Gd (not burnable poison). Effects of different nuclear data files are large (>10%) for the productions of ^{243}Am, ^{243}Cm, ^{244}Cm, ^{245}Cm, ^{246}Cm and ^{155}Gd (mainly produced via fission, capture of ^{154}Gd and β-decay of ^{155}Eu).

For further investigation, the following activities are progressing: 1)Addition of benchmark calculation results for the assembly problems and new results based on JENDL-3.3, 2)Sensitivity study to breakdown void, Doppler and Hot-to-Cold reactivities into contributing nuclides, reaction types and energy ranges, 3) Post irradiation analysis with different nuclear data libraries (JENDL-3.2/3.3, JEF-2.2, ENDF/B-VI.5/VI.8) for relatively high enriched and high burn-up fuel samples (4.1wt.% UO_2) irradiated up to 47GWd/t in Japanese PWR.

References

1) A. Yamamoto, T. Ikehara, T. Ito and E. Saji, "Benchmark Problem Suite for Reactor Physics Study of LWR Next Generation Fuels", *J. Nucl. Sci. Technol.* **39**, No.8, pp.900-912 (2002).

2) K. Okumura, H. Unesaki, T. Kitada and E. Saji, "Benchmark Results of Burn-up Calculation for LWR Next Generation Fuels", *Proc. of Int. Conf. on the New Frontiers of Nuclear Technology : Reactor Physics, Safety and High-Performance Computing (PHYSOR 2002)*, 9A-03, Seoul, Korea, 7-10 October, (2002).

Table 2.2.1 Participants with their codes and nuclear data libraries

No.	Organization	Code (method)	Base Library	Pin Cell		PWR		BWR	
				UO_2	MOX	UO_2	MOX	UO_2	MOX
1	JAERI	MVP-BURN (MC[a])	JENDL-3.2	X	X				
2	JAERI	SRAC95 (CP[b])	JENDL-3.2	X	X		X		
3	JAERI	SRAC95 (CP)	ENDF/B-VI(R5)	X	X				
4	JAERI	SRAC95 (CP)	JEF-2.2	X	X				
5	KURRI[*1]	MVP-BURN (MC)	JENDL-3.2			X	X		
6	Osaka Univ.	MVP-BURN (MC)	JENDL-3.2					X	X
7	TEPSYS[*2]	CASMO-4 (MOC[c])	JEF-2.2	X	X			X	X
8	NFI[*3]	CASMO-4 (MOC)	ENDF/B-IV	X	X	X	X		X
9	NFI	NULIF	ENDF/B-V	X	X				
10	NUPEC[*4]	CASMO-4 (MOC)	ENDF/B-IV					X	X
11	SEPCO[*5]	SHETRAN (MOC)	ENDF/B-VI(R3)	X	X	X	X		
12	GNF-J[*6]	TGBLA	ENDF/B-V	X	X			X	
13	GNF-J	VMONT (MC)	JENDL-3.2	X	X			X	
14	Toshiba	MCNP-BURN (MC)	JENDL-3.2	X	X				
15	CRIEPI[*7]	FLEXBURN (SN[d])	JENDL-3.2	X	X	X	X		
16	EPDC/KCC[*8]	LWRWIMS (CP)	JEF-2.2	X	X				
17	KAERI[*9]	HELIOS (CCCP[e])	ENDF/B-VI	X	X	X	X		X
Total	12	11		14	14	5	6	5	5

[*1] Kyoto University Research Reactor Institute
[*2] TEPCO Systems Corporation
[*3] Nuclear Fuel Industries, Ltd.
[*4] Nuclear Power Engineering Corporation
[*5] Shikoku Electric Power Company
[*6] Global Nuclear Fuel Japan
[*7] Central Research Institute of Electric Power Industry
[*8] Electric Power Development Co., Ltd./Kaihatsu Computing Service Center
[*9] Korea Atomic Energy Research Institute

[*a] Monte Carlo method
[*b] Collision Probability method
[*c] Method of Characteristics
[*d] Discrete Ordinate (Sn) method in arbitrary square meshes
[*e] Current Coupling Collision Probability method

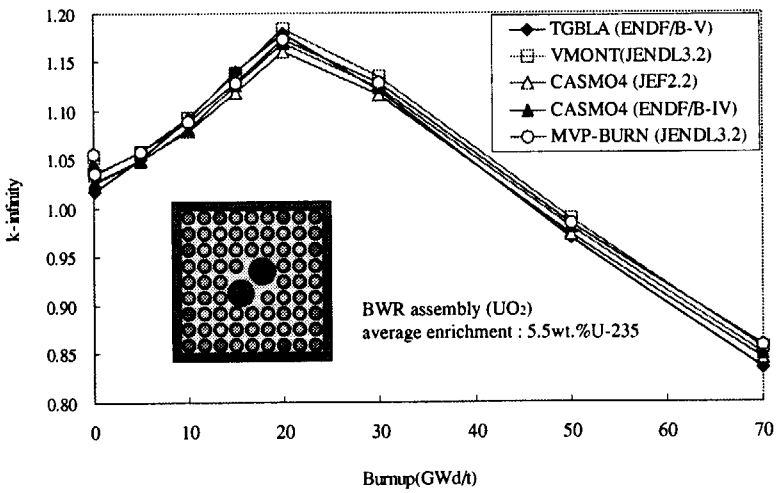

Fig.2.2.1 Comparison of k-infinities in BWR assembly (UO_2) problem

2.3 Application of Acceleration Methods to a Prism Geometry Nodal Diffusion Code MOSRA-Prism

T. Fujimura and K. Okumura
E-mail : okumura@mike.tokai.jaeri.go.jp

A prototype version of a diffusion code has been developed to analyze the hexagonal core in reduced moderation reactors. The hexagonal core is divided into regular triangular prism nodes in the three-dimensional code MOSRA-Prism and a polynomial expansion nodal method (PEN)[1] is applied to approximate the neutron flux distribution by a cubic polynomial given by

$$\phi_g = C_1^g + C_u^g u + C_v^g v + C_w^g w + C_z^g z + C_{2u}^g u^2 + C_{2v}^g v^2 + C_{2w}^g w^2 + C_{2z}^g z^2 + C_{uz}^g uz + C_{vz}^g vz + C_{wz}^g wz + C_{sz}^g (u^2 + v^2 + w^2)z + C_{3u}^g u^3 + C_{3v}^g v^3 + C_{3w}^g w^3 + C_{3z}^g z^3$$

, where u, v, w and z are co-ordinate parameters and g is the index of energy group. By taking account of dependence of co-ordinate parameters, 15 coefficients are determined from the node equation $A^g \phi^g = b^g$ for

$$\phi_u^b, \phi_v^b, \phi_w^b, \qquad \phi_u^t, \phi_v^t, \phi_w^t, \qquad \bar{\phi}_u, \bar{\phi}_v, \bar{\phi}_w, \bar{\phi}_b, \bar{\phi}_t, \qquad \bar{\phi}, \tilde{\phi}_x, \tilde{\phi}_y, \tilde{\phi}_z$$

which show 6 corner point fluxes, 5 surface averaged fluxes and 4 moment fluxes. The equation is composed by source free conditions at 6 corner points, flux continuity conditions at 5 node surfaces and 4 moment conditions in the node. The multi-group system equation $A\phi = b$ is solved iteratively with usual inner and outer iterations and the effectiveness of acceleration methods is ascertained by applying an adaptive acceleration method and a neutron source extrapolation method, respectively. The concrete algorithms are given in the literatures[2),3)].

Sample Calculation with IAEA benchmark problem

The two dimensional benchmark problem given for (x, y) geometry[4] was modified as shown in Fig.2.3.1 with 12.12 cm pitch. Three-dimensional calculations were performed applying reflective conditions to the axial direction. For bad convergence of inner iteration,

the inner iteration limit was set to 60, and the flux and eigenvalue convergence criterion were set to 10^{-4} and 10^{-5}, respectively. When only the adaptive acceleration was applied, it was remarkably effective till the maximum flux deviation 10^{-3}. However, the total speed up ratio was confined to1.67. On the other hand, when only the source extrapolation was applied, it was really applied twice in 32 outer iterations and the speed up ratio 1.76 was attained. When both the accelerations were applied simultaneously, the speed up ratio was 2.59 and this proved the independence of the acceleration numerically.

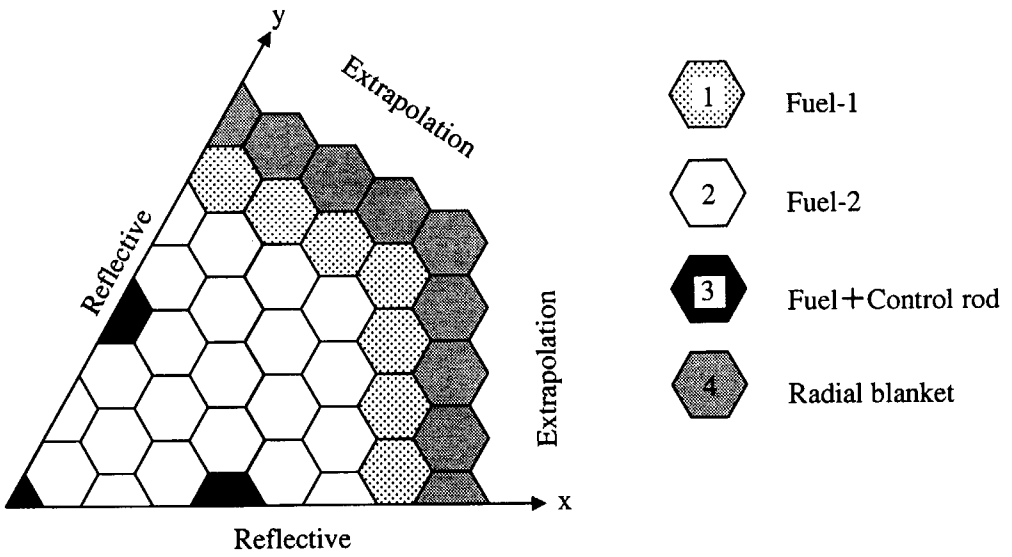

Fig.2.3.1 Core geometry of modified IAEA 2-dimensional benchmark problem

References

1) J. Y. Cho and C. H. Kim, "Higher order polynomial expansion nodal method for hexagonal core neutronics analysis, *An. Nucl. Energy*, **25**, No.13, 1021 (1998).

2) T. Fujimura and K. Okumura, "Analysis of the Applicability of Acceleration Methods for a Triangular Prism Geometry Nodal Diffusion Code, JAERI-Research 2002-024 (2002). [in Japanese]

3) K. Okumura, "MOSRA-Light; High Speed Three-Dimensional Nodal Diffusion Code for Vector Computers", JAERI-Data/Code 98-025 (1998). [in Japanese]

4) Argonne Code Center, "Benchmark Problem Book", ANL-7416, Suppl. 2, Argonne National Laboratory (1977).

2.4 Determination of Reactivity and Source Intensity Based on the Maximum Likelihood Method

K. Nishihara, K. Iwanaga, T. Yamane and S. Okajima

(*E-mail*: nishi@omega.tokai.jaeri.go.jp)

During the experiments using a critical assembly at subcritical state with a neutron source where reactivity or neutron source intensity is varied and the core shifts to another stationary state, neutron flux transitionally changes. In the present study, a new technique has been developed to obtain reactivity and neutron source intensity by analyzing a neutron flux profile during the transient. The new method can be applied to obtain the solution of the reactivity and neutron source when two conditions are satisfied; (1) the reactivity and neutron source are constant and (2) neutron flux changes. The conventional method such as the integration method[1], grouping method[2], method proposed by M. Itagaki[3] and method proposed by S. Tamura[4] can be also applied to obtain the solution, but statistic errors of flux measurement have not been theoretically treated. Therefore, likelihoods of the solution by the conventional methods are not largest and the errors of the solutions brought by the statistic errors of the flux measurement are unknown.

The new method named "IK-ML method" (Inverse Kinetics - Maximum Likelihood method) aims to obtain a set of the reactivity and neutron source so as the solution has the maximum likelihood. The likelihood is defined as follow.

$$L(\rho,S)=\prod_{j=1}^{N} f\left(P_j^m, P^c(\rho,S;t_j)\right) \tag{1}$$

,where L is the likelihood, N is the number of flux measurement points, P_j^m is flux value measured at measurement time t_j, P^c is calculation value of flux at the time (t_j), and f is the probability density of flux measurement to be P_j^m when the true value of flux is supposed to be P^c. f is represented as follows for the Poisson and normal distribution, respectively.

$$\text{Poisson distribution: } f\left(P_j^m, P^c(t_j)\right) = P^{c P_j^m} e^{-P^c} \Big/ P_j^m! \tag{2}$$

$$\text{Normal distribution: } f\left(P_j^m, P^c(t_j)\right) = \left(2\pi P^c\right)^{-1/2} \exp\left(-\left(P_j^m - P^c\right)^2 / 2P^c\right) \tag{3}$$

P^c is calculated for a set of (ρ, S) by solving following differential equation.

$$\Lambda \frac{d}{dt} P^c(\rho,S;t) = (\rho - \beta) P^c(\rho,S;t) + \sum_i \lambda_i C_i^c(\rho,S;t) + S \tag{4}$$

$$\frac{d}{dt} C_i^c(\rho,S;t) = \beta_i P^c(\rho,S;t) - \lambda_i C_i^c(\rho,S;t) \tag{5}$$

$$\text{Boundary conditions: } P^c(\rho,S;t_0) = P_0^m, \quad C_i^c(\rho,S;t_0) = C_{i0}^m \tag{6}$$

The IK-ML method is illustrated in Fig. 2.4-1, in which an example of flux measurements is pointed. For an incorrect set of (ρ, S) a calculation of P^c is far from the points as shown by a broken line and the likelihood given by Eq.(1) is small. On the other hand, a solid line for a correct set of (ρ, S) is positioned at the center of

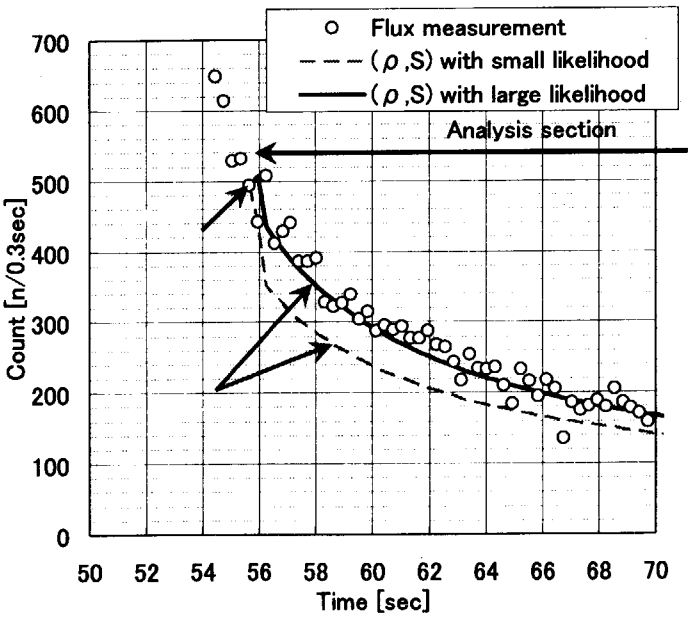

Fig.2.4-1 Concept of IK-ML method

the points, and the likelihood is large. To obtain the set of (ρ, S) with maximum likelihood, the numerical repetition and conversion using the Gauss-Newton or Marquardt method are necessary. The IK-ML code was developed to obtain the solution.[5)]

Fig. 2.4-2 shows the result of a reactivity and source measurement by a rod drop experiment which was done at FCA. M4, M5, M8 and P1 are names of U-235 fission chambers at different positions and efficiencies. The results can be given with error bars meaning 1σ only by the IK-ML method. Some of the results by the conventional methods are significantly different from the IK-ML method over the error bars and the results show tendencies such that the results by the method of Tamura are farther to criticality than others.

References

1) E. F. Bennett, ANL-7966, Argonne National Laboratory (1976).

2) J. E. Hoogenboom, et al., Ann. Nucl. Eng, 15[12], pp.553 (1998).

3) M. Itagaki, et al., Annual meeting of the Atomic Energy Society of Japan, pp.371 (1999).[in Japanese]

4) S. Tamura, Fall meeting of the Atomic Energy Society of Japan, pp.491 (2001). [in Japanese]

5) K. Nishihara, et al., JAERI-Research 2002-030, in print (2002). [in Japanese]

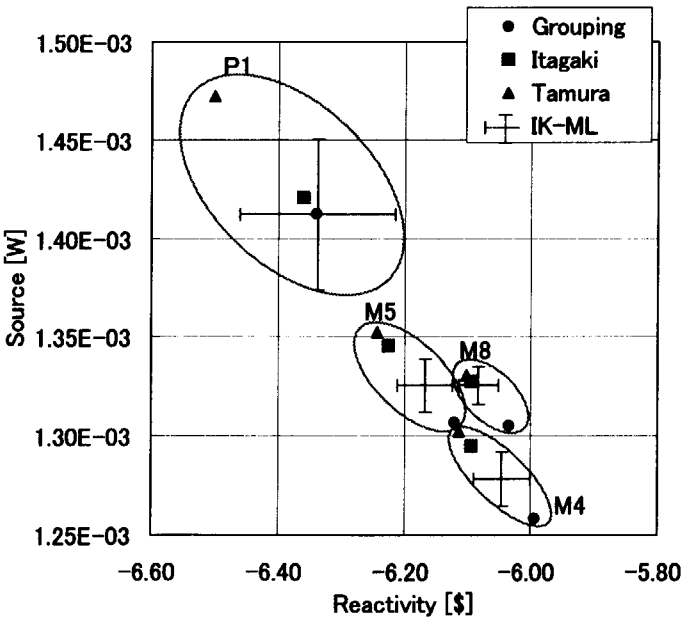

Fig.2.4-2 The result for a rod drop experiment

2.5 Measurement of Void Reactivity Effect in Light Water Moderator Lattices by Subcritical Bubbling Method

T. Suzaki, K. Murakami, S. Kohmoto*, S. Fujisaki, Y. Hoshi,
M. Kurosawa and M. Fumizawa
(*E-mail* : suzaki@mike.tokai.jaeri.go.jp)

The reactivity effect of moderator-void is one of the most important parameters in light water reactors. The reactivity is designed to be negative to ensure the inherently safe property against abnormal power increases of the reactor core. This requirement is also the case in the reduced-moderation light water reactor (RMLWR) being investigated in our department now. The reactivity has been measured at some critical facilities by using materials to mock up moderator-void such as Al tubes, Al brocks and low-density plastics. For a very tight triangular lattice adopted in RMLWR, however, the use of such mock-up materials is almost impossible, and the other methods should be developed.

For the purpose to develop a measurement method of void-reactivity applicable to the tight lattice core, availability of a real-void formation method utilizing a bubbler was examined at the TCA, in comparison with the conventional method using the mock-up materials. It is required in the former method that the test cores must not be supercritical even when the bubbler abruptly stops. Therefore, we selected the neutron source multiplication method at subcritical states for measuring the void reactivity in all of the present experiment through.

The core studied was a two-regional one as shown in Fig. 2.5.1. The central test region separated by an Al channel box from the surrounding driver region was composed of 7x7 2.7%-enriched UO_2 fuel rods. At the bottom of the channel box, a bubbler shown in Fig. 2.5.2 was furnished, and compressed air supplied to the bubbler formed air bubbles in water containing 10 wt.% ethanol, of which height without bubbles was about 1 m. The low surface tension of ethanol was effective to keep the bubble size small[1)], and then, to obtain almost flat spatial distribution of the volume ratio of air bubble to water (void ratio) inside the channel box. In addition, natural boron was solved in several concentrations to moderator water in the test region. The void ratio was measured by a differential pressure gauge, which had two detecting points of water head with a vertical span of 50 cm.

*Nagoya University

To test the performance of the differential pressure gauge, the same bubbling system composed of an acrylic cannel box and 7x7 Al tubes of similar diameter to the fuel rod was set up outside the reactor core, and the void ratio was measured from the change in ^{137}Cs γ-ray intensity as a reference method. The result of comparison between the two methods was given in Fig. 2.5.3. One can see that the void ratio up to about 30% is measurable satisfactorily by using the differential pressure gauge. Also it was found by using the gauge of 20 cm-span that the void ratio increases vertically by about 1%/10 cm when the average ratio is 30%.

The standard core without boron and void in the test region attained criticality when the water level in the driver region was 88.79 cm from the lower end of active fuel zone. The subcritical water level for the neutron source multiplication experiment was fixed at 78.32 cm, and the reference reactivity of standard core ρ_0 was determined as –0.89 dollars from the measured reactivity worth of water level. The neutron source and the detector shown in Fig. 2.5.1 were vertically positioned at the nodes of the second and the third harmonics, respectively, to reduce the effect of higher modes.[2] The reactivity effects of perturbation caused by void and boron $\delta\rho$ were obtained from the relation that $\delta\rho = \rho_0(CR_0/CR\text{-}1)$ [2] with the neutron count rate for the standard core CR_0 and that for the voided core CR of different boron concentration, and the results are shown in Fig. 2.5.4. In the same figure, are also shown the results of neutron source multiplication experiment for the conventional method using Al and low-density polystyrene brocks with several combinations to mock up the moderator void. One can see that the result of bubbling method for the case without boron agrees well to that of conventional method, which means that the new method is applicable to the measurement of void reactivity effect. Also in the bubbling method for borated water, it is clearly observed that the negative reactivity effect of void decreases with increasing boron concentration, and turns positive when the boron concentration exceeds about 2,000 ppm.

References:

1) H. Watanabe, et al.: "Development of Quick-Response Area-Averaged Void Fraction Meter", JAERI-Research 2000-043, (2000), [in Japanese].

2) T. Suzaki, et al.: "Determination of Large Perturbation Reactivity by Neutron Source Multiplication Method", JAERI-Review 2002-005, pp. 35-36(2002).

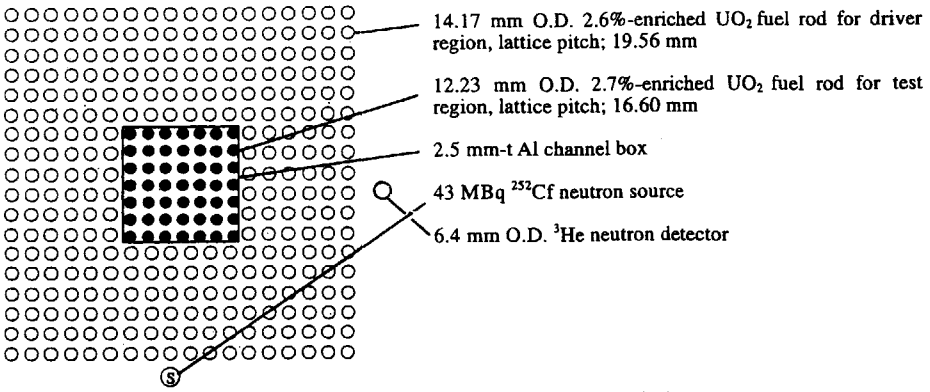

Fig. 2.5.1 Plan of core and arrangement of neutron source and detector

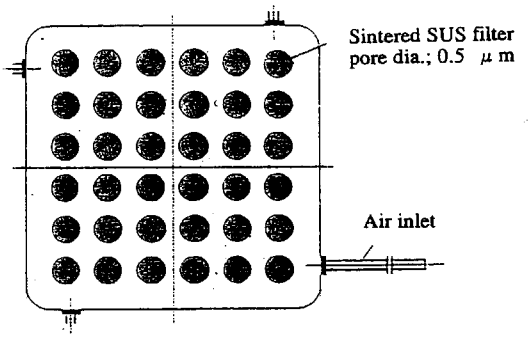

Fig. 2.5.2 Bubbler

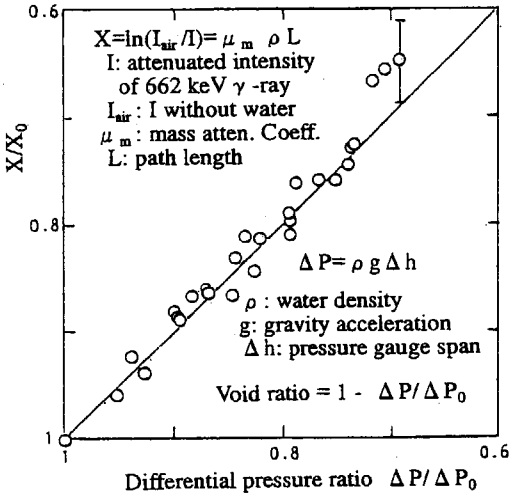

Fig. 2.5.3 Correlation between γ -ray intensity and differential pressure

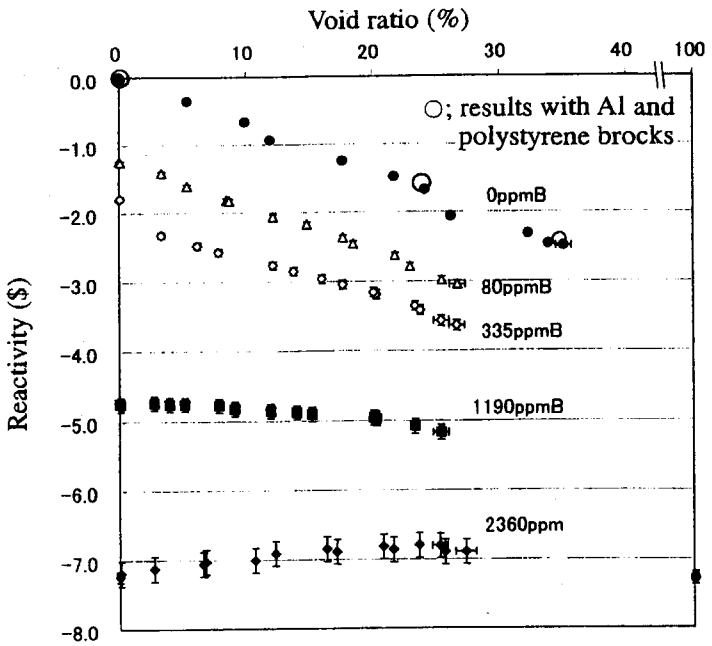

Fig. 2.5.4 Reactivity effect of void in borated moderator water

2.6 Benchmark Test for JENDL-3.3 Library by Analyses of FCA Cores

S. Okajima and S. Iijima
(*E-mail*: okajima@fca001.tokai.jaeri.go.jp)

Introduction

The evaluated nuclear data library JENDL-3.3 was released in May 2002[1]. Some of the main revised data from JENDL-3.2 library are as follows: (1) the elastic scattering cross section of C, (2) the resonance parameters of structural materials and (3) the resonance parameters, the fission cross section and the capture cross sections of ^{235}U. To validate those data, a benchmark test on keff values was made by analyzing a series of experiments at the Fast Critical Assembly (FCA) of JAERI. In the test the Monte Carlo calculation code was used. The results were compared with those of JENDL-3.2 library[2].

Brief Description of FCA Assemblies

Nine different FCA assemblies were selected from a viewpoint of benchmark test; the assemblies IX-1 to IX-7[3], X-1 and X-2[4]. The assemblies IX-1 to IX-6 were composed with 93% enriched uranium and diluent material of graphite or stainless steel for adjusting neutron spectrum in lower energy region or in higher energy region, respectively. The assembly IX-7 was composed with 20% enriched metal uranium. The core cell patterns were designed to be symmetric within one-drawer unit cell so as to make calculation simple. These cores were simple in geometry. Each core was composed of a core region and axial and radial blanket regions. Neutron spectrum is the softest in the assembly IX-1 and becomes harder for an assembly of later number except for IX-7. Higher component of neutron spectrum depends on the diluent material.

The assemblies X-1 and X-2 were composed with Pu fuels and 20% enriched metal uranium. These assemblies were constructed for the mockup experiment of the Fast Experimental Reactor "JOYO" Mark II Core. The assembly X-1 had a cylindrical core surrounded by a depleted uranium blanket, while the assembly X-2 consists of the core and reflector regions comprised of sodium and stainless steel. The core cell patterns were designed to be symmetric within one-drawer unit cell so as to make calculation simple. Both cores had a similar geometry and fuel configuration in core cells.

Table 2.6.1 summarizes the geometries and the atomic number densities of the core

region in these assemblies.

Analyses for Criticality

A continuous-energy Monte Carlo code MVP[5] was used to minimize the uncertainties of core geometrical modeling and data processing for the multi group cross sections generation.

Each assembly is modeled as precisely as possible in the calculations. The calculation model includes the gap between the halves of FCA assemblies, void space in the square matrix tubes, the heterogeneous configuration of each fuel plate.

The number of neutron histories was 1.4 million in all of keff calculations.

Results and Discussion

The ratios between calculated and experimental values, C/E values, are shown in Table 2.6.2. The C/E values range from 0.993 to 1.001.

The calculated results were compared between JENDL-3.3 and JENDL-3.2 libraries. For the assemblies IX-1 to –3, the C/E values of the JENDL-3.3 are 0.993, 0.999 and 1.003, respectively. The value decreases as the neutron spectrum becomes softer. On the other hand this tendency is not found in the JENDL-3.2 calculations. This spectrum dependency might be caused by the revised capture cross section of ^{235}U. Further investigation is required to make the sensitivity study in detail. For the assemblies IX-4 to IX-7, there is no large discrepancy in the C/E values between JENDL-3.3 and JENDL-3.2. In the assembly X-1 the JENDL-3.3 gives better C/E value than the JENDL-3.2.

References

1) S. Shibata, *et al.*: *J. Nucl. Sci. and Technol.*, **39**, 1125 (2002).

2) T. Nakagawa, *et al.* : *ibid.*, **32**, 1259 (1995).

3) M. Nakano, *et al.*: *Proc. The 1983 Symposium on Nuclear Data, JAERI-M 84-010*, p.308-311 (1984).

4) S. Iijima: (private communication)

5) T. Mori, *et al.*: *J. Nucl. Sci. and Technol.*, **29**, 325 (1992).

Table 2.6.1 Core geometries and atomic number densities for principal isotope in FCA assemblies

Assembly	IX-1	IX-2	IX-3	IX-4	IX-5	IX-6	IX-7	X-1	X-2
Core geometry (cm)									
Radius	30.4	23.1	17.9	27.6	20.4	22.9	17.3	28.6	28.0
Height	60.7	40.6	35.6	50.8	40.6	40.6	35.6	50.8	50.8
Atomic number densities (10^{22}#/cm^3)									
U-235	0.226	0.452	0.678	0.452	0.678	0.678	0.748	0.074	0.074
U-238	0.017	0.034	0.051	0.034	0.051	0.051	3.112	0.521	0.521
Pu-239	-	-	-	-	-	-	-	0.209	0.209
C	6.529	6.079	5.660	-	-	-	-	-	-
O	-	-	-	-	-	-	-	1.283	1.283
Na	-	-	-	-	-	-	-	0.766	0.766
Cr	0.184	0.184	0.184	1.416	1.327	0.457	0.184	0.367	0.367
Fe	0.669	0.669	0.669	5.024	4.715	1.680	0.669	1.356	1.356
Ni	0.080	0.080	0.080	0.620	0.579	0.244	0.080	0.169	0.169

Table 2.6.2 Ratio of calculated to experimental keff values in FCA assemblies

Assembly	IX-1	IX-2	IX-3	IX-4	IX-5	IX-6	IX-7	X-1	X-2
JENDL-3.3	0.9934	0.9990	1.0043	1.0005	0.9995	0.9978	0.9950	0.9958	1.0012
JENDL-3.2	1.0058	1.0054	1.0057	1.0002	0.9982	0.9973	0.9964	0.9930	1.0009

Calculation error : ±0.002 (3σ)

3. Advanced Reactor System Studies

The conceptual design study of Reduced-Moderation Water Reactor (RMWR) is being conducted. Design and investigation on four types of RMWR cores were performed. 1) The high conversion BWR type core: A detailed design study has been performed on control rod operation plan and investigation of the core characteristics in the situation of multiple recycling of plutonium under the JAERI's simplified PUREX reprocessing scheme. 2) The high burn-up BWR type core: The higher burn-up core design more than 80GWd/t was investigated. The improvement of the void tube assembly was also performed to attain higher performance in the void reactivity coefficient and the response characteristics during the transient. 3) The ABWR compatible type core: The study has been performed for extending the discharge burn-up by modifying the axially heterogeneous core specifications of the original design. 4) The PWR type core: The light water cooled type RMWR with the electric power of 1350MWe has been investigated. The core arrangement with flattened hexagonal seed fuel assemblies around a regular hexagonal blanket fuel assembly was employed in this design. Also concerning to PWR type core, the optimal arrangement of seed-blanket type core was investigated through parametric studies. The optimal parameters such as the number of layers of seed and outer blanket and height of seed and axial blanket were obtained. Other topics related to the RMWRs are as followings: The dynamical response characteristics of the BWR type small size RMWR core were investigated. The sufficiently stable response characteristics were confirmed against the disturbance. The calculations of geysering experiments were performed with TRAC-BF1 code to assess the applicability of the code to geysering stability analysis. The calculation results showed that the stability boundary of geysering can be precisely predicted. The thermal and mechanical feasibility of MOX fuel rod of RMWR was evaluated with the MOX fuel performance analysis code FEMAXI-RM. The integrity of the fuel rod was confirmed through the evaluation. For realizing fuel recycling relevant for RMWR with economical competitiveness, an advanced reprocessing process, namely simplified PUREX process with Np separation function, was proposed.

As another research area concerning to development of anomaly detection system of nuclear power plants, a new scheme of software integration based on standard I/O data communication stream was proposed and applied it to the anomaly detection system .

3.1 Study on High Conversion Ratio BWR Type RMWR Core

T.Okubo, R.Takeda*[1], T.Iwamura, K.Yamamoto*[2] and H.Okada*[3]
(*E-mail:* okubo@hems.jaeri.go.jp)

A detailed design study on the BWR type reduced-moderation water reactor (RMWR) with the high conversion ratio has been performed [1), 2)]. A concept has been established achieving the *Puf* conversion ratio of 1.06 and the negative void reactivity coefficients. On this concept, further detailed investigation has been performed as in the following. Namely, the control rod operation plan has been investigated throughout the start-up and the full power operation situations. The start-up scheme has also been studied. In addition, the core characteristics under the situation of multiple recycling of plutonium (Pu) have been investigated, under the JAERI's simplified PUREX reprocessing scheme with a little low decontamination factors (DFs) for fission products (FPs) and minor actinides (MAs).

On the control rod operation plan, detailed analyses have been performed to avoid a serious power peaking occurrence. There are 295 Y-shaped control rods in the 1,100 MWe core, which is the reference design. Based on the detailed core calculations, the control rods are divided into three groups. The first group is further divided into three sub-groups of 1A, 1B and 1C. They consist of 34 control rods each, and are completely withdrawn in the order from 1A to 1C. The core becomes the critical during the 1B withdraw. Then the second group, which is also divided into three sub-groups of 2A, 2B and 2C, is withdrawn. They also consist of 34 control rods each, but are withdrawn gradually with some axial steps in the order from 2A to 2C. The third group is divided into four sub-groups of 3A, 3B, 3C and 3D. The last one is for the operation. They consist of 9, 12, 9, and 61 control rods.

When all the start-up control rods of 1A through 3C are withdrawn, the core power is at the level around 30 % of the rated one. Then the core water flow rate is increased to the rated value and the core power becomes to the level around 40 % of the rated one. The operation control rods are then withdrawn gradually. Their radial and axial positions at the rated power initiation, *i.e.* the beginning of cycle (BOC), are shown in Fig. 3.1.1. Their radial positions are indicated by the circles with some numbers in the figure. The number in

*1 Hitachi, Ltd., *2 The Japan Atomic Power Company, *3 Tokyo Electric Power Company

the circle indicates the relative axial position, *i.e.* insertion step, of the control rod out of 48 steps for the complete insertion of the rod. Therefore, the figure indicates the control rods are inserted up to around the top of the lower MOX region, which corresponds to the number of 18.

The control rods are withdrawn gradually during the cycle compensating the reactivity loss, and are completely withdrawn at the end of cycle (EOC). The axial power distributions in the core part at BOC and EOC are shown in Fig. 3.1.2 together with the void fraction distributions. As shown in the figure, the axial power factors in both MOX regions are almost the same level at BOC, although the void fraction is much lower in the lower MOX region. This is because the control rods are inserted in the lower MOX region at BOC as shown in Fig. 3.1.1, and well controls the axial power peaking by suppressing the power in the lower MOX region. The power factor in the lower MOX region becomes larger at EOC, because all the control rods are completely withdrawn. However, the axial power peaking is not serious, and is around 1.6 at both BOC and EOC as shown in Fig. 3.1.2.

On multiple recycling of Pu, the effects of residual MAs and FPs in the MOX fuel on the core characteristics have been investigated under the economical simplified PUREX reprocessing scheme with a little lower DFs, which is proposed by JAERI and described in Section 3.9. The estimated DFs are around 10^5 for FPs, Am and Cm, although it is about 100 for Np using a special treatment for Np removal without purification processes as presented in Section 3.9. The analysis results show the core characteristics for multiple recycling situation under the concerned JAERI's reprocessing scheme are almost the same as for the reference core design, although the length of both MOX regions are to be increased by about 5 % due to usage of fuel with a little lower DFs for FPs, Am and Cm.

References:

1) T. Okubo, *et al.* : "Conceptual Designing of Reduced-Moderation Water reactors (1) – Design for BWR-type Reactors –", *Proc. ICONE-8*, ICONE-8422 (2000).

2) T. Okubo, *et al.* : "Advanced Concept of Reduced-Moderation Water Reactor (RMWR) for Plutonium Multiple Recycling", *Proc. GLOBAL2001*, 022 (2001).

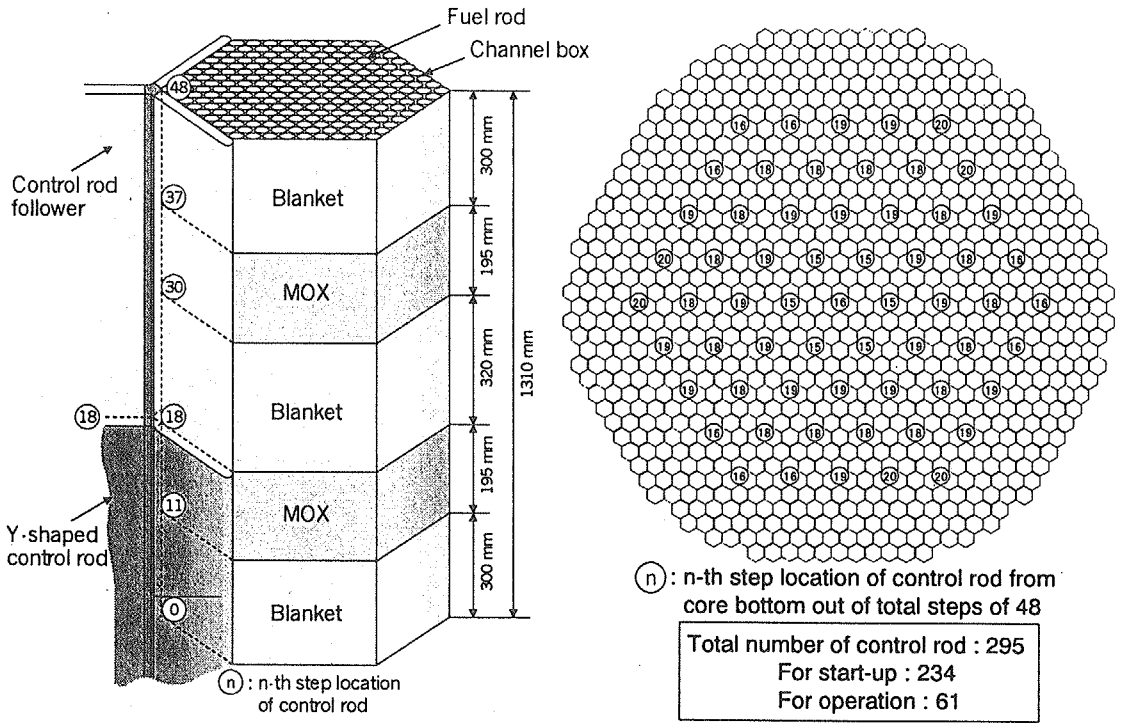

Fig. 3.1.1 Control rod positions at BOC

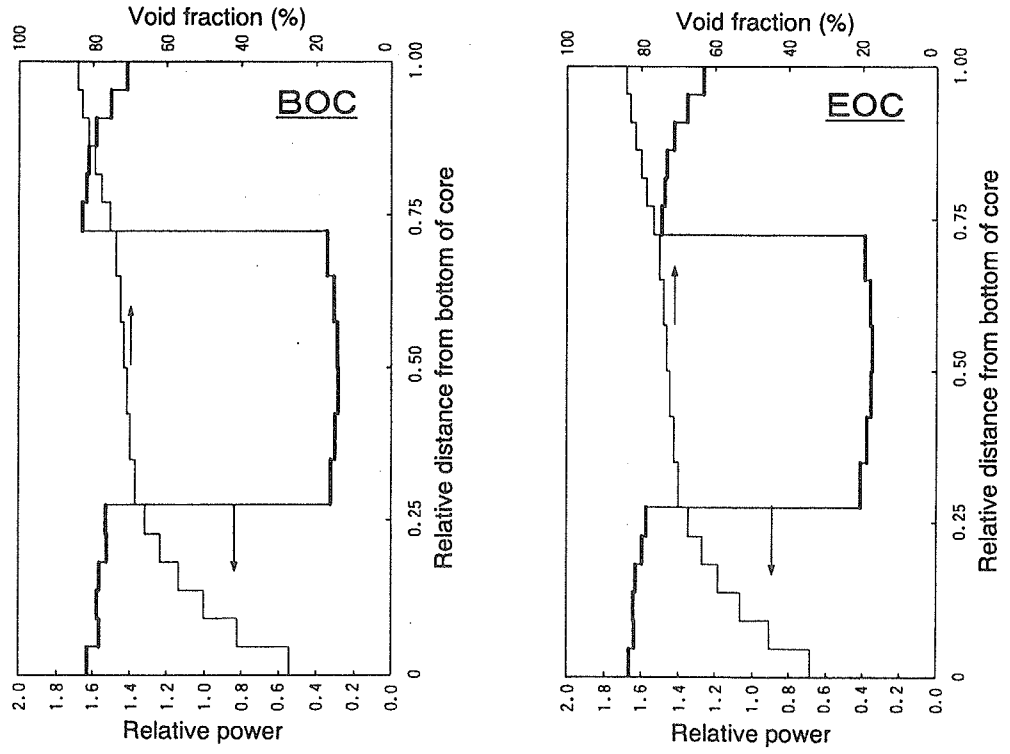

Fig. 3.1.2 Axial power and void fraction distributions in core part at BOC and EOC

3.2 Study on High Burn-up BWR Type RMWR Core

T.Okubo, T.Yokoyama*[1], T.Shirakawa, T.Iwamura, K.Yamamoto*[2] and H.Okada*[3]
(*E-mail:* okubo@hems.jaeri.go.jp)

A BWR type reduced-moderation water reactor (RMWR) aiming at the long operation cycle more than two years and the high burn-up around 60 GWd/t has been studied [1), 2)], under the high conversion ratio more than 1.0 and the negative void reactivity coefficient. The reactor with such a long operation cycle and high burn-up is mainly expected to be beneficial in reduction of radioactive waste production as well as the economical aspects. In the previous study [1)], a basic core design concept has been established achieving the design goals mentioned above, by newly introducing a special assembly named the void tube assembly, which makes the total core void reactivity coefficient negative overcoming the positive value in the fuel assembly part.

On this concept, further investigation has been performed as in the following. Namely, the higher burn-up core design more than 80GWd/t was investigated, based on the prospects obtained in the basic parametric survey on the possibility for the much longer operation cycle and/or higher burn-up [2)]. The improvement of the void tube assembly was also performed to attain the higher performances in the void reactivity coefficient and in the response characteristics during the transient situation such as the flow reduction transient. The third one was the safety analyses focusing on the stabilities in BWRs and the flow reduction type transient.

Increasing the burn-up is a very favorable point for the RMWR from the economical point of view in the fuel cycle cost. In the previously performed basic parametric survey on the possibility for the much longer operation cycle and/or higher burn-up, the promising prospects have been obtained for the higher burn-up core design more than 80 GWd/t [2)]. This is summarized in Table 3.2.1. At 80 GWd/t, the conversion ratio is over 1.0 for 2.67 years operation cycle and 4-batch refueling scheme case. The burn-up is expected to be increased, when the refueling batch number is increased. Therefore, much higher burn-up is expected to be possible, by increasing the refueling batch number and decreasing the

*1 Toshiba, Co., *2 The Japan Atomic Power Company, *3 Tokyo Electric Power Company

operation cycle. Based on these prospects, the core characteristics were investigated for the increased refueling batch numbers of 5 and 6 under keeping the operation cycle at 2 years. Since the conversion ratio, the negative void reactivity coefficient and the burn-up are in what is called the "trade-off" relation in the tight lattice core design, increasing the burn-up will result in increasing in the void reactivity coefficient and decreasing in the conversion ratio. Therefore, the maximum possible burn-up is limited by the increasing limit of the void reactivity coefficient up to 0.0 or the decreasing limit of the conversion ratio down to 1.0.

The calculated results are summarized in Table 3.2.2. From these results, by introducing 5-batch refueling scheme, a high burn-up of 84 GWd/t would be attained under the conversion ratio of 1.02 and the negative void reactivity coefficient of -1.0×10^{-4} Δk/k/%void. Furthermore, by introducing 6-batch refueling scheme, a very high burn-up of 101 GWd/t would be possible under the conversion ratio of 1.00 and the negative void reactivity coefficient of -0.36×10^{-4} Δk/k/%void. However, since these values for the conversion ratio and the void reactivity coefficient are very close to be the allowable limits for the design targets, the maximum possible burn-up is considered to be 100 GWd/t under this design concept.

As described in the note of Table 3.2.2, the improvement in the void tube design is also introduced in the present calculations. Although the previous design [1] is the diving-bell type one, which is filled with saturated steam under normal operation condition and has open bottom structure, the improved one is the closed-cylinder type one filled with helium gas. The difference between the steam and the helium gas results in the more negative void reactivity coefficient and a little higher conversion ratio for the helium case, and hence, the difference in the burn-up for the 4-batch refueling and 2-year cycle cases in the two Tables.

References:

1) T. Okubo, *et al.* : "Conceptual Designing of Reduced-Moderation Water reactors (1) – Design for BWR-type Reactors –", *Proc. ICONE-8*, ICONE-8422 (2000).

2) T. Okubo, *et al.* : "Conceptual Designing of Reduced-Moderation Water reactors (3) – Study on Long Operation Cycle BWR Type Core –", *Nuclear Energy System Department Annual Report (April 1,1999 –March 31, 2000)*, JAERI-Review 2001-010, 60 (2001).

Table 3.2.1 Burn-up characteristics for long operation cycle and/or higher burn-up

Burn-up range		60GWd/t			80GWd/t			100GWd/t		
Operation cycle	Year	2	4	8	2.67	5.33	10.67	3.33	6.67	13.3
Batch number	-	4	2	1	4	2	1	4	2	1
Burn-up	GWd/t	61	61	60	81	80	79	100	100	97
Pu content (Inner / Outer)	%	16.1/ 18.6	16.6/ 18.9	18.0/ 20.2	16.9/ 19.5	17.9/ 20.5	19.8/ 22.2	18.0/ 20.7	18.6/ 24.2	21.8/ 24.4
Conversion ratio	-	1.04	1.02	0.98	1.02	0.99	0.92	0.98	0.95	0.88
Burn-up reactivity	%Δk/k	2.5	5.1	10.1	3.3	6.9	13.7	4.2	8.7	17.1

Note) Pu composition : Pu238/239/240/241/242/Am241=2.7/47.9/30.3/9.6/8.5/1.0 wt%

Table 3.2.2 Burn-up characteristics for higher burn-up under increased batch number

Batch number		4	5	6
Operation cycle	Year	2		
Burn-up	GWd/t	68	84	101
Pu content (Inner / Outer)	%	16.2/ 17.8	16.8/ 18.5	17.4/ 19.1
Conversion ratio	-	1.03	1.02	1.00
Void reactivity coefficient	10^{-4} Δk/k/%void	-2.2	-1.0	-0.36
Burn-up reactivity	%Δk/k	2.6	2.6	2.6

Note) 1. Pu composition : Pu238/239/240/241/242/Am241=2.7/47.9/30.3/9.6/8.5/1.0 wt%
2. Improved void tube design is introduced.

3.3 Study on ABWR Compatible RMWR Core

H. Akie, Y. Nakano, H. Shirakawa and T. Nakatsuka
(*E-mail*: akie@mike.tokai.jaeri.go.jp)

As one of the RMWR concepts, there has been proposed the 1350 MWe class ABWR compatible core. The ABWR compatible core has the fuel assemblies of square cross section, and the radial size and pitch are the same as the ABWR assembly [1]. Although the conversion ratio of 1.0 and the negative void coefficient is achieved, the discharge burnup of the fuel is only about 25 GWd/t. It is therefore studied to extend the discharge burnup of this core.

The increase in only discharge burnup can be simply achieved by increasing the Pu enrichment of the fuel. But in this case, the conversion ratio decreases and the void reactivity coefficient changes to positive side, at the same time. To increase the conversion ratio, it is effective to decrease moderator to fuel ratio. This, however, makes the void coefficient worse. The void reactivity increase can be avoided to some extent by modifying the axially heterogeneous core specifications of original ABWR compatible core by reducing the Pu enrichment in low enriched regions. In this case, on the other hand, the axial power peaking factor becomes larger. In this study, it was tried to optimize these parameters, i.e. discharge burnup (k_{eff}), conversion ratio, void reactivity and peaking factor (cladding surface heat flux).

For the reduction of Vm/Vf value, a triangular fuel pin arrangement in the ABWR square assembly is considered as shown in Fig. 3.3.1. Here, the pin pitch was fixed to be 11 mm. In addition, the core averaged void fraction is increased to about 55 %. One-dimensional core burnup calculations were carried out by using the SRAC95 system [2] to determine the suitable gap distance between adjacent pins, and the axial Pu enrichment distribution. The pin diameter (D) was changed in the range from 10.0 mm to 9.0 mm in the calculations. The Pu enrichment

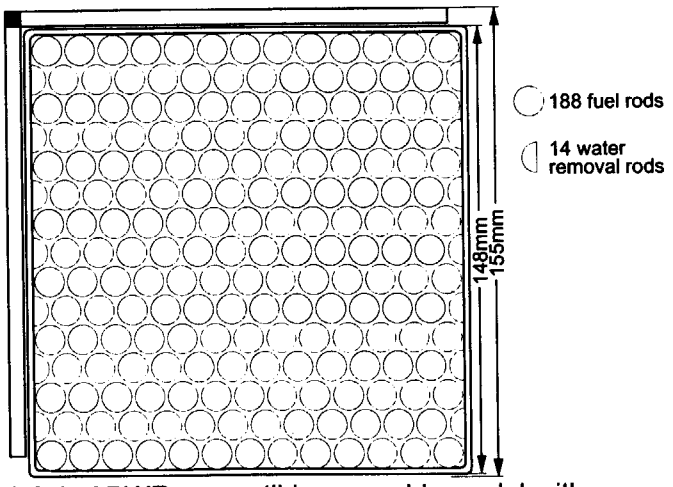

Fig. 3.3.1 ABWR compatible assembly model with triangular fuel lattice

in the high enriched region (*Eh*) was surveyed up to 20 wt.% fis. Pu, and the enrichment in low enriched region (*El*) from 0 to a few wt.% fis. Pu. For the reduction of power peaking due to larger enrichment difference between *Eh* and *El* than in the original ABWR compatible core, 4 layers (instead of 3 layers) of high and low enriched regions were considered. The core height of high enriched region (*Hh*) was changed in the range from 20 to 30 cm and the height of low enriched region (*Hl*) was changed from 35 to 25 cm, respectively. A low enriched region is at the core bottom, and the top of the core is a high enriched region. The total core height is fixed to be 2.2 m.

In the parametric calculations, the target discharge burnup was tentatively set to be 40 GWd/t. With the assumption of 4 batch refueling, the burnup period of 40 GWd/t is divided into 4 cycles, and the following core characteristics were evaluated : (1) Effective multiplication factor at the middle of 3rd cycle (k(2.5c)), which indicates the multiplication factor at EOC of a 4 batch refueling core. (2) Instantaneous conversion ratio at the end of 2nd cycle (CR(2c)), to represent burnup integrated conversion ratio. (3) Void reactivity at the middle of 3rd cycle (VR(2.5c)). The void reactivity at EOC, which is worse than that at BOC, can be estimated. The void reactivity values here is evaluated as a reactivity when the number density of hydrogen is reduced by 0.9 times in all the moderator regions but bottom reflector. (4) Maximum heat flux at cladding surface at the end of 1st cycle (q"(1c)). The power peaking factor is the largest at BOL, but is usually suppressed by control rod, burnable poison, etc.

The target values of these parameters were 1.0 for k(2.5c) to reach 40 GWd/t discharge burnup, 1.0 for CR(2c) and a negative value for VR(2.5c). In order to limit the maximum heat flux to 1.0 MW/m^2 and taking into account the core radial and local power peaking in assemblies, q"(1c) was aimed to be less than 0.85 MW/m^2.

From the parametric survey calculation, the aimed core characteristics seem possible to be achieved with the core specifications of pin-to-pin gap of 1.3 mm (D = 9.7 mm), *Hh*=25 cm and *Hl*=30cm. The enrichments *Eh* will be 16 ~ 17 wt.%, and *El* will be 0.5 ~ 1 wt.%.

To confirm the core performance obtained by the one-dimensional calculation, the 3-dimensional core burnup calculation was performed by simulating 4 batch assemblies refueling. The 872 assemblies are arranged in the core with 155 mm assembly pitch, and the core diameter is about 5.4 m without radial blanket. The enrichment in the high enriched region is 16 wt.% fis. Pu, and in low enriched region is 1 wt.% fis. Pu.

As a result, the discharged burnup is 40 GWd/t, and the burnup averaged conversion

ratio is 1.03. The discharge burnup agrees well with that estimated in the one-dimensional calculations, but the conversion ratio becomes smaller than predicted. The void reactivity is about $+1.6\times10^{-3}$ dk/k at EOC, while in the one-dimensional calculation it can be estimated to be about $+6\times10^{-4}$ dk/k. The 3-dimensional calculation has shown the worse conversion ratio by about 0.03 and the worse void reactivity by about 1.0×10^{-3} than those in the one-dimensional calculation.

For the improvement of particularly void reactivity, additional one-dimensional core burnup calculations were made, by taking into account the difference from 3-dimensional calculation. Firstly, by reducing *El* to 0 wt.%, the void reactivity becomes about -8×10^{-4} dk/k, and is not negative enough. In addition, q" value becomes as large as 0.89 MW/m^2. On the other hand, when pin-to-pin gap is increased to 2.0 mm, it is possible to make the void reactivity sufficiently negative. In this case, however, the conversion ratio becomes less than 1.0. Finally, *El* is reduced to 0 wt.% at the same time of increasing pin gap. As shown in Fig. 3.3.2, both the void reactivity of less than -1.0×10^{-3} and the conversion ratio of larger than 1.03 can be realized when pin gap is 1.7 mm. But in this case, the heat flux value is very large. From these results, it can be concluded very difficult to extend the discharge burnup of ABWR compatible RMWR core to 40 GWd/t. In comparison with the other type of RMWRs, the discharge burnup of only less than 40 GWd/t is a big disadvantage. By utilizing a special method such as the void tube assembly, the core characteristics will be improved, while losing the simplicity of the core.

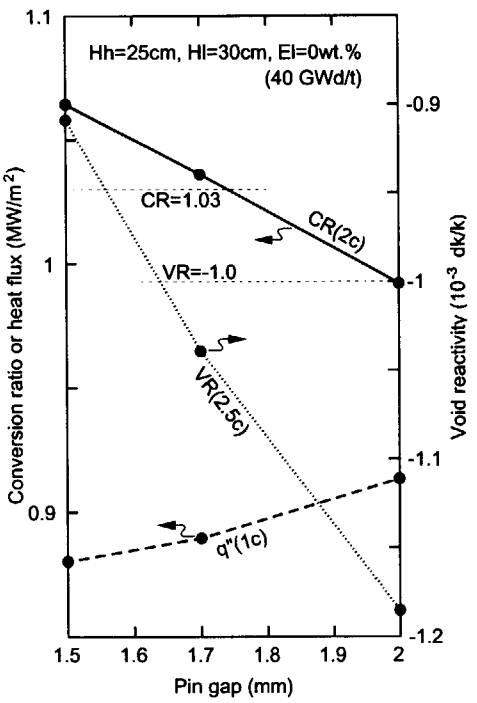

Fig. 3.3.2 Void reactivity, conversion ratio and heat flux (El=0 wt.%)

References

1) T. Okubo, et al. : "proc. 8th international Conference on Nuclear Engineering (ICONE-8)", ICONE-8422 (2000) [CD-ROM].

2) K. Okumura, et al. : JAERI-Data/Code 96-015, (1996) [in Japanese].

3.4 Study on PWR Type RMWR Core

S. Shimada[*1], T. Okubo, T. Iwamura, K. Hibi[*2], K. Yamamoto[*3] and H. Okada[*4]
(*E-mail* : shimada@popsvr.tokai.jaeri.go.jp)

As a light water cooled PWR type reduced-moderation water reactor (RMWR) core, a concept with seed-blanket fuel assemblies has been investigated [1].

The core concept with the electric power of 1000MWe have been obtained, which keeps conversion ratios over 1.0 and negative void reactivity coefficients.

In the present year, light water cooled type RMWR with the electric power of 1350MWe has been investigated to get higher burn-up for total heavy metal in the core by reducing blanket fuel inventory. Burn-up calculation has been performed by the MVP-BURN code with three dimensional Monte Calro method.[2] The operation length of the reference core is 14 EFPM/cycle and the number of fuel exchange batch is six. The core specification is shown in Table 3.4.1. We have employed the core arrangement with flattened hexagonal seed fuel assemblies around a regular hexagonal blanket fuel assembly as shown in Figure 3.4.1 and Figure 3.4.2. The average burn-up of 25GWd/t for total heavy metal and 53GWd/t for seed including inner blanket have been attained. The average conversion ratio under the equilibrium cycle is about 1.0 and the maximum void reactivity coefficient is negative. Procedures on startup, full power operation and shutdown have been evaluated for the reference core. The core is controlled with only control rods. Using an axially two-parted control rod for reactivity control during about one month and optimizing an arrangement of control rod have kept the maximum linear heat rate under 32.5 kW/m as shown in Figure 3.4.3. The main core characteristics are shown in Table 3.4.2.

The above studies have clarified the feasibility of PWR fast neutron spectrum core with conversion ratios over 1.0 and negative void reactivity coefficients.

---

*1 Engineering Development Co., Ltd., *2 Mitsubishi Heavy Industries, Ltd.,
*3 The Japan Atomic Power Company, *4 Tokyo Electric Power Company

References

1) S.Shimada, et al.: " Conceptual Designing of Reduced-Moderation Water Reactor (4)--Study on PWR Type Core with Light Water Coolant—", JAERI-Review 2002-005, pp.55-57 (2002).

2) K.Hibi, et al.: "Conceptual Designing of Reduced-Moderation Water Reactor (28)--Study on PWR Type Core with Light Water Coolant—", 2002 Annual Meeting of the Atomic Energy Society of Japan, G22 (2002).

Table 3.4.1 Core specification

Item	Specification
Thermal Power	3915MWt
Electric Power	1350MWe
Cycle Length	14EFPM
No. of Batch	6
Effective Core Diameter	5.4m
No. of Inner Seed Assembly	420
No. of Outer Seed Assembly	108
No. of Blanket Assembly	211
No. of Flatten Blanket Assembly	54
Axial Configuration	
Seed Fuel	115cm×2
Axial Blanket	30cm×2
Inner Blanket	40cm
Radial Blanket	330cm
Fuel Total Length	330cm
Inlet Temperature	290°C
Outlet Temperature	325°C
Pressure	15.5MPa

Table 3.4.2 Core characteristics

Item	Characteristics
Fissile Plutonium Enrichment	15.43/19.00 wt%
Total Plutonium Enrichment	26.83/33.04 wt%
Burn-up Defect	1.28 %Δk/k
Maximum Linear Power	31.2 kW/m
Maximum Assembly Power	7.28 MW
Equilibrium Cycle Conversion Ratio	1.00
Plutonium Fissile Conversion Ratio	1.01
Total Void Reactivity Coefficient	-0.13 ～-0.45%Δk/k
Discharge average Burn-up	
Total Heavy Metal	24.8 GWd/t
Seed+Inner Blanket	53.1 GWd/t
Inner Seed	62.1 GWd/t
Outer Seed	55.9 GWd/t
Radial Blanket	9.4 GWd/t
Axial Blanket	4.6 GWd/t
Inner Blanket	8.9 GWd/t
Fuel Inventory	
Total Plutonium (BOEC/EOEC)	33.78/33.71 ton
Fissile Plutonium (BOEC/EOEC)	19.74/19.71 ton
TRU Inventory (BOEC/EOEC)	0.91/1.11 ton
Total Pu Annual Loading/Discharge	5.74/5.71 ton
Fissile Pu Annual Loading/Discharge	3.34/3.34 ton

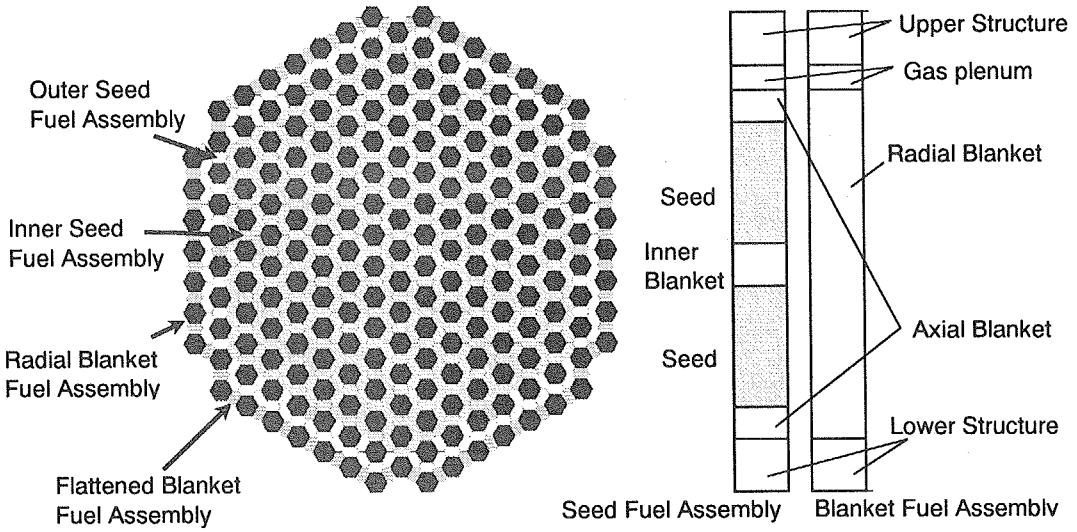

Figure 3.4.1 Core configuration

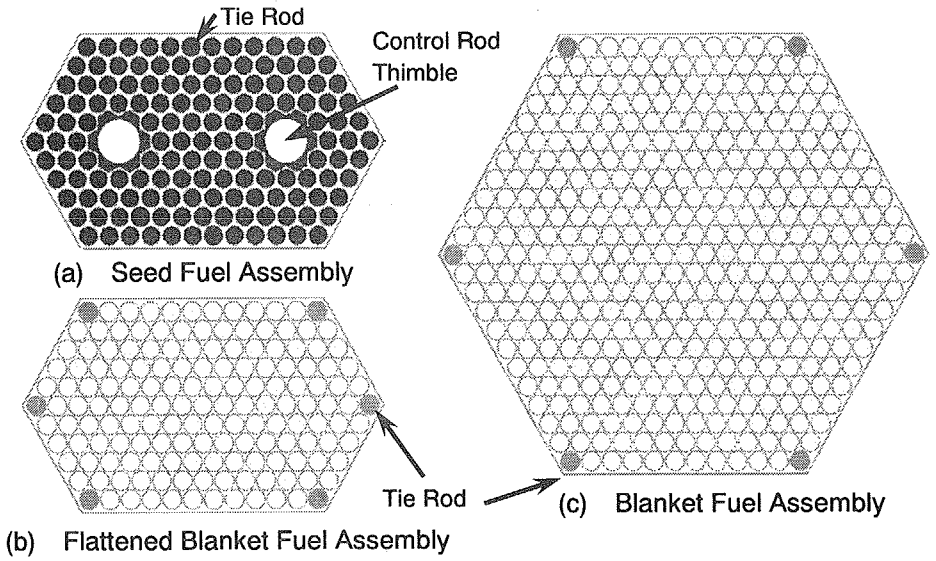

Figure 3.4.2 Horizontal view of fuel assembly

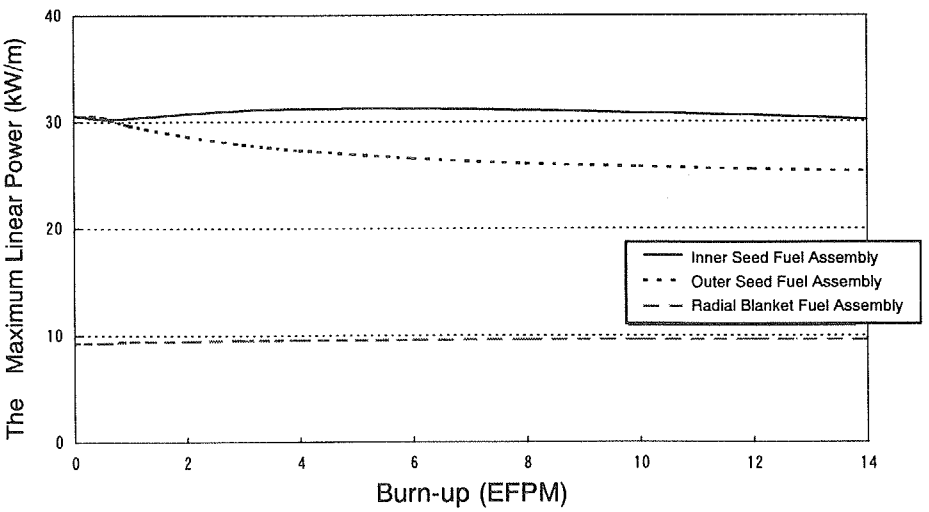

Figure3.4.3 The maximum linear power as a function of equilibrium cycle burn-up

3.5 Optimization a Seed-blanket Type RMWR Fuel Assembly

A. Shelley, S. Shimada[1], T. Kugo, T. Okubo and T. Iwamura
(*E-mail:* shelley@popsvr.tokai.jaeri.go.jp)

Parametric studies have been done for a PWR-type reduced-moderation water reactor (RMWR) with seed-blanket fuel assembles to achieve a high conversion ratio of 1.0, negative void reactivity coefficient and a high burnup of 45 GWd/t by using MOX fuel[1)].

In seed-blanket assembly, MOX is in seed fuel region and depleted UO_2 is in blanket fuel region. The height of seed is considered to be 100cm x2, the axial blanket is 20cm x2 and the internal blanket is 30 cm as the reference for parametric survey. The pitch of seed and blanket fuel rod is 1.3 cm, rod diameter is 1.2cm, pellet diameter is 1.048 cm. In burnup calculation, the thermal power of assembly is adjusted to achieve the average linear heat rate of 20 kW/m in seed. The composition of Pu is assumed to be Pu-238/Pu-239/Pu-240/Pu-241/Pu-242/Am-241 = 2.7/47.9/30.3/9.6/8.5/1.0 wt%. For a nominal case, the temperature of fuel is set to be 889.4 K, clad is 626 K and moderator is 580 K. For void coefficient calculation, void fraction is changed from 0% to 99%. Survey calculations have been done by the MVP-BURN code with 70,000 histories, in which 10,000 particles times 70 batches; plus initial 20 batches skipped from the tally.

A series of calculations were performed by changing the numbers of layers of seed and outer blanket, the height of seed, axial blanket and internal blanket, and the gap of blanket fuel rod. From these calculations we could optimize a seed-blanket type RMWR assembly for high conversion ratio, negative void coefficient and high burnup. Figure 3.5.1 (a) and (b) shows the effect of seed-blanket arrangement on the integrated conversion ratio and void coefficient, respectively. In Fig. 3.5.1, horizontal axis is considered as the percentages of seed fuel rod in seed-blanket assembly. It has been seen from Fig. 3.5.1 (a) that the integrated conversion ratio decreases with increasing the percentages of seed fuel rod in seed-blanket assembly. Also, it has been seen that the integrated conversion ratio increases with increasing the number of seed-blanket layers up to 20, after that it does not change. Figure 3.5.1(b) shows that the void coefficient becomes more positive with increasing the percentages of seed

[1] Engineering Development Co. Ltd.

fuel rod in a seed-blanket assembly. The effect of number of layers on the void coefficient is very small. Therefore it is concluded from Fig. 3.5.1 that 50% to 60% of seed fuel rod in a seed-blanket assembly is the most effective combination to achieve a high-integrated conversion ratio and considerable void coefficient. However, from these seed blanket arrangement, the conversion ratio is less than 1.0 and void coefficient is positive for the average burnup of 45 GWd/t in [Seed (S) + Internal Blanket (IB) + Outer Blanket (OB)] region. Therefore, it is necessary to improve the conversion ratio and void coefficient. For these purposes, parametric studies have been done on the (1) Blanket fuel rod gap (2) Axial blanket height (3) Internal blanket height and (4) Seed height. It is assumed that the conversion ratio will be improved by adjusting the gap of blanket fuel rod and axial blanket height. By increasing the height of internal blanket or decreasing the height of seed it may be possible to improve the void coefficient of a seed-blanket assembly.

By the parametric survey on the different geometrical parameters, a seed-blanket fuel assembly is optimized in which the integrated conversion ratio is 1.0. In the optimized fuel assembly, the height of axial blanket is 40cm x2, internal blanket is 15 cm and seed is 100cm x2 and the seed-blanket layer is S15B5. The horizontal and vertical view of recommended seed-blanket assembly is shown in Fig. 3.5.2. In S15B5 arrangement, the burnup is 38.18 GWd/t in (S + IB + OB) region and 57.45 GWd/t in (S + IB) region. Though the void coefficient is +21.81 pcm/%void (1pcm = 10^{-5} dk/k) in S15B5 arrangement, but it will be negative in the core calculation. For 1350 MWe power reactor, the required number of assembly is 162 by using S15B5 seed-blanket arrangement. And the diameter of this core is 6.1 m

Also, S15B5 seed-blanket fuel assembly is possible to use for a high burnup of 45 GWd/t in (S + IB + OB) region, in which the height of seed is 50cm x2, axial blanket is 40cm x2 and internal blanket is 15 cm. In this assembly, the conversion ratio is 0.97 and the void coefficient is 20.81 pcm/% void. In S15B5 arrangement, the initial loaded fissile Pu is 24.98 ton and the discharged amount of fissile Pu is 23.90 ton. For 1350 MWe power reactor, the required number of assembly is 324 by using S15B5 arrangement and the diameter of the core is 8.7 m.

Finally it is concluded that in seed-blanket type PWR, a fuel assembly with 15 layers of seed fuel rod and 5 layers of blanket fuel rod (S15B5) has higher conversion ratio and higher burnup compared to the other assembles of seed-blanket. Though the void coefficient

is about +20 pcm/%void (1pcm = 10^{-5}dk/k) in S15B5 arrangement, it is expected that it will become negative in the whole core calculation.

Reference:

1) A. Shelley, S. Shimada, T. Kugo, T. Okubo and T. Iwamura, Annual Meeting of the Atomic Energy Society of Japan, G21, (2002).

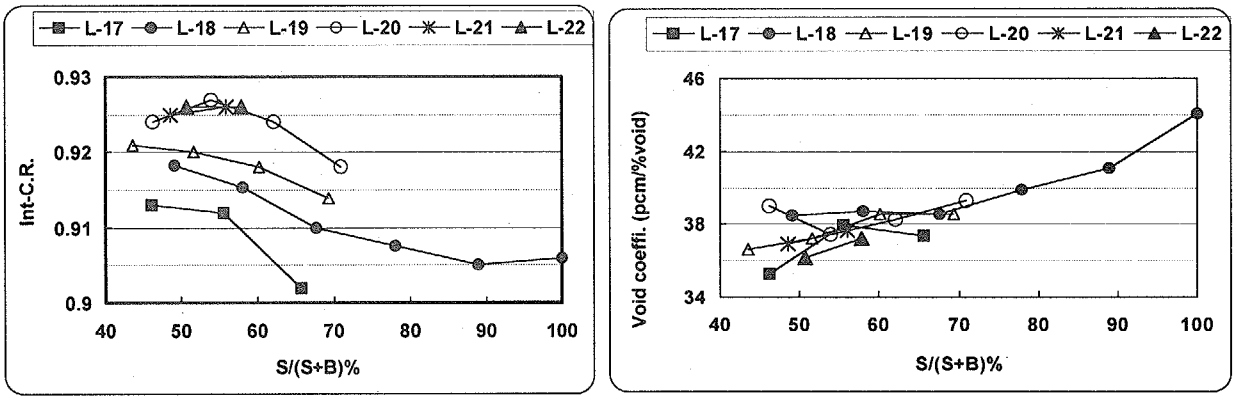

(a) (b)

Fig. 3.5.1 Effect of seed-blanket arrangement on (a) integrated conversion ratio and (b) void coefficient

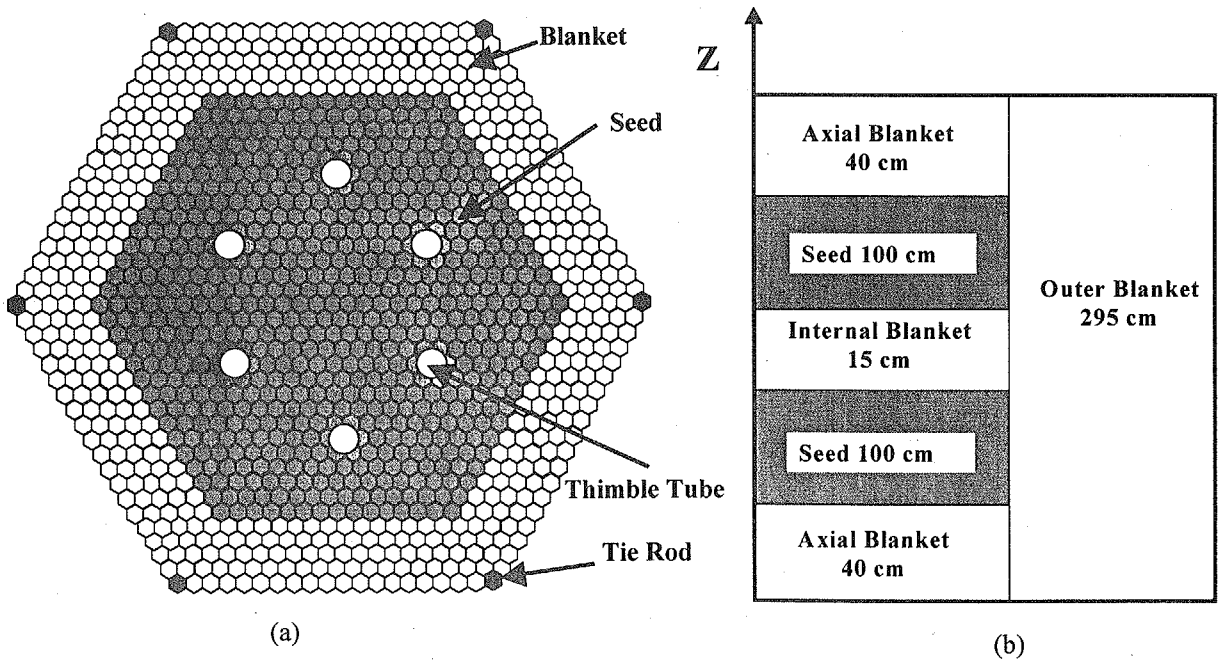

(a) (b)

Fig. 3.5.2 (a) Horizontal and (b) vertical view of optimized seed-blanket arrangement for integrated conversion ratio 1.0

3.6 Study on Dynamical Response Characteristics of RMWR Core

N. Ishikawa, T. Nakatsuka, T. Okubo and T. Iwamura

(*E-mail:* ishikawa@clsu3a0.tokai.jaeri.go.jp)

The Reduced-Moderation Water Reactor (RMWR) has specific features such as tight lattice core, and being operated at low flow rate and high void fraction condition to improve the conversion ratio. To investigate the dynamical response characteristics of RMWR core, analysis was preformed for the BWR type small size RMWR core (330MWe) [1] by modeling the components inside the reactor vessel including re-circulation loop utilizing the transient analysis code TRAC-BF1[2]. Although this RMWR core was designed for natural circulation operation, forced circulation was assumed in this analysis for simplicity.

This RMWR core is composed of 282 fuel bundles. Heated part of the fuel bundle is consisted of MOX region and blanket region. The length of the heated part is 1.30[m] and the total length of the fuel bundle is set to 2.92[m] including the channel box extension for the control rod follower guide. The fuel bundle was modeled by CHAN component of TRAC-BF1 code. To check the fuel bundle characteristics, the pressure boundary condition was introduced by setting the BREAK components at the top and bottom of the fuel bundle as shown in Fig.3.6.1. Figure 3.6.2 shows the pressure distribution of the fuel bundle obtained by steady state setting calculation. Total pressure drop is approximately 40kPa.

To investigate the dynamical response characteristics, we have assumed the geometry inside the reactor vessel as shown in Fig.3.6.3. Figure 3.6.4 is the component noding of TRAC-BF1 input data for modeling this geometry. Dynamical response characteristics were evaluated in the case of changing the pressure loss coefficient at the separator part within the flow loop. In the analysis, pressure drop at the separator is set to 48[kPa] and 70[kPa], respectively. Pump head required to realize the rated core flow rate is 34[kPa] for the separator pressure drop of 48[kPa], and 56[kPa] for the separator pressure drop of 70[kPa]. Figures 3.6.5 - 3.6.7 show the responses of core power, core flow rate and void fraction at the core exit when the reactivity disturbance of 5[cents] was added. The results show that the larger the separator pressure drop becomes, the more the magnitude of flow rate fluctuation increases because of the enlargement of pressure drop in the two-phase region. However, no oscillation is observed in the core power response due to the small absolute value of the void

reactivity coefficient of RMWR core. Also the response of void fraction exhibits a stable response characteristic. It is confirmed that the RMWR core shows the stable response characteristics against the disturbance within the result of this analysis.

The present study was supported by the governmental funding from the innovative and viable nuclear energy technology (IVNET) development project.

References

1) R. Takeda, et al.: "Conceptual Designing of Reduced-Moderation Water Reactor –Design of Small Core with Natural Circulation-- ", 2002 Annual Meeting of the Atomic Energy Society Japan, G23 (2002).

2) J. A. Borkowski, et al.: "TRAC-BF1/MOD1: An Advanced Best-Estimate Computer Program for BWR Accident Analysis", NP-1850-CCM, NUREG/CR-4356 (1992).

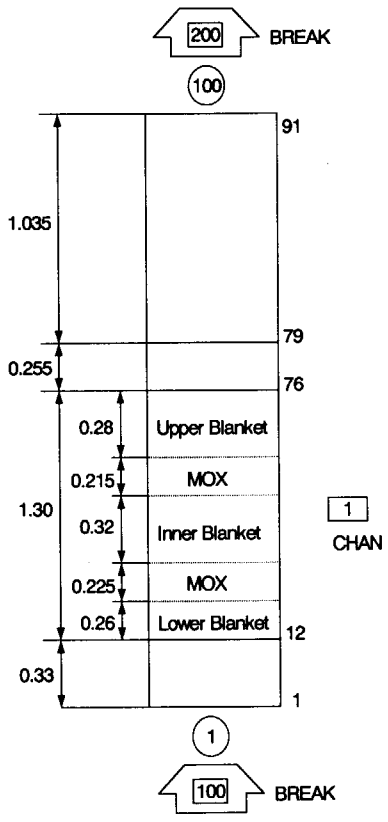

Fig.3.6.1 Fuel bundle model

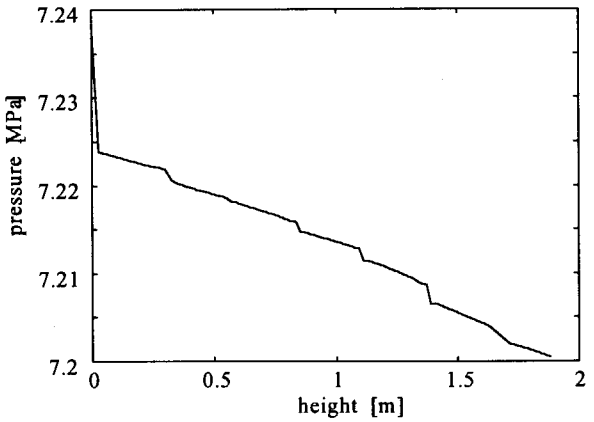

Fig.3.6.2 Pressure distribution

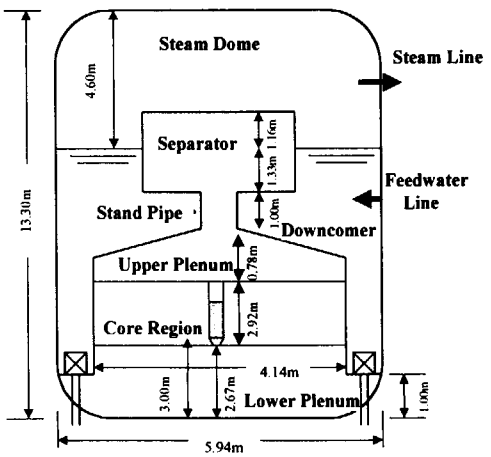

Fig.3.6.3 Geometry within reactor vessel

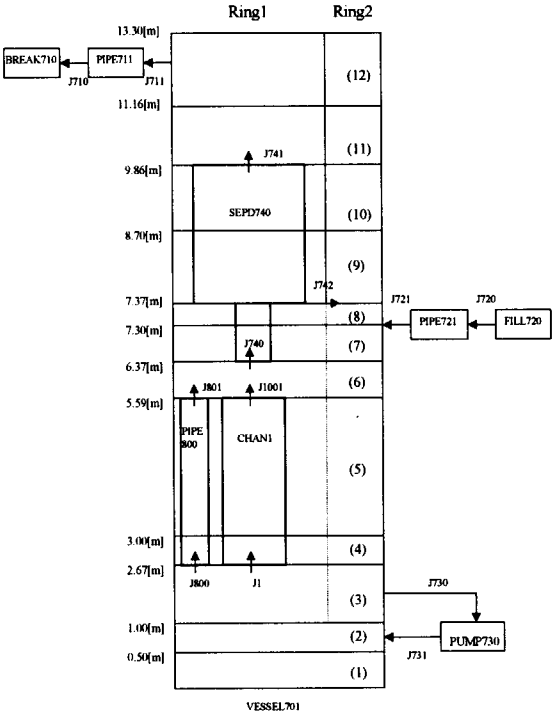

Fig.3.6.4 Reactor vessel model

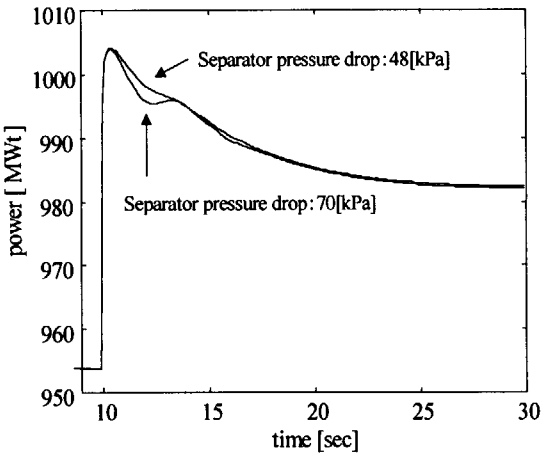

Fig.3.6.5 Core power response

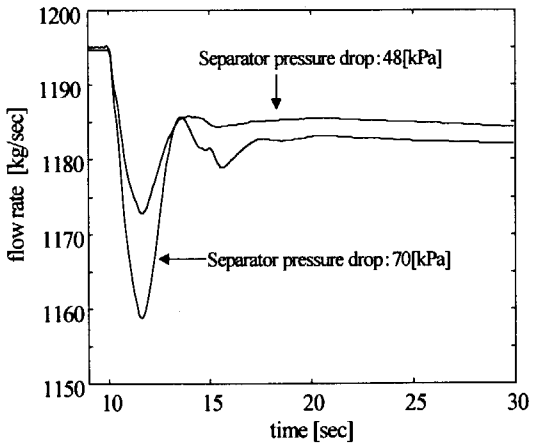

Fig.3.6.6 Core flow response

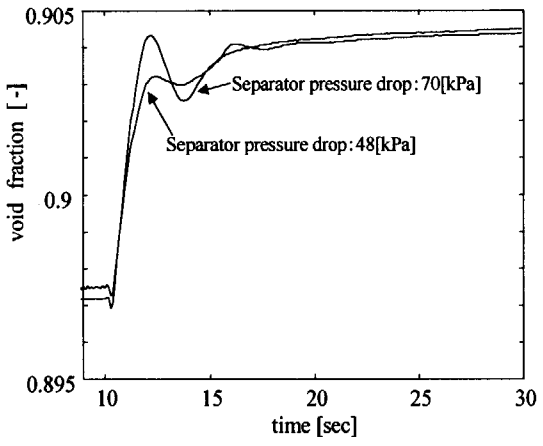

Fig.3.6.7 Void fraction response

3.7 TRAC-BF1 Simulation of Geysering Experiments for Start-up Analysis of BWR Type RMWR with Natural Circulation Core Cooling

T. Nakatsuka, F. Araya, N. Ishikawa and T. Iwamura
(*E-mail*: nakatuka@popsvr.tokai.jaeri.go.jp)

Adoption of natural circulation cooling with passive safety systems is thought to be a way to enhance reactor safety and plant simplicity of BWR type Reduced-Moderation Water Reactor (RMWR). From thermal hydraulic aspects, there were concerns about geysering instabilities which may occur during the start-up of the SBWR[1]. Geysering instabilities can be avoided with appropriate start-up procedures[2]. Therefore, it is important to assess the conditions that geysering occurs and to build rational start-up sequences for each natural circulation BWR. In the present study, geysering experiments with two parallel heated parts performed by Aritomi et al.[3] were simulated with TRAC-BF1 code to assess the applicability of the code to geysering stability analysis for natural circulation BWRs.

As depicted in Fig. 3.7.1, inlet pipes were modeled with FILL component to set a flowrate boundary to simulate flow control by forced circulation. The inlet plenum was modeled with three TEE components to simulate coolant branch. The heated part which consists of two parallel channels is modeled as two CHAN components. Outlet pipes were modeled with BREAK component to set a pressure boundary. The outlet plenum is modeled with TEE components like the inlet plenum. The CHAN components were axially divided into 132 meshes to exclude dependence on the mesh length.

Figure 3.7.2 shows a typical example of geysering calculation. The coolant velocities from the inlet plenum to the left and the right part inlets are shown in the figure. The oscillations for the right and the left side are 180 degrees out of phase each other. Although the geysering was reproducible in the calculation, the difference existed in the amplitude of the oscillation. For the amplitude prediction, it is required to tune the pressure loss coefficient of the inlet orifice.

Figure 3.7.3 shows calculated results compared with the flow stability map acquired from the experimental data. The heat flux of the boundary is well in agreement with the

experimental data within about 10% of error. The onset of geysering can be predicted in good accuracy with TRAC-BF1. It was concluded that TRAC-BF1 can be applicable to the analysis for rational start-up sequences for natural circulation RMWR.

The present study was conducted with the governmental funding from the innovative and viable nuclear energy technology (IVNET) development project operated by the Institute of Applied Energy (IAE).

References:

1) T. Takemoto, et al.: "Experimental Study on The Driving Mechanism of Geysering – The coalescence Mechanism of Slug Bubbles", Proc. Second Japan-Korea Symposium on Nuclear Thermal Hydraulics and Safety (NTHAS2), Fukuoka, Japan, Oct. 15-18, pp. 652-657 (2000).

2) J.H. Chiang, et al.: "Fundamental Study on Thermo-Hydraulics during Start-Up in Natural Circulation Boiling Water Reactors, (III) Effects of System Pressure on Geysering and Natural Circulation Oscillation", J. Nuclear Science and Technology, Vol. 31, 9, pp. 883-893 (1994).

3) M. Aritomi, et al.: "Geysering in parallel boililng channels", Nuclear Engineering and Design, 141, pp.111-121 (1993).

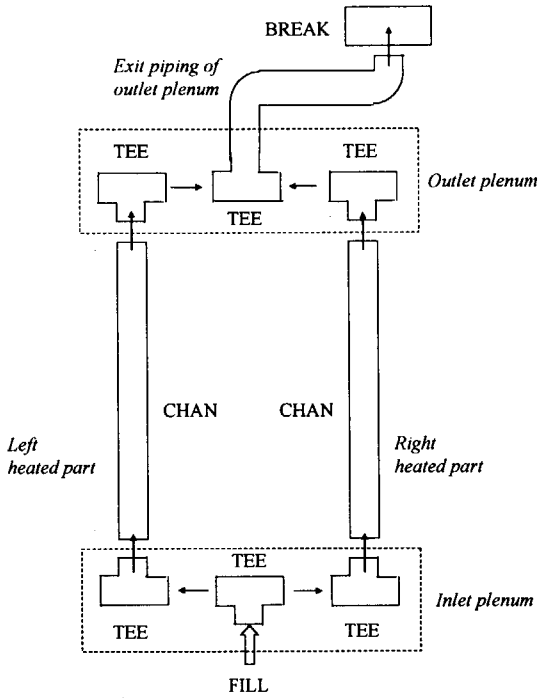

Fig. 3.7.1 TRAC-BF1 analysis model for geysering experiments

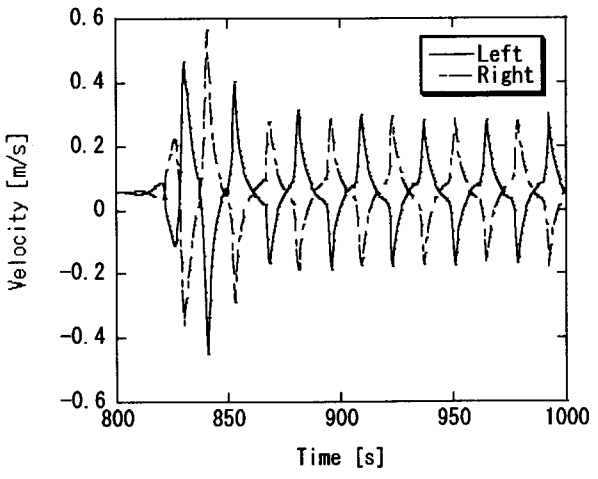

Fig.3.7.2 Coolant velocity from inlet plenum to heated part inlet

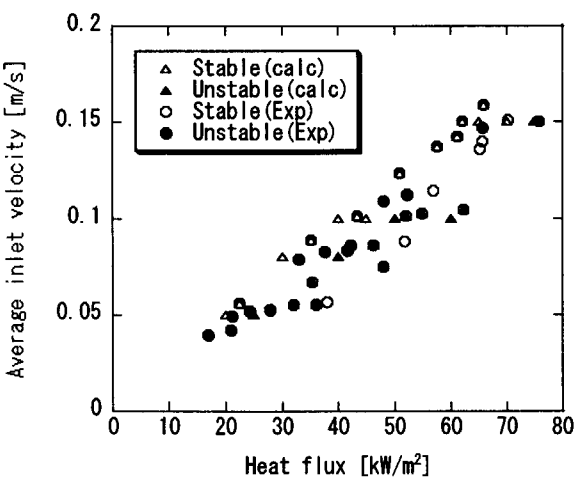

Fig.3.7.3 Calculated results compared with flow stability map

3.8 Analysis of MOX Fuel Behavior in RMWR by FEMAXI-RM Code

M. Suzuki, T. Okubo and T. Iwamura
(*E-mail:* motoe@popsvr.tokai.jaeri.go.jp)

To assess the thermal and mechanical feasibility of MOX fuel rod design in RMWR irradiation conditions, MOX fuel performance code FEMAXI-RM has been developed as an extended version of FEMAXI-V[1] and analysis on the in-pile behaviors of the MOX rod has been carried out. In the calculation, specifications of the rod have been input in conformity with the design of RMWR[2], and the rod is divided into 34 axial segments, in which pellet chemical composition, linear power, and fast neutron flux are designated by input to predict temperature, fission gas release, internal pressure, deformations, and PCMI.

With respect to the MOX fuel thermal conductivity, results of two cases have been compared; a conservative case with Baron model[3], and non-conservative case with MATPRO-11 model[4]. Baron model assumes considerable degradation with burnup, while the other has no burnup dependence. For fission gas release, White-Tucker-Speight model[5,6] has been adopted, and for pellet swelling, Studsvik model[7] has been adopted.

Figure 3.8.1 shows the pellet center temperatures at peak power elevation of MOX fuel. The temperature is higher with Baron model than the other. However, the highest temperature is around 2400K at 49.4 GWd/t, having a large safety margin in comparison with the melting point of 31%Pu-MOX fuel of 2950K by MATPRO-11.

Figure 3.8.2 shows internal pressure rise, which is attributed mainly to the fission gas release. It is 6.2 MPa at the maximum with Baron model and does not exceed the coolant pressure of 7.2MPa, suggesting that the cladding will not cause creep-out by overpressure.

Figure 3.8.3 shows cladding diameter change. From 30 to 40 GWd/t, the diameter increase is slightly larger in the Baron model case due to higher pellet temperature than in the other, while above 40GWd/tHM the increase is smaller in the Baron model case due to enhanced fission gas release from grain boundary gas bubbles. Throughout this process, the cladding diameter strain remains within 1%, suggesting that the cladding integrity is kept. However, growth of fission gas bubbles are capable of having a significant contribution to pellet swelling in high burnup MOX fuel. Therefore, observation of actual fuel swelling behavior will be required.

In conclusion, calculated fuel center temperature of MOX fuel does not reach the melting point by a large margin, internal pressure enhanced by fission gas release is below the coolant pressure level, and cladding diameter increase remains within 1%. These results permit to predict that the MOX fuel rod integrity will be held during irradiation in RMWR, though actual behaviors of MOX pellet swelling requires to be investigated in detail.

The present study was supported by the governmental funding from the innovative and viable unclear energy technology (IVNET) development project operated by the Institute of Applied Energy (IAE).

References:

1) M. Suzuki: "Light Water Reactor Fuel Analysis Code FEMAXI-V(ver.1)", JAERI-Data/Code 2000-030 (2000).
2) T.Okubo, M.Suzuki, T.Iwamura, et al.: "Design of small Reduced-moderation water reactor (RMWR) with natural circulation cooling", PHYSOR 2002, Seoul, Korea (2002).
3) D.Baron and J.C.Couty: Proc. IAEA TCM on Water Reactor Fuel.Element Modelling at High Burnup, Windermere, U.K. (1994).
4) D.L.Hagrman and G.A.Reyman: MATPRO-Version11, NUREG/CR-0497, TREE-1280, Rev.3. (1979).
5) R.J.White, and M.O Tucker: "A new fission gas release model", J.Nucl.Mater.,118, 1-38 (1983).
6) M.V.Speight: Nucl.Sci.Eng.37, 180 (1969).
7) D.Schrire, A.Kindlund, and P.Ekberg: "Solid Swelling of LWR UO_2 Fuel", HPR-349/22, Enlarged HPG Meeting, Lillehammer, Norway (1998).

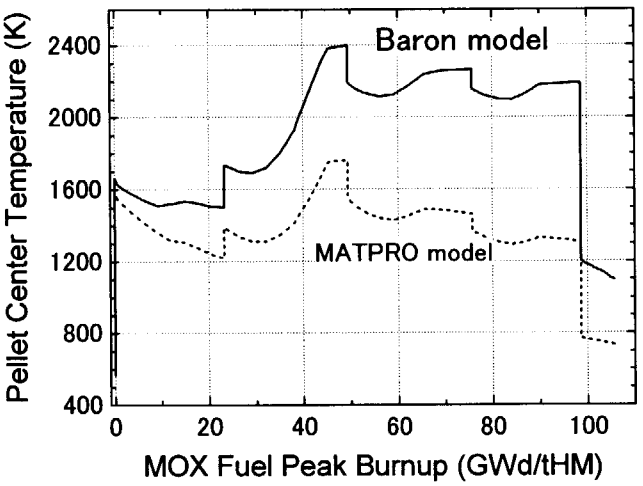

Fig.3.8.1 Calculated MOX pellet center temperatures.

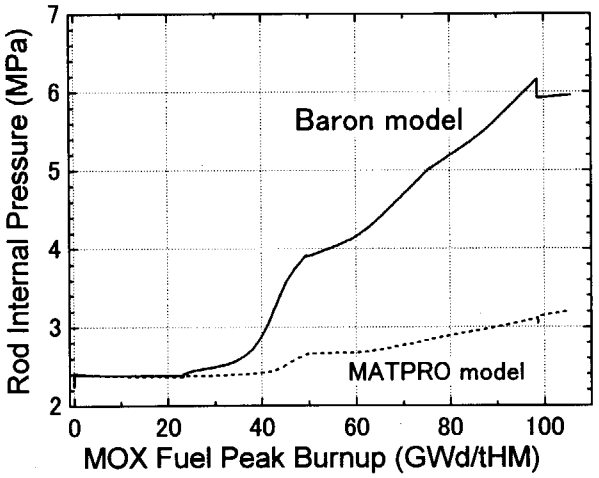

Fig.3.8.2 Calculated internal pressures.

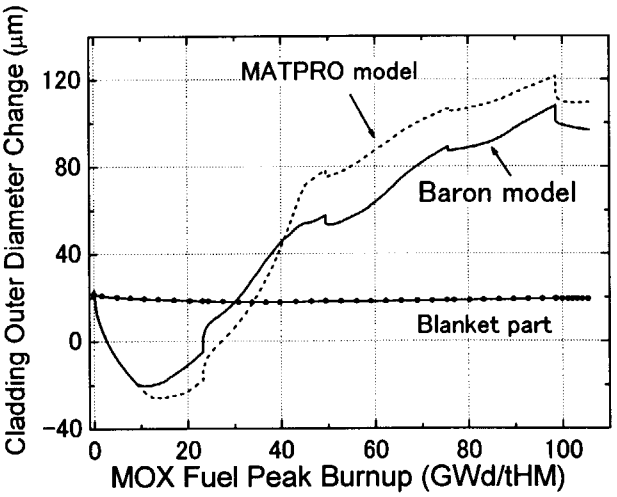

Fig.3.8.3 Calculated cladding diameter changes for MOX fuel part and blanket part.

3.9 Study on Economical Reprocessing Process Relevant for RMWR

H. Mineo, T. Okubo and T. Iwamura
(*E-mail:* mineo@procsafe.tokai.jaeri.go.jp)

Study on reprocessing processes was carried out to select a candidate reprocessing technology and propose a reprocessing process concept, which could be relevant for RMWR fuel recycling with economical competitiveness of power generation to LWRs.

Technology evaluation was made among current Purex method, single-cycle Purex method, oxide electrorefining, metal electrorefining and fluoride volatility method, in terms of effectiveness for reprocessing cost reduction, achievable decontamination factor and technological maturity. Among them, the single-cycle Purex method was finally selected as the candidate technology for RMWR fuel reprocessing[1),2)].

As shown in Fig. 3.9.1, current Purex process consists of a co-decontamination step, a U/Pu partitioning step and purification steps for separated U and Pu, which can achieve high decontamination factor more than 10^7 with respect to fission products (FP). Spent RMWR fuel is a MOX fuel containing about 11 wt% of Pu. Therefore, the capacity of Pu purification step should be enlarged when current Purex method is applied to reprocess RMWR fuel at the same amount of throughput as LWR fuel reprocessing. This would cause higher reprocessing cost. Since RMWR fuel cycle does not require such high extent of purification[3)], the purification step may be deleted, which could reduce reprocessing cost significantly. However, Np has an adverse effect on RMWR core performance and could lower conversion ratio. Therefore, retention of Np from the MOX product was required. Multi-recycling performance of RMWR was evaluated and showed that the conversion ratio of 1.06 could be maintained when the FP decontamination factor and the Np decontamination factor were 10^5 and 100, respectively[3)].

Literature survey showed that the single-cycle Purex process could achieve a FP decontamination factor of about 10^5. As for Np retention, JAERI has been developing a novel reprocessing technology, namely PARC process, which is basically single-cycle with Np retention function. Spent LWR fuel test on the process has been performed and the Np separation function was confirmed, recently[4)].

From those studies, an advanced reprocessing process for RMWR was proposed[1,2)],

which is exhibited in Fig. 3.9.2. Spent MOX fuel from RMWRs is dissolved and radioactive iodine is removed. Am, Cm and FP are separated into the high-level liquid waste stream. Np and FP, particularly Tc are separated from U/Pu stream before U and Pu partitioning step and introduced into the high-level liquid waste stream. Pu is recovered with portion of U and the rest of U is recovered. Features of the proposed reprocessing process are:

(1) Reprocessing cost can be reduced comparing to current Purex method.

(2) Medium extent of decontamination factor can be achieved, which is relevant for multi-recycling by RMWR. In addition, it would be possible that the MOX product from the reprocessing process enables to apply current MOX fuel fabrication technology to RMWR fuel fabrication, which could achieve near-term deployment of RMWR fuel cycle.

(3) Simplified process can minimize waste arising from the process. Salt-free solvent washing technology can be applied for further waste reduction.

(4) Purified Pu does not exist in the process, which could strengthen proliferation resistance. Furthermore, accurate Pu accountancy technology can be utilized, which has been already developed for current Purex process.

In conclusion, key technology of the proposed process is the Np separation from U/Pu stream. Further study is required, particularly on determination of relevant decontamination factor for each element, optimization of Np separation flow sheet and demonstration of the flow sheet by spent fuel tests.

Portion of the present study was supported by the governmental funding from the innovative and viable nuclear energy technology (IVNET) development project operated by the Institute of Applied Energy (IAE).

References

1) H. Mineo, et al.: "Study on Reduced-Moderation Water Reactors (RMWRs) (36) – Study on Reprocessig Process for RMWR system –", Preprints of 2002 AESJ Fall Meeting, M28, (2002) [in Japanese].

2) H. Mineo, et al.: "PARC Process for Reprocessing Spent Fuels from Advanced Nuclear Reactors", Proc. the 13th Pacific Basin Nuclear Conference (PBNC2002), (2002).

3) T. Okubo, et al.: "Design Study on Reduced-Moderation Water Reactor (RMWR)", Proc. the 8th National Symposium on Power and Energy Systems (SPES 2002), JSME, 2002

[in Japanese].

4) G. Uchiyama et al.: "Advanced Technologies for Long-lived Nuclides Separation in Reprocessing", Proc. GLOBAL 2001, (2001).

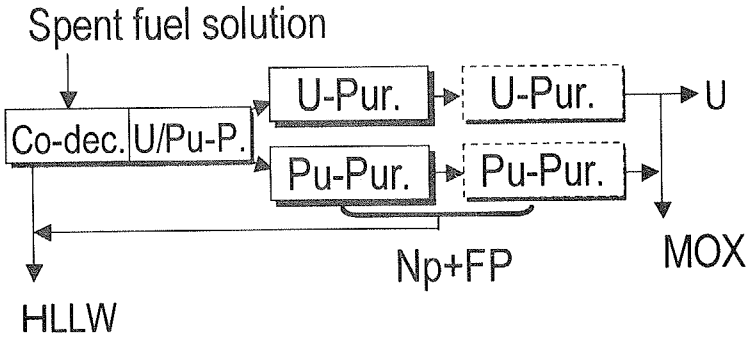

Co-dec.: Co-decontamination step
U/Pu-P.: U/Pu Partitioning step
U-Pur.: U-Purification step
Pu-Pur.: Pu-Purification step

Fig. 3.9.1 Schematic of current Purex process

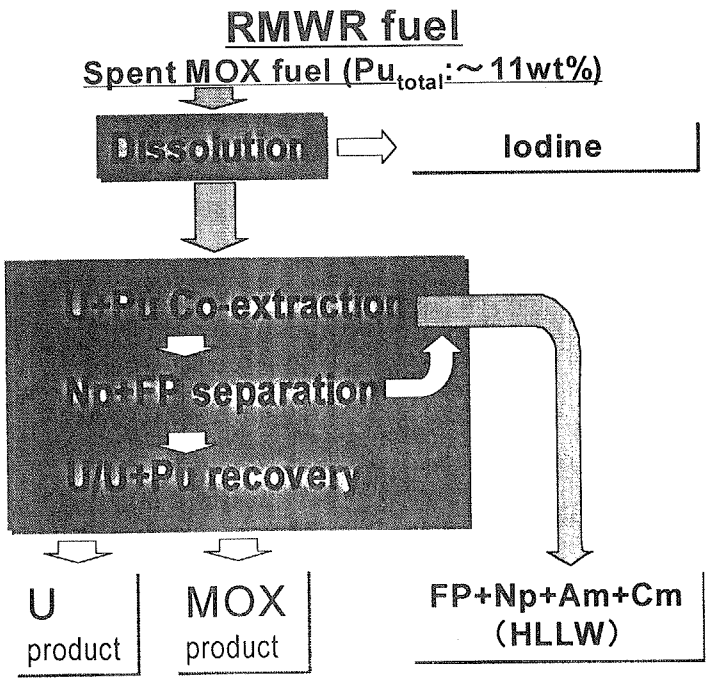

Fig. 3.9.2 Proposed advanced reprocessing process for RMWR

3.10 Smart Software Integration for Intelligent Monitoring Systems

T. Suzudo and K. Nabeshima
(*E-mail:* suzudo@clsu3a0.tokai.jaeri.go.jp)

This paper proposes a new scheme of software integration for developing monitoring systems using standard I/O data communication stream between different software modules. The data communication between modules is established by connecting the standard I/O stream of a module to that of another. This methodology naturally makes it much easier for any software code to adapt to the new on-line data environment, because almost all programming languages have the standard I/O libraries. In addition, each module can be located at any platform with remote login server functionality. The new concept proposed here is to create each module as a TTY-based interactive program; it reads from and writes to a standard I/O so that humans can operate it. If human operation were fast and reliably accurate enough, it would have been possible to make a real-time distributed system with such modules and a human operator.

In reality, it is necessary to create a program that interacts with and administrates the modules; what can be called an administration program. In principle, it is possible to control a program from another program; an operating system is one such kind of program. Thus, a script program automating human operations necessary for administrating all the modules will satisfy the basic requirements of the administration program. Fortunately, a convenient toolkit for automating interactive programs, called Expect[1] is available as free software. Expect was developed by Don Libes in the National Institute of Standards and Technology of USA. At the moment Expect functions can be called from C/C++ and Tcl. Tcl is a portable interpreter language and is suitable for a relatively small program[2].

To demonstrate the usefulness of the new concept, we have applied it to ANNOMA System, which is a neural-network-based anomaly detection system. It is composed of three modules whose software requirements are as follows:

a) The data acquisition module has access to an analog-to-digital converter, which is connected to multi-channel analog inputs from the plant signal panel. The module logs a set of digitized plant data and sends it to other modules in real-time.

b) The neural network module accepts the digitized real-time plant data set from the data acquisition module, then it calculates the expected value for each plant parameter. The neural network is trained in advance using past plant data so that the expected and measured values are adjacent when the plant state is normal. The deviations of each expected value from the corresponding measured value, say `errors', are sent to the graphical user interface (GUI) module. Detail of the neural network in use are given by Nabeshima et al[3].

c) The GUI module acquires the measured plant parameters from the data acquisition module and the corresponding errors from the neural network module. Operators can request the module to display the plant parameters. In addition, if at least one of the error values exceeds the threshold determined in advance, it gives an alarm to operators.

The schematic picture of the system is shown in Fig. 3.10.1. With this design, the data communication between different modules became easy and the source code became more portable. In fact, we merely inserted several lines of READ or WRITE statements in the FORTRAN source code of the neural-network module. This is the greatest advantage of this communication methodology, that is, any data analysis techniques tested in an off-line environment can be easily embedded into the real-time environment. The main procedure of the real-time process was designed as follows.

1) The administration program sends a "get" command to the standard input of the data acquisition module.

2) When the data acquisition module read the "get" command, it writes the recent plant data on the standard output to be read by the administration program.

3) The administration program sends the plant data to the standard input of the neural network module.

4) On accepting the plant data from the standard input, the neural network module makes the necessary calculation described above and writes the results on the standard output to be read by administration program.

5) The administration program sends the plant data measured by the data acquisition program and the calculated data by the neural network module to the

standard input of the GUI module.

6) On reading the data sets above, the GUI module makes necessary updates.

7) The administration program waits for the next timing for AD conversion. When time is up, go to 1).

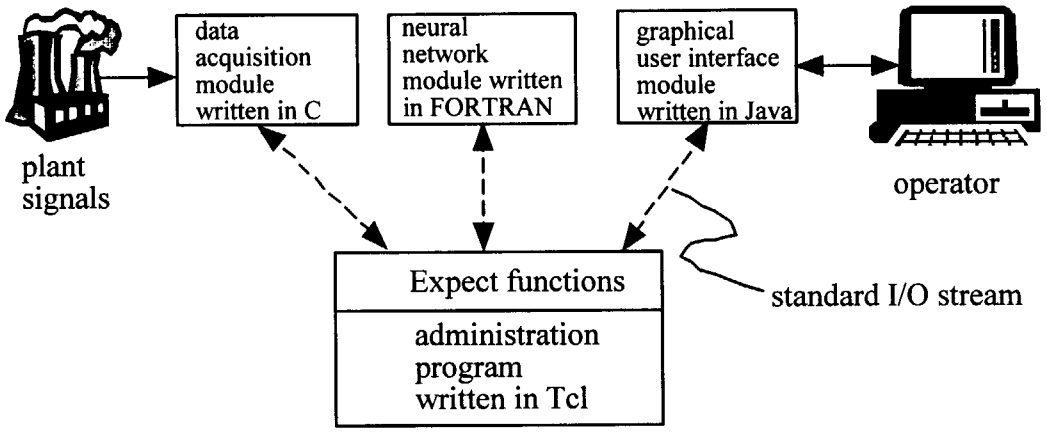

Fig. 3.10.1 Basic software configuration of ANNOMA system

Reference

1) D. Libes D.: "Exploring Expect; A Tcl-Based Toolkit for Automating Interactive Programs", O'Reilly (1995).

2) J. K. Ousterhout: "Tcl and Tk Toolkit", Addison-Wesley (1994).

3) K. Nabeshima, T. Suzudo, T. Ohno and K. Kudo: "Neuro-expert monitoring system for nuclear power plant", Fifth International Conference on Knowledge-Based Intelligent Information Engineering Systems & Allied Technologies, Osaka and Nara, Japan (2001).

4. Thermal and Fluid Engineering

Advanced computer programs have been developed and several tests were performed to develop thermal hydraulic analyses method in next-generation nuclear systems such as reduced moderation water reactors (RMWRs), and fusion reactor.

A critical heat flux (CHF) test for a high conversion type BWR design was performed using the tight-lattice fuel assembly including seven heater rods arranged in the triangular array with 1.0 mm rod gap size. Measured critical heat fluxes were higher than those calculated with the design correlation by about 60 %. The test results support the feasibility of the current core design. An assessment study of subchannel analysis code, COBRA-TF, was started to check the applicability to the tight-lattice core.

A multidimensional two-phase flow analysis code based on the two-fluid model (we named ACE-3D) has been improved by installation of boundary fitting coordinate (BFC) function for the simulation of thermal hydraulic behavior inside fuel assembly. Test calculations confirmed that the BFC function was successfully installed. A two-phase flow simulation code with interface tracking (we named TPFIT code) was started in FY 2000 to optimize and evaluate the thermal hydraulic design of RMWRs. In FY 2001, a new interface tracking method was developed to reduce the numerical diffusion. To validate these advanced codes, very detail information is required. To measure the void fraction distribution inside a tight lattice core, a new 3D measuring system has been developed using neutron radiography technique combined with the computer tomography technique.

A series of experiments on thermal-hydraulic safety in a fusion reactor has been performed to get validation data for safety analysis codes of fusion reactors as one of International Thermonuclear Experimental Reactors (ITER) subtasks since FY 1998. In FY 2001, the ITER subtask has been completed. Several analytical works were performed for ingress-of-coolant-event (ICE) and dust mobilization behavior during loss-of-vacuum events. It was found from a series of experimental and analytical works that the ITER vacuum vessel pressure suppression system is very effective to reduce the pressure rise during the ICE. The developed codes for thermal hydraulic safety analyses in ITER were validated for the ICE and the dust mobilization behavior successfully.

4.1 Critical Power Experiments of Tight-Lattice Bundle for BWR-Type Reduced Moderation Water Reactor

M. Kureta, T. Sato and H. Akimoto
(*E-mail*: kureta@hflwing.tokai.jaeri.go.jp)

The purpose of this experiment is to estimate the safety margin of Reduced-Moderation Water Reactor (RMWR), which is the light water breeder reactor. Critical power of forced convective flow boiling of water in a tight lattice bundle was measured parametrically. [1] In this paper, (1) parameter effects, (2) evaluation results of design equation (Arai correlation) and (3) new critical power correlation are described.

Experimental test channel was a 7-rod bundle with rod diameter of 12.3mm, rod gap of 1.0mm and heated length of 1.8m as shown in Fig. 4.1.1. Axial power distribution was flat. Exit pressure of the test section was ranged from 1.0 to 8.5 MPa, inlet water subcooling from 2 to 50 K, mass velocity from 0 to 2500 kg/(m^2s) and transverse heat flux ratio from 0.97 to 1.6. Nominal setting was exit pressure of 7.2 MPa, inlet water subcooling of 7 K, mass velocity of 500 kg/(m^2s) and transverse heat flux ratio of 1.37.

Figure 4.1.2 shows the effect of mass velocity on critical power. Critical power increases monotonously along with the exit perfect evaporation condition. Effect of inlet water temperature on critical quality is shown in Fig. 4.1.3. The critical quality increases slightly with increases the inlet quality under mass velocity > 400 kg/(m^2s). Effect of exit pressure on critical quality is shown in Fig. 4.1.4. The critical quality increases with increasing the exit pressure under nominal condition (mass velocity = 500 kg/(m^2s)). Effect of transverse heat flux ratio on critical quality is shown in Fig. 4.1.5. The critical quality decreases slightly with increasing the transverse heat flux under nominal condition.

Arai correlation has been used as the design equation of the critical power of the RMWR. Extensibility of the Arai correlation to the tight lattice core should be evaluated at the early phase of the development of the RMWR. [2] Figure 4.1.6 shows the comparison of the Arai correlation with the present data. Arai correlation tends to underestimate the critical power at nominal condition. As the power of the RMWR was designed about 30% lower than the correlation, it can be confirmed from this study that existing design of RMWR core is feasible for the subject of critical power.

In order to achieve the best estimation for the critical power by a transient analysis code, critical power correlation was newly developed. The new correlation was derived

using the present data and Bettice Atomic Power Lab. (BAPL) data.[3] Figure 4.1.7 shows the test section of the BAPL. Comparison of the new correlation with the BAPL data is shown in Fig. 4.1.8. New correlation can calculate the trend of critical power taken under the BAPL test condition with a high accuracy. Comparison of the new correlation with all data (371 points) is shown in Fig. 4.1.9. Prediction accuracy of the new correlation is ±4.6%.

References

1) Kureta, M. et al. : "Critical Heat Flux Experiment for Reduced-Moderation Water Reactor (RMWR)", Proc. of the Int. Congress on Advanced Nuclear Power Plants (ICAPP), No.1129, Florida, USA, (2002).

2) Arai, K. et al. : "Critical Power Characteristics of a High Conversion Boiling Water Reactor", IAEA Technical Committee on Technical and Economic Aspects of High Converters, (1990).

3) LeTourneau, B. W. et al., Nucl. Eng. Des., 54, (1973), 214-232.

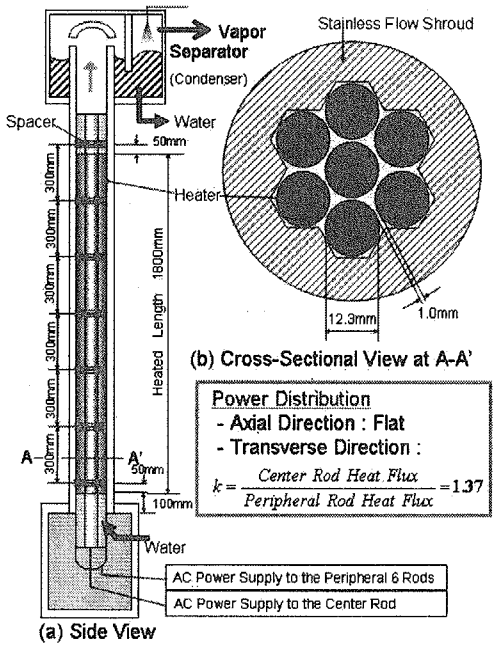

Fig. 4.1.1 Schematic view of the test section

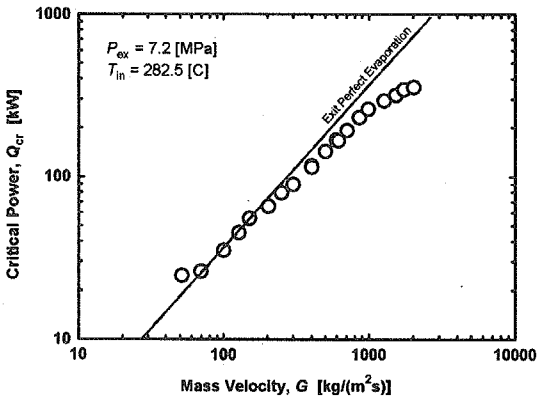

Fig. 4.1.2 Effect of mass velocity on critical power

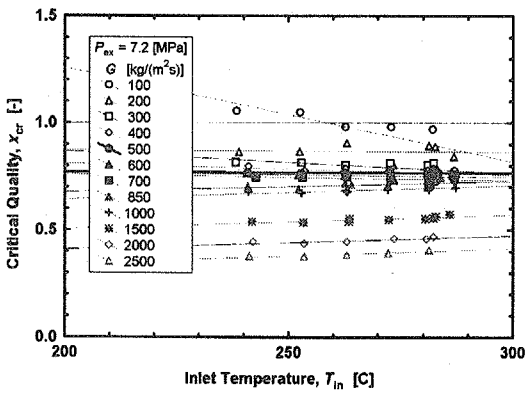

Fig. 4.1.3 Effect of inlet water temperature on critical quality

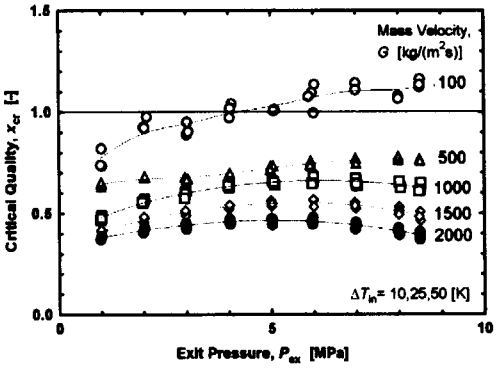

Fig. 4.1.4 Effect of exit pressure on critical quality

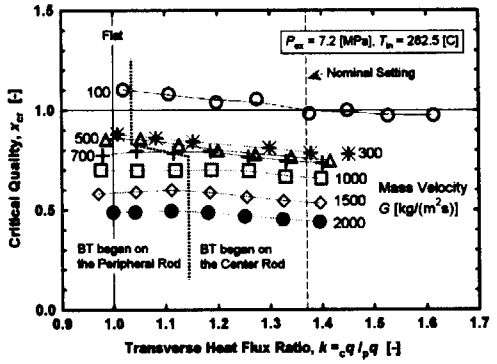

Fig. 4.1.5 Effect of transverse heat flux ratio on critical quality

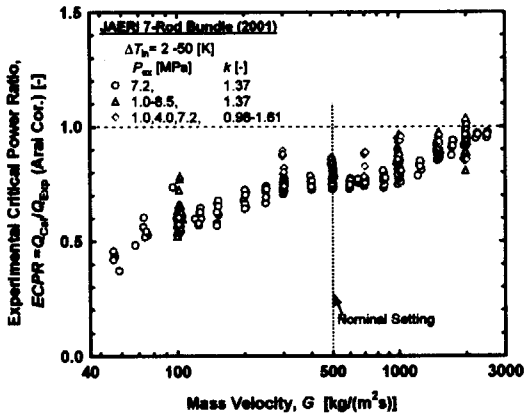

Fig. 4.1.6 Extensibility of the Arai correlation to the tight-lattice rod bundle

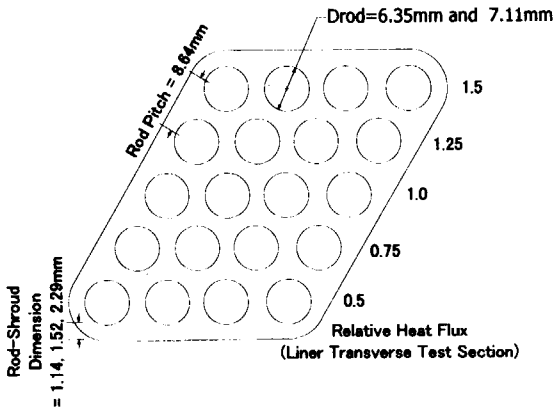

Fig. 4.1.7 Cross-sectional view of the test section of BAPL

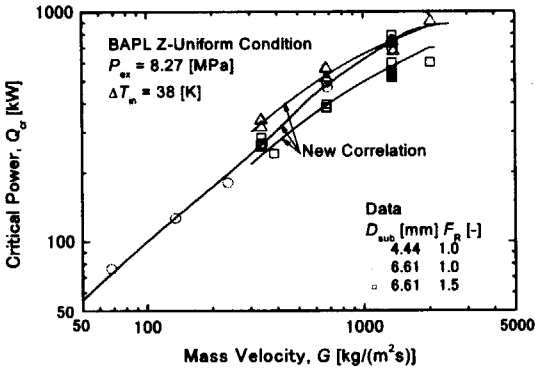

Fig. 4.1.8 Comparison of the new correlation with BAPL data

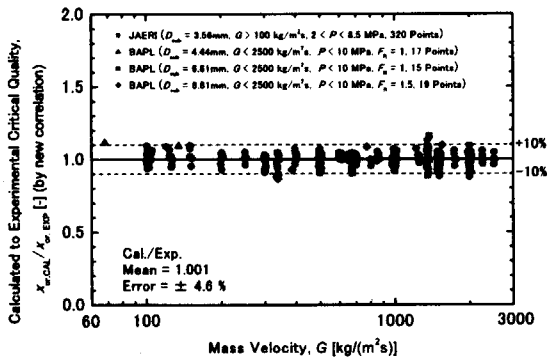

Fig. 4.1.9 Calculation accuracy of the new correlation

4.2 Subchannel Analysis of CHF experiments for Tight Lattice Core with COBRA-TF

T. Nakatsuka, M. Kureta, T. Okubo and H. Akimoto
(*E-mail*: nakatuka@popsvr.tokai.jaeri.go.jp)

Reduced-Moderation Water Reactors [1] comprises tight lattice fuel assemblies with gap clearance around 1.0 mm to reduce water volume ratio to achieve a high conversion ratio. It is important to evaluate the thermal margin of the tight lattice core. Subchannel analyses are expected to be useful to prediction of critical heat flux (CHF) and may provide valuable information to supplement thermal hydraulic experiments. In the present study, to assess the applicability of subchannel analysis for tight lattice cores, series of tight lattice CHF experiments performed in JAERI [2] were analyzed with COBRA-TF code [3].

The test section was a 7-rod bundle with rod diameter of 12.3 mm, rod gap of 1.0 mm and heated part length of 1.8 m (Fig. 4.2.1). Axial power distribution was flat. Experimental conditions are shown in Table 4.2.1. Figure 4.2.2 shows COBRA-TF noding. For simplicity, a 1/6 symmetry model was adopted. The heated part is simulated with 3 heater rods and 4 subchannels and axially divided into 34 nodes. The local pressure loss coefficient was tuned with the single phase experiment data.

In the calculation, boiling transition (BT) was found by heat transfer mode shift from nucleate boiling to transition boiling or single phase vapor. Figure 4.2.3 shows the comparison of the calculated critical powers and experimental data. For the mass velocity of higher than 800 kg/(m^2s), the predicted critical power exceeded the exit perfect evaporation condition. It was because the calculated enthalpy of superheated liquid highly exceeded the saturated enthalpy and that suppressed evaporation. To solve this problem, the interfacial heat transfer model was modified. As in Fig. 4.2.4, the predicted critical powers with the modification became closer to the measured values in the high mass velocity region.

It was found that COBRA-TF gives good prediction of critical power for mass velocity of around 500 kg/(m^2s), while it underestimates the critical power for lower mass velocity and overestimates for higher mass velocity.

Predicted boiling transition (BT) positions corresponded with the experiments axially. However, the predicted subchannel position was channel 3 or 5 and differed from the measured position, channel 2. Figure 4.2.5 shows predicted amounts of continuous liquid in each subchannel. Continuous liquid mass velocity in channel 3 or 5 is lower than that in channel 2 and the dryout takes place in those channels. It is required to predict the flow distribution in a tight lattice bundle system precisely.

In the future, further studies will be carried out on the factors which affect BT in a tight lattice bundle system

References:

1) T. Okubo, T. Shirakawa, R. Takeda, T. Yokoyama, T. Iwamura and S. Wada : " Conceptual Designing of Reduced-Moderation Water Reactors (1) -Design for BWR-Type Reactors-", Proc. ICONE-8, ICONE-8422 (2000).

2) M. Kureta, H. Akimoto, K. Yamamoto and H. Okada: "Critical heat flux experiment for Reduced-Moderation Water Reactor (RMWR)", Proceedings of International Congress on Advanced Nuclear Power Plants (ICAPP) (CD-ROM) (2002).

3) T. Okubo, A. Ezzidi and Y. Murao: "Assessment of Models in COBRA-TF Code for Liquid Entrainments in Film-Mist Flow", JAERI-M 93-069 (1993).

Table 4.2.1 Experimental conditions

Parameter	Experimental range
Inlet subcooling [K]	2 - 50
Mass velocity [kg/(m^{2}s)]	50 - 2,500
Pressure [MPa]	1.0 - 8.5

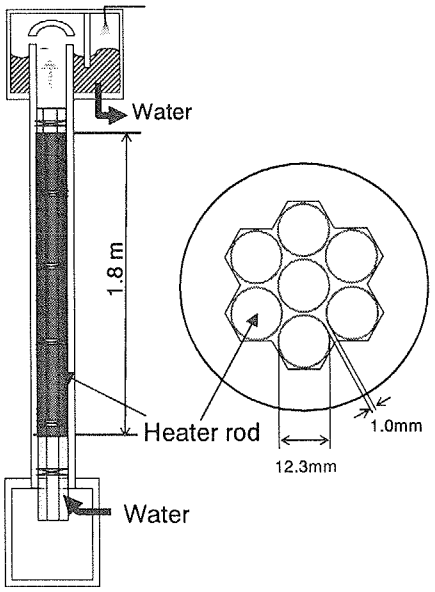

Fig. 4.2.1 Schematic of test section

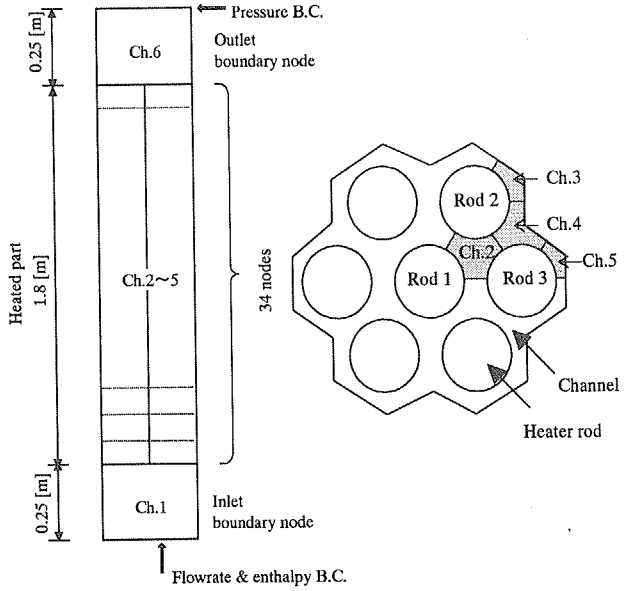

(a) Axial (b) horizontal

Fig. 4.2.2 COBRA-TF Noding

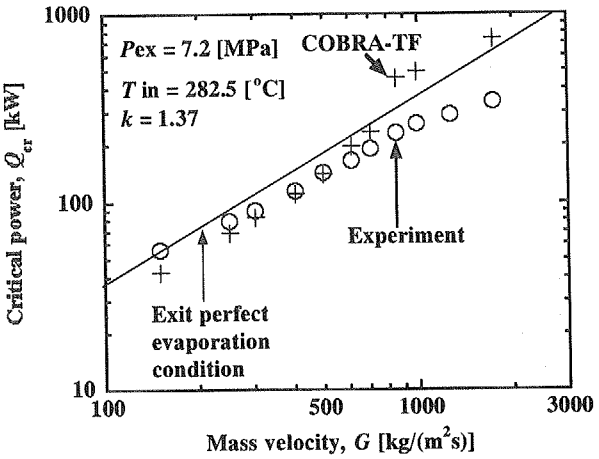

Fig. 4.2.3 Comparison of calculated critical power (without modification) and experimental data

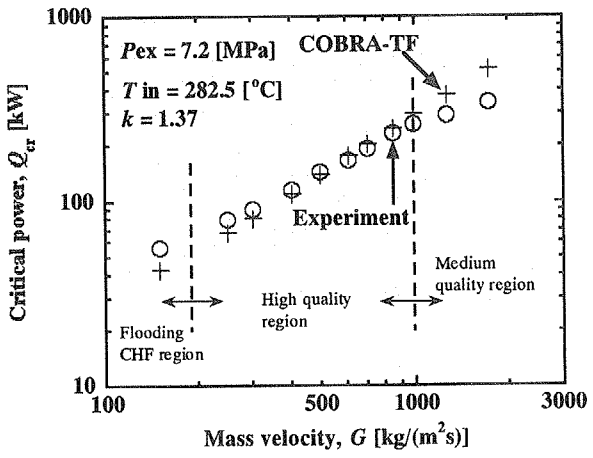

Fig. 4.2.4 Comparison of calculated critical power (with modification) and experimental data

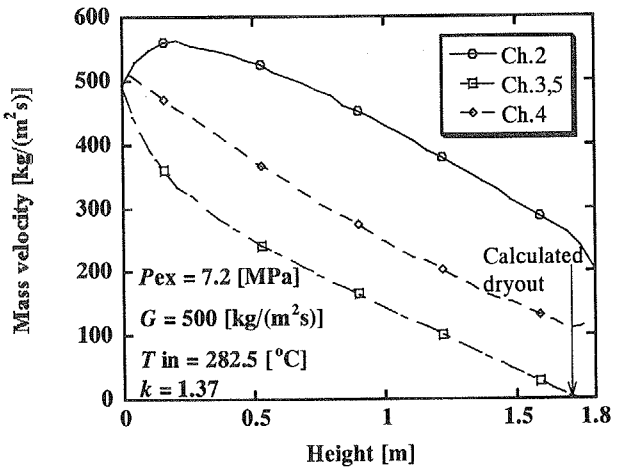

Fig. 4.2.5 Continuous liquid field mass velocity vs. height

4.3 Development of the Neutron Radiography 3D CT (NR3DCT) for Measuring the Void Fraction Distribution in Tight-Lattice Bundle

M. Kureta and H. Akimoto
(*E-mail*: kureta@hflwing.tokai.jaeri.go.jp)

New 3D void fraction measurement system has been developed using neutron radiography technique with taking in the computer tomography (CT) technique, named NR3DCT. The purpose of this development is to measure the void fraction distribution in tight lattice bundles which simulates the Reduced-Moderation Water Reactor (RMWR) core. In this report, the measurement system is described and some measurements are shown for void fraction distribution of air/water two-phase flow.

Figure 4.3.1 shows the NR3DCT system. The NR3DCT system consists of neutron radiography imaging system, water circulating loop with a tight lattice test section, position control motor and camera link system for the CT, image processing computer system and visualization computer system. JRR-3M is used as the neutron source.

Imaging system is a cold-CCD camera with neutron-to-visible light converter. Original images are automatically saved in the motor-camera link system. Figure 4.3.2 shows the original image recorded by the cold-CCD camera system. Spatial resolution of the image is 0.1mm.

All images are transformed into the parallel computer in order to calculate void fraction distribution with the CT reconstructing technique. Image processing program has been newly developed for the NR3DCT. In this measurement program, γ-ray reduction which is newly developed, brightness and position corrections and CT reconstructing processing to calculate the cross-sectional distribution of the macro cross section Σ are included. By this program, we can obtain the local void fraction and the position information of the test section materials (called "Mask Processing", which is newly developed for visualization of 3D data effectively). Then we can visualize the spatial distribution of the void fraction on 3D and 2D image viewers.

CT reconstructing is conducted by the convolution filtered back projection method (FBP) with a Shepp-Logan filter function. This FBP is the fastest CT reconstructing method. However, since the image size is so large to calculate the 3D distribution of the void fraction, we needed few days to calculate the 3D output. Therefore, the program has been modified to the parallel processing (MPI).

Figure 4.3.3 shows the cross-sectional view of the void fraction. Distribution of water film can be measured by this technique. Close-up view of the void fraction distribution is shown in Fig. 4.3.4. Three-dimensional distribution of the water film is clearly recognized.

Boiling flow will be measured by the NR3DCT as the next step.

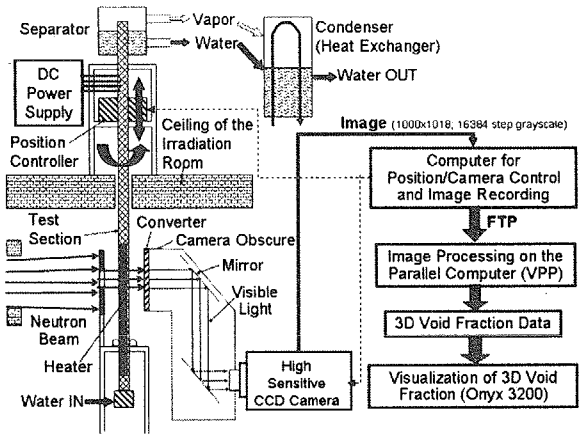

Fig. 4.3.1 Schematic diagram of the NR3DCT system

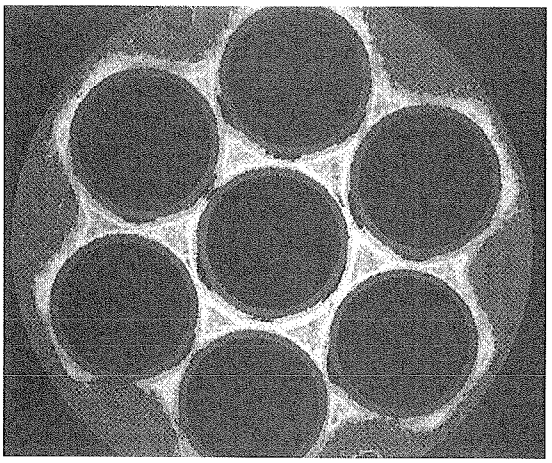

Fig. 4.3.3 Cross-sectional view of the void fraction distribution

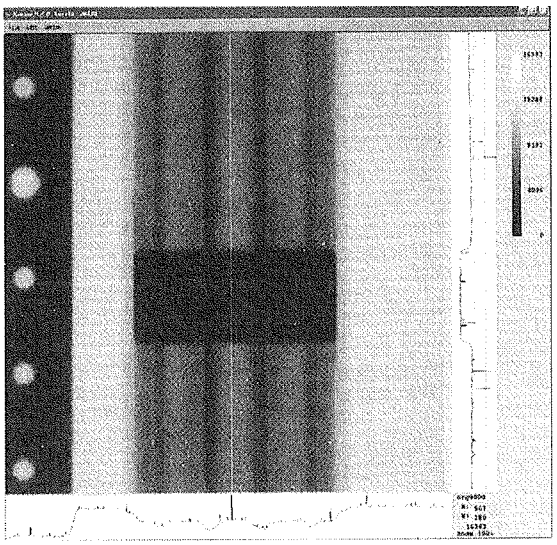

Fig. 4.3.2 Original image taken by the cold-CCD camera

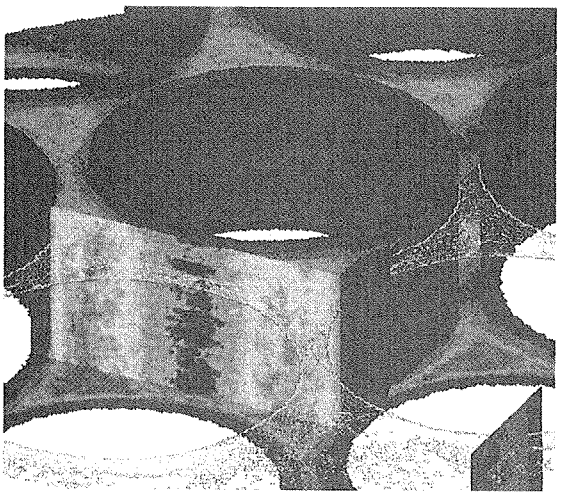

Fig. 4.3.4 Three-dimensional view of the void fraction around the center rod

4.4 Development of Mechanistic Boiling Transition Model - Installation of Boundary Fitting Coordinate Function -

A. Ohnuki, H. Yoshida and H. Akimoto
(*E-mail*: ohnuki@hflwing.tokai.jaeri.go.jp)

Design studies of reduced-moderation water reactors are being carried out at JAERI as one candidate for future reactors.[1] The reactor adopts a tight lattice core with about 1 mm gap between adjacent fuel rods. To optimize the thermal design, boiling transition (BT) in such a tight lattice core is one of most important subjects to be evaluated, but effects of the gap and spacer configuration have not been fully investigated. To evaluate the feasibility and to optimize the thermal design, a full-scale bundle test is required but several systematic full-scale tests are difficult to perform during an initial design phase. Thus, we made a plan to develop a mechanistic BT model to evaluate the geometry effects by a numerical simulation. This section indicates the master plan for the BT model development and describes an outline of improved numerical simulation code.

Figure 4.4.1 shows the master plan. Multi-dimensional thermal-hydraulic model for annular-dispersed flow is constructed and the function to treat a general curvilinear coordinate is installed to simulate the rod bundle including grid spacers. The validity of entrainment and droplet dispersion models is investigated using air-water experimental data in a vertical pipe and the applicability is verified by experimental data in a flow path with obstacles and in a rod bundle. We also have a plan to obtain database for rod bundle with heat transfer by neutron radiography CT and for that under full-pressure condition.

The general curvilinear coordinate system was introduced to the two-fluid model code ACE-3D[2] which was developed at our institute. We changed discrete methods for the basic equations, k-ε turbulent models and boundary conditions. The method by Yang et al.[3] was applied for the discrete of convection terms in order to reduce a numerical error due to a curvature of grid system. We also introduced an up-wind finite difference scheme with 3rd-order interpolation.

The change of discrete methods was assessed against so-called bench-mark problems under single-phase and two-phase flows, and no problems were recognized. Then, we applied the improved ACE-3D for air-water two-phase flow around a circular cylinder. This application was performed in order to evaluate the capability of the boundary fitting coordinate function.

Figure 4.4.2 indicates a snap shot of the calculated results. The geometry and the calculation conditions were derived from experiments by Inoue et al.[4] In the calculation, vortex was generated alternately near two separation points at the cylinder surface. The present method predicts an air concentration to vortex regions behind the cylinder and a temporal fluctuation of vortex intensity; these two phenomena have been observed in experiments. It is clarified that the phenomena depend on a relative relationship between the drag force and the inertia of bubbles due to pressure fields.[5]

The installation of boundary fitting coordinate function was successfully achieved and we made the prediction method to evaluate the geometry effects for the tight lattice core. The verification of the mechanistic BT model will be performed by this method in future.

References

1) Dep. Nuclear Energy System: "Study on Reduced-Moderation Water Reactor (RMWR) Core Design -Joint Research Report (FY1998-1999)-", JAERI-Research 2000-035 (2000) in Japanese.

2) A. Ohnuki, H. Kamo and H. Akimoto: "Development of Multidimensional Two-Fluid Model Code ACE-3D for Evaluation of Constitutive Equations", JAERI-Data/Code 96-033 (1996).

3) H.Q. Yang, S.D. Habchi and A.J. Przekwas, "General Strong Conservation Formulation of Navier-Stokes Equations in Nonorthogonal Curvilinear Coordinates", AIAA J., 32 [5], pp. 936-941 (1994).

4) A. Inoue et al.,: "Studies on Two-Phase Cross Flow. Part I: Flow Characteristics around a Cylinder", Int. J. Multiphase Flow, 12 [2], pp. 149-167 (1986).

5) A. Ohnuki, M. Akamatsu and H. Akimoto: "Numerical Analysis of Air-Water Two-Phase Flow around a Circular Cylinder", Proceedings of the 5th Organized Multiphase Flow Forum, Fukushima, Sep. 13-14 (2001).

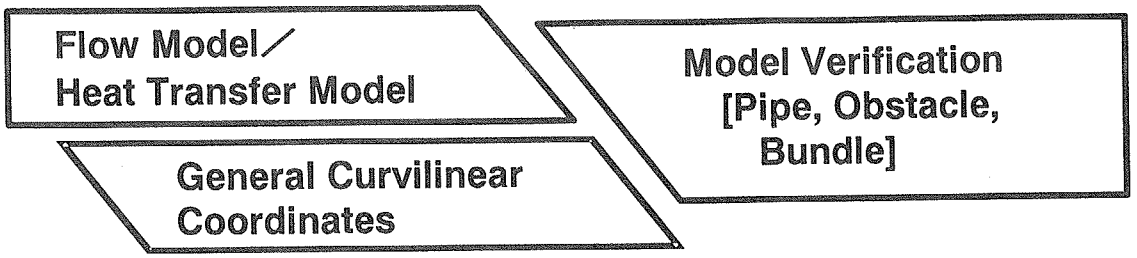

Fig. 4.4.1 Master plan for development of BT model

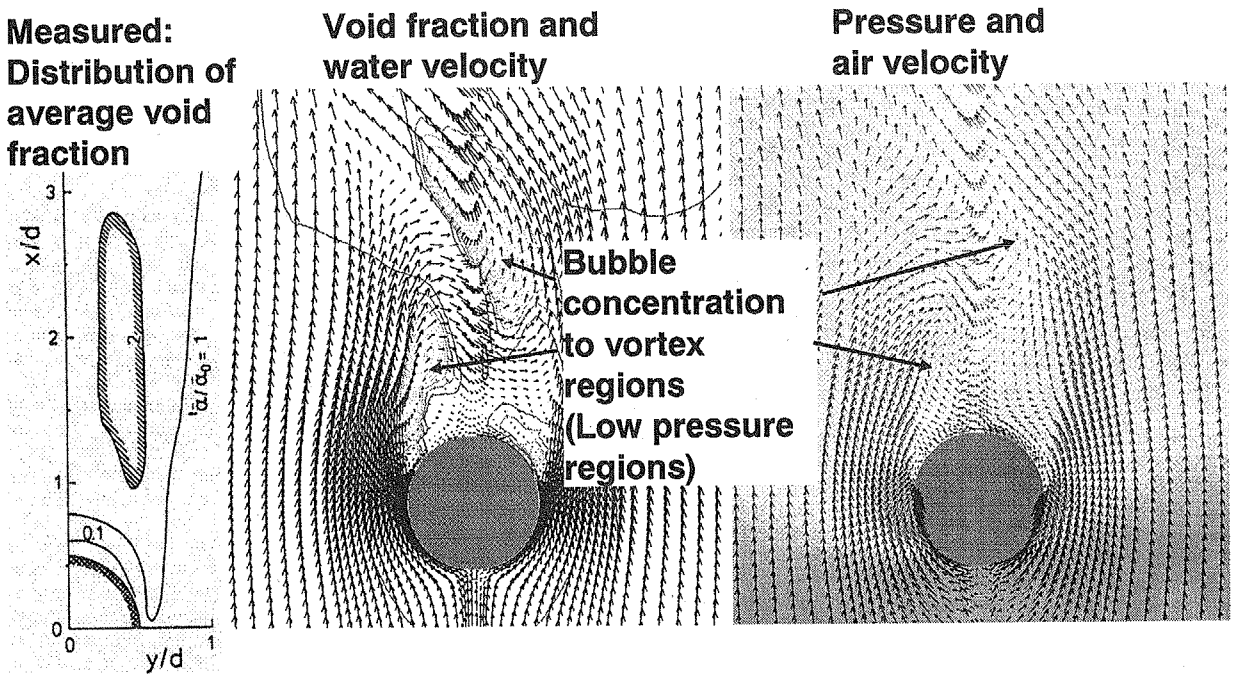

Fig. 4.4.2 Prediction of bubbly flow around a circular cylinder and comparison with experiments

4.5 Development of Algorithm for Reduction of Numerical Diffusion against Interface Tracking Method

H. Yoshida, A. Ohnuki, Y. Ose, K. Takase and H. Akimoto.
(*E-mail: yoshida@hflwing.tokai.jaeri.go.jp*)

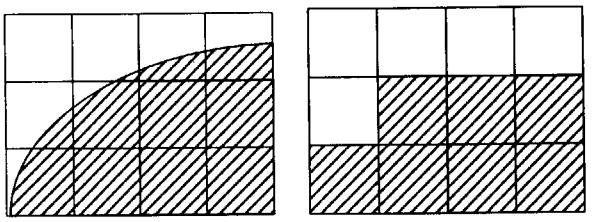

(a) Without digitizer (b) With digitizer

Fig.4.5.1 Effect of digitizer on interface shape

When we use CIP (Cubic Interpolated Pseudo-particle) method[1] to track gas-liquid interface, precise simulation is not obtained because diffusion of the density at the interface is large. To reduce the diffusion at the interface, tangent function (called "digitizer") is used to be applied. However, in the case the digitizer is used, detailed information at the interface is lost (see, Fig. 4.5.1). To track the interface without digitizer, fine computational grid is needed. In that case, huge calculation resources are required. In this study, we developed an interface tracking method which can simulate the interface movement with high accuracy under a coarse grid system.

The diffusion at the interface occurred from errors of evaluating transport between the computational grids, and the following 2 factors are influencing. The first factor is the error of evaluating flux at computational boundaries. Figure.4.5.2 shows a segment of interface moving with velocity V. At initial state, the flux at the cell interface equals to $V\Delta A$ and is fixed to the value during a small time step. However, the flux gradually decreases in the case shown in Fig.4.5.2, and then the hatched area becomes error.

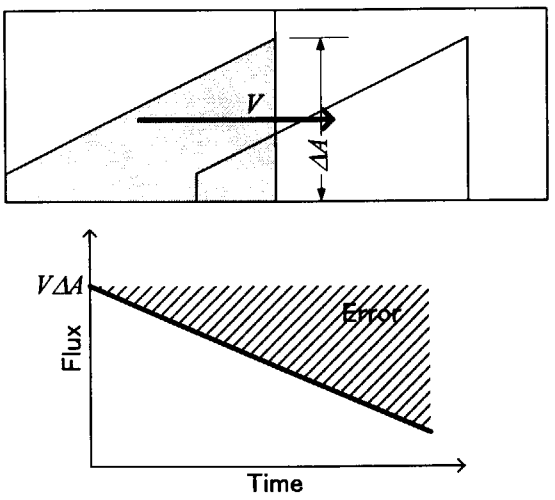

Fig.4.5.2 Flux on computational grids

Another factor occurs from evaluating the transport of mass flux at boundaries of the computational grids. Figure.4.5.3 shows transport volume from computational cell A to cell B, C, and D. The segment of interface is moving with velocity V. True (real) results are

shown in (b), and the volume in the cell A allocates to surrounding cells. In previous methods, it is not possible to transfer the volume to cell D directly from cell A. Two cases can be considered theoretically by previous methods. Those are shown in (c-1) and (c-2). If fluxes at cell boundaries are correctly predicted, (c-1) is obtained. And, if total transport volume from cell A is correctly given, (c-2) is obtained. In both cases, the area painted blackly becomes errors. In the previous methods, these errors can not be prevented.

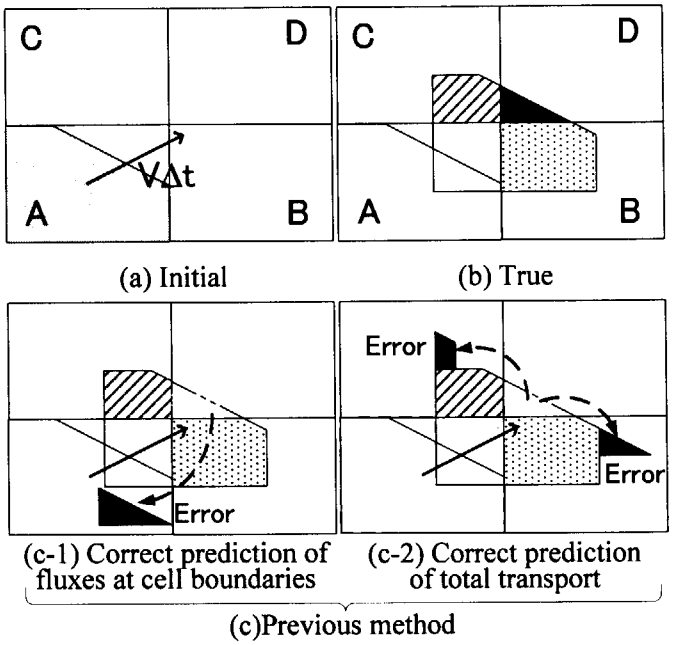

Fig.4.5.3 Transport between computational grids

Then, we decided to develop an advanced method to evaluate the mass transport without the flux at the computational grid boundaries. The advanced interface tracking method approximates the gas-liquid interface with a linear function. A gradient of the interface (*a*, *b* in Fig.4.5.4) is estimated by using least-squares method (choose eight nearest neighbors for 2-dimensional case). In Fig.4.5.4, "A" is the area of the polygon that is made by the linear line and calculation grid boundary. Segment (c) is adjusted as fraction $A/\Delta x\Delta y$ agrees with volume of fluid (see Fig.4.5.4). This polygon is moved in accordance with the flow field, and the polygon area is allocated to each computational grid (see Fig.4.5.5). The volume fraction at new time step is evaluated by the following equation.

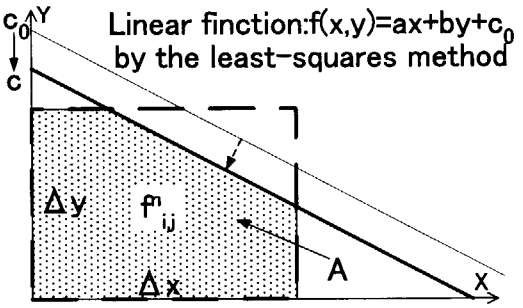

Fig.4.5.4 Estimate linear function *f(x,y)*

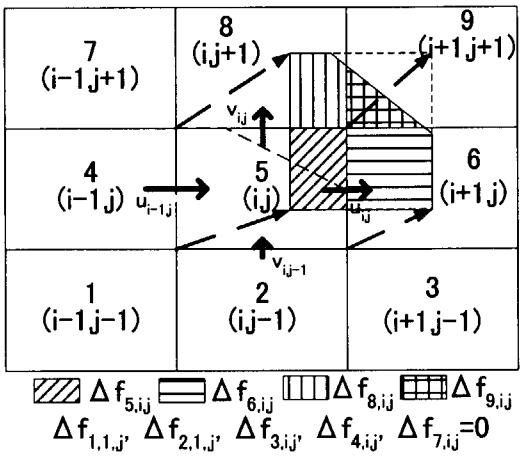

Fig.4.5.5 Transfer rate of volume fraction

$$f_{i,j}^{n+1} = \Delta f_{1,i+1,j+1} + \Delta f_{2,i,j+1} + \Delta f_{3,i-1,j+1} + \Delta f_{4,i+1,j} + \Delta f_{5,i,j} + \Delta f_{6,i-1,j} + \Delta f_{7,i+1,j-1} + \Delta f_{8,i,j-1} + \Delta f_{9,i-1,j-1}$$

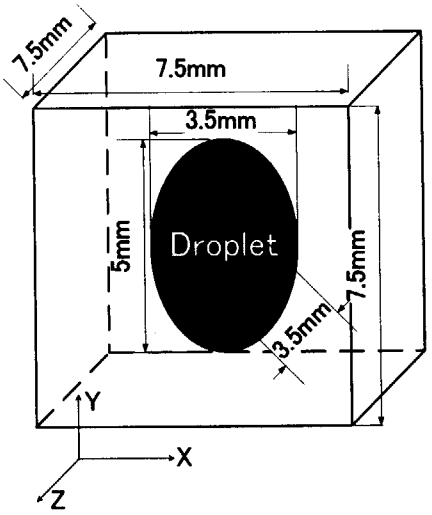

Fig. 4.5.6 Initial arrangement

In order to verify the potential of the advanced interface tracking method, 3-dimensional analyses of the vibration of a liquid drop under zero gravity were carried out. In the simulation, the CSF model[2] is incorporated to estimate surface tension. Initial arrangement of the droplet is shown in Fig. 4.5.6. In the simulations, two computational grids were used, one is a fine grid (41×41×41, case A) and another is a course grid (9×9×9, case B). Diameters of the droplets are shown in Fig.4.5.7. The vibration cycle is about 0.02 seconds and agrees with the theoretical value. The results of the case A and those of the case B are almost the same, and the effect of the different grid number is small. The diffusion at the gas-liquid interface was not observed. We confirmed the effectiveness of the advanced interface tracking method.

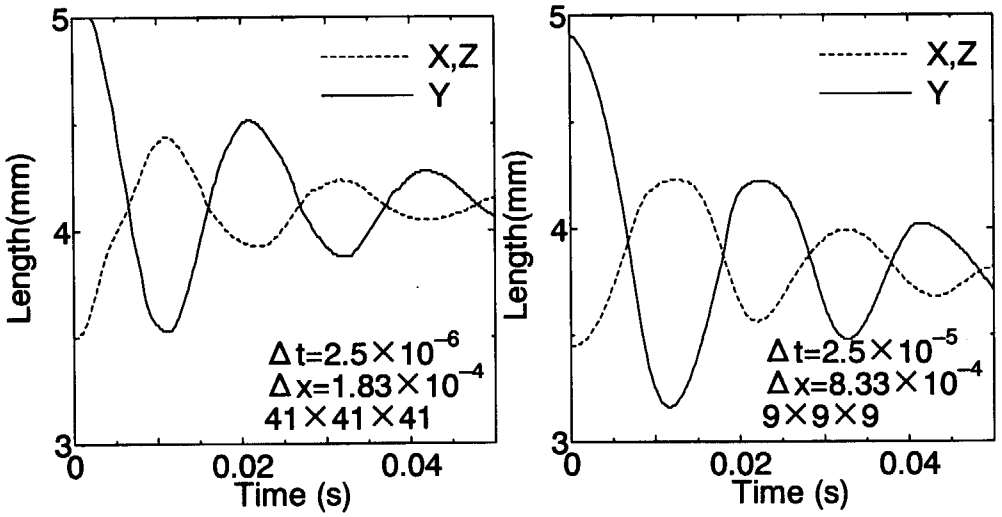

Fig. 4.5.7 Diameters of droplets

References:

1) T. Yabe et al. Computer Physics Communications, 66, pp.233, (1991).

2) J. U. Brackbil et al. J. Computational Physics, 100, pp.335 (1992).

4.6 Numerical Simulation of the Slug Flow using Interface Tracking Method

H. Yoshida, A. Ohnuki, Y. Ose, K. Takase and H. Akimoto.
(*E-mail: yoshida@hflwing.tokai.jaeri.go.jp*)

A design study of a Reduced Moderation light Water Reactor (RMWR) is being carried out at the Japan Atomic Energy Research Institute (JAERI). Figure 4.6.1 shows example of the RMWR fuel assembly. In the RMWR core, remarkably narrow gap spacing between rods (about 1mm) is used to reduce the moderation of the neutron. In such a tight-lattice core, there is not sufficient information about the effects of the gap spacing and grid spacer shapes on the boiling transition (BT). As described in sec. 4.4, JAERI has a plan to evaluate the geometry effects by a mechanistic numerical simulation method. In this study, we made advanced two-phase flow simulation code with interface tracking (named TPFIT) in order to verify the BT model in sec. 4.4. The advanced interface tracking method (see sec.4.5) was adopted in the code. To estimate surface tension, the CSF model[1)] is incorporated. In this section, we will demonstrate the code capability for air-water two-phase flow between flat plates.

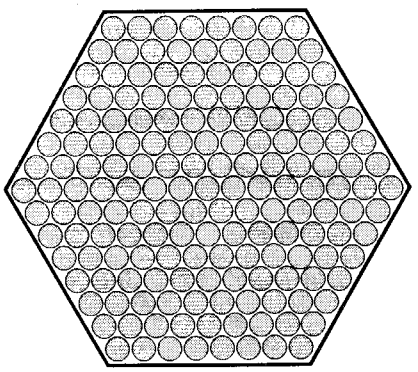

Fig. 4.6.1 Example of RMWR fuel assembly

Flow configuration is shown in Fig.4.6.2. The plates spacing is 25mm, and the length is 1m. Air is injected to the flow region through central nozzle, and the nozzle width is 8.3mm. Inlet air and water velocities (V_G, V_L) are parameters of the simulation. In Case 1, V_G and V_L are set to 1.5 and 1.0m /s, respectively and in Case2, V_G and V_L equal to 0.5 and 1.5m /s. Figure.4.6.3 compares Case 1 and Case 2 flow conditions with Mishima-Ishii flow pattern map[3)]. The conditions in Case 1 and Case 2 correspond to those in the slug and bubbly flow regions,

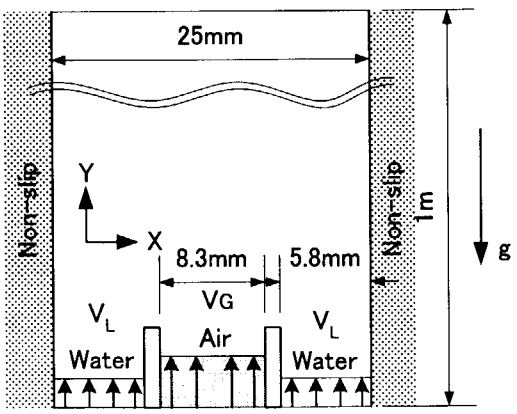

Fig. 4.6.2 Flow configuration

respectively.

Figures 4.6.4 and 4.6.5 indicate an evolution of air-water interface along the calculation domain. In Fig.4.6.4, slug flow is recognized, and many cap bubbles are realized in Fig.4.6.5. The present method can reproduce the two-phase flow pattern.

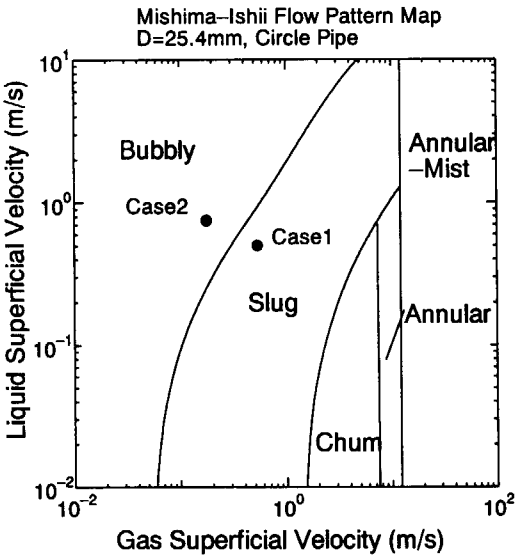

Fig. 4.6.3 Flow pattern map

References:

1) J. U. Brackbill et al.: J. Computational Physics, 100, pp.335 (1992).

2) K. Mishima et al.: Int. J. Heat Mass Transfer, 23, 5,pp. 723 (1984).

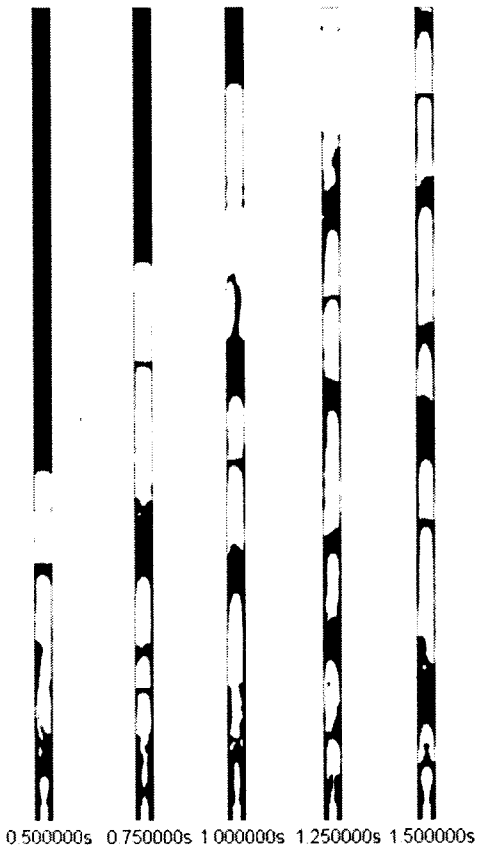

Fig. 4.6.4 Results of Case 1

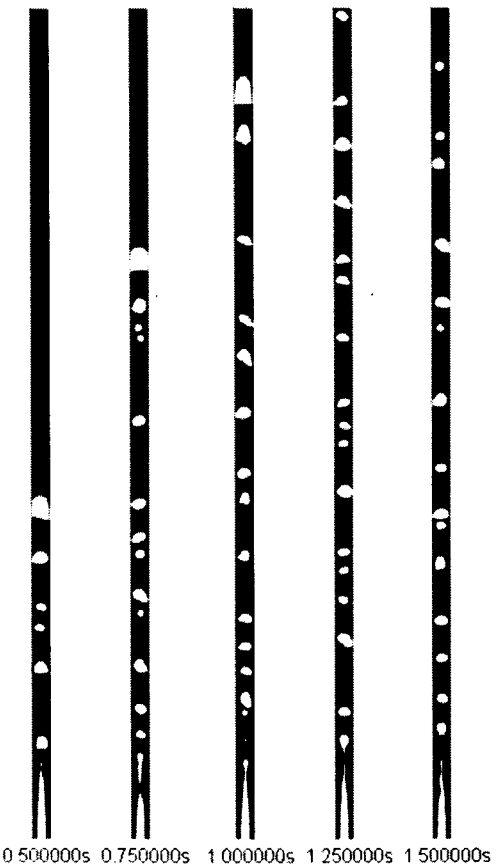

Fig. 4.6.5 Results of Case 2

4.7 Experimental Verification of Effectiveness of a Pressure Suppression System in ITER

K. Takase, M. Shibata, H. Watanabe and H. Akimoto
(*E-mail*: takase@popsvr.tokai.jaeri.go.jp)

If cooling tubes of the plasma-facing components (PFCs) in ITER[1] are broken, water under high temperature and pressure will be discharged into a vacuum vessel (VV). Then, the discharged water will impinge on the hot surface of the PFCs and evaporate. As a result, the VV will be filled with vapor and the pressure in the VV may increase rapidly. This is called an Ingress-of-Coolant Event (ICE). In the present study, effectiveness of the ITER vacuum vessel pressure suppression system (VVPSS) during the ICE was investigated.

Figure 4.7.1 shows a concept of the ITER VVPSS. It mainly consists of a suppression tank, drain tank, relief pipes, drain pipe and rapture disks. The suppression tank initially holds water under low temperature and pressure (25°C and 2.3 kPa) and is connected through three relief pipes with the PFC. The drain tank is connected through a drain pipe with the bottom of the VV. Because of the pressurization during the ICE the rapture disks at the relief and drain piping are broken. Consequently, the generated vapor in the PFC during the ICE flows through the relief pipes into the suppression tank and condenses. On the other hand, the remained water in the PFC goes through the divertor and drain pipe to the drain tank.

Figure 4.7.2 shows an outline of the integrated ICE test facility[2]. It simulates the ITER VVPSS components with a scaling factor of around 1/1600 of the ITER volume. The PFC in Fig.4.7.2 is a cylinder with a diameter of 0.6 m and length of 2.1 m. The VV diameter and length are 0.5 and 1.7 m. The VV volume was calculated based on the difference between the PFC and VV volume in ITER. In the present experiments the magnetic valve was used instead of the rapture disk in ITER. For considering of the scaling factor, the authors took notice of the magnitude of the maximum pressure because the VV is broken if the maximum pressure during the ICE is over the VV design pressure in ITER. The test facility volume and the injected water flow rate were reduced with the same scaling factor, and then, the injected water temperature and pressure were set up similarly to the ITER conditions. Therefore, it is evident numerically that if the VV wall temperature in the test facility can be controlled as be equal to that in ITER, the maximum pressure in the test facility during the ICE is almost equivalent to that in ITER.

Figure 4.7.3 shows an effect of the number of relief piping on the pressure rise in the PFC during the ICE. The solid, dashed and dotted lines represent the experimental results when the number of relief piping is 1, 2 and 3, respectively. Experimental conditions satisfy the ITER conditions mostly as: water temperature 125°C; water pressure 2 MPa; PFC wall temperature 230°C; and VV wall temperature 100°C. Moreover, the injected water flow rate and the water leakage area simulate the ITER multiple-pipe break condition. The pressure decreases with increasing the number of relief piping. This reason is that a lot of vapor flows into the suppression tank and condenses with the increase in a cross-sectional area of the relief piping. By adjusting a cross-section area of the relief piping it is possible to reduce the maximum pressure in the PFC during the ICE. It was found from a series of the experimental results that the ITER VVPSS was very effective to reduce the pressure rise during the ICE.

References

1) Aymer, R.:"ITER R&D: Executive Summary: Design Overview", Fusion Engineering and Design, 55, pp.107-118(2001) .

2) Takase, K., Akimoto, H. and Topilski, L.:"Results of Two-Phase Flow Experiments with an Integrated Ingress-of-Coolant Event (ICE) Test Facility for ITER Safety", Fusion Engineering and Design, 54, pp.593-603(2001).

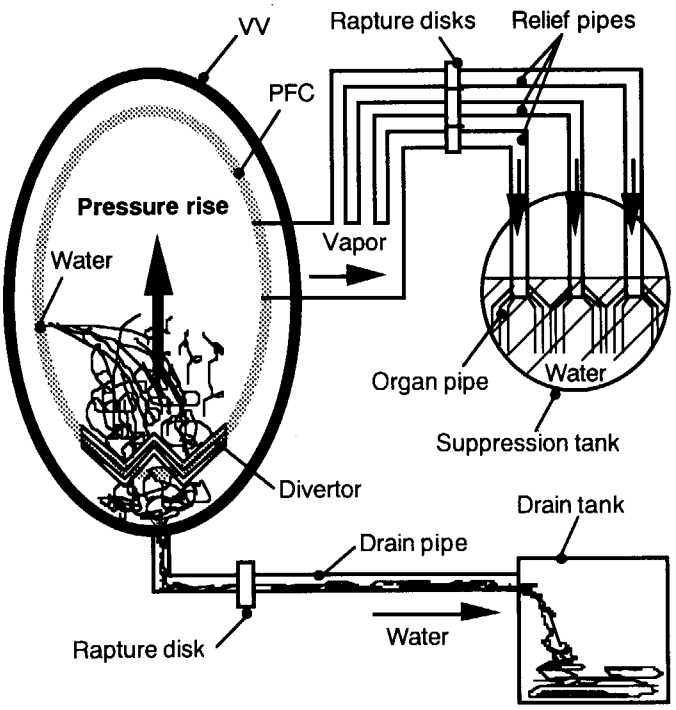

Fig. 4.7.1 A concept of a vacuum vessel pressure suppression system in ITER

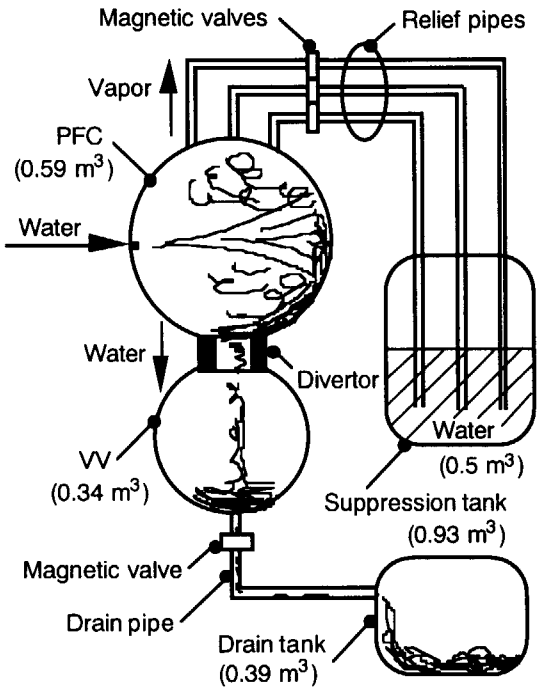

Fig. 4.7.2 Outline of an integrated ICE test facility, which simulates the ITER VVPSS components with a small scale

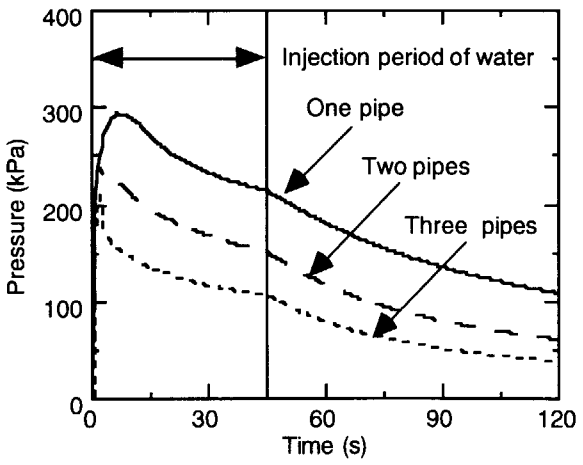

Fig. 4.7.3 Effect of the number of relief piping on the pressure rise in the PFC during the ICE

4.8 Analysis of Thermal-Hydraulic Characteristics in a Fusion Experimental Reactor during In-Vessel LOCA by a Modified TRAC-PF1 Code

K. Takase, Y. Ose and H. Akimoto
(*E-mail*: takase@popsvr.tokai.jaeri.go.jp)

The water-vapor two-phase flow characteristics inside the test facility during an ingress-of-coolant event (ICE) were predicted using the Transient Reactor Analysis Code (TRAC)[1]. The original TRAC was developed for the accident analysis in light water reactors and it was modified by authors[2] to obtain superior predictions under the fusion reactor conditions. In order to predict the thermal-hydraulic characteristics during the ICE with high accuracy, it is required to grasp the water and vapor distributions precisely. Then, the authors carried out three-dimensional computations using the modified TRAC.

Figure 4.8.1 shows a three-dimensional nodalization diagram. The plasma chamber (PC) is a cylinder with a diameter of 600 mm and length of 2100 mm and is modeled using the VESSEL component. The water injection nozzle and boiler are modeled by the VALVE and VESSEL components. The N_2 gas piping and N_2 gas supplier are modeled by the VALVE and BREAK components. The simulated divertor has four slits. This slit simulates an evacuation slit area at the ITER divertor section with a scaling factor of 1/1600 and is modeled by the PIPE component. The VV is modeled using the VESSEL component and its diameter and length are 500 and 1720 mm. Three relief pipes are modeled by the VALVE component. The suppression tank (ST) is modeled by the VESSEL component and is connected through the relief pipe to the top of the PC by opening the magnetic valve. The ST includes low temperature water so as to condense the vapor during the ICE. The drain tank is modeled by the VESSEL component and is connected through the drain pipe to the bottom of the VV by opening the magnetic valve.

Figure 4.8.2 shows the predicted void fraction distribution in the integrated ICE test facility just after the water injection is completed. In a map of the void fraction, it is 0 when water is 100% and 1 when vapor is 100%. Calculated conditions are as follows: water temperature 125°C; water pressure 2 MPa; PC wall temperature 230°C; VV wall temperature 100°C; water injection time 45 s; water injection nozzle diameter 7.3 mm; and, three water injection nozzles were used. The two-phase flow behavior during the ICE in the ICE test facility was visualized numerically by the present numerical procedure. The water in PC

flows through the simulated divertor to the VV and to the drain tank, and then, the vapor in the PC goes through the relief pipe to the ST and is condensed there.

Figure 4.8.3 shows a comparison of the experimental and analytical pressure transients in the PC. The predicted maximum pressure (211 kPa) agreed well with an error less than 1 % with the measured maximum pressure (210 kPa). From the present study it was verified that the modified TRAC code can predict the thermal-hydraulic characteristics in the ITER VVPSS with sufficiently accuracy.

References

1) Liles, D. R.:"TRAC-PF1/MOD1: An Advanced Best-Estimate Computer Program for Pressurized Water reactor Thermal-Hydraulic Analysis", NUREG/CR-3858 (LA-10157-MS), (1986).

2) Takase, K., Ose, Y. and Akimoto, H.:"Analysis of Pressure Rise in an ITER-Like Fusion Reactor during In-Vessel LOCA by a Modified TRAC-PF1 Code", Fusion Technology, 39, pp.1050-1055(2001).

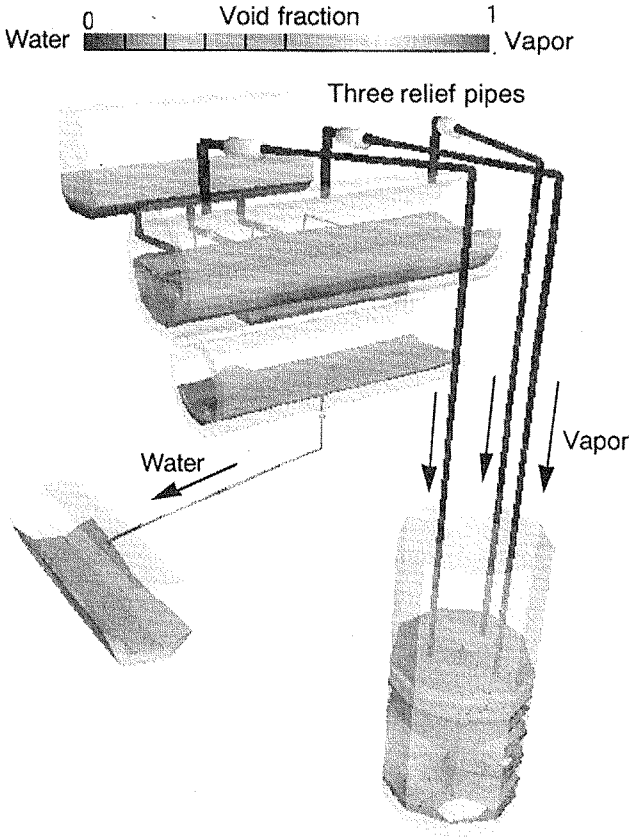

Fig.4.8.2 Predicted void fraction in the integrated ICE test facility at three relief piping case

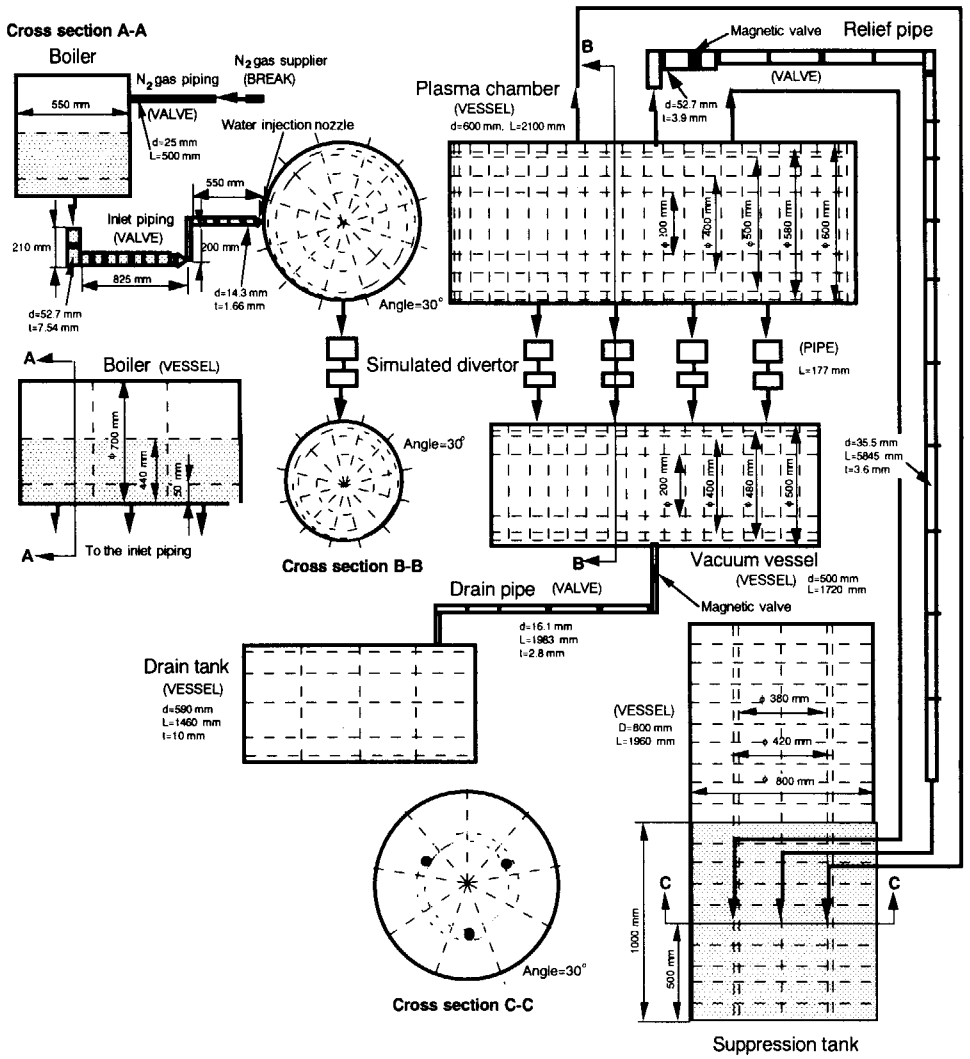

Fig. 4.8.1 Three-dimensional nodalization diagram

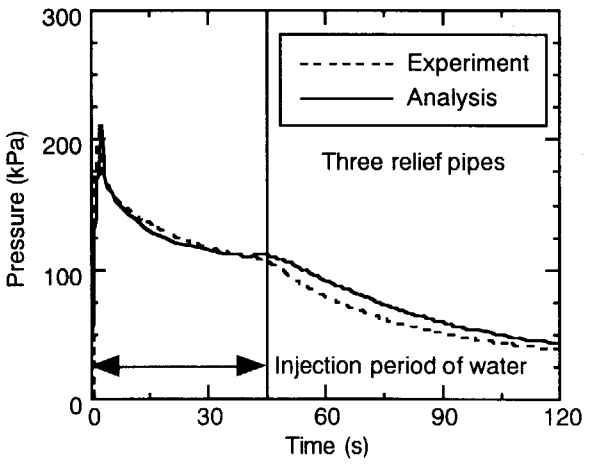

Fig. 4.8.3 Experimental and analytical results on the pressure rise the PC

4.9 Numerical Analysis on Direct-Contact Condensation of Vapor Injected into Low-Temperature Water

K. Takase, Y. Ose and H. Akimoto
(*E-mail*: takase@popsvr.tokai.jaeri.go.jp)

A pressure suppression system is considered in order to protect facility components in a vacuum vessel (VV) of a fusion reactor from the rapid pressurization during an ingress of coolant event (ICE). The pressure suppression system mainly consists of a suppression tank and relief piping. The suppression tank initially holds water under low temperature and pressure (about 3.2 kPa in saturation pressure), and therefore, the vapor generated by the ICE is sent from the VV through relief piping into the suppression tank and condenses. As a result of this, the pressure in the VV is decreased. Therefore, it is very important to clarify quantitatively the performance of the condensation of vapor in the suppression tank during the ICE from the viewpoint of the fusion reactor safety. The pressure suppression system has been made use of in boiling light-water reactors (BWRs) and its performance has already investigated under the condition of more than atmospheric pressure, however, the suppression tank of the fusion reactor is operated under vacuum. Then, numerical analyses were carried out to clarify the condensation characteristics of the water and vapor inside the suppression tank.

In the present study the MARS (Multi-interfaces Advection and Reconstruction Solver) method was applied. It can analyze directly the water-vapor two-phase flow without any assumptions and empirical equations in comparison with typical conventional analytical models such as two-fluid model and drift flux model. The MARS method was developed by Kunugi[1] and is based on the PLIC (Piece-wise Linear Calculation)[2] as a volume tracking procedure and the continuum surface force model (CSF)[3] for surface tension.

Figure 4.9.1 shows a three-dimensional analytical model and consists of a simulated organ pipe and water tank. They simulates the structural components in the fusion reactor suppression tank system. The water tank is filled with cold water and the simulated organ pipe is installed into the water tank. The vapor is injected into the cold water from the outlet of the simulated organ pipe. Dimensions of the water tank are 870 mm in height, 560 mm in width and depth. An inner diameter of the simulated organ pipe is 16 mm and its length is 510 mm. The number of calculation mesh is 140, 140 and 174 in the x, y and z direction and

the uniform mesh division was chosen. The time step is 0.00001 s and the FACOM VPP5000 is used. The equivalent heat flow method[4] is chosen as a phase change model. Initial conditions are as follows: water temperature and pressure in the tank are 20°C and 2.3 kPa; vapor temperature and velocity at the inlet section are 111°C and 25 m/s; and initially the inside of the simulated organ pipe is filled with vapor. Here, the vapor temperature 111°C means the saturation temperature at 150 kPa in vapor pressure. Boundary conditions are as follows: every wall is adiabatic; velocity is zero on the wall; and the vapor changes water under 110.5°C.

Figure 4.9.2 shows the predicted void fraction distributions and velocity vectors at the center plane of the analytical region. Figs. 4.9.2(a), (b), (c) and (d) represent 0.005, 0.1, 1 and 5 s later from the calculation, respectively. The void fraction is 0 when water is 100%, on the other hand, it is 1 when vapor is 100%. The vapor is injected like a jet from the simulated organ pipe and hits the bottom of the water tank and then a circulating flow takes place along every corner in the water tank. The predicted flow configurations with the condensation of vapor agreed well with the results of the flow visualization experiment. From the results of the present study it was concluded that the present numerical approach is very effective to estimate the phase change behavior between water and vapor under low pressure.

References

1) Kunugi, T.:"Direct Numerical Algorithm for Multiphase Flow with Free Surfaces and Interfaces",ISAC'97 High Performance Computing on Multiphase Flows",pp. 25-30(1997).
2) Youngs, D. L.,Morton, K. W. and Baine, M. J.:"Numerical Methods for Fluid Dynamics", Academic Press, pp. 273-468 (1982).
3) Brackbill, J. U.,Kothe, D. B. and Zemach, C.:"A Continuum Method for Modeling Surface Tension", J. of Computational Physics, 100, pp. 335-354 (1992).
4) Ohnaka, I.:"Introduction of Computational Heat Transfer and Solidification Analysis", Maruzen, pp. 202-208(1984). [in Japanese]

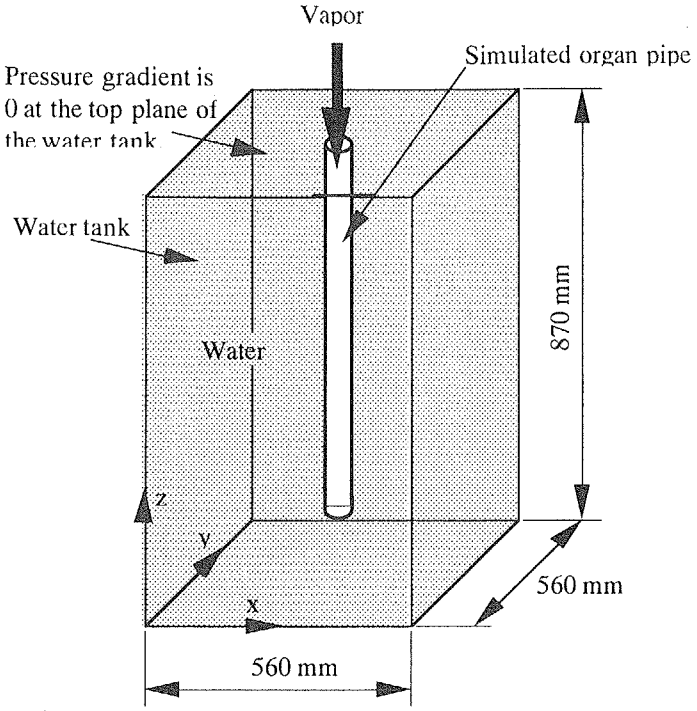

Fig. 4.9.1 A three-dimensional analytical model and boundary conditions

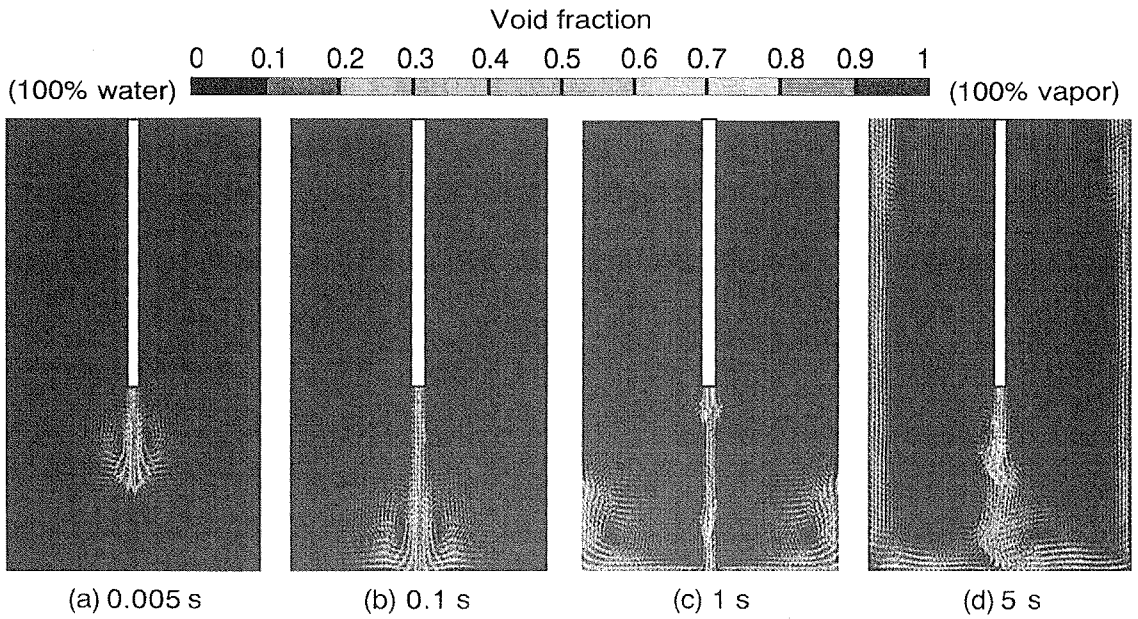

Fig. 4.9.2 Predicted void fraction distributions and velocity vectors

4.10 Numerical Simulations of Air Ingress and Dust Mobilization Behavior in a Fusion Reactor during a Loss-of-Vacuum Event

K. Takase and H. Akimoto
(*E-mail*: takase@popsvr.tokai.jaeri.go.jp)

If a loss-of-vacuum-accident event (LOVA) occurs in the International Thermonuclear Experimental Reactor (ITER), air may flow into the inside of a vacuum vessel (VV) through breaches. After the inside pressure of the VV equalizes with the outside pressure, the buoyancy-driven exchange flows will take place through the breaches due to the temperature difference between the inside and outside of the VV. At the same time, the activated dust accumulated inside the VV may be entrained with the exchange flows from the inside of the VV through the breaches to the outside.

Although the exchange flow characteristics were investigated quantitatively using a preliminary LOVA apparatus by Takase et al.[1], and after that, some information on the dust mobilization during the LOVA were requested from the viewpoint of the thermofluid safety of ITER. However, since the estimated mean size of dust is small (less than 0.1 mm), the quantitative measurement on the microscopic dust moving with the fluid is also not easy. Therefore, a newly thermofluid analysis code[2] was developed to characterize the dust mobilization behavior during the LOVA, and then, effects of the breach size and the dust density on the activated dust mobilization were analyzed numerically.

The analytical model simulates the dimensions and configurations of the actual ITER design. The no-slip and adiabatic boundary conditions were adopted to the walls in the analytical region. Here, the VV of ITER was simulated as a simple double cylinder. Namely, the internal components of the VV, such as a divertor, were not simulated. The authors thought that this analytical model can eliminate the effect of the internal components on the dust mobilization and then it is more conservative to the analytical results. The dust particle conditions were as follows: diameter 10-100 μm; initial velocity 0 m/s; total particle number 10^4; and the initial position of the dust is on the floor of the VV. Five kinds of dust with different densities were chosen: Beryllium with a density of 1840 kgm^{-3}; Carbon 2220 kgm^{-3}; Stainless steel 7900 kgm^{-3}; Copper 8900 kgm^{-3}; and Tungsten 19220 kgm^{-3}. In the current ITER design those materials are used as component materials inside the VV. The input conditions were set up based on an assumption that the fluid is in the continuum region (i.e.,

Knudsen number<0.01).

A visualized example of the three-dimensional numerical simulation on the dust mobilization behavior is shown in Fig. 4.10.1. The breach size is 0.02 m^2. Here, the VV is cut into a half and is indicating by 3-dimensional visualization so that it may be legible. Fig. 4.10.1(a) is the initial condition. Five kinds of dust with different densities are installed on the floor of the VV radially. The number of each dust particles is 2000. Fig. 4.10.1(b) shows the visualized dust mobilization just before the inside pressure of the VV equalizes with the outside pressure. A circulation flow is formed in the VV by air flowing out of the outside of the VV through the breach, and the dust spreads throughout the inside of the VV.

The effect of the dust density on the dust mobilization is shown in Fig. 4.10.2. Here, the one-pointed, broken, dashed, solid and dotted lines indicate the predicted results of beryllium, carbon, stainless steel, copper and tungsten, respectively. The VV becomes an equal pressure at about 340 s after the LOVA, and then, the dust mobilization to the outside starts, and after around 500 s the mobilized dust fraction shows the fixed value mostly. Predicted results showed that the mobilized dust fraction of beryllium, carbon, stainless steel, copper, and tungsten were 1.7%, 0.7%, 0.5%, 0.4%, and 0.1%, respectively. These results suggest that the dust with small density can be mobilized easier than that with heavy density. However, the mobilized dust fraction of each dust is less than 2% and it can be thought that the effect of the dust density on the dust mobilization is small under the LOVA conditions in ITER.

References

1) Takase, K., Kunugi, T., Ogawa, M. and Seki, Y.,:"Experimental Study on Buoyancy-Driven Exchange Flow Though Breaches of a Tokamak Vacuum Vessel in a Fusion Reactor under the LOVA Condition", Nuclear Science and Engineering, Vol. 125, No.3, pp.223-231(1996).

2) Takase, K.,:"Three-Dimensional Numerical Simulations of Dust Mobilization and Air Ingress Characteristics in a Fusion Reactor during a LOVA Event", Fusion Engineering and Design, Vol.54, pp.605-615(2001).

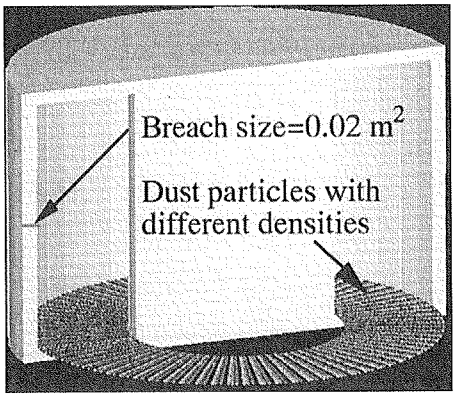

(a) Initial condition

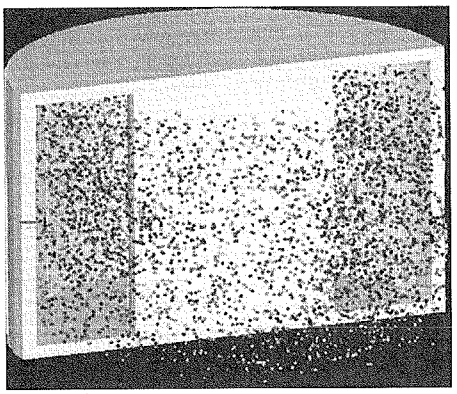

(b) Mobilized dust inside the VV

Fig. 4.10.1 Visualized example of the three-dimensional numerical simulation on the dust mobilization behavior inside the VV during the LOVA

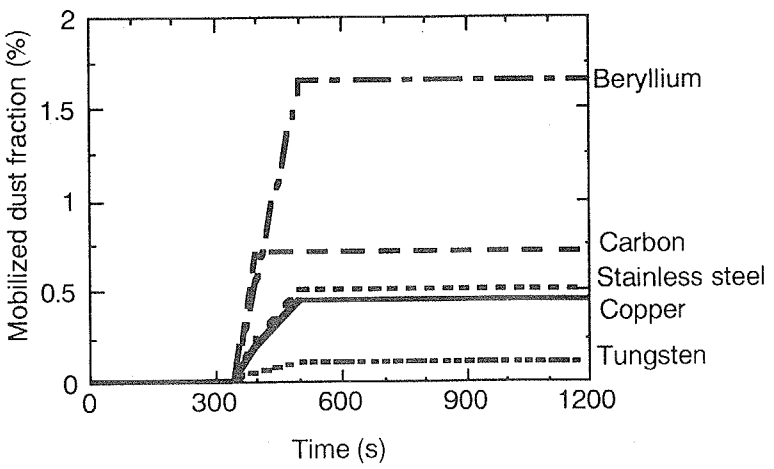

Fig. 4.10.2 Effect of the dust density on the mobilized dust fraction to the outside of the VV

5. Energy System Analysis and Assessment

Considering the future expansion of nuclear power generation in Japan, natural uranium consumption, amounts of spent fuel stock, and appropriate schedule of spent fuel reprocessing were analyzed with different scenarios on the use of future reactor types. Although the ultimate consumption is different because of differences in breeding ratios of RMWR and FBR, it was confirmed that the consumption of the natural uranium can be controlled at a certain finite level even if RMWR has such a low breeding ratios as 1.06.

Recycling characteristics of RMWRs were analyzed from the viewpoints of changes in conversion ratios and plutonium enrichment of fresh fuel to be loaded to RMWRs when they use various types of plutonium recovered from reprocessing. Five types of plutonium that are thought to be typical in future nuclear fuel cycle systems in Japan were defined for this purpose. There was no experience of fabricating and reprocessing MOX fuel with a plutonium enrichment higher than 30% in the history of FBR fuel development, therefore it is necessary to demonstrate its feasibility.

A preliminary study was made on possible economic impacts of nuclear phase-out in Japan. In the integrated model future demands for energy services are endogenous variables that are directly linked with either GDP or sectorial economic outputs. While, the data on future energy service demand in the MARKAL model are based on certain assumed economic growths. The substantial impact to GDP might largely be alleviated by expanding the capacity of renewable power generation technologies. In the current integrated model, changes in energy production costs are not reflected in economic activities determined by the macroeconomic model.

A literature survey was made on risk and externality studies on electric power generation in developed countries. There are much less reports about risk and/or externality estimate written by the Japan's experts than other countries. It would be obvious that Japan needs the information and database more specific to Japan's electrical power generation circumstances.

5.1 Nuclear Power and Its Fuel Cycle Scenario in Japan - Roles of Reduced-Moderation Water Reactors -

K. Tatematsu, O. Sato
(*E-mail* : ktate@ruby.tokai.jaeri.go.jp)

Considering the future expansion of nuclear power generation in Japan, natural uranium consumption, amounts of spent fuel stock, and appropriate schedule of spent fuel reprocessing were analyzed with different scenarios on the use of future reactor types. The analysis, aiming at clarifying the role of Reduced Moderation Water Reactors (RMWRs) in future nuclear power systems in Japan was carried out by using the improved nuclear fuel cycle simulation model that can consider loss of plutonium during storage due to the decay of Pu-241.

Major assumptions of the analysis are as follows. Reactor types considered are LWR, Partially MOX fueled LWR (P-MOX), Fully MOX Fueled LWR (F-MOX), RMWR, and FBR. Cooling time of spent fuel was assumed to be 4 years for LWR, P-MOX and F-MOX, and 2 years for RMWR and FBR. Loss of fuel material was assumed as 0.5% for both fuel fabrication and reprocessing process. It was also assumed that the Rokkasho Reprocessing Plant operates until 2045, and the second reprocessing plant becomes available after 2046 with a scale of 1,600 ton/year.

The analystical cases are, as listed in Table 5.1.1, case A with only plutonium utilization by LWRs, case B with RMWR and case C with FBR of the sodium-cooled type. In addition, the case in which plutonium was not recycled at all was calculated in order compare natural uranium consumption.

The comparison of natural uranium cumulative consumption is shown in Fig. 5.1.1. In the case where plutonium is not utilized at all, and also in the case A with only plutonium utilization by LWRs, the consumption continues to increase with time. On the other hand, the cumulative consumption of natural uranium can be reduced by 349,000 tons with the plutonium utilization by LWRs at the year 2200. The ultimate consumption of natural uranium in case B and C is the 1,778,000 and 1,188,000 ton, respectively. Although the ultimate consumption is different because of differences in breeding ratios of RMWR and FBR, it was confirmed that the consumption of the natural uranium can be controlled at a certain finite level even if RMWR has such a low breeding ratios as 1.06.

The comparison of main results of the analysis is shown in Fig. 5.1.2. They are installed capacity, reprocessing scale, stock of spent fuel from the top in the order. A share of installed capacity by plutonium utilization reactors is about 12.5%, when plutonium

utilization is made only in LWRs. In the case C, the utilization of enriched uranium fueled LWRs ends in a comparatively short time period, because of a high breeding ratio of FBR. While, In the case B using RMWRs, enriched uranium fueled LWRs are utilized over very long time period. The scales of long-term reprocessing in case A, B and C are about 1200 ton and 2800 ton and 1600, respectively. Larger reprocessing plant is necessary in case B because of the large plutonium requirement of RMWRs. Finally, the stock of spent MOX fuel keeps increasing, when plutonium utilization is made only in LWRs. On the other hand, control of the stock of spent MOX fuel becomes possible by using the breeder reactors.

Table 5.1.1 Analytical Cases

Case	LWR	P-MOX	F-MOX	RMWR	FBR	NOTE
A	X	X	X			
B	X	X	X	X		RMWRs is available after 2020.
C	X	X	X		X	FBRs is available after 2050.

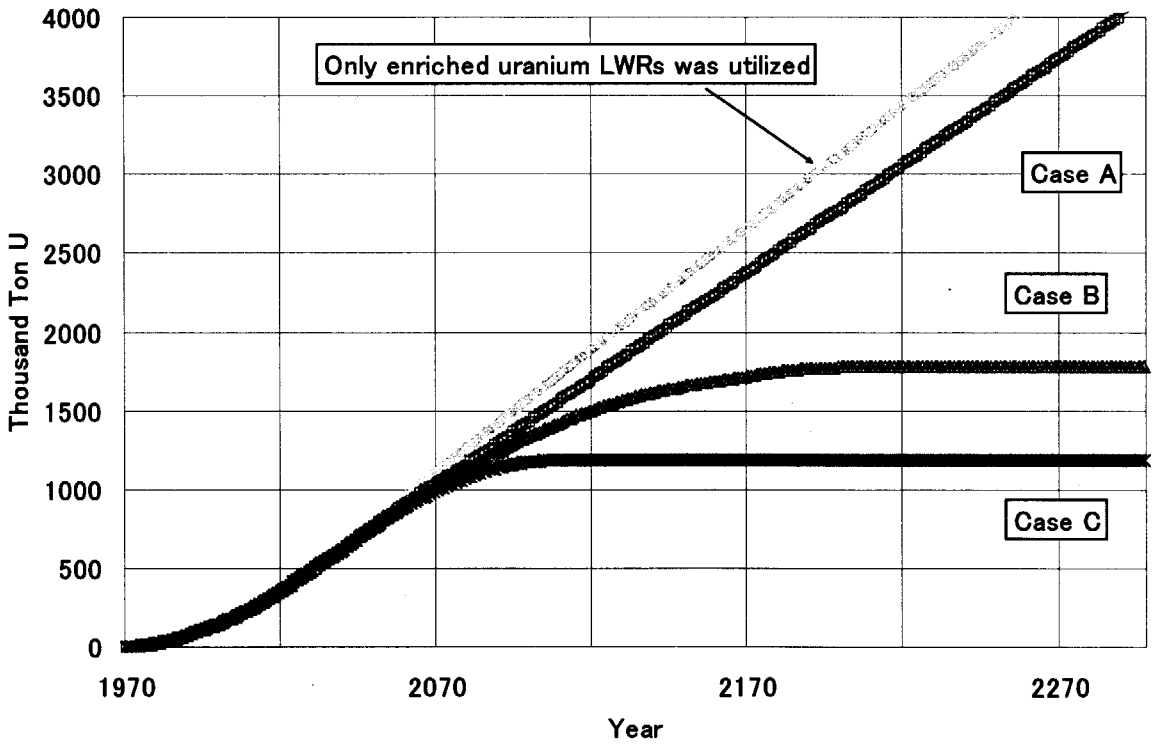

Fig. 5.1.1 Consumption of Natural Uranium

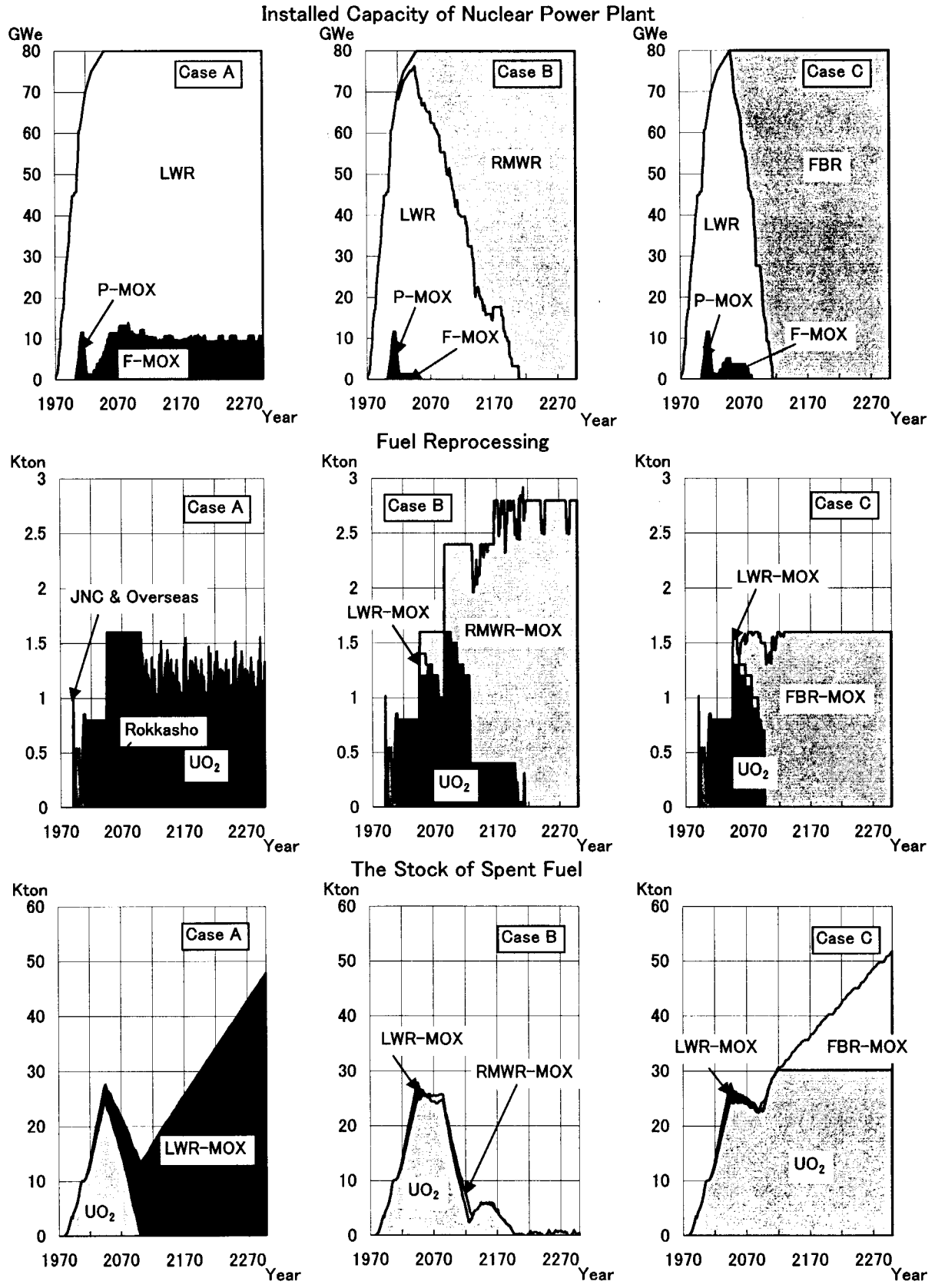

Fig. 5.1.2 Comparison of major result

5.2 A Study on the Plutonium Recycling Characteristics of Reduced Moderation Water Reactors

O. Sato and Y. Tanaka
(*E-mail*: sato@ruby.tokai.jaeri.go.jp)

Reduced Moderation Water Reactors (RMWRs) are expected to realize plutonium breeding cycle by achieving conversion ratios higher than 1.0, and thereby to contribute to controlling ultimate consumption of natural uranium at certain finite levels. However, in order to build the breeding cycle RMWRs must be enough flexible in using various types of plutonium recovered after reprocessing. It is known that plutonium recovered by reprocessing spent MOX fuel from conventional LWRs includes larger amount of higher isotopes, and this is preventing multi-recycling of plutonium in LWRs.

In this study recycling characteristics of RMWRs were analyzed from the viewpoints of changes in conversion ratios and plutonium enrichment of fresh fuel to be loaded to RMWRs when they use various types of plutonium recovered from reprocessing. Five types of plutonium that are thought to be typical in future nuclear fuel cycle systems in Japan were defined for this purpose as shown in Table 5.2.1. As a reference RMWR core, the one designed under the cooperative study between JAERI and Japan Atomic Power Company was selected. It is of a BWR type with rated capacity 1100MWe and a design conversion ratio about 1.06.

At the initial stage of commercialization RMWRs are expected to use plutonium provided only from LWRs. However, spent fuel of RMWRs will be reprocessed sooner or later, and recovered plutonium will be also recycled to RMWRs. Therefore, two recycle modes were considered in the study; an external supply mode where all plutonium loaded to RMWRs is fed by LWRs (one of the types A - E) and a self-recycling mode where plutonium type A or D is fed by LWRs for the initial core of RMWRs but replacement loading is made by using plutonium discharged from RMWRs. In the self recycling mode it was assumed that at each refueling time isotopic composition of plutonium to be loaded is same with that of plutonium discharged then.

After a set of burn-up calculation by using the Monte-Carlo burn-up code MVP-BURN, fuel input and output characteristics were determined for RMWRs that meet design fuel burn-up. Table 5.2.2 gives the results on fuel characteristics of RMWRs with the external supply mode. It is evident from this table that conversion ratios are kept well over 1.0 even when degraded plutonium from spent MOX fuel is used. It is also indicated that the amount of fissile plutonium (Puf) to be loaded will be less, but the amount of total plutonium (Put) will be larger when plutonium from spent MOX fuel is used.

In the case of self-recycling, the initial composition of plutonium changes gradually with recycling toward the one determined by neutron spectrum specific to nuclear reactors. In this study calculation was terminated at 5 times recycling where plutonium composition is thought to reach almost at an equilibrium state. Fuel characteristics of RMWRs in this case are summarized in Table 5.2.3. As

shown in this table conversion ratios of RMWRs are also kept over 1.0. Although additional cases were analyzed where an advanced reprocessing method with lower decontamination factors was used for reprocessing of RMWR fuel, differences are not significant as compared with the case using a Purex method with high decontamination factors.

It should be noted that Table 5.2.2 and Table 5.2.3 give 'average' plutonium enrichment of MOX fuel to be loaded to RMWRs. Since percentages of plutonium in highest enrichment fuel are higher than average by 7%, maximum plutonium enrichment will exceed 30% in all cases of this study. There was no experience of fabricating and reprocessing MOX fuel with a plutonium enrichment higher than 30% in the history of FBR fuel development, therefore it is necessary to demonstrate its feasibility.

In addition, void reactivity coefficients of reactor core could have positive values when degraded plutonium is loaded at a high enrichment. The analysis was not made in this regard. It is necessary to confirm that the coefficients are negative values by making feedback reactivity analysis. If the safety margins are judged not enough, reactor configuration must be readjusted for this purpose.

Table 5.2.1 Types of plutonium to be recycled to RMWRs

Types of Plutonium	A	B	C	D	E
Source	LWR-UO_2	LWR-UO_2	LWR-UO_2 (High Burn-up)	LWR-MOX	LWR-MOX
Discharge Burn-up (GWd/t)	45	45	60	45	45
Cooling Time before Reprocessing (Years)	5	30	5	5	30
Reprocessed by	Purex	Purex	Purex	Purex	Purex
Time after Reprocessing (Yeas)	2	2	2	2	2
Ratio of Fissile Isotopes (%)	63.6	61.3	60.6	52.2	47.8
Pu-238	2.6	2.3	3.9	2.8	2.6
Pu-239	53.1	57.9	49.9	39.2	43.5
Pu-240	25.1	27.7	25.0	32.7	37.7
Pu-241	10.5	3.4	10.7	13.0	4.3
Pu-242	7.7	8.4	9.4	11.0	12.1
Am-241	1.1	0.4	1.1	1.3	0.4

Table 5.2.2 Fuel characteristics of RMWRs in external supply mode

Types of Plutonium		A	B	C	D	E
Percent Put	%	29.2	30.5	30.1	33.1	35.9
Percent Puf	%	18.5	18.7	18.2	17.3	17.2
Conversion Ratio		1.037	1.059	1.044	1.053	1.100
Initial Inventory						
Total Heavy Metal	t/GWe	188.93	188.96	188.96	189.06	189.14
Put	t/GWe	17.50	18.46	18.05	19.87	21.75
Puf	t/GWe	11.24	11.35	11.05	10.52	10.44
Equilibrium Loading						
Total Heavy Metal	t/GWe/y	32.09	32.09	32.09	32.11	32.12
Put	t/GWe/y	2.97	3.21	3.07	3.38	3.69
Puf	t/GWe/y	1.91	1.93	1.88	1.79	1.77
Equilibrium discharge						
Total Heavy Metal	t/GWe/y	31.11	31.12	31.12	31.13	31.15
Put	t/GWe/y	3.09	3.27	3.17	3.43	3.77
Puf	t/GWe/y	1.98	2.04	1.96	1.88	1.95

Note : 1. Common parameters.
Plant Capacity Factor = 90%, Number of Batches in Equilibrium Cycyle = 4.53,
Fuel Discharge Burnup = 45 GWd/t

2. Initial inventory is estimated assuming the same percentage ratio of plutonium as in equilibrium loading.

Table 5.2.3 Fuel characteristics of RMWRs in self-recycling mode

Reprocessing		Purex		Advanced	
Types of Plutonium		A	D	A	D
Percent Put	%	29.7	31.4	31.7	33.8
Percent Puf	%	18.9	18.5	18.8	18.2
Conversion Ratio		1.051	1.060	1.057	1.070
Initial Inventory					
Total Heavy Metal	t/GWe	188.93	188.99	189.00	189.07
Put	t/GWe	18.13	19.00	18.13	19.10
Puf	t/GWe	11.42	11.23	11.42	11.07
Equilibrium Loading					
Total Heavy Metal	t/GWe/y	32.08	32.09	32.09	32.11
Put	t/GWe/y	3.05	3.23	3.79	3.24
Puf	t/GWe/y	1.95	1.91	1.93	1.88
Equilibrium discharge					
Total Heavy Metal	t/GWe/y	31.11	31.12	31.12	31.14
Put	t/GWe/y	3.19	3.35	3.25	3.40
Puf	t/GWe/y	2.05	2.02	2.05	2.01

Note : 1. Common parameters.
Plant Capacity Factor = 90%, Number of Batches in Equilibrium Cycyle = 4.53,
Fuel Discharge Burnup = 45 GWd/t

2. Initial inventory is estimated assuming the same percentage ratio of plutonium as in equilibrium loading.

5.3 Possible Impacts of Nuclear Phase-out in Japan – Preliminary Study by the Integrated Energy and Macroeconomic Model

O. Sato
(*E-mail*: sato@ruby.tokai.jaeri.go.jp)

By using the integrated MARKAL and macroeconomic model developed in JAERI with cooperation of the Mitsubishi Research Institute, a preliminary study was made on possible economic impacts of nuclear phase-out in Japan. Main assumptions for the analysis are summarized in Table 5.3.1 together with the analytical cases.

In the integrated model future demands for energy services are endogenous variables that are directly linked with either GDP or sectorial economic outputs. While, the data on future energy service demand in the MARKAL model are based on certain assumed economic growths, therefore we need to make calibration runs in order to ensure that the integrated model gives these assumed economic growths. All economic parameters in the macroeconomic model are determined in this process. This calibration was made for the reference case N1 where nuclear power is expanded in the future and cumulative emissions of carbon dioxide over the time period 2002.5 - 2052.5 are limited to 54.5 billion ton.

First, the case N1 was compared with the case N2 where limits to cumulative CO2 emissions are 52.5 billion ton, lower than N1 by 2 billion ton. In the case N2 the energy mix changed from N1 in favor of natural gas than coal as shown in Fig. 5.3.1 and Fig. 5.3.2. But almost no impacts were found in GDP as indicated in Fig. 5.3.3.

Then, the phase-out cases R1 and R2 were analyzed. In the cases R1 and R2 no nuclear investment was allowed after the year 2000 under the same conditions with the cases N1 and N2, respectively. In both these cases consumption of natural gas increased substantially, although renewable energy also increased much in response to the nuclear phase-out. Since almost all amount of natural gas is imported, a large amount of national income is used for the import of natural gas in the case R1 and R2. Reflecting this, GDP reduced in these cases as shown in Fig. 5.3.3. The reduction is particularly large in the case R2 where emissions are more strictly controlled; more than 2 trillion yen in each year after 2020.

Since there is large uncertainty in the future prices of natural gas, a sensitivity analysis was made for the case with higher prices than assumed above. In the above cases, two sources of natural gas were assumed, one with normal imported prices and the other with the 1.2 times higher prices than normal. In the case R2a, the prices of this high-price natural gas was assumed 1.5 times higher than normal. Other conditions were unchanged from the case R2.

In this case energy mix changed a little from R2 with a small part of natural gas replaced by coal. Economic impacts are much more remarkable than the change in energy mix. Fig. 5.3.3 shows

that annually more than 10 trillion yen of GDP will be lost with nuclear phase-out when future natural gas prices are high as assumed above. The rate of reduction is in the range 1.3 - 1.5% during the time period from 2010 to 2050.

This substantial impact to GDP might largely be alleviated by expanding the capacity of renewable power generation technologies. In the case R2b, upper limits to the installed capacity of solar PV are increased, i.e. by 40GWe in 2050. This additional capacity provides only 5% of total electricity demand in 2050. However the decrease of natural gas imports is very effective in alleviating the impact to GDP. As indicated in Fig. 5.3.3 the amounts of GDP lost by the nuclear phase-out are less than 4 trillion yen over the entire time period.

In the current integrated model, changes in energy production costs are not reflected in economic activities determined by the macroeconomic model. Therefore, the economic impact of installing additional capacity of solar PV is not considered at all. If this requires much higher costs than using nuclear option, the economic impact might not be neglected. The model must be improved further in this regard.

Table 5.3.1 Assumptions and cases for the analysis

-Time period : 1995–2050
-GDP growth rates : 2000–2010 1.5%
2010–2030 1.0%
2030–2050 0.5%
- Discount rate : 3%
- Analytical cases : As below

Cases	Nuclear power *1	CO_2 Emissions [50 years during 2002.5–2052.5]		Note
		Cumulative (Bton CO2)	Annual average (Bton/year)	
N1	Yes	54.5	1.09	Reference
N2		52.5	1.05	
R1	No	54.5	1.09	
R2		52.5	1.05	
R2a		52.5	1.05	*2
R2b		52.5	1.05	*3

*1 Yes : Installed capacity is 80GWe in 2030, 100GWe in 2050
No : No nuclear investment after 2000
*2 Higher prices (up 25%) for additional imports of natural gas
*3 R2a＋Expansion of solar PV capacity (100GWe ➔ 140GWe in 2050)

Fig. 5.3.1 Primary energy supply

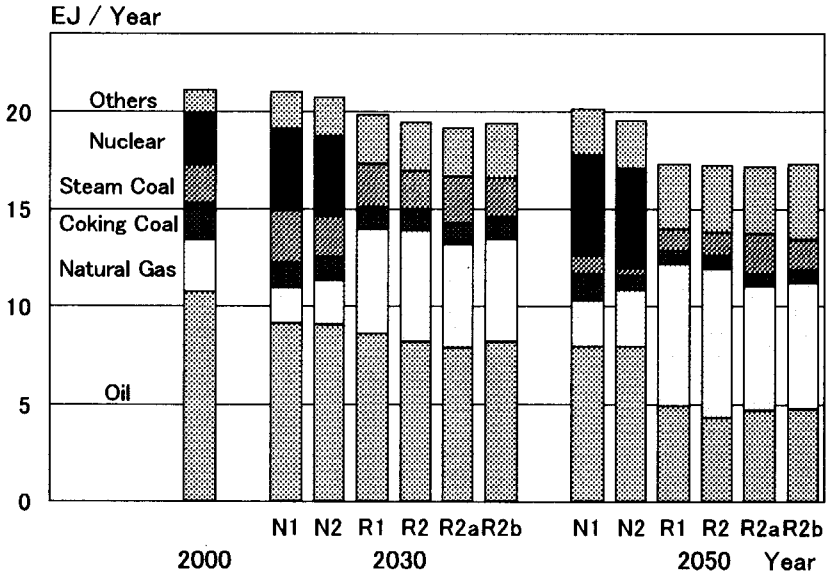

Fig. 5.3.2 Electric power generation

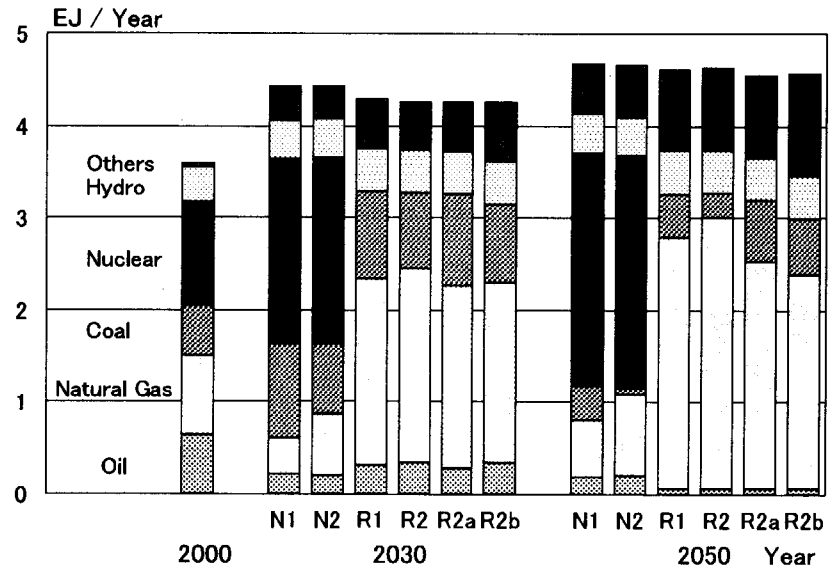

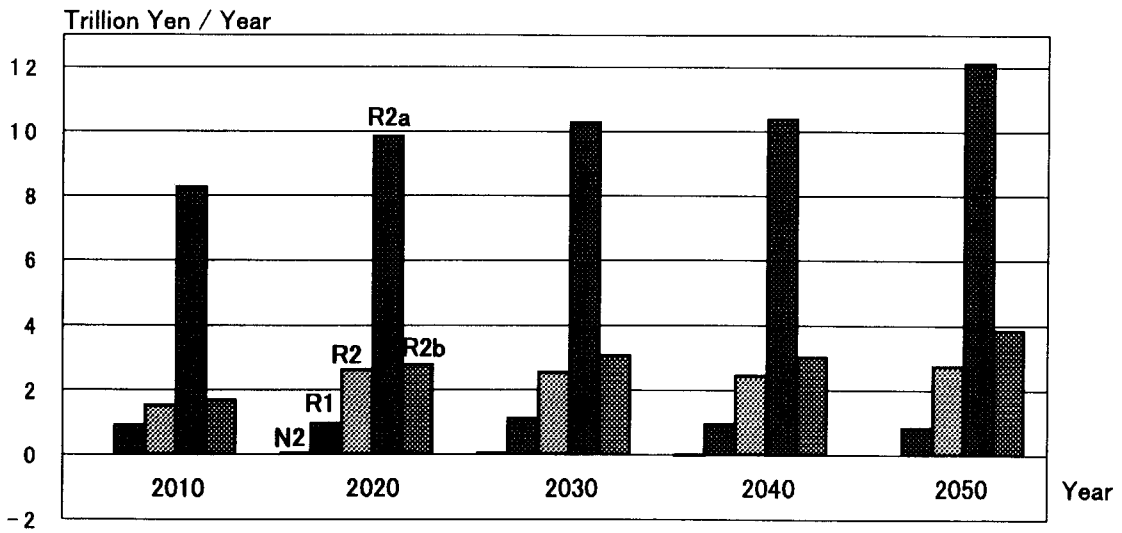

Fig. 5.3.3 Reduction of GDP from Case N1

5.4 A Review of Risk and Externality Studies on Electric Power Generation

K. Kunii and T. Sato
(*E-mail*: kunii@popsvr.tokai.jaeri.go.jp)

A literature survey was made on risk and externality studies on electric power generation in developed countries. The progress of the studies on external costs is reviewed as well as the remarks.

Progress of Estimation of Risk and Externality[i.e. 1)] Most estimation on power generation has been made for risk and/or externality of damages to the worth of human health and environment, and not for energy security or financial management, estimates of which would be said difficult in general. Important features of the estimates for human health and environment are described as follows:

(i) For external costs

- Increase of estimation on damages to human health by air pollution caused by fossil fuel power generation, sometimes including impacts of secondary air pollutants.
- Estimated results dependent largely on countries or areas even for the same type of power generation.
- Lower external cost of nuclear power generation in comparison with fossil fuel power generation, as shown in Fig.5.4.1.

(ii) For risk of radioactivity by nuclear power generation

- Lower risk at severe accident estimated by the PSA(Probabilistic Safety Assessment) approach than at normal operation.
- Highest risk at mining and milling of nuclear material than at power generation and other fuel cycle processes.
- Difficulty in estimating risk of human's fear for possibility of nuclear accident, classified as risk perception.

Remarks on Risk and Externality Studies[i.e. 2)] Estimates of risk and externality have progressed so much that the worth of human health and environment can be expressed in terms of indicators, such as the Value of a Statistical Life, Value of Life Years Lost, Willingness To Pay, Willingness To Accept, etc. Difficulties for the estimates, however, have remained. Some remarks about those are described as follows:

(i) Application of the estimated results - for assurance and transferability -

- Important to know the practical information behind the estimation, such as lack of data, quoted data-source, because of large differences between estimated values as shown in Fig. 5.4.2, as well as large dependency of the estimates on countries or areas.
- Necessary to make estimation specific to countries or areas.

(ii) Some insights in order to make more efficient application taking into account of social and technological constraints

- Estimating the values in each area or country by using original database.
- Applying positively estimated results in making policies to secure resources and environment.
- Considering the inadequacy of estimation, such as lack of sufficient analysis, measures of damages to the worth of human activities and assurance and transferability for estimated results, new or unknown risk or externality arising, attempt to deal with risk aversion or perception.
- Analyzing both positive and negative economical implications in the society where any application taking risk or externality into account would be put into practice. For reference, some reports are based on aiming at economical advantage, such as written by the United States' experts.

There are much less reports about risk and/or externality estimate written by the Japan's experts than other countries. It would be obvious that Japan needs the information and database more specific to Japan's electrical power generation circumstances.

References

1) European Commission: ExternE (Externalities of Energy) Project, http://externe.jrc.es/.
2) OECD/NEA: "Methodologies for Assessing the Economic Consequences of Nuclear Reactor Accidents" , OECD (2000).

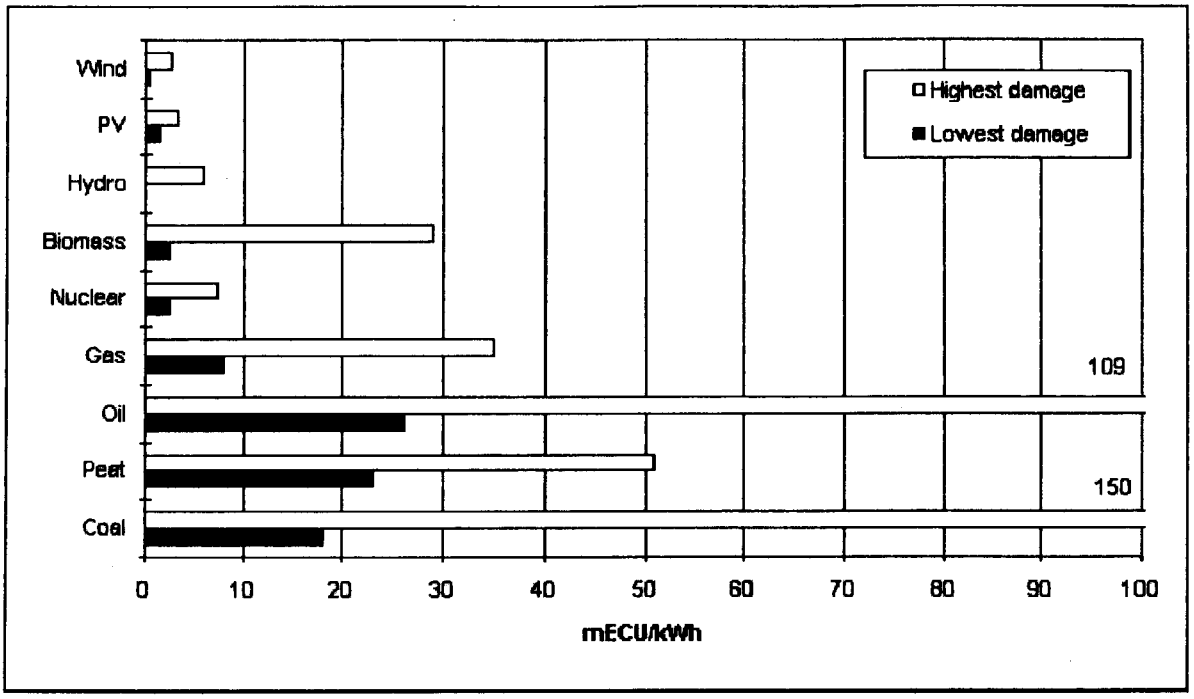

Fig. 5.4.1 Estimated external costs of electrical power generations (fuel cycles) in EU countries[1)]

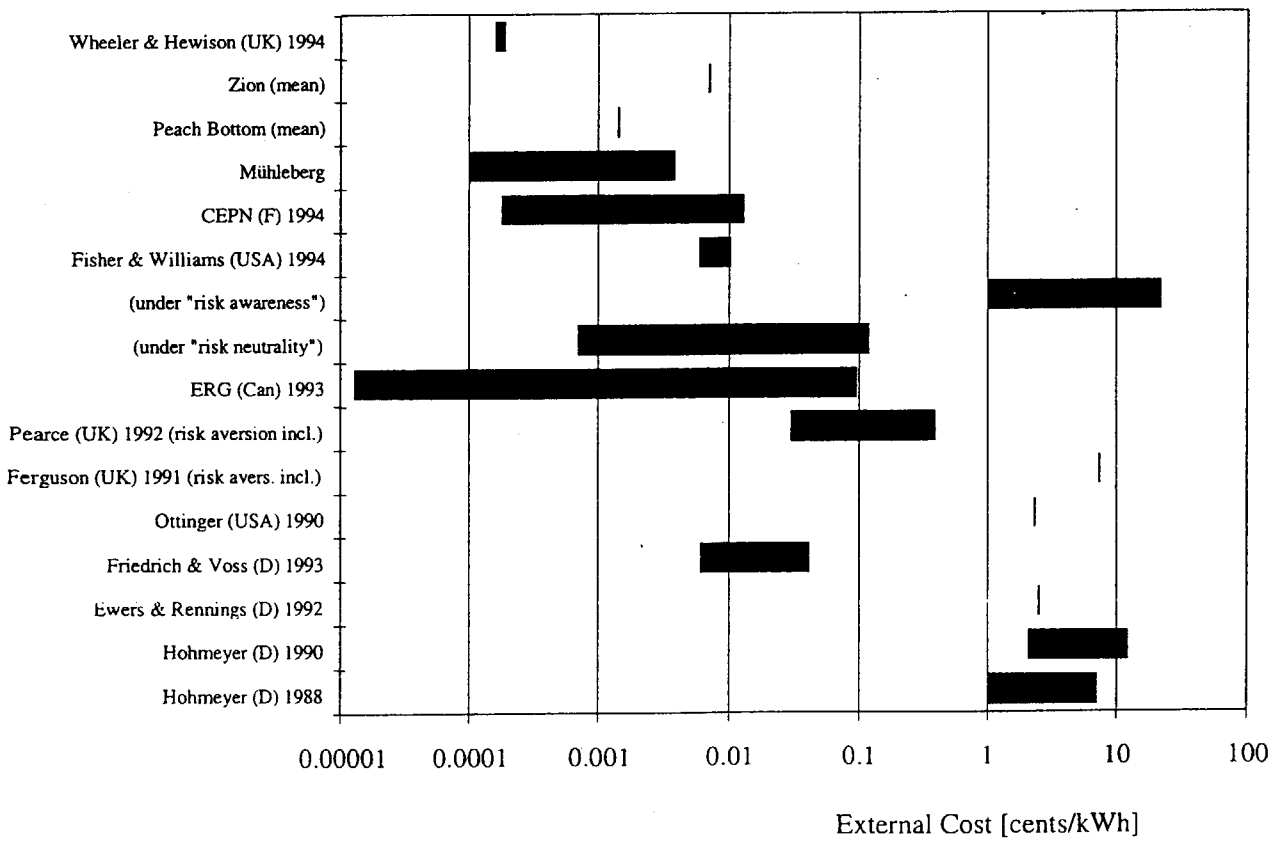

Fig. 5.4.2 Range of estimated external costs of severe reactor accidents[2)]

6. Reactor Structural Materials

In-core structural materials used in the light water reactors (LWR) are exposed to the high flux radiation in high temperature water. Irradiation assisted stress corrosion cracking (IASCC) is known as a degradation phenomenon that is caused by synergistic effects of neutron irradiation, stress/strain and high temperature water on the structural materials. From the view point of the life management of the core components of the aged LWR, IASCC is concerned to be one of the key issues.

Water temperature dependence of susceptibility to IASCC of type 316LN-IG was studied on specimens irradiated up to about 1 dpa at the High Flux Isotope Reactor of the Oak Ridge National Laboratory. The estimated irradiation temperature is about 473K. After the irradiation, Slow Strain Rate Testing (SSRT) in oxygenated water was performed at 423, 513, 573 and 603K. Although susceptibility to IASCC increased with increasing water temperature, specimen irradiated to about 7 dpa did not show IASCC at 473K.

It is essential to evaluate corrosion behavior of irradiated materials for mechanistic understanding of IASCC. Corrosion behavior of ion irradiated materials and the influence of radiation damage, and irradiation temperature and H and/or He implantation were evaluated using the atomic force microscope (AFM). For this study, high purity Fe-18Cr-12Ni specimens were irradiated by Ni ion using the tandem accelerator at Takasaki ion accelerators for advanced radiation application (TIARA).

The phenomenon during SSRT includes both the crack initiation and the crack growth stages. A separation of crack initiation stage from crack growth stage will be very useful for understanding IASCC phenomenon. Therefore we designed and developed a SSRT facility with an capability of the in-situ observation of irradiated specimen surface during SSRT.

It is essential to perform in-pile SCC tests, which are material tests under the conditions simulating those of actual LWR operation, to clarify the precise mechanism of the phenomenon. Therefore, we are developing the test technique for uniaxial constant loading test with small tensile specimens in irradiation capsule which will be loaded into the core of JMTR. Although it is difficult to detect the crack initiation in in-pile SCC tests, the crack initiation can be evaluated by the detection of specimen rupture if the cross section area of the specimen is small enough.

The distributed material database system named "Data-Free-Way" which can be shared from the Internet has been developed. In order to create additional values of the system, knowledge base system, in which knowledge extracted from the material database is expressed, is planned to be developed for more effective utilization of Data-Free-Way.

6.1 Water Temperature Dependence of IASCC Susceptibility of 316LN-IG

Y. Miwa, S. Jitsukawa, T. Tsukada and H. Tsuji
(*miway@popsvr.tokai.jaeri.go.jp*)

Water temperature dependence of susceptibility for the irradiation assisted stress corrosion cracking (IASCC) of type 316LN-IG was studied using a slow strain rate testing (SSRT) after neutron irradiation. Sheet type specimens, 7.86 mm long x 1.52 mm wide x 0.76 mm thick in gage section, were prepared from solution annealed (SA) 316LN-IG plates. Some specimens were prepared from a plate jointed by the hot-isostatic-pressing (HIPing) procedure. Detail of HIPing process and specimens was presented elsewhere[1]. The specimens were irradiated at the High Flux Isotope Reactor of the Oak Ridge National Laboratory. The estimated irradiation temperature is about 473K. Calculated fast and thermal neutron fluence were 1.6×10^{25} n/m^2 (E>0.1MeV) and 2.4×10^{25} n/m^2 (E<0.5eV), respectively. Corresponding dose is about 1 dpa. After the irradiation, SSRT in oxygenated (dissolved oxygen, DO=10 wt.ppm) water was performed at 423, 513, 573 and 603K with strain rates of 2×10^{-7} s^{-1}. Tensile test was also carried out at same temperature range with a strain rate of 1×10^{-4} s^{-1}. Fracture surfaces were observed using scanning electron microscopy (SEM).

Results of tensile tests and SSRT at both 423K and 513K were reported in reference[2]. Stress-strain curves after SSRT were similar to those after tensile tests. SEM observation exhibited that specimen failed in fully ductile mode. Below 513K, therefore, brittle fracture by IASCC is difficult even in oxidizing environment.

Fig. 6.1.1(a) shows engineering stress-strain curves at 573K. Stress-strain behavior of SSRT is different from that of tensile test. Total strain in SSRT was shorter than that in tensile test. In specimens of both SA and HIPed plate, the total strain in SSRT was almost same. As seen in Figs. 6.1.2(a) and (b), these specimens failed by fully ductile mode after tensile test, but they failed by intergranular (IG) and transgranular (TG) stress corrosion cracking (SCC) after SSRT.

Fig. 6.1.1(b) shows engineering stress-strain curves at 603K. Specimen tested by SSRT failed earlier than that by tensile test. Total strain by SSRT at 603K was equivalent to that at 573K. On fracture surface of tensile-tested specimen, only dimple pattern was observed. After SSRT, specimen failed by IG and TG SCC (Fig. 6.1.2(d)).

Fluctuation of stress during tensile tests was observed only above 573K, as seen in Fig. 6.1.3. IASCC occurred at same temperature range. Fig. 6.1.4 shows initiation and propagation of small crack after SSRT at 573K. The crack propagated along slip lines. It is speculated from these results that local deformation is necessary for IASCC initiation in SSRT.

Jitsukawa reported that local deformation mode such as channel deformation became more active at higher temperature in irradiated and hardened stainless steel[3]. Simonen reported channel deformation occurred easier in a slower strain rate testing like SSRT[4].

Water temperature dependence of fraction of IG and TG SCC area is shown in Fig. 6.1.5. Fraction of IGSCC area (%IGSCC) increased with increasing water temperature. It is well known that unirradiated, thermally sensitized stainless steels also show similar water temperature dependence on IGSCC behavior. However, the sensitized stainless steels have IGSCC susceptibility even in 423K water[5]. Fig. 6.1.6 shows water temperature dependence of IASCC susceptibility on type 316L stainless steels irradiated at temperature range from 473 to 513K. All data[6-8] was obtained by SSRT in oxygenated water. In specimen irradiated to about 7 dpa, IASCC did not occur at 473K. It is speculated from these figures that irradiation damage of 1 dpa at 473K is not enough for 316LN-IG to occur IASCC or occurrence of IASCC is difficult below 473K.

References

1) J. Nakano et al., J. Nucl. Mater., in press.
2) Y. Miwa et al., JAERI-Review 2002-005, p.134.
3) S. Jitsukawa, Doctoral theses, (1994)
4) E. P. Simonen et al., Proceedings of 7th Int. Symp. on Environmental Degradation of Materials in Nuclear Power Systems – Water Reactors, NACE, (1995) p.1081.
5) F. P. Ford et al., Corrosion Vol.35, (1979) p.569.
6) T. Tsukada et al., Proceedings of 8th int. Symp. on Environmental Degradation of Materials in Nuclear Power Systems – Water Reactors, ANS, (1997) p.795.
7) T. Tsukada et al., Corrosion 92, (1992) paper No.104.
8) P. Lorenzotto et al., J. Nucl. Mater. 233-237 (1996) p.1387.

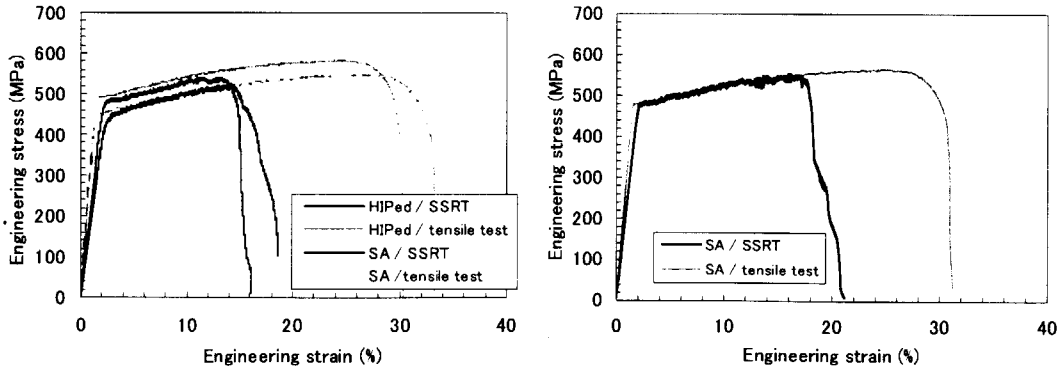

(a) Stress-strain curves at 573K (b) Stress strain curves at 603K

Figure 6.1.1 Engineering stress-strain curves of type 316LN-IG irradiated at 473K to 1 dpa.

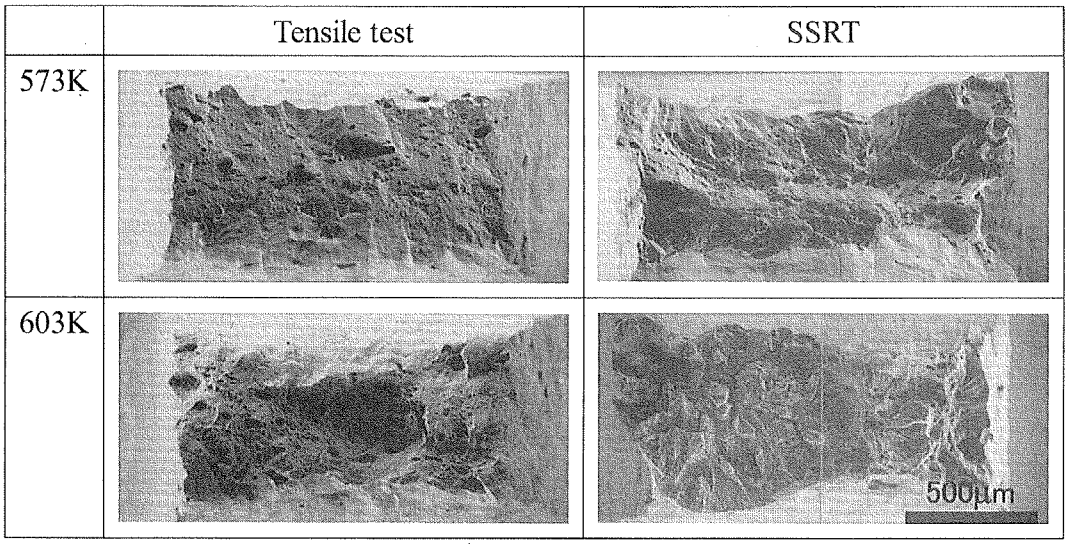

Fig. 6.1.2 Fracture surface of type 316LN-IG irradiated at 473K to 1 dpa

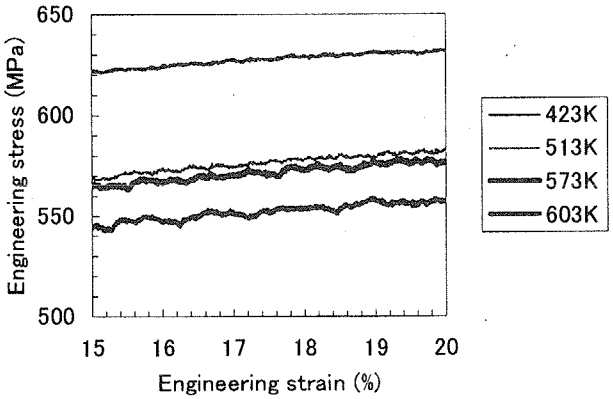

Fig. 6.1.3 Stress- strain behavior in tensile tests

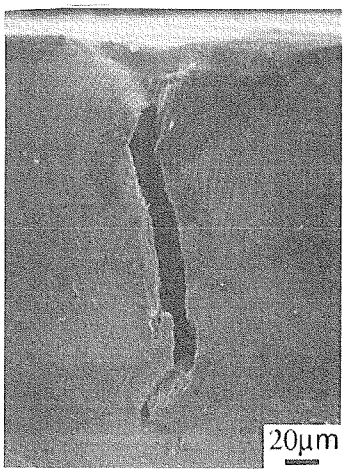

Fig. 6.1.4 IASCC initiation

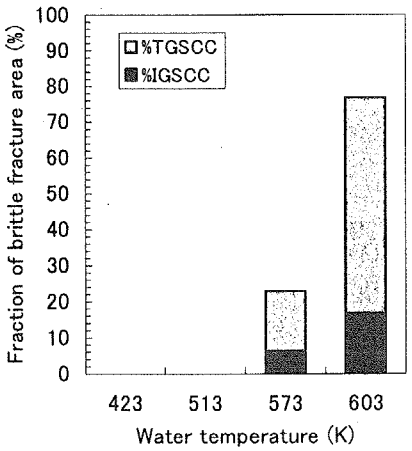

Fig. 6.1.5 Water temperature dependence on IASCC susceptibility.

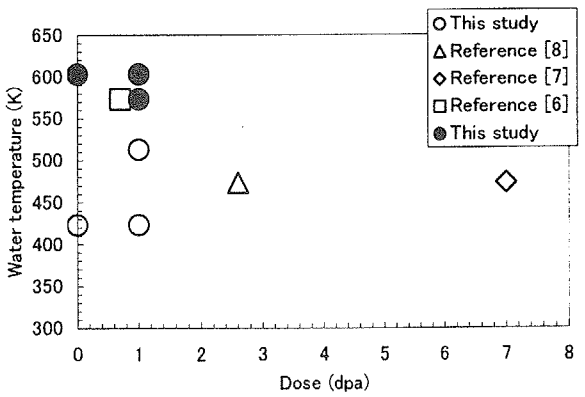

Fig. 6.1.6 IASCC susceptibility map of type 316L irradiated at 423-513K. (Closed symbol: IASCC, Open symbol: No cracking)

6.2 AFM Evaluation for Corrosion Behavior of Ion Irradiated Stainless Steel

Y. Nemoto, Y. Miwa, H. Tsuji and T. Tsukada
(*E-mail:* y.nemoto@popsvr.tokai.jaeri.go.jp)

Irradiation assisted stress corrosion cracking (IASCC) of austenitic stainless steel has been studied as one of main concerns of aging problem of light water reactor (LWR) materials. It is essential to evaluate corrosion behavior of irradiated materials for mechanistic understanding of IASCC. The aim of this work is to evaluate corrosion behavior of ion irradiated materials using the atomic force microscope (AFM), and evaluate the influence of radiation damage, H and He implantation and irradiation temperature.

High purity Fe-18Cr-12Ni specimens were used in this study. Chemical composition of the specimen is given in Table 6.2.1. Ni ion was irradiated to solution annealed specimens at 573K and 673K, using tandem accelerator at the Takasaki ion accelerators for advanced radiation application (TIARA). An illustration of specimen shapes and irradiation direction is given in Fig.6.2.1. Depth profile of radiation damage and implanted ion contents calculated by TRIM85 code is given in Fig.6.2.2. The peak damage level was estimated as 5dpa and 35dpa. H and He were implanted up to 1750 - 17500appm respectively during irradiation. Irradiation condition is given in Table 6.2.2. After irradiation, irradiated surface of specimen was plated by Cu film for protection, and the cross section of specimens was polished to be flat. Potentiostatic corrosion procedure was conducted on the cross section of irradiated specimens, at passivating potential (150mV) for 500s, at 303K. After corrosion procedure, the specimens were examined with AFM.

The expected peak area of radiation damage was corroded, but the other area was not corroded. On the specimen irradiated up to 5dpa, grain boundary and some parts of surface of grains were locally corroded. On the other hand, on the specimens irradiated up to 35dpa, all of the peak area of radiation damage was corroded. Measurement method of corrosion volume is shown in Fig.6.2.3. AFM line measurement was conducted across the corroded area, and cross section of the corroded area was evaluated as corrosion volume. The corrosion volume depending on radiation damage is given in Fig.6.2.4. Corrosion volume increased with radiation damage. H implantation dependence of corrosion volume is given in Fig.6.2.5. On the specimen irradiated up to 35dpa, H implantation at 573K stimulated corrosion, but H implantation at 673K did not stimulate corrosion. He implantation dependence of corrosion volume is given in Fig.6.2.6. He implantation at

573K and 673K suppressed corrosion, and corrosion volume was greater for the specimens irradiated at 673K than these at 573K. H, He dual implantation dependence of corrosion volume is given in Fig.6.2.7. Dual implantation of H plus He suppressed corrosion when it was 1750appm H plus 1750appm He (50H/dpa+50He/dpa), but it did not suppress corrosion when it was 17500appm H plus 17500appm He (500H/dpa+500He/dpa).

In this work, corrosion volume increased with radiation damage. It could be considered because radiation defects, radiation induced precipitates and radiation induced segregation increased with radiation damage, thus corrosion resistance decreased. H and He implantation changed corrosion behavior. It could be considered because these H and He atom involved to radiation induced diffusion in specimens, however further studies using electron microscope is required to understand the mechanism.

Table 6.2.1 Chemical composition of specimen

C	N	Si	P	S	Ti	Mn	Cr	Ni	Al	Fe
0.003	0.0014	0.01	0.001	0.0014	0.01	1.36	18.17	12.27	0.16	Bal.

Table 6.2.2 Irradiation condition

Radiation dose (dpa)	Temperature (K)	H content (appm)	He content (appm)
5	673	0	0
35	573	0	0
35	673	0	0
35	573	17500 (500H/dpa)	0
35	673	17500 (500H/dpa)	0
35	573	0	1750 (50He/dpa)
35	673	0	1750 (50He/dpa)
35	573	0	17500 (500He/dpa)
35	673	0	17500 (500He/dpa)
35	573	1750 (50H/dpa)	1750 (50He/dpa)
35	673	1750 (50H/dpa)	1750 (50He/dpa)
35	573	17500 (500H/dpa)	17500 (500He/dpa)
35	673	17500 (500H/dpa)	17500 (500He/dpa)

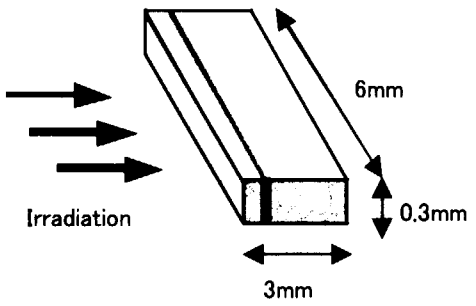

Fig. 6.2.1 Specimen dimension

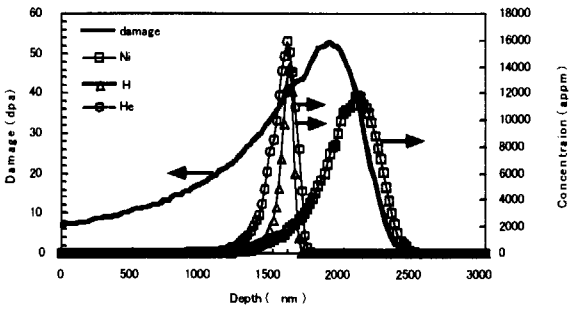

Fig. 6.2.2 Profile of irradiation damage, ion implantation

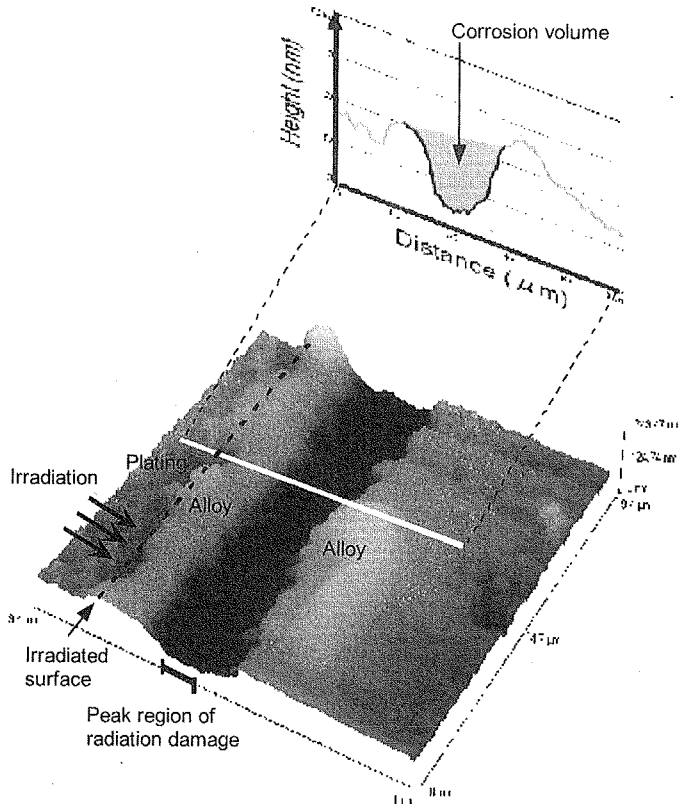

Fig. 6.2.3 Measurement method of corrosion volume

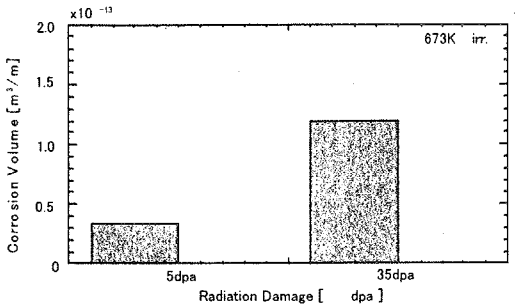

Fig. 6.2.4 Effect of Radiation damage for corrosion volume

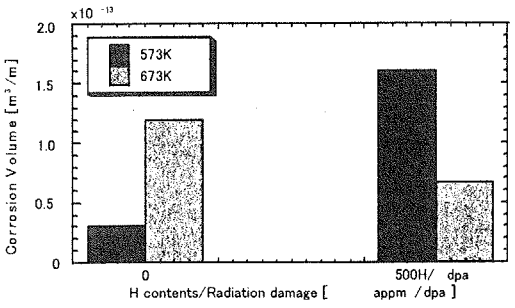

Fig. 6.2.5 Effect of H implantation for corrosion volume

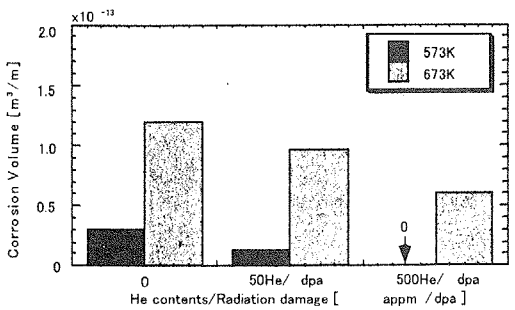

Fig. 6.2.6 Effect of He implantation for corrosion volume.

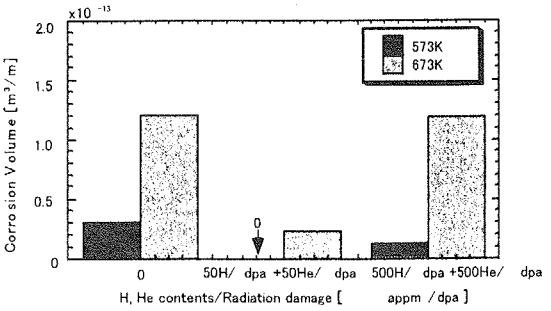

Fig.6.2.7 Effect of H, He dual implantation for corrosion volume

6.3 Present Status of SSRT Facility for in-situ Observation in High Temperature Water of Irradiated Materials

J. Nakano, T. Tsukada and H. Tsuji
(E-mail:lantis@popsvr.tokai.jaeri.go.jp)

In-core structural materials used in the light water reactors (LWR) are exposed to high flux neutron in high temperature water environment. Irradiation assisted stress corrosion cracking (IASCC) is known as a degradation phenomenon that is caused by synergistic effects of neutron irradiation, stress/strain and high temperature water on the structural materials. From the view point of the life management of the core components of the aged LWR, IASCC is concerned to be one of the key issues. To evaluate SCC susceptibility on stainless steels, slow strain rate test (SSRT) in corrosive environment has often been applied generally and the in-situ observation on specimen surface during SSRT for unirradiated materials have been reported.[1,2] The phenomenon during SSRT includes both the crack initiation and the crack growth stages. To isolate the crack initiation stage from the crack growth stage will be very useful for understanding the IASCC phenomenon. Therefore we designed and developed a SSRT facility with an efficiency of in-situ observation on the specimen surface during SSRT for irradiated materials.

The autoclave has a window for in-situ observation of the specimen and Fig. 6.3.1 shows the design of window can be observed specimen during SSRT through the window and recorded using a CCD camera system. To avoid the shadow of chuck on the specimen surface, lighting and observation are carried out from the same direction. As a material for window, sapphire with deterioration resistance in high temperature water is used. Since refraction index (1.7) of sapphire is larger than that (1.0) of air, the specimen surface can be observe from the outside of the autoclave.[2] Fig. 6.3.2 shows equipments for in-situ observation. Images taken by the CCD camera inside the hot cell are reproduced on a monitor outside the hot cell and recorded. To obtain images with high quality, the CCD camera has 2.1 M pixels. Since concrete wall between the CCD camera and the recorder is thick for radiation protection, cable with 5 m in length was required. The recorder with an automatic timer and a hard disk drive (10 GB) for recording since SSRT takes long test period. The equipments put in the hot cell are designed to be easy to be operated by manipulators.

In-situ observation during tensile test using unirradiated material was carried out in high temperature water as a trial run. The flat sheet type specimen with 20 mm in gage length, 4 mm in width and 1 mm in thickness was machined from type 304 stainless steel. Two notches

were introduced on both side of the gage length of the specimen to fix a fracture point on the specimen surface. Tensile test was conducted in high-purity and oxygenated (DO ; 8 wt. ppm) water at 561 K. Applied speed of cross head was 0.04 mm/min. Load-elongation curve and images obtained from the tensile test of notched specimen in high temperature water are shown in Fig. 6.3.3. First initiation of crack from right side of the specimen was confirmed at 0.55 kN in load. Next, the first crack continued to grow and initiation of other cracks was observed from other point of right side. Initiation of crack from left side of the specimen was confirmed at 0.95 kN in load soon after. Finally, cracks from both side of the specimen coalesced and the specimen fractured. The lengths of the crack observed at 0.55 kN and 0.95 kN are about 0.4 mm and 0.3 mm, respectively. Change of about 0.1 mm in length could be discriminated from resolution on the image obtained from the observation. Clearer images will be able to be obtained by increasing of the amount of light. From the results of in-situ observation during tensile test using unirradiated material, the capabilities of the SSRT facility were confirmed. As next step, in-situ observation for irradiated materials during SSRT will be carried out to isolate the crack initiation stage from the crack growth stage.

Reference:

1) Tani, J., Hirano, H. and Kato, S. : "Trial Making of In-Situ Stress-Corrosion Crack Observation System in High-Temperature Water and Evaluation of Water Chemistry on Crack Initiation" , Komae Research Laboratory Rep. No. T97014, Central Research Institute of Electric Power Industry (1998).

2) Shibata, T. and Haruna, T. : "Research on the Mechanism of Inhibition of Stress Corrosion Cracking by Water Chemistry of Nuclear Reactor" , JAERI-Tech 2000-061 (2000).

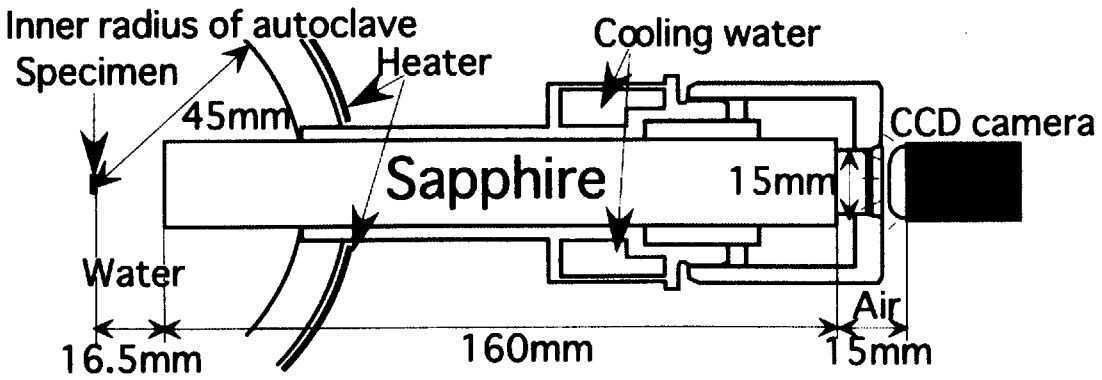

Fig. 6. 3. 1 Window for observation during SSRT.

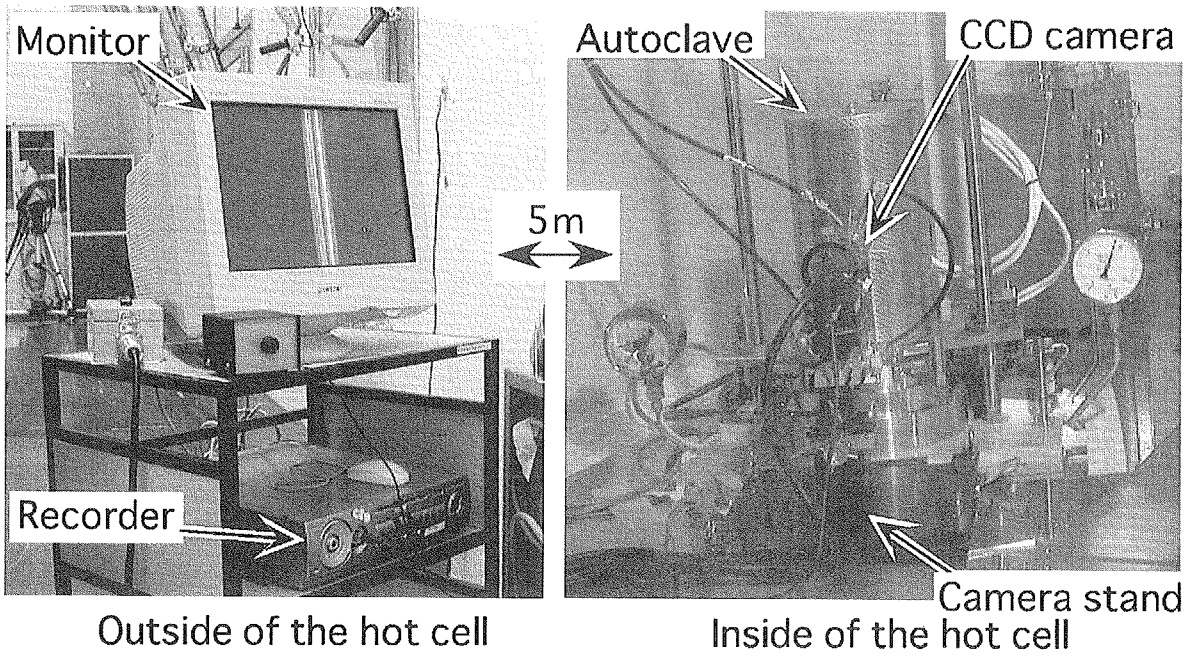

Fig. 6. 3. 2 Equipments for in-situ observation on specimen.

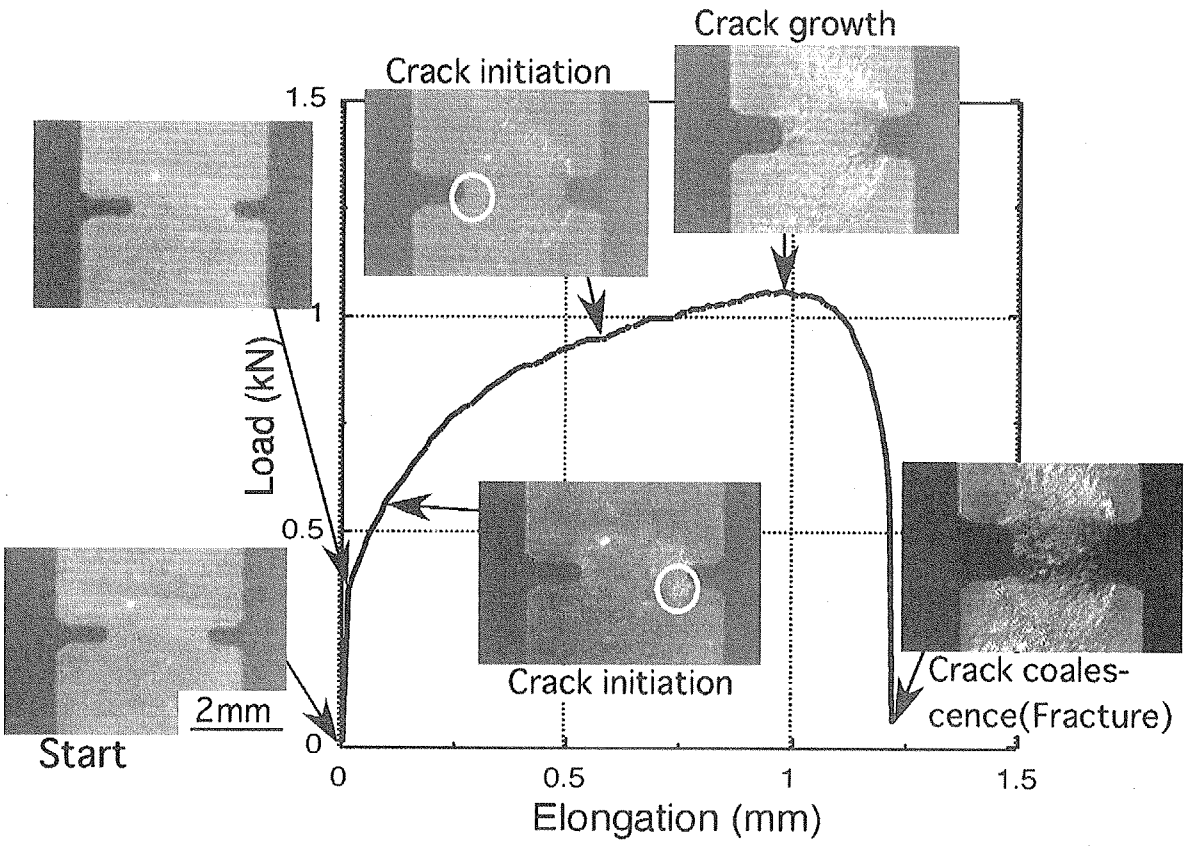

Fig. 6. 3. 3 Load-elongation curve and images of notched specimen in water at 561K.

6.4 Development of In-pile and Out-of-pile Uniaxial Constant Loading SCC Test Technique in High Temperature Water

H. Ugachi, T. Tsukada, Y. Matsui, Y. Kaji , T. Kouya, S. Endo and H. Tsuji
(*E-mail:* ugachi@cat.tokai.jaeri.go.jp)

Irradiation assisted stress corrosion cracking (IASCC) is caused by the synergistic effects of neutron irradiation, stress and corrosion by high temperature water. It is, therefore, essential to perform in-pile SCC tests, which are material tests under the conditions simulating those of actual LWR operation, to clarify the precise mechanism of the phenomenon, though mainly out-of-pile SCC tests for irradiated materials have been carried out in this research field. There are, however, many difficulties to perform in-pile SCC tests. Performing in-pile SCC tests, essential key techniques must be developed. Hence as a part of development of the key techniques for in-pile SCC tests, we have embarked on development of the test technique which enables us to obtain the information concerning the effect of such parameters as applied stress level, water chemistry, irradiation conditions, etc. on the crack initiation behavior. Although it is difficult to detect the crack initiation in in-pile SCC tests, the crack initiation can be evaluated by the detection of specimen rupture if the cross section area of the specimen is small enough. Therefore, we adopted the uniaxial constant loading test with small tensile specimens.

A few kinds of testing units were designed. Pressurized high temperature water flows outside of the testing unit. Loading level is controlled by controlling the pressure difference between the internal helium gas of the bellows and the external water. In order to obtain relationship data between gas pressure, tensile load and deflection of bellows, a monitoring system apparatus was developed. The schematic figure of this apparatus is shown in Fig. 6.4.1.

There are contact points in the bellows for detecting contraction of the bellows. A detection system design of the specimen rupture is shown in Fig. 6.4.2. When the specimen is ruptured, the bellows contract over the gap and the points keep in touch. The electric resistance between these contact points is remotely monitored. The specimen rupture can be

indicated as the reduction of electric resistance.

As comparison between in-pile and out-of-pile USL test data, a testing apparatus for irradiated materials was set up in a hot cell of Waste Safety Testing Facility (WASTEF). The appearance of the testing apparatus is shown in Fig.6.4.3. The apparatus consists of a pressurized high temperature water loop and four tensile testing systems with autoclaves. In the last quarter of this fiscal year, a trial run of the apparatus is being made.

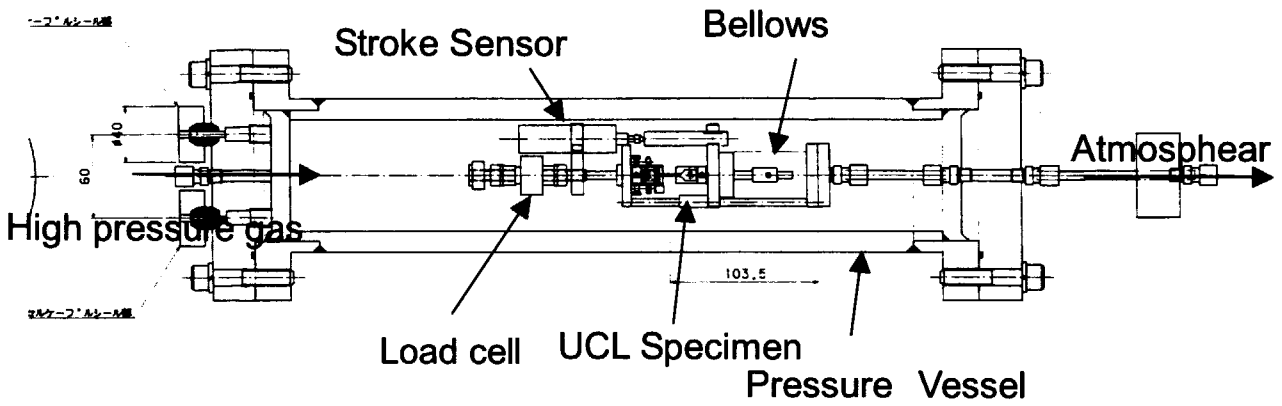

Fig. 6.4.1 Schematic figure of monitoring system apparatus for USL test unit

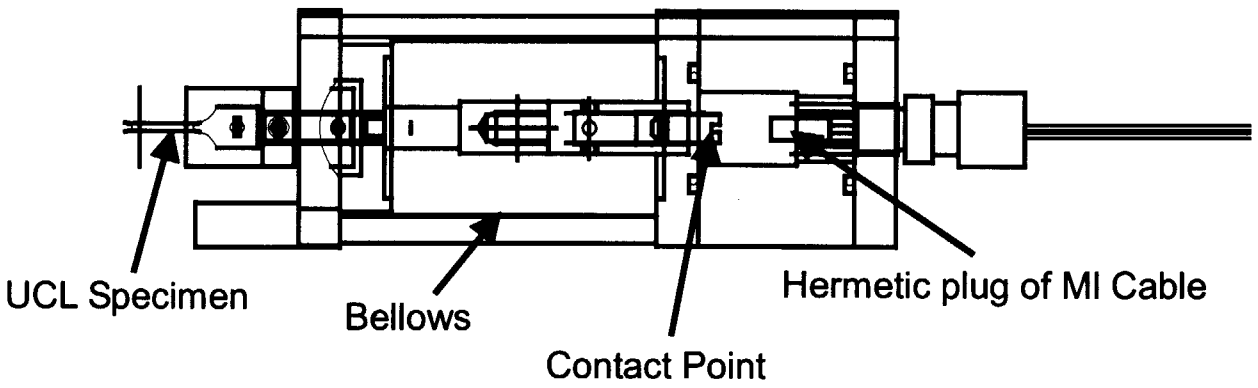

Fig. 6.4.2 Detection system of specimen rupture in UCL test unit

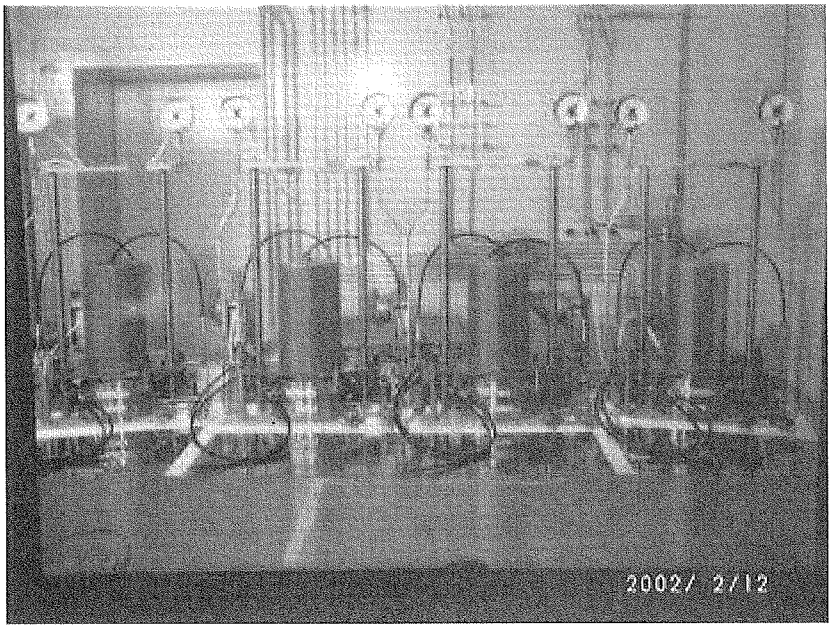

Fig.6.4.3 Testing apparatus for irradiated materials in a hot cell of WASTEF

6.5 Description Method for Knowledge Extracted from Data-Free-Way

Y. Kaji, H. Tsuji, M. Fujita[*1], J. Kinugawa[*1], K. Yoshida[*2], S. Mashiko[*3],
K. Shimura[*2], S. Miyakawa[*3] and S. Iwata[*4]
(*E-mail:* kaji@popsvr.tokai.jaeri.go.jp)

The distributed material database system named "Data-Free-Way" which can be shared from the Internet has been developed under the collaboration of four organizations of the National Institute for Materials Science (NIMS), the Japan Atomic Energy Research Institute (JAERI), the Japan Nuclear Cycle Development Institute (JNC), and the Japan Science and Technology Corporation (JST)[1-4]. In the system, the retrieved results are displayed as tables and graphs, and the users judge the meaning of the retrieved results. Such a function is enough for the expert. However, if the meaning of the retrieved results and the analyzed results are stored as knowledge, the system becomes more beneficial for many users. Therefore, in order to create additional values of the system, knowledge base system, in which knowledge extracted from the material database is expressed, is planned to be developed for more effective utilization of Data-Free-Way.

The world wide web (WWW) home page and the WWW server have been prepared. As the data input-output supporting system, the additional functions have been prepared to reinforce the linkage function between the database and the WWW, such as the retrieval-layout function of image data, the simple graph preparation function, the linkage function between numerical data and image data, the preparation function of a standard type retrieval screen, the saving-reproducing function of retrieval conditions, etc. The on-line manual, dictionary on data items and unit conversion function have been prepared as a users' supporting system. NIMS prepares mechanical properties data for stainless steels and superalloys. JAERI prepares mechanical properties data for nuclear materials as a database for research reactors, light water reactors, high temperature gas-cooled reactors and fusion reactors. JNC prepares liquid metal corrosion database for fast breeder reactors and

[*1] National Institute for Material Science
[*2] Japan Science and Technology Corporation
[*3] Japan Nuclear Cycle Development Institute
[*4] University of Tokyo

mechanical properties database of irradiated stainless steels. JST prepares public fact data as a database of irradiated stainless steels. At present, the data of more than 35000 specimens in various kinds of materials are stored in the common database.

A standard type retrieval screen is prepared for users' convenience in Data-Free-Way. If typical retrieved results through the standard type retrieval screen are available, users do not need to retrieve the database under the same conditions. Moreover, if the meaning of the retrieved results and the analyzed results are stored as knowledge, the system becomes more beneficial for many users [5].

Figure 6.5.1 shows the concept of retrieval of Data- Free-Way, the knowledge note making function, and the knowledge base. Specialists in each organization retrieve the data, make the graph and evaluate the data by the distributed material database (Data-Free-Way), then if they find new knowledge, they make knowledge notes with knowledge information, etc. Not only knowledge, but also retrieved procedures for a specialist are recorded in a knowledge note. The knowledge notes are stored in each site and users can retrieve and read them through management system for knowledge base. In this system, one knowledge note described with XML (eXtensible Markup Language) is stored as a knowledge which composes the knowledge base. Therefore, the laymen can retrieve in the same way as specialists by using the retrieved procedures without trial and error.

Knowledge notes can be made at each stage of the data retrieval, the display of the retrieved results, or the graph making. A set condition at each stage can be reproduced from the knowledge note. Storing knowledge obtained as retrieved results, the items shown in the left side of Fig. 6.5.2 are described with XML. And a knowledge note can be displayed using XSL (eXtensible Style Language) as shown in the right side of Fig. 6.5.2.

Since this knowledge note is described with XML, the user can easily convert the display form of the table and the graph into the data format which the user usually uses. Moreover, additional information to the retrieved numerical values such as a unit can be easily conveyed.

Reference

1) H. Tsuji et al., "Distributed Database System for Mutual Usage of Material Information (Data-Free-Way)", Materials for Advanced Power Engineering 1998, Part III, pp.1739-1745, Liege (Belgium) (1998).

2) H. Tsuji et al., "Distributed Database System for Advanced Nuclear Mutual Materials (Data-Free-Way)", Proc. 9th Inter. Conf. on Modern Materials & Technologies, pp.417-424, Florence (Italy) (1999).

3) H. Tsuji et al., "Present Status of Data-Free-Way (Distributed Database System for Advanced Nuclear Materials)", Journal of Nuclear Materials, 271&272, pp.486–490 (1999).

4) M. Fujita et al., "Application of the Distributed Database (Data-Free-Way) on the Analysis of Mechanical Properties in Neutron Irradiated 316 Stainless Steel", Fusion Engineering and Design, 51-52, pp.769-774 (2000).

5) Y. Kaji et al., "Development of Knowledge Base System Linked to Material Database", 18th Int. Conf. CODATA 2002, Montreal, Canada (2002).

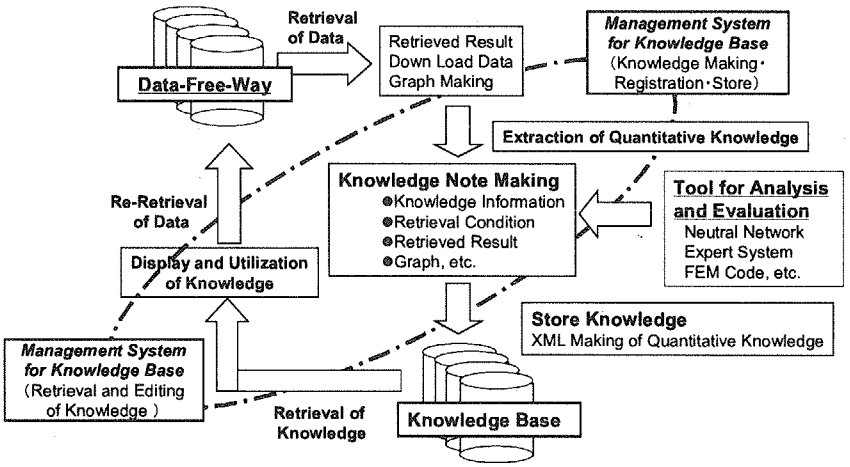

Fig. 6.5.1 Concept of Data-Free-Way, knowledge making function and knowledge base

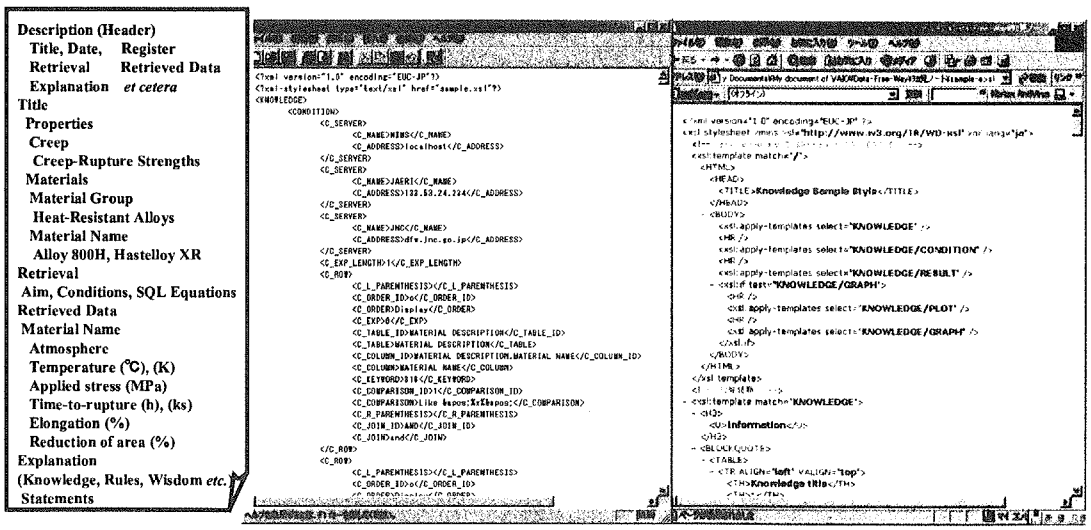

Fig. 6.5.2 Description format of knowledge note with XML and XSL

7. Research on Advanced Materials for Light Water Reactors and Reprocessing Plants

On the development of new cladding materials applied to the advanced light water reactors aiming at the ultrahigh burn-up and reduced spectrum modulation, the melting and thermo-mechanical treatment processes of Fe-25Cr-35Ni-0.2Ti candidate alloy was optimized for obtaining the enough austenite phase stability under heavy neutron irradiation. The excellent resistance to IGSCC and the sufficient mechanical strength was confirmed by slow strain rate tensile tests of specimens with thermal history simulated to irradiation aging. From the observation of micro-structural evolution by TEM specimens irradiated by triple ion beams in TIARA facility, the excellent phase stability under heavy irradiation of the candidate alloy was clarified. The estimation of tensile properties of the narrow region damaged by ion irradiation was achieved by micro-indentation tests and the new-developed mechanistic analysis for load-depth curves. From analysis with thermo-fluid dynamics, it was found that the resistance to FP gas release in cladding tubes of the candidate alloy was superior to that of Zircaloys.

On the development of new anti-corrosion technologies applied to equipment materials used in Purex reprocessing process, the susceptibility to SCC of zirconium in boiling nitric acid solutions was clarified with the oxidation potential that was relation to the concentration of nitric acid and surface temperature under heat flux control. The oxidation potential was explained with the partial pressure of oxidant gas NO_x ,which based on thermodynamic analysis of nitrogen-oxygen system. Two types of in-situ corrosion monitoring systems by modifying the electrical resistance method were developed for evaluating wall thinning. From 3rd in-service inspection of the mock-up evaporator for nitric acid recovery and laboratory tests, the acceleration effect on the wall thinning of heat transfer tubes was analyzed with two mechanisms. One is the anodic dissolution with dependent on the formation rate of oxidant ions such as neptunium (Np^{6+}) and the metal surface temperature under heat flux control. The other is the accelerated IGC penetration due to the local chemical reactions in the front of IGC.

7.1 Development of Advanced Fuel Cladding Materials Applied for Ultra-high burnup Light Water Reactors

N.Maruyama, M.Tanabe, I.Ioka and K.Kiuchi
(*E-mail* : maruyama@galileo.tokai.jaeri.go.jp)

In austenitic stainless steels, irradiation assisted stress corrosion cracking (IASCC) and loss of ductility by irradiation are serious problems. It is supposed that these problems become more serious in the case of ultra-high burnup condition. In this study, fully austenitic stainless steels with high Cr and Ni concentration were selected for the candidate materials to be applied for advanced fuel cladding tubes, aimed at ultra-high burnup of more than 100GWd/t MOX. For the purpose of solving these problems, purification of materials by electron beam melting was tested, and the adjustment of chemical composition was evaluated from the viewpoint of austenitic phase stability and mechanical properties.

Austenitic stainless steels with the composition of Fe-25Cr-35Ni-0.2Ti, Fe-22.5Cr-35Ni-0.2Ti and Fe-20Cr-35Ni-0.2Ti were purified by electron beam melting with the intention of reducing the content of interstitial impurities, especially carbon and oxygen. The melting furnace was equipped with cold hearth which facilitates elimination of inclusions such as oxides and of volatile impurities from liquid metal, attributed to shallow metal pool and wide surface area of the pool. Figure 7.1.1 illustrates a schematic diagram of the electron beam melting furnace with cold hearth. The interstitial impurities analyzed before and after electron beam melting for each run are given in Table 7.1.1. It is obvious that oxygen and carbon contents are remarkably reduced through electron beam melting. On the other hand, effective elimination is not shown with respect to nitrogen and sulfur because of low content in the vacuum induction melted feed stock, which means no contamination was kept during the electron beam melting process. Figure 7.1.2 shows a correlation between the quantity of decarburization, Δ[C], and that of deoxidation, Δ[O], in the electron beam melting process. From the correlation, it is inferred that the deoxidation proceeds through combination of flotation of oxide inclusions and degassing of carbon monoxide produced by the reaction, C＋O＝CO(gas). It is apparent that electron beam melting is very useful process to produce high pure and clean materials with extremely low content of interstitial impurities.

The ingots purified by the electron beam melting were processed with the SAR treatment (strain aging at 873K for 15hours and recrystallization at 1048K for 10 hours) after hot

working and cold working. Figure 7.1.3 shows TEM micro-structures of the SAR treated and finally 7% cold rolled materials. Relatively large precipitates were observed in the matrix of 25Cr-35Ni specimens. The precipitates were identified as Cr-rich α-phase. As shown in the figure, the number of precipitates has a tendency to decrease with decreasing chromium content. In the case of 20Cr-35Ni , only γ-phase was observed. From TEM observation, it was also clarified that titanium, scavenger element, combined with residual interstitial impurities and formed fine nitride and oxide with uniform distribution. Fig.7.1.4 indicates the results of tensile tests. From the mechanical examination, it was shown that higher strength and lower ductility were exhibited as the chromium content increased, namely the number of precipitate increased.

Although most suitable chemical composition should be selected on the basis of the consideration of corrosion resistance, irradiation properties and so on, the composition of 23Cr-35Ni is seems to be preferable from the viewpoint of phase stability and mechanical properties at the present time. Further evaluation has been conducted for the selection of optimum chemical composition.

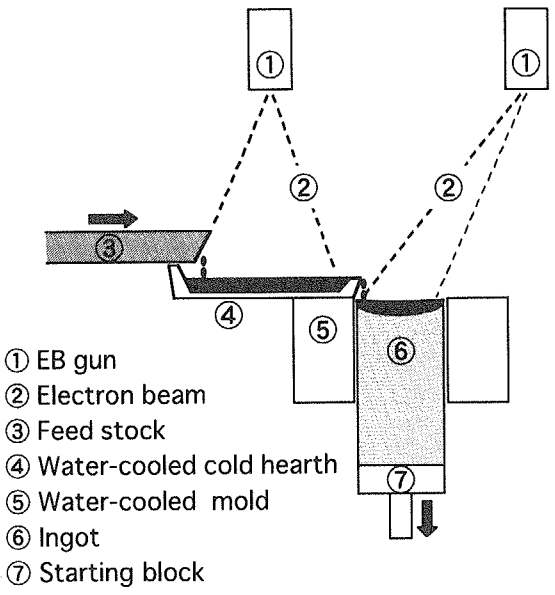

Fig.7.1.1 Schematic diagram of electron beam cold hearth melting

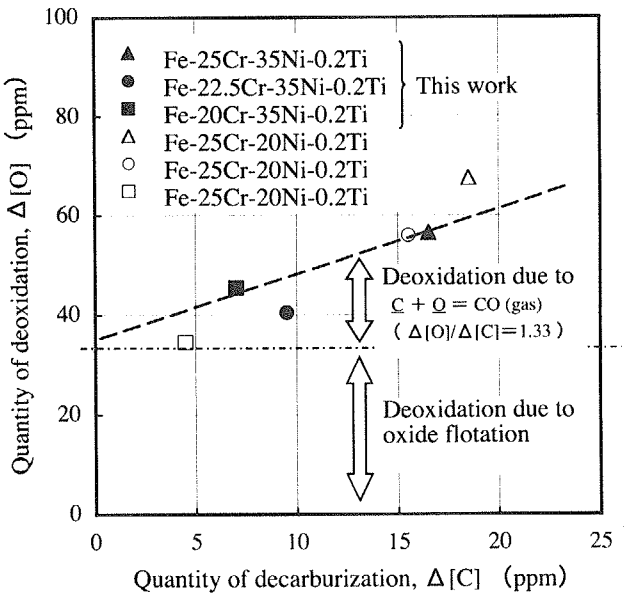

Fig.7.1.2 Correlation between quantity of decarburization and that of deoxidation in electron beam melting

Table 7.1.1 Chemical analyses of feed stock and ingot (wt%)

		Cr	Ni	Ti	C	O	N	S
①	Feed stock (Before EB melting)	25.59	34.81	0.24	0.0026	0.0070	0.0009	0.001
	Ingot (After EB melting)	24.46	35.30	0.22	0.0010	0.0014	0.0009	0.001
②	Feed stock (Before EB melting)	23.23	34.87	0.24	0.0019	0.0059	0.0009	0.001
	Ingot (After EB melting)	22.39	35.27	0.22	0.0010	0.0019	0.0009	0.001
③	Feed stock (Before EB melting)	20.75	34.86	0.23	0.0017	0.0071	0.0007	0.001
	Ingot (After EB melting)	19.88	35.76	0.22	0.0010	0.0026	0.0010	0.001

① Fe-25Cr-35Ni-0.2Ti, ② Fe-22.5Cr-35Ni-0.2Ti, ③ Fe-20Cr-35Ni-0.2Ti

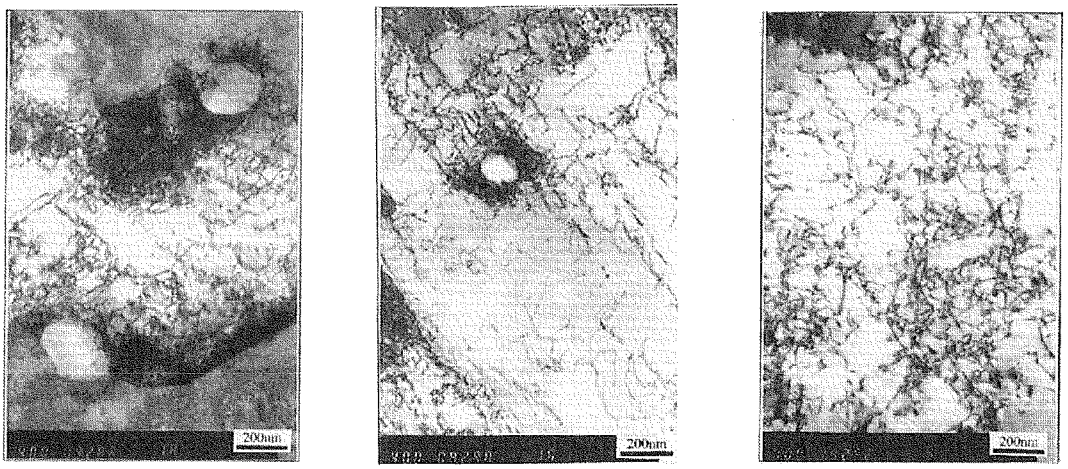

Fe-25Cr-35Ni-0.2Ti　　Fe-22.5Cr-35Ni-0.2Ti　　Fe-20Cr-35Ni-0.2Ti

Fig.7.1.3 Transmission electron micrograph of austenitic stainless steel

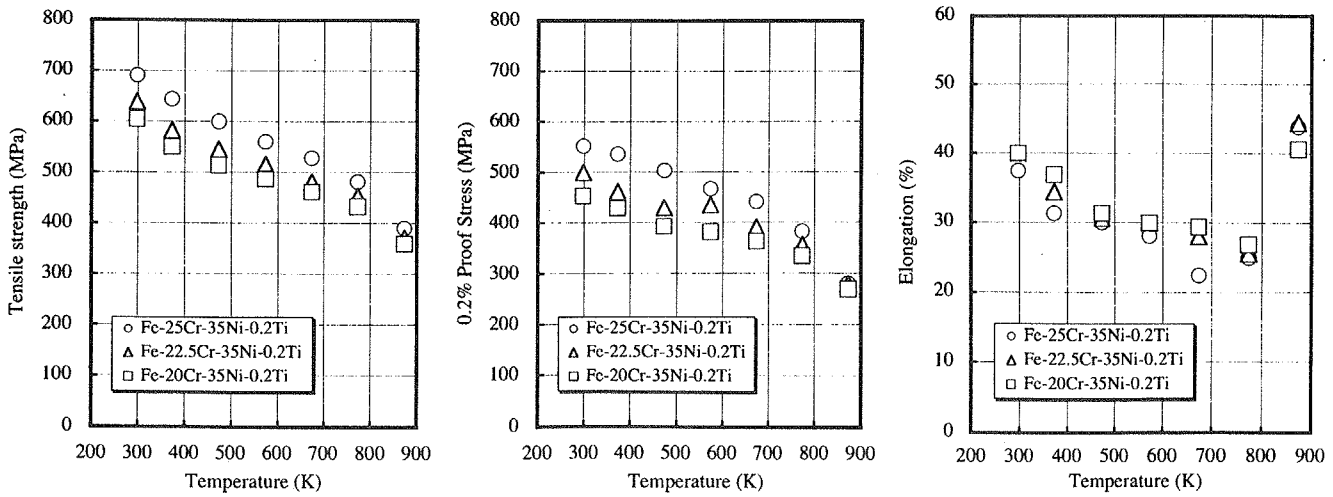

Fig.7.1.4 Tensile properties as a function of temperature

7.2 Improvement of Micro-cracking Susceptibility in Welding Fully Austenitic Stainless Steel

N.Maruyama, M.Tanabe and K.Kiuchi
(*E-mail* : maruyama@galileo.tokai.jaeri.go.jp)

An austenitic stainless steel of R-SUS304ULC is to be used as a heat transfer tube materials of the evaporator for nitric acid recovery in the Rokkasho Reprocessing Plant. In the mock-up test operation for 20,000 hours, however, detachment of grains from the inner wall of the heat transfer tubes were observed. This phenomenon is attributed to intergranular corrosion. In order to maintain the reliability, it is necessary to develop candidate materials with good resistance to intergranular corrosion.

In this research, high chromium full austenitic stainless steel, R-SUS310ULC, containing 0.2wt% of Ti as a scavenger was selected as an alternative for R-SUS304ULC. Concerning full austenitic stainless steel, however, it is well known that the material shows a sensitivity to hot cracking in welding, which is attributed to segregation of impurities. Two types of cracking have been reported. One is solidification cracking, and the other is cracking in reheating weld metal of multipass weldments. It is indicated that manganese reduces the sensitivity to cracking and the optimum content is between 2 and 6wt%.[1] Manganese, however, has a harmful effect on corrosion resistance. For the purpose of both improving micro-cracking susceptibility and suppressing intergranular corrosion, R-SUS310ULC was purified by a combination of vacuum induction melting and electron beam melting with the special intention of obtaining ultra-high pure materials. The trans-varestraint test and the fissure bend test were adopted in order to evaluate the effect of filler metal composition on the micro-cracking susceptibility in the TIG welded joint. Table 7.2.1 shows the chemical composition of base metal and filler metals. The base metal was fabricated from the materials purified by the above-mentioned method. Two types of filler metal were used, manganese free with nearly the same composition as base metal and 2wt% of manganese added. The latter was classed as a low manganese filler metal, denoted RY310ULC, with respect to the reprocessing standard. Figure 7.2.1 and Fig.7.2.2 illustrate the trans-varestraint test and the fissure bend test, respectively. Figure 7.2.3 illustrates the preparation of specimens for the welding crack test. In the trans-varestraint test, the specimen on which welding torch was running along the pre-deposited beads was forced sudden bending action, by which the characteristic of solidification cracking could be evaluated. On the other hand, sensitivity to

cracking in underlying weld runs reheated by subsequent passes could be evaluated by the fissure bend test. Figure 7.2.4 shows the maximum crack length, sum of crack length and number of cracks obtained from the trans-varestraint test. In the case of using manganese free high pure filler metal, all of the values were large to some extent in comparison with the case of 2wt% manganese added filler metal, but the difference between the two cases was very small. Table 7.2.2 shows the result of the fissure bend test. No cracks were observed in both cases. From the welding crack tests, it was thought that manganese free filler metal was as applicable as manganese added filler metal in a practical sense. In order to evaluate the corrosion resistance of weld metal, corrosion test similar to the Huey test was conducted with respect to the all deposited metal. Figure 7.2.5 illustrates the preparation of specimens for the corrosion test. Test solution was 8N HNO_3+1.0g/L Cr^{6+}, and was renewed every 48 hours. As shown in Fig.7.2.6, manganese free samples indicated superior corrosion resistance to that of manganese added samples. From this study, it was confirmed that the attainment of both low susceptibility to hot cracking and high corrosion resistance in weld metal might be possible by the use of high pure base metal and filler metal, even in welding full austenitic stainless steel, R-SUS310ULC.

Reference:

1) J.Honeycombe and T.G.Gooch : Metal Construction and British Welding Journal, December (1972) , p.456-460

Table 7.2.1 Chemical compositions of welding materials

(wt%)

Material		C	Si	Mn	P	S	Ni	Cr	Ti	O	N
Base metal		0.0007	<0.01	<0.01	<0.003	0.002	21.41	24.51	0.23	0.0015	0.0012
Filler metal	Manganese free	0.0008	<0.01	<0.01	<0.003	0.002	21.38	24.59	0.22	0.0022	0.0012
	2% manganese added	0.0026	<0.01	2.44	0.001	0.003	20.70	25.79	0.19	0.0010	0.0013

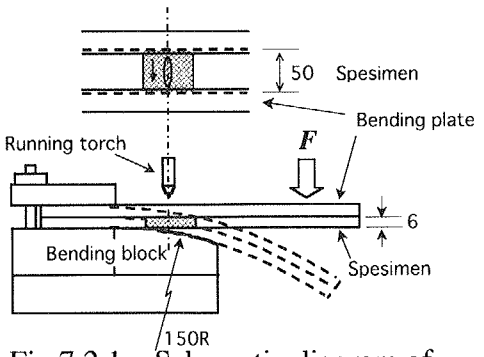

Fig.7.2.1 Schematic diagram of the trans-varestraint test

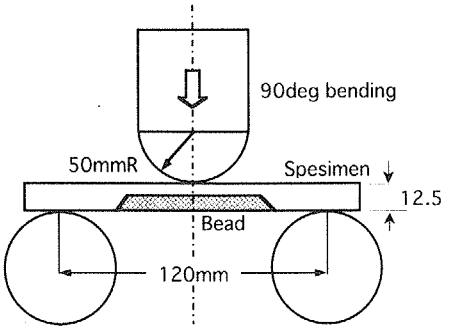

Fig.7.2.2 Schematic diagram of the fissure bend test

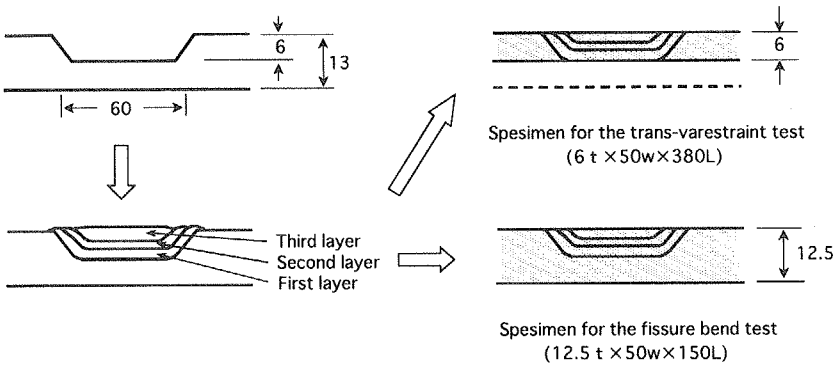

Fig.7.2.3 Preparation of specimens for the welding crack test

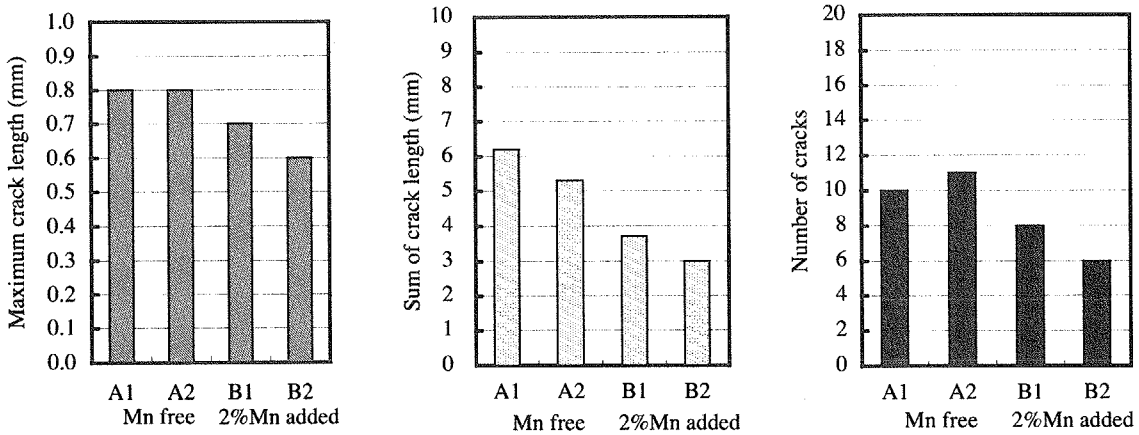

Fig.7.2.4 Result of the trans-varestraint test

Table 7.2.2 Number of cracks observed in the fissure bend test

Specimen (Type of filler metal)	Number of cracks
A1 (Manganese free)	0
A2 (Manganese free)	0
B1 (2% manganese added)	0
B2 (2% manganese added)	0

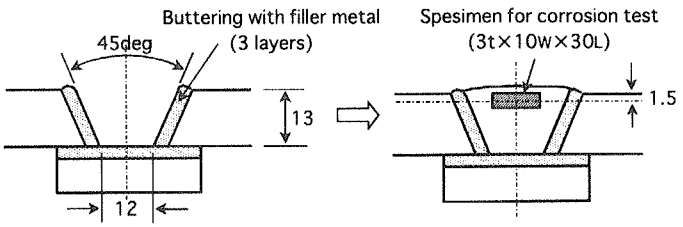

Fig.7.2.5 Preparation of specimens for corrosion test of the all deposited metal

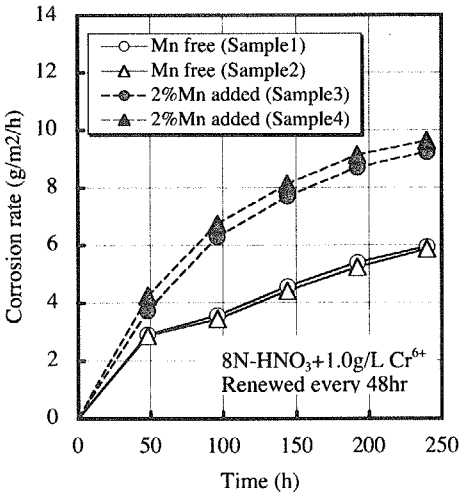

Fig.7.2.6 Corrosion rate of the all deposited metal formed by the use of Mn free and 2wt%Mn added filler metal

7.3 Effect of Triple Ion Beam Irradiation on Microstructural Evolution of High Chromium Austenitic Stainless Steel

Y.Nanjo, I.Ioka, A.Naito, K.Kiuchi, Y.Kuroda* and T.Anekawa**
(*E-mail*: nanjou@galileo.tokai.jaeri.go.jp)

The advanced material well-adapted to the burnup extension more than 100GWd/t with MOX fuel was developed, because the burnup extension was effectual technology for reduction of nuclear waste, ecological and economical utilization of nuclear resource[1]. The advanced material was the stabilized austenitic stainless steel containing higher Cr and Ni than any other austenitic stainless steels. Austenitic stainless steels have popular problems such as IGSCC or ductility loss through the use at nuclear power plants. Therefore, the advanced material was taken several countermeasures which were adjustment of chemical composition for Cr depletion near intergranular and gamma phase stabilization, purification in the alloy, thermo-mechanical treatment for obtaining the fine grain and uniformly dispersed precipitates. Those effects were evaluated through the adaptability test under the condition simulated ultra high burnup. In this study, effects of triple ion beams irradiation on microstructure evolution of the advanced material processed to the tube were investigated before neutron irradiation, and their microstructure evolution was observed with TEM. For comparison, 304SS of the fuel cladding material utilized in "Mutsu" atomic power ship was irradiated and observed in the same method. The irradiation resistance was evaluated with the comparison of the number density of dislocation loops formed in both irradiated materials.

Experimental

Chemical compositions of the advanced material and 304SS, the fuel cladding material utilized in "Mutsu" atomic power ship, as the comparer are shown in Table 7.3.1. Ultra high purity ingots for the advanced material were produced by the melting method composed with VIM (vacuum induction melting) and CCIM (cold crucible induction melting). The ingots were annealed at 1330 K for 30 minutes, and processed to the tube with 60% cold work. The two heat treatments were taken continuously to the tube, the first heat treatment was aging treatment at 823 K for 15 hours to uniformly stabilize impurities as precipitations, and the second one was

Table 7.3.1 Chemical composition of the advanced material and 304SS of 'Mutsu'(wt%)

	Fe	Cr	Ni	Ti	C	N	O	S	Si	Mn	P
Advanced material	bal.	24.55	34.99	0.18	0.0013	0.0014	0.0011	0.0009	<0.005	0.001	0.001
304SS of 'Mutsu'	bal.	18.72	10.27	-	0.063	-	-	0.012	0.49	1.45	0.016

*The Japan Atomic Power Company
**Tokyo Electric Power Company

recrystallized treatment at 1048 K for 10 hours to obtain fine grain. Finally, the tube was stretch formed with 7% cold work for obtaining sufficient strength and straightening. By above processes, the advanced material tube, 11.3mm in outer diameter and 0.4mm in thickness, was prepared. 304SS tube, 10.5mm in outer diameter and 0.4mm in thickness, was produced with the normal tube making process. The outside of the tube was planarized with mechanically polishing, and the specimen for ion irradiation was taken from the planarized surface by slurry drill. The curved surface, which the inside of the tube was turned to, of the disk was mechanically polished, and the irradiation side was buff-polished and electrochemically polished. The specimen, 3mm in diameter and 0.2-0.15mm in thickness, were prepared.

For simulating the (n,p), (n,α) reactions and displacement damage by neutrons under 100GWd/t of ultra high burnup, the specimen was irradiated at 573K with triple ion beams of 12MeV Ni^{3+}, 380KeV H^+ and 1.1MeV He^+ at TIARA of JAERI Takasaki. H^+ and He^+ ions were irradiated through the energy degraders for spreading the implanted range, and were implanted to 1.0-1.5 μm in depth. The depth distributions of Ni, H, He concentration and displacement damage was calculated with TRIM(ver. 1998 code)[2]. The disk was irradiated to 50 dpa, which was equal to the simulated result under ultra high burnup for 10 years, at 1.2-1.3μm in depth from the bombarded surface. At 1.2-1.3μm in depth, increase in Ni concentration was less than 1.0 at%, and H, He concentration were about 30 appm/dpa and 3 appm/dpa, respectively. Bombarded surface was electrochemically removed to 1.2-1.3μm, and masked with the insulator. Then, a part of the unbombarded surface was electrochemically removed, and TEM specimen was prepared. Microstructures were examined with a JEOL 2000FX electron microscope operated at 200KeV.

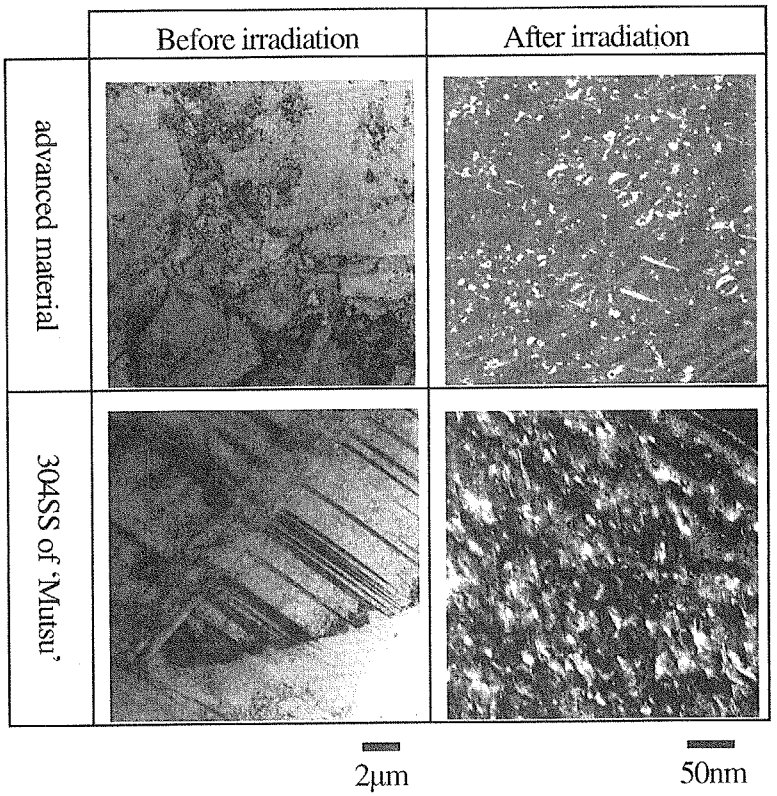

Fig.7.3.1 Microstructure evolution of the advanced material and 304SS of 'Mutsu' before and after irradiation.

Results and Discussion

Figure 7.3.1 shows microstructures of the advanced material and 304SS before and after irradiation. The micrographs after irradiation observed were (110) plane in a dark field. 304SS was almost uniform around 20 micrometer grain, and many twin crystals existed in it. No precipitations were observed in

grain and grain boundary, but stress induced ferrite was confirmed by X-ray diffraction analysis as shown in Fig.7.3.2. The advanced material had fine grains in the range of several micrometers to tens of micrometers. Precipitations were uniformly distributed in grains. Target metallography was obtained. Precipitations were extracted and evaluated by X-ray diffraction analysis. Precipitates consisted of ferrite, TiN, Ti_2O_3 as shown in Fig.7.3.3. After irradiation, dislocation loops and stacking fault tetrahedron were observed in both materials. But voids and bubbles were not observed. It is supposed that irradiation temperature of 573 K is low and ion irradiation rate is faster than that in actual condition. Figure 7.3.4 shows the number density of dislocation loop in the advanced material and 304SS, respectively. Total number of dislocation loops in the advanced material was almost equal to that of 304SS. However, peak diameter of dislocation loop of the advanced material and 304SS are 7nm and 9nm, respectively. Loops larger than 30 nm were observed in 304SS only. From the difference of the rate of ecological growth, the microstructural evolution of the advanced material is expected to be lower than that of 304SS. Cr segregation around grain boundary will be evaluated in future.

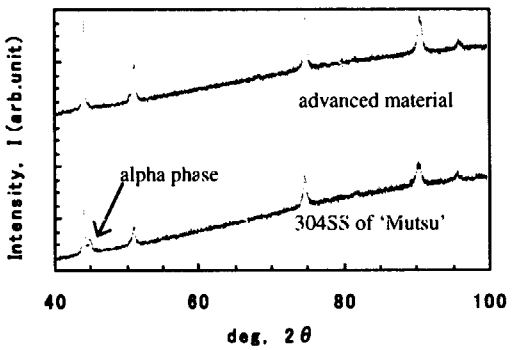

Fig.7.3.2 X-ray diffraction analysis of the advanced material and 304SS of 'Mutsu'.

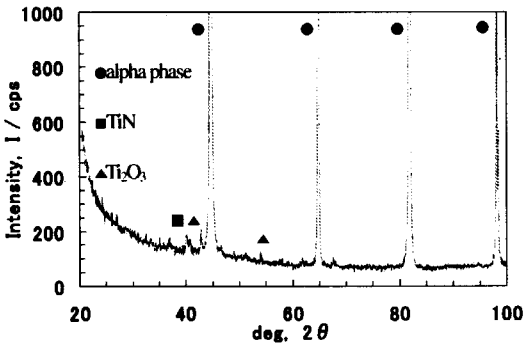

Fig.7.3.3 X-ray diffraction analysis of the residues extracted from the advanced material.

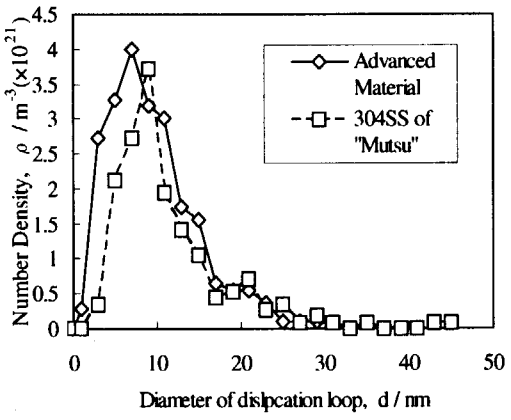

Fig.7.3.4 Number density of the dislocation loop in the advanced material and 304SS of 'Mutsu'.

References:

1) K. Kikushi et.al., "Development of Advanced Cladding Materials for Burnup Extension", IAEA TCM Reports on Technical and Economic Limit to Fuel Burnup Extension, Argentina, Nov 15-19 (1999)

2) J.F. Ziegler et.al., "The Stopping and Range of Ion in Solids", vol.1, Pergamon Oress, New York (1985)

7.4 Effect of Triple Ion Beam Irradiation on Mechanical Properties of High Chromium Austenitic Stainless Steel

I.Ioka, Y.Nanjyo, K.Tachibana, K.Suzuki, M.Tanabe, N.Maruyama and K.Kiuchi
(E-mail: ioka@popsvr.tokai.jaeri.go.jp*)*

The change in apparent hardness of the very shallow surface layer of the ion-irradiated material was calculated from the results of microindentation test. The Swift's power low constitutive of the damaged parts was derived from the microindentation test combined with an inverse analysis using a finite element method (FEM). The material properties of the candidate material were compared with those of Type 304SS.

The chemical composition of candidate material is shown in Table 7.4.1. The tube of 11.3mm in outer diameter, 0.4mm in thickness and 1000mm in length was produced by incorporating the thermo-mechanical treatment so-called SAR (strained, aged and recrystallized) from the candidate material. Type 304SS tubes which had been used to the cladding tube of the past commercial LWRs were also examined as a reference.

The irradiation condition was selected based on the condition calculated with computer simulation by assuming 100Gwd/t(MOX) on ABWRs. The dose rate, helium by (n, α) reaction and hydrogen by (n, p) reaction were simulated by the ion irradiation of 12MeV Ni^{3+}, 1.1MeV He^{+} and 380keV H^{+} at 573K corresponding to cladding surface temperature. The He^{+} and H^{+} ions were implanted in depth ranges from 1.0 to 1.5μm using energy degraders of aluminum foil. The concentration of He^{+} and H^{+} ions in the implanted range were 100-150 appmHe and 1000-1600 appmH, respectively. The dose was about 30-70dpa in the implanted range.

The microindentation test was carried out on the surface of specimens at room temperature. Two types of indenters were used for the microindentation test. One was the Berkovich indenter for measuring the apparent hardness, the other was the conical indenter that has a hemispherical apex with radius of 1.2μm for deriving the constitutive equation.

The inverse analysis was carried out using an explicit FEM code, LS-DYNA, which enables us to roughly analyze a large deformation accompanying with contacting behavior. In the analysis, the indenter and specimen were treated as axisymmetric two-dimensional bodies to take calculative efficiency into account. The modeled indenters were perfectly rigid. The mesh size is determined to be sufficiently fine to keep accuracy: the minimum element size around the apex contacting zone was 0.05μm.

The constitutive equation of the material installed into the model was assumed to be a simple power-law which is generally believed to be applicable to normal metallic materials as

follows:

$$\sigma = E\varepsilon \quad \sigma \le \sigma_y \tag{1}$$

$$\sigma = A(\varepsilon_0 + \varepsilon)^n \tag{2}$$

$$\varepsilon_0 = (\sigma_y / A)^{1/n} - (\sigma_y / E) \quad \sigma > \sigma_y \tag{3}$$

where, σ is true stress, ε true strain, E Young's modulus, σ_y yield stress, A work hardening coefficient and n work hardening exponent. Hereafter, we identified the following material constants; σ_y, A and n through the inverse analysis on the load-depth, L-D, curve.

The relationships between load and depth obtained by the microindentation test of 25Cr-35Ni-Ti UHP and Type 304SS were expressed as the L/D-D curves. The slope of L/D-D curve is in direct proportion to the appearance hardness of the material. Fig.7.4.1 shows the relative ratio of appearance hardness for the irradiated specimens normalized to that of unirradiated specimens.

Figure 7.4.2 shows the L-D curves measured using the conical indenter, and the calculated results using material constants in Eqs. (1)-(3) identified according to the method with the inverse analysis on the L-D curve. The calculated L-D curves agree well with the experimental ones. The material constants estimated from the inverse analyses on the L-D curves of 25Cr-35Ni-Ti UHP and Type 304SS are summarized in Table 7.4.2. Increase in yield stress of Type 304SS was bigger than that of the 25Cr-35Ni-Ti UHP. It is well known that hardness can be related to a yield stress. The result is in fairly good agreement with the change in apparent hardness as shown in Fig.7.4.1. The change in the value of A is the same for both specimens by ion irradiation. The value of n corresponds to the uniform deformation of the material. After ion irradiation, the decrease in n of Type 304SS was bigger than that of 25Cr-35Ni-Ti UHP. So, it seems that the ductility loss of Type 304SS by ion irradiation is larger than that of 25Cr-35Ni-Ti UHP. As a result, the irradiation hardening of the candidate is expected to be lower than that of Type 304SS from Fig.7.4.2 and the estimated material constants.

The mechanical properties of the ion-irradiated material which is a candidate for ultra-high burnup fuel cladding were examined using the novel technology used for the indentation test combined with numerical calculation.

(1) The apparent hardness of Type 304SS was higher than that of the candidate after ion irradiation.
(2) The constants in the constitutive equation for the ion irradiated thin layer were determined by the inverse analyses.
(3) The mechanical properties of the irradiated thin layer were deduced using the obtained constitutive equation.
(4) Increase in yield stress of Type 304SS was bigger than that of the candidate. The result is in fairly good agreement with the result of apparent hardness.

Table 7.4.1 Chemical Composition of the Material Tested in Weight Percent (%).

Materials	Fe	C	Si	Mn	P	S	Cr	Ni	Ti	N	O	Co
25Cr-35Ni-Ti UHP	bal.	0.0013	<0.005	0.001	0.001	0.0009	24.55	34.99	0.18	0.0014	0.0011	
Type 304SS	bal.	0.063	0.49	1.45	0.016	0.012	18.72	10.27				0.03

Table 7.4.2 Material constants estimated from the inverse analyses on the L-D curves of 25Cr-35Ni-Ti UHP and Type 304SS

		σ_y, MPa	A, MPa	n
Type 304SS	Unirrad.	213	1464	0.29
	Irrad.	528	1564	0.23
	Irrad./Unirrad.	2.45	1.07	0.79
25Cr-35Ni-Ti UHP	Unirrad.	191	1397	0.36
	Irrad.	411	1492	0.33
	Irrad./Unirrad.	2.15	1.07	0.92

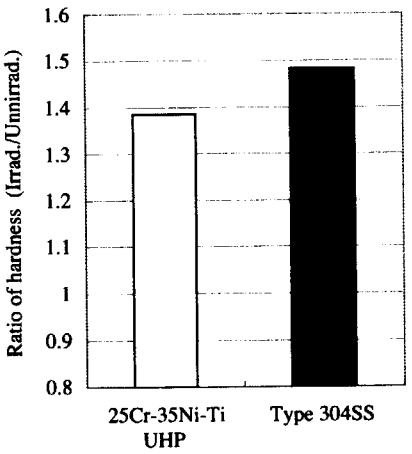

Fig.7.4.1 Relative ratio of hardness for specimens irradiated 50dpa by triple ion beams to that of unirradiated specimens

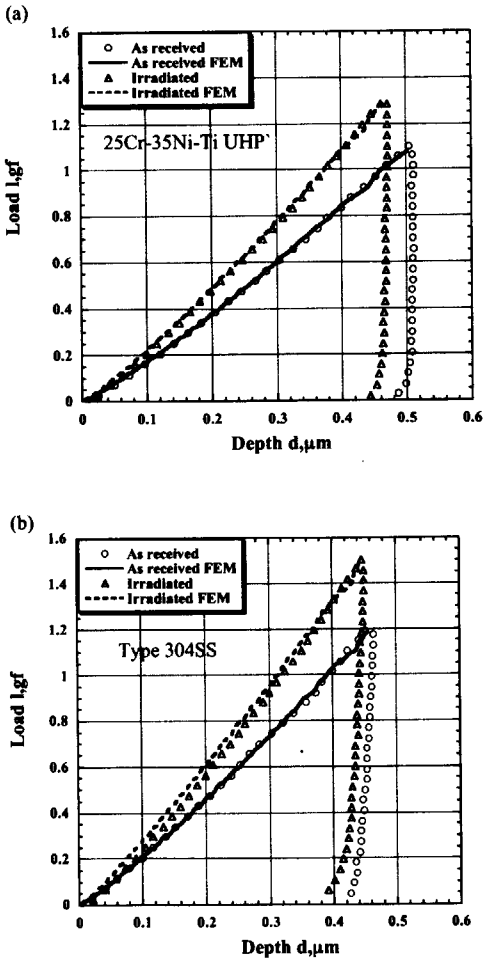

Fig.7.4.2 L-D curves measured using the conical indenter, and the calculated results by the inverse analysis

7.5 SCC Susceptibility of High Chromium Austenitic Stainless Steels for High Burnup Cladding Material

I.Ioka, K.Tachibana, K.Suzuki, M.Tanabe, N.Maruyama, Y.Nanjyo and K.Kiuchi
(E-mail: ioka@popsvr.tokai.jaeri.go.jp*)*

Many fuel cladding tubes made of austenitic stainless steels such as Types 304SS and 316SS had been used in early BWR and PWR plants[1-4]. However, these tubes had been suffered from environmental cracking along with longitudinal direction after operated a few cycles. It was considered to be caused by IASCC (irradiation assisted stress corrosion cracking, mainly IGSCC) at water side[2-4]. Therefore, it is important to suppress on the development of new Fe-Cr-Ni austenitic alloys applied to cladding tubes. A candidate cladding material was developed with conducting the new countermeasure. It is composed to adjust major elements, to make ultra high purity ingot and to modify the metallographic structure by the thermo-mechanical treatment so-called SAR developed by JAERI.

As a basic study for SCC susceptibility of the candidate material after irradiation, a slow strain rate test (SSRT) of specimens which simulated the radiation induced microstructural evolution by each heat treatment of thermal aging (923K×15hr) and low-temperature strain aging (50% cold rolling +723K×1000hr) was carried out. The thermal aging causes the sensitization (depletion of the chromium concentration at grain boundary) of stainless steels which must be the main factor of IASCC. The low-temperature strain aging simulates the possibility of the radiation induced microstructural evolution related to γ phase stability at the practical temperature. The specimens made of the candidate material (25Cr-35Ni-Ti UHP) with high austenite stability at irradiation temperature and commercial materials (SUS304, SUS316). The SSRT in oxygened(dissolved oxygen, DO=8ppm) water was performed at 561K with strain rate of $1x10^{-6}$ s^{-1}. The specimens were examined with SEM after the tests.

Figure 7.5.1 shows the change in fracture elongation of the candidate material and SUS304 after thermal aging. Decreasing rate in the fracture elongation of the candidate material and SUS304 were 50% and 10%, respectively. The fracture surface of the candidate material and SUS304 after the SSRT were shown in Fig.7.5.2. Though the grain boundary fracture was included about 30% in the fracture surface of SUS304, the only dimple pattern was observed in the fracture surface of the candidate material. It is believed that the countermeasure (composition control, purification, γ phase stabilization) for the sensitization is effective.

The change in 0.2% proof stress and fracture elongation of the candidate material and

SUS316 subjected to the low-temperature strain aging were shown in Fig.7.5.3. The decrease in tensile properties such as fracture elongation and 0.2% proof stress of both materials were not observed by the low-temperature strain aging processing. Fig.7.5.4 shows the fracture surface of the candidate material and SUS316. Many minute dimples were observed in fracture surface of the candidate material, which means the high-ductile material. Though no grain boundary fracture was observed in SUS316, the fracture surface of SUS316 was smoother than that of the candidate material. There was large difference in both deformation behaviors. It is considered that the fracture energy of SUS316 is smaller than the candidate material after the low-temperature strain aging.

References:

1) Pashos T.J., "Experience with Stainless Steel as a Fuel Clad Material in Water-Cooled Power Reactors," APED-4260(1963).
2) Ducan R., "Stainless Steel Failure Investigation Program,"GEAP-5530(1968).
3) Milter I., "European Operating Experience," Joint Topical Meeting on Commercial Nuclear Fuel Technology Today," 75-CAN/ANS-100(1975).
4) Pasupathi V. and Lingensmith P., "Investigation of Stainless Steel Clad Fuel Rod Failures and Fuel Performance in Connecticut Yankee Reactor," EPRI NP-2119(1981).

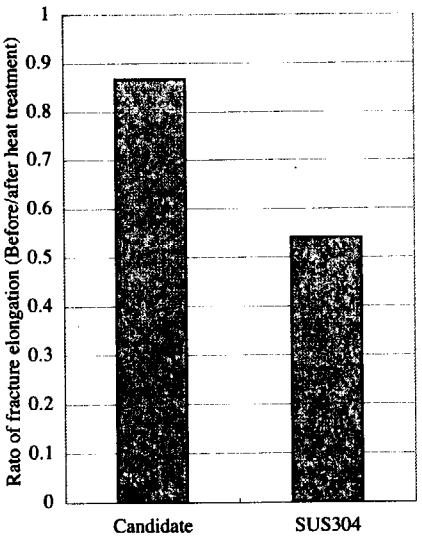

Fig.7.5.1 Change in fracture elongation of the candidate material and SUS304 after thermal aging

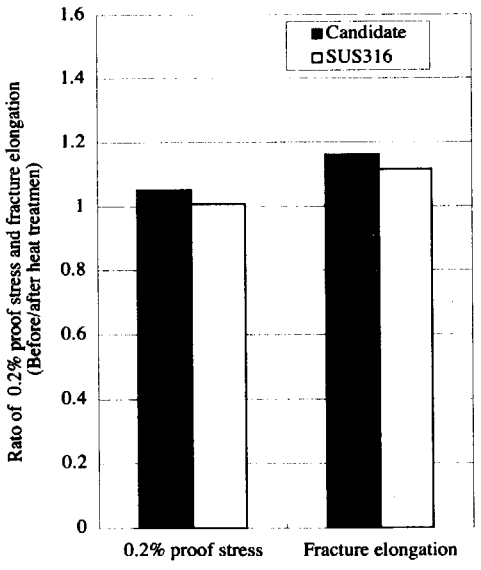

Fig.7.5.3 Change in 0.2% proof stress and fracture elongation of the candidate material and SUS316 subjected to the low-temperature strain aging

(a) Candidate

(b) SUS304

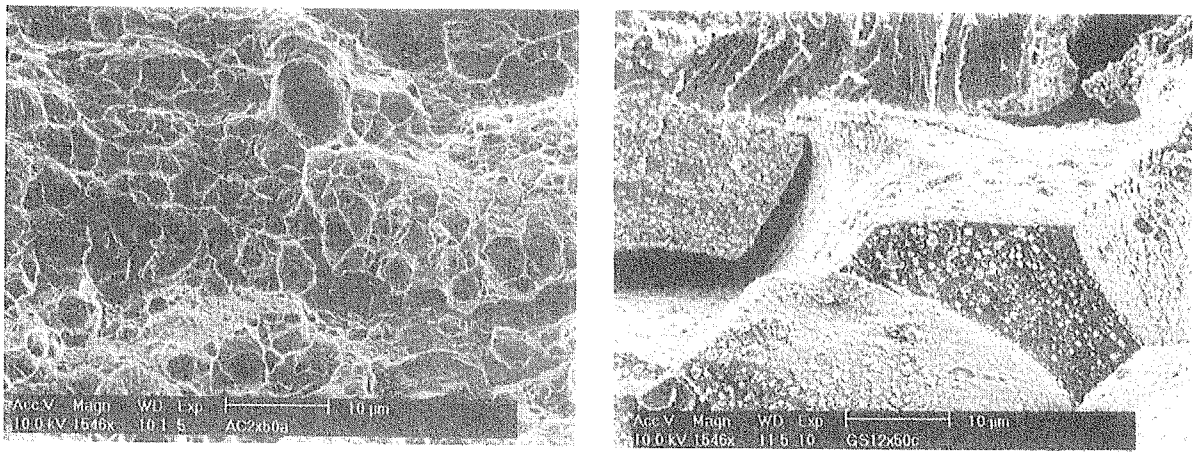

Fig.7.5.2 Fracture surface of thermal aged candidate and SUS304 after SSRT

(a) Candidate

(b) SUS316

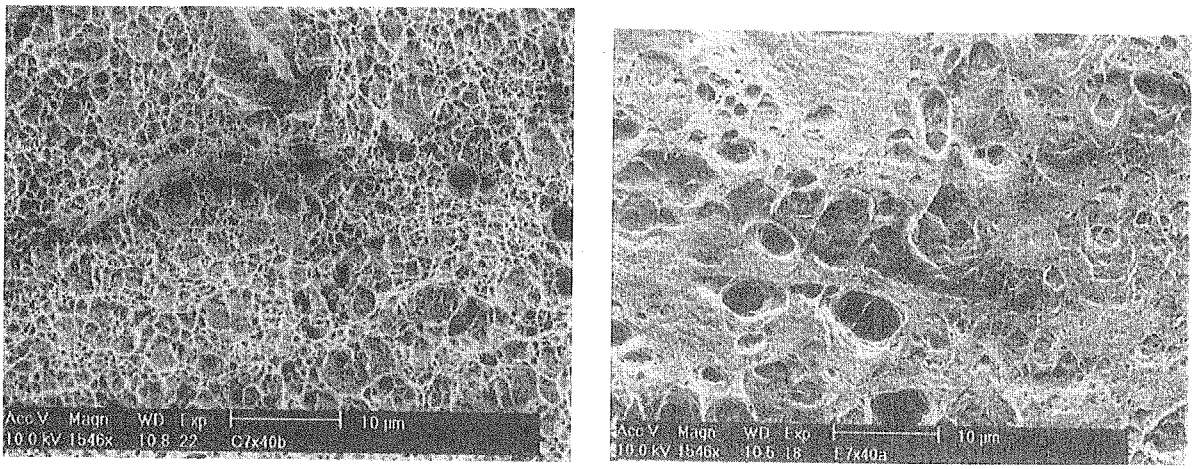

Fig.7.5.4 Fracture surface of low-temperature strain aged candidate and SUS316 after SSRT

7.6 Evaluation of the Advanced Cladding Materials for the Ultra High-Burn Fuels

R. Onishi, K. Kiuchi and M. Takizawa*

(*E-mail*: onishi@galileo.tokai.jaeri.go.jp)

Utilizing advanced MOX fuel which produces a high burn-up of more than 100GWd/t is expected to reduce the cost for maintenance of a nuclear power plant. In order to accomplish the long durability of the fuels under heavy irradiation, the development of a new cladding material is required.

On this background, the research concerning to advanced material for a high burn-up fuel was carried out from 1998 to 2001, and the material candidates were selected from austenitic Fe-Ni-Cr alloy with niobium liner. Thermal and structural behaviors of a fuel on RIA conditions were investigated on the models and parameters shown in Fig. 7.6.1 and 7.6.2. The fluid and heat-conducting analysis models were created for a cooling fluid, pellet, clad, and gap between pellet and clad. Figures through 7.6.3 to 7.6.6 present computed results of the analyses performed under the conditions of increased pellet temperature, decreased heat transfer coefficient due to the release of FP gases in a gap, decreased gap distance due to the pellet swelling, and increased clad temperature induced by the growth of outer oxide film. Figure 7.6.3 and Fig.7.6.4 are the pellet and clad temperatures obtained from the RIA analysis for the 100GWd/t burn-up case. A peak power of 150Kcal/g is attained at about 0.2 sec., which produces the rapid rise of pellet temperature for the initial short seconds. After the reactor is tripped at 0.3sec. and the power is downed to minimum level at 0.4 sec., then the pellet temperature becomes to decrease. As shown in Fig.7.6.4, clad temperature changes with some delays to the pellet temperature. It is supposed that the clad have a damage associated with PCMI within initial few periods, if the temperature is too small to alleviate the stresses induced by pellet swelling. Thermal damage will also be appeared in a clad surface, when clad is hold at high temperature for the long time.

The heat-conducting performances of both zircaroy-2 and stainless steel are shown in Fig.7.6.5 and Fig.7.6.6, respectively. From Fig.7.6.5, a SS 0.4(stainless steel with 0.4mm thickness) is supposed to have the almost same performance as a Zry 0.7 (Zircaroy-2 with 0.7mm thickness).

*Safety Science Research Div., Mitsubishi Research Institute, Inc.

Future research will be focused on a fracture mechanics and corrosion kinetics under heavy irradiation environments. Basic irradiation data concerning to candidate materials required for the computational analysis will be obtained by the irradiation tests.

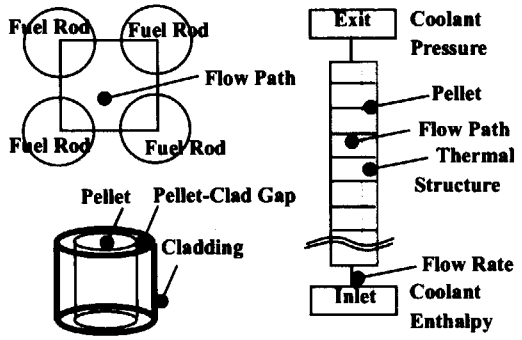

Fig. 7.6.1 Heat-conducting flow model of pellet, clad, gap, and cooling fluid.

Fuel Rod Length	**407cm**
Pellet Dia.	**1.03cm**
Clad Internal/external Dia.	**1.05/1.19cm**
Fuel Rod Pitch	**1.544cm**
Fuel Rods for One Cluster	**81**
Coolant	**Water**
Core Exit Temperature	**287℃**
Operational Pressure	**72.8Kg/cm²a**

Fig. 7.6.2 Major parameters used in heat-conducting analysis for the ABWR claddings.

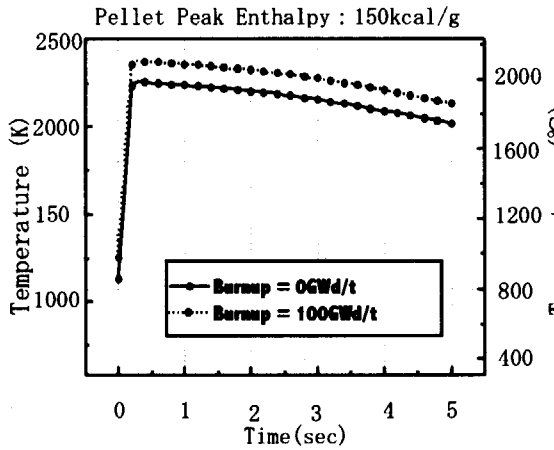

Fig. 7.6.3 Temperature of the pellet center.

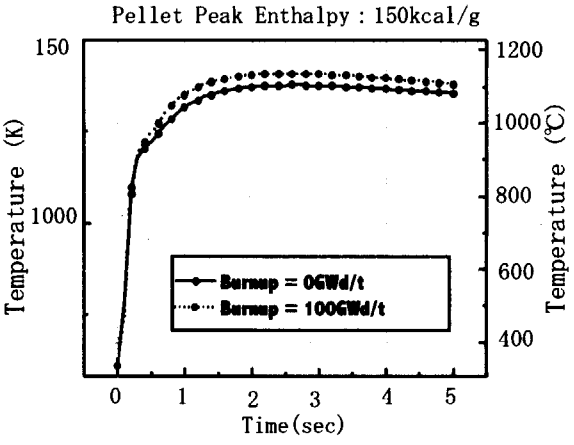

Fig. 7.6.4 Temperature of the clad surface.

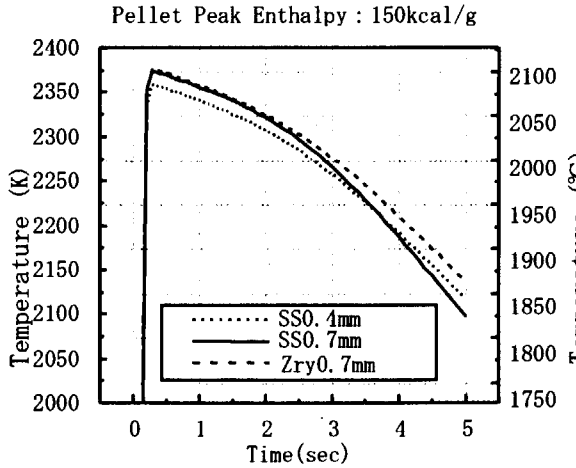

Fig. 7.6.5 Temperature of the pellet center. (SS and Zr Clad)

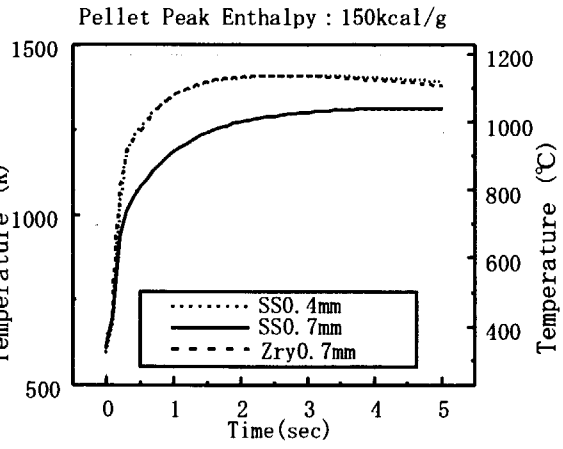

Fig. 7.6.6 Temperature of the clad surface. (SS and Zr Clad)

7.7 Extraction of Mechanical Properties from Load-depth Curve by Using Spherical Indenter and Inverse Analysis

M. Futakawa, T. Wakui*, Y. Tanabe, and I. Ioka
(*E-mail* : futakawa@popsvr.tokai.jaeri.go.jp)

Hardness has not been sufficiently interpreted from the viewpoint of physical meaning yet, although it is broadly used to qualitatively evaluate the change of mechanical properties as a sort of non-distractive technique. In particular, micro-hardness measurements have been used to characterize mechanical properties in metals induced by irradiation, because the micro-hardness is the simple test applicable to small volumes of irradiated materials. As for the indentation technique with a depth sensing measuring system, the authors present the technique used the indentation technique combined with numerical calculation to identify the material constants describable the stress-strain relationship. Inverse analyses on the loading and unloading curves measured by the instrumented indentation machine with the hemispherical indenter were carried out using Kalman filter. The technique was applied to aluminum alloy A5056 and nickel based alloy Inconel 600. The simulation with the estimated material constants was carried out to compare with the deformation under uniaxial tensile loading.

The inverse analysis was carried out using an explicit FEM code, LS-DYNA, which enables us to robustly analyze a large deformation accompanying with a large strain gradient and contacting behavior. In the analysis, the indenter and specimen were treated as axi-symmetric two-dimensional bodies to take calculative efficiency into account. The shapes of indenter apexes were varied to examine the shape effect on the estimated material constants: conical and hemispherical ones. The mesh size was given to be sufficiently fine to keep accuracy: the minimum element size around the apex contacting zone was 0.05 mm. The total number of the elements used in the model was 1509. The constitutive equation of the material installed into the model was assumed to be a simple power-law that is generally believed to be applicable to normal metallic materials. Hereafter, we have to identify the following material constants; $\mathbf{E}, \mathbf{s}_y, \mathbf{A}$ and $\mathbf{n}$ through the inverse analysis on the load-depth, L-D, curve.

The flow chart of the identification with inverse analysis is illustrated in Fig. 7.7.1. Here, $\mathbf{C}$ and $\mathbf{E}$ are determinants of material constants and estimated errors of material constants. $\mathbf{Z}$ and $\mathbf{Y}$ are determinants of experimental and calculated values on L and dL/dD. $\mathbf{R}$ is determinant of error in measuring systems. S_{max} is the maximum number of steps in the divided L-D curve. $\mathbf{H}$ is $\partial\mathbf{Y}/\partial\mathbf{C}$. The procedure of the inverse analysis is as follows.

(1) $\mathbf{C}_0, \mathbf{E}_0, \mathbf{R}$ and S_{max} are input as initial values.

(2) $\mathbf{Z}_s$ of L and dL/dD at step S is input.

(3) $\mathbf{Y}_s$ of L and dL/dD at step S is calculated by FEM code.

(4) The estimated values on **C** and **E** are given by the following equation of Kalman filter using each value, $\mathbf{C}_s$, $\mathbf{E}_s$, $\mathbf{Y}_s$, $\mathbf{H}_s$ and **R** at step S,

$$\mathbf{C}_S = \mathbf{C}_{S-1} + \mathbf{E}_S\mathbf{H}_S\mathbf{R}^{-1}\left(\mathbf{Z}_S - \mathbf{Y}_S\right) \qquad (7.7.1)$$

$$\mathbf{E}_S = \left(\mathbf{E}_{S-1}{}^{-1} + \mathbf{H}_S{}^T\mathbf{R}^{-1}\mathbf{H}_S\right)^{-1} \qquad (7.7.2)$$

(5) Go back to (7.7.2) and repeat the process up to S_{max}. Finally we can obtain the optimal values $\mathbf{C}_{Smax}$ estimated at final step S_{max}.

In order to investigate the effects of the shape of indenter on the estimated material constants, the numerical simulations were carried out systematically by using the FEM model. The simulated materials have the material constants that are hardly distinguished through the L-D curve using the conical indenter among them as reported by Cheng, et al [1]. However, the L-D curves obtained by the hemispherical indenter reflect sufficiently the differences of their material constants. That is because the plastic zone develops analogously in the case of the conical indenter but changes un-analogously along to the depth in the case of the hemispherical indenter. So that, the different stress distribution is formed with the indentation depth under the hemispherical indenter. As long as using the conical indenter, the contact angle between the indenter and the material is constant independently of the indent depth. On the other hand, the contact angle changes as increasing the indent depth in the case of the spherical indenter. That is, to use spherical indenter has the same effect as to use the indenters with different apex angles that are applicable for identification of material constants [2]. The load and elongation curves were measured from the uniaxial tensile test using plate and rod specimens and were compared with the calculated results using the FEM models that have the estimated material constants. Figure 7.7.2 shows the load and elongation curves up to the onset of necking behavior. The calculated results give an appropriate agreement with the experimental one. The accuracy between calculated and experimental results could be dependent on the sensitivity of the indentation load and depth curve to the size of the indentations. So-called size effect has been explained in terms of a number of factors such as the weakening effect of grain boundaries, the influence of the anisotropy, and the trend towards isotropic deformation at small grain sizes, etc. In order to give the high accuracy on the evaluation using this method, we have to consider the size effects. Nevertheless, the presented method is adequately useful to estimate the constitutive equation describable the relationship between strength and elongation, in particular for a small area.

References

1) Y. Cheng and C. Cheng, " Can stress-strain relationships be obtained from indentation curves using conical and pyramidal indenters ?", J. Mater. Res., 14 (9), pp.3493-3496, (1999).

2) M. Futakawa, T. Wakui, Y. Tanabe, and I. Ioka, "Indentation of the constitutive equation by the indentation technique using plural indenters with different apex angles", J. Mater. Res., 16 (8), (2001).

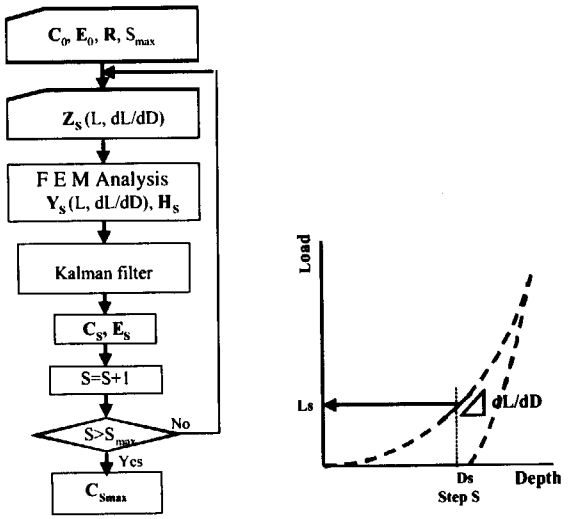

Fig. 7.7.1 Flow of inverse analysis for indentation

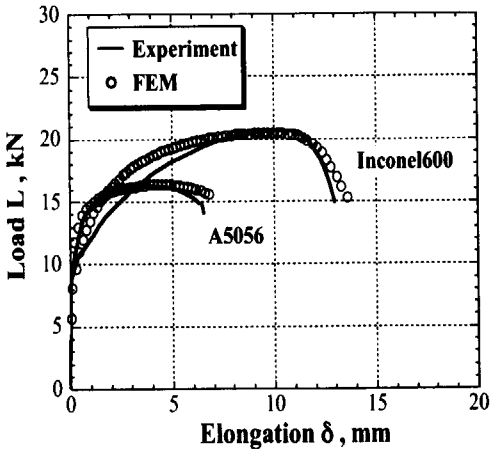

Fig.7.7.2 Comparison of load-elongation curves between experimental and calculated results

7.8 Fatigue Strength Reduction Factor of T-joint Weld with Incomplete Penetration

H. Nishi and M. Nakahira

(*E-mail*: nishi@popsvr.tokai.jaeri.go.jp)

The vacuum vessel (VV) of ITER is designed adopting double-walled structure and composed of inner and outer shells jointed by welded stiffening ribs. Some welds are not full penetration joints, which are not qualified in the conventional design standards for light water reactor. It is important to develop the integrity evaluation method for the weld based on proper structural design code. Namely, weld joint efficiency and fatigue strength reduction factor for primary stress should be developed. As for the VV, low cycle fatigue caused by the cyclic electromagnetic and thermal stresses is identified to be the dominant failure modes. Evaluation of the effect of weld defects on the fatigue strength is most important problem from view points of fatigue design related to welded structures. Therefore, fatigue life of the weld was evaluated based on fracture mechanics to discuss the effect of weld defects on the fatigue strength.

In this study, the weld was T-joint which is employed for connection between the outer shell and rib. The T-joint was welded by the MAG welding after the TIG welding for a root pass and included incomplete penetrations(IP) at the both side root faces without root opening gap as shown in Fig.7.8.1. The welding process and condition are summarized in Fig.7.8.2. Fatigue test was carried out using as-welded large specimen with a hydraulic fatigue machine at frequency 0.5Hz. Crack growth was monitored with taking photos of cracks during the fatigue test in order to obtain fatigue crack propagation rates of the weld. Fatigue crack propagation test of the weld metal using CT specimen was also carried out to compare the crack propagation rates of the weld.

In order to evaluate crack propagation rates in engineering structures, stress intensity factor range, ΔK, is widely used. In this study, ΔK was used as a correlation parameter and was calculated

with FEM analysis taking account for linear misalignment of as-welded large specimen. Figure 7.8.3 shows the results of stress intensity factor divided by applied stress, K/σ, at the maximum load obtained by the FEM analysis. The K/σ of right side crack was smaller than that of left side crack owing to the bending moment caused by the linear misalignment, though the depth of the right side crack was larger than that of left side crack as indicated in Fig.7.8.1. The K/σ of right side crack gradually decreased with increasing the depth of left side crack.

The fatigue specimen of weld fractured at the IP and the crack propagated through the weld metal perpendicularly to the loading direction. As shown in Fig.7.8.4, the crack propagated almost from the left side IP because of the large stress intensity factor range. The crack propagation rates, da/dN, are shown in Fig.7.8.5. In this figure, the da/dN of the weld metal are also indicated to compare with those of the weld. The da/dN of the weld were corresponding to those of the weld metal for both side cracks, while the ΔK and the depths of right side cracks were smaller than those of the left side cracks.

The fatigue strength of the weld is shown in Fig.7.8.6 making comparison with that of smooth specimen. The fatigue strength of the weld was extremely lower than that of smooth specimen and fatigue strength reduction factor K_f was approximately 11. In order to evaluate fatigue life of the weld and the effect of IP on the fatigue strength, the fatigue life of weld were analyzed based on fracture mechanics using the da/dN of the weld. The calculation was performed not only for the specimen used for the fatigue test but also for the specimen contained IP of 1 mm depth. The evaluated fatigue life for the used fatigue specimen was corresponding to the experimental fatigue life. So the fatigue life could be predicted based on the fracture mechanics. As for the specimen contained IP of 1 mm depth, the fatigue strength reduction factor K_f was about 7, while the fatigue life were several times as long as those of the fatigue specimens. The fatigue strength of weld with the IP was extremely decreased against the smooth specimen even if the depth of IP became small.

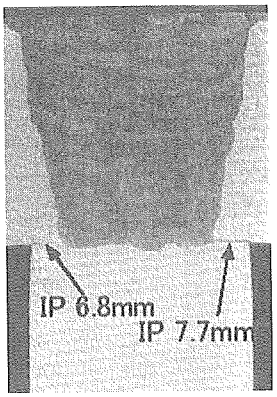

Fig.7.8.1 Macro-structure of weld.

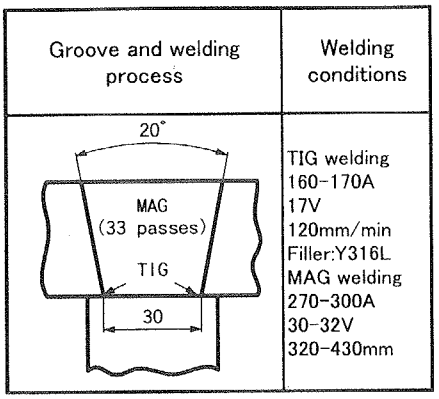

Fig.7.8.2 Welding processes and conditions.

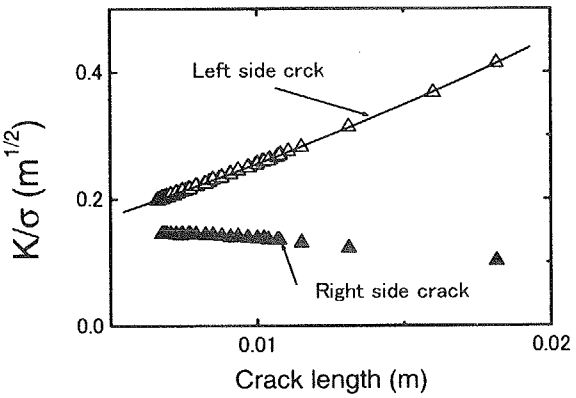

Fig.7.8.3 Stress intensity factors obtained by FEM.

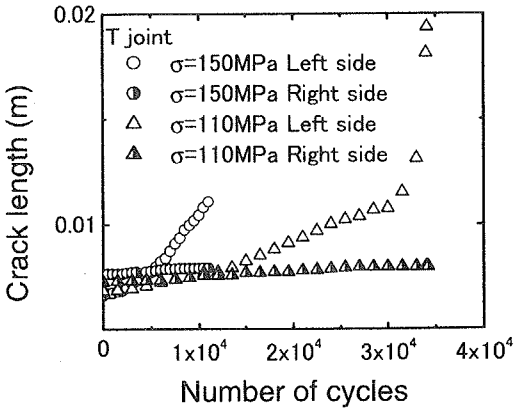

Fig.7.8.4 Crack propagation curves of weld.

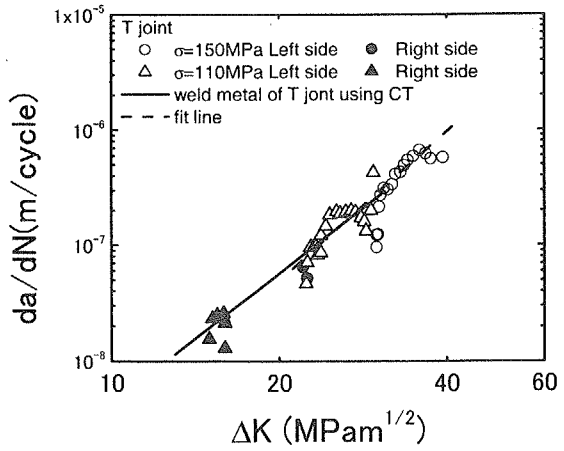

Fig.7.8.5 Crack propagation rates of weld.

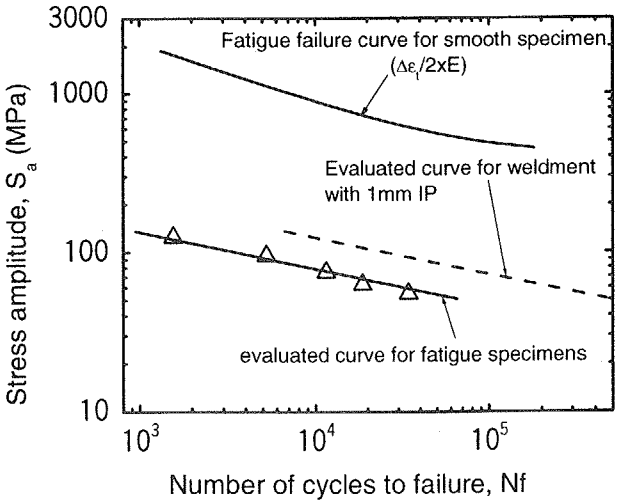

Fig.7.8.6 Comparison of fatigue lives.

7.9 Operation and In-service Inspection of Demonstration Testing Equipments for Acid Recovery Evaporator and Dissolver

T. Yanagihara and K. Kiuchi
(*E-mail* : yanagi@galileo.tokai.jaeri.go.jp)

In this paper, we describes the operation and in-service inspection (ISI) from Feb. 18, to Mar. 1, 2002 for demonstration testing equipments for the Rokkassho Reprocessing Plant (RRP) have been operated at Ehime Works in Sumitomo Chemical Co., Ltd. The 4th ISI of the mock-up of acid recovery evaporator was done after 6,914 hours operation from the third in-service inspection. The third in-service inspection of the dissolver was done after 7,177 hours operation.

Acid Recovery Evaporator

After the 3rd ISI, the four heat conducting tubes of an evaporator portion are evaluated with the precise analysis of corrosion behavior by a destructive method. The results obtained by the ultrasonic immersion measurement coincident well with those obtained by a destructive method using an optical microscope.

The operation parameter of above evaporator was examined for estimating the testing conditions at steady-state operation. The steam temperature of evaporator was controlled at 98, 96, 94 and 92℃ for a short time respectively. The relationship between the feed flow rate and steam temperature is shown in Fig.7.9.1. By decreasing the feed flow rate from 178 to 112kg/h, the circulation flow rate was decreased from 860 to 790kg/h, and the flow rate in by-pass tube was increased from 21 to 667kg/h.

To investigate the corrosion behavior of evaporator portion of the evaporator at the normal operating conditions of the RRP's, The steam temperature of evaporator was controlled at 94℃ and the chemical composition of nitric acid solution in the evaporator was controlled as following: 9N HNO_3, 1200mg/l Fe^{3+}, 300mg/l Cr^{3+}, 5mg/l Ru^{3+} and 200mg/l V^{3+} for simulating precisely the solution of the RRP 's. The seven heat conducting tubes consist of three old tubes and four new tubes of same material of type R-SUS304ULC.

During the operation of the evaporator, we monitored the chemical composition of nitric acid solution in the evaporator. The corrosion rate of heat conducting tubes estimated by Ni ion dissolved from heat conducting tubes is shown in Fig.7.9.2. The corrosion rate of heat

conducting tubes is increased two times by changing the operating conditions that are steam temperature (from 100℃ to 94℃) and V concentration (from 50mg/l to 200mg/l).

The 4th ISI was done after 6,914 hours operation from the 3rd ISI. Comparing with data of old tubes, the corrosion behavior of new tubes was different due to the difference in steam temperature and V contents in the test solution as shown in Fig.7.9.3. Although the corrosion rate at part A was lowered, it at part B was enhanced due to the high formation rate of oxidizer V ions.

Dissolver

The dissolver has a steam jacket ($0.19m^2$) made of reprocessing grade zirconium with 8mm in thickness. The liquid volume of the dissolver is 170L. The dissolver was operated at 107℃ of a boiling point of testing solution. The steam temperature is 165℃ under 0.71MPa. The steam flow rate is about 30kg/h. The nitric acid evaporated from the dissolver is cooled in a condenser and dropped in the dissolver. The testing solution is 3N nitric acid solution contains 142g/l $Al(NO_3)_3$, 1200mg/l V^{5+}, 1000mg/l Ce^{4+} and 1500mg/l Ru^{3+} for simulating the dissolver solution of the reprocessing plant. The solution was replaced every three months. The compositional change of the solution was little, through the three months. After 7,177 hour operation, the inside wall surface was covered with an adhered film and some deposits. These were identified as a mixture of ruthenium oxide and vanadium oxide deposited from the dissolver solution. In the third in-service inspection, Radiographic test and dye penetrating test were carried out along the welding lines for detecting defects such as cracking. There are no defects in tested parts. The wall thickness of the dissolver was measured by ultrasonic testing using 10MHz sensor. The wall thinning was not detected.

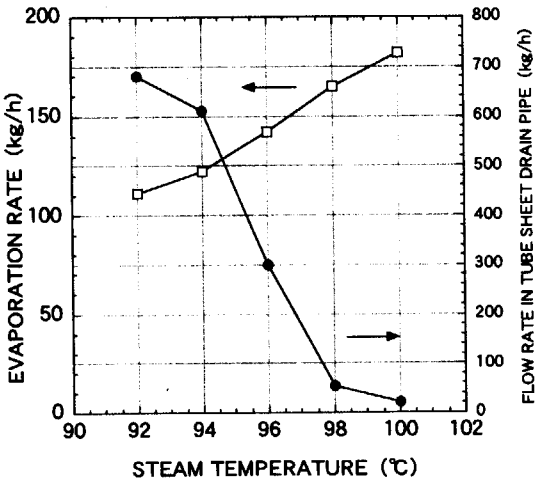

Fig. 7.9.1 The relationship between each flow rate in the mock-up evaporator and steam temperature obtained for optimizing the operation parameter

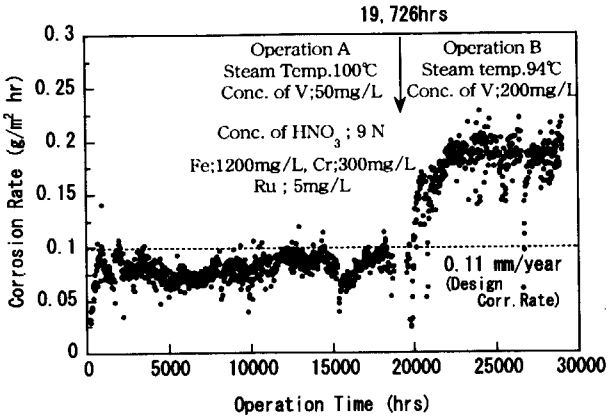

Fig. 7.9.2 The average corrosion rate of heat transfer tubes estimated from the Ni contents dissolved in the concentrated nitric acid

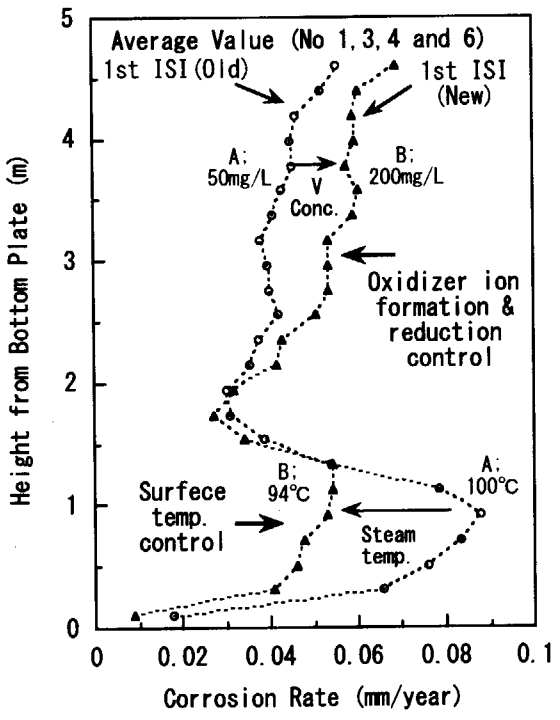

Fig. 7.9.3 The difference in corrosion rates between new tubes obtained by 4th ISI and old tubes obtained by 1st ISI

7.10 Effects of a Heat-transfer on Corrosion of Zirconium in a Boiling Nitric Acid Solution

C. Kato and K. Kiuchi
(*E-mail* : multi@popsvr.tokai.jaeri.go.jp)

It is required that equipment materials used in the purex type nuclear fuel reprocessing plants have the excellent corrosion resistance in boiling nitric acid solutions with high corrosion potentials caused by oxidizing ions dissolved from spent nuclear fuels. Zirconium has been the excellent corrosion resistance in nitric acid solutions. So, zirconium has considered to be a most promising material for very corrosive condition in the nuclear fuel reprocessing plants recently. However, zirconium has the susceptibility to stress corrosion cracking (SCC) in fuming nitric acid solution and in nitric acid solution below azeotrope concentration with high corrosion potential. In addition, the oxidizability of nitric acid is enhanced by boiling heat transfer, and there is possibility that the corrosion resistance of zirconium on a boiling heat transfer surface is lower.

We have studied the corrosion resistance on a boiling heat transfer surface, REDOX potential of nitric acid solutions on a boiling heat transfer surface and SCC initiation potential of zirconium on a boiling heat transfer surface.

The effects of heat-transfer on the corrosion of zirconium was examined in boiling nitric acid solutions with various concentrations. Corrosion mass losses and electrochemical polarization curves were measured on the heat-transfer and isothermal surfaces in the solutions. Under isothermal conditions, solution temperature and surface temperature of specimen are equal. Under heat-transfer conditions, surface temperature, T_{surf}, of specimen is higher than boiling points of solutions. Fig.7.10.1 shows Schematic diagram of heat-transfer test apparatus for corrosion, electrochemical tests. Under measurement of polarization curve, both ends of liquid junction bridge were installed porous glass filter and it was enclosed concentrated nitric acid solution, 14.4 mol/dm^3 HNO_3 in order to prevent boiling of liquid junction in bridge and unstable of liquid junction

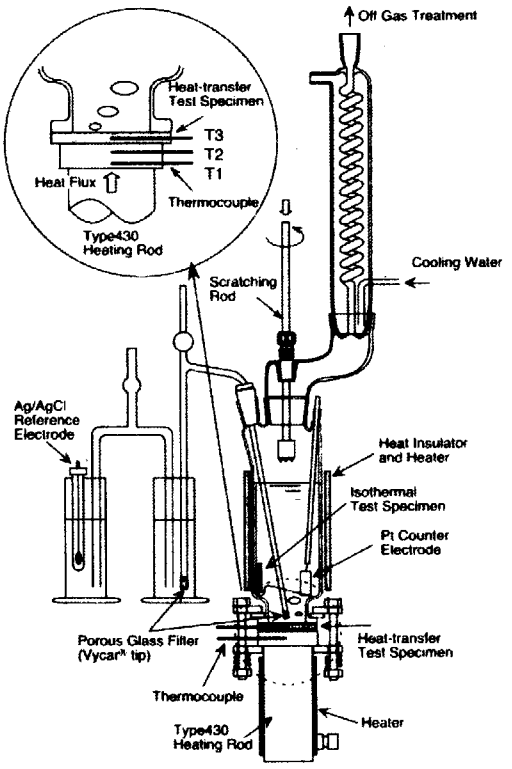

Fig.7.10.1 Schematic diagram of heat-transfer test apparatus for corrosion, electrochemical and scratch tests.

under strong boiling condition.

Figure 7.10.2 shows relationship between concentration of nitric acid and corrosion rate in boiling nitric acid solutions under heat-transfer and isothermal conditions. It was found that the corrosion rate of zirconium was higher on the heat-transfer surface than that on the isothermal surface. It is considered that the effect of boiling heat transfer appeared. In other word, it is assumed that the oxidizability of nitric acid on boiling heat transfer surface is enhanced by higher surface temperature than boiling point in nitric acid solution. However, the corrosion rate of zirconium on boiling heat transfer surface in 14mol/dm^3 nitric acid solution was less than 0.01mm/year and there was no the localized corrosion as intergranular corrosion. Zirconium had the excellent corrosion resistance on boiling heat transfer surface.

To understand the effect of boiling heat transfer, we measured redox potential of nitric acid solution on boiling heat transfer surface by electrochemical technique. It is index of oxidizability of nitric acid solution. Figure 7.10.3 shows the relationship between surface temperature, T_{surf}, and redox potential, E_{Pt}, of Pt electrode under heat-transfer and isothermal conditions in nitric acid solutions with different concentrations. The redox potential on boiling heat transfer surface was subject to surface temperature (heat flux) and boiling and it was higher than potential in boiling point. The change rate of potential against temperature on boiling heat transfer surface (3.8mV/K) was twice higher than it on isothermal surface (1.7mV/K). From the results, it made clear that the redox potential of nitric acid solution have the effect of nucleate boiling in addition to the effect of surface temperature. This difference appeared over 6 mol/dm^3 HNO_3. In a general way, the redox potential of nitric acid solution is determined by the equilibrium reaction of nitric acid and nitrous acid (Eq.1).

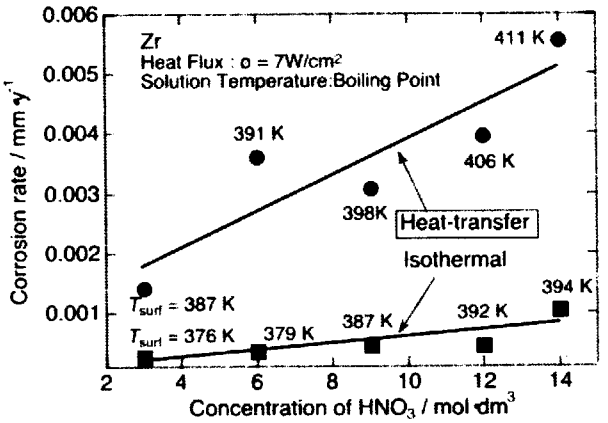

Fig.7.10.2 Relationship between concentration of nitric acid and corrosion rate in boiling nitric acid solutions under heat-transfer and isothermal conditions. Under isothermal conditions, solution temperature and surface temperature, T_{surf}, of specimen are equal. Under heat-transfer conditions, T_{surf} is higher than boiling points of solutions.

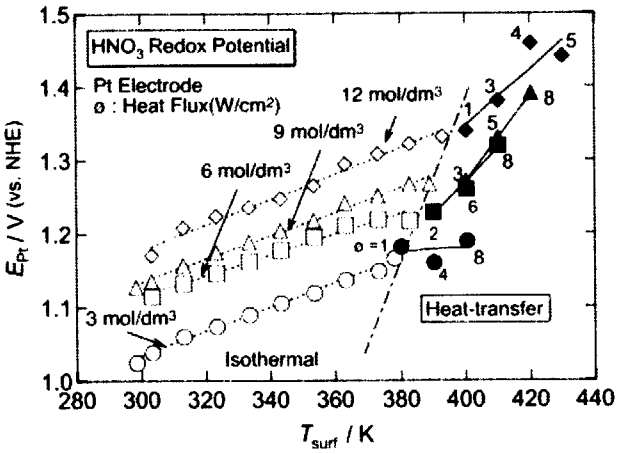

Fig.7.10.3 Relationship between surface temperature, Tsurf, and redox potential, E_{Pt}, of Pt electrode under heat-transfer and isothermal conditions in nitric acid solutions with different concentrations.

$$HNO_3 + 2H^+ + 2e^- = HNO_2 + H_2O \quad (1)$$

Therefore, the redox potential of nitric acid solution is determined in equation by Nernst's low (Eq.2).

$$E = E_0 - 4.605\frac{RT}{2F}pH + \frac{RT}{2F}\ln(\frac{a_{HNO_3}}{a_{HNO_2}}) \quad (2)$$

From the above equation, it indicates that the redox potential of nitric acid solution with a constant nitric acid concentration is dependent on temperature and nitrous acid concentration.

We measured polarization curve of Pt electrode on boiling heat transfer surface in nitric acid solution in order to consider in redox reaction of nitric acid solution on boiling heat transfer surface. From the results of polarization curve of Pt electrode (Fig.7.10.4), we estimated that increasing redox potential on boiling hear transfer surface was caused by accelerating heat decomposition of nitrous acid and it cause a rise HNO_3/HNO_2 equilibrium potential deciding potential of nitric acid solution.

This was caused to raise thermal decomposition (Eq.3 and 4) by temperature.

$$2HNO_2 = NO_2 + NO + H_2O \quad (3)$$

$$HNO_3 + HNO_2 = 2NO_2 + H_2O \quad (4)$$

The increased oxidization potential on a boiling heat-transfer surface was attributed to the reduction of nitrous acid concentration by the thermal decomposition on the surface and the removal of the decomposition product from solution by boiling bubbles.

We examined the breakdown potential of zirconium on boiling heat transfer surface by electrochemistry method. Figure 7.10.5 shows the effect of surface temperature on anode polarization curves of zirconium under a boiling heat-transfer and isothermal surface in 9 mol/dm^3 nitric acid solutions. The current density of passive state on boiling heat transfer surface was about 5 times showed larger than value on

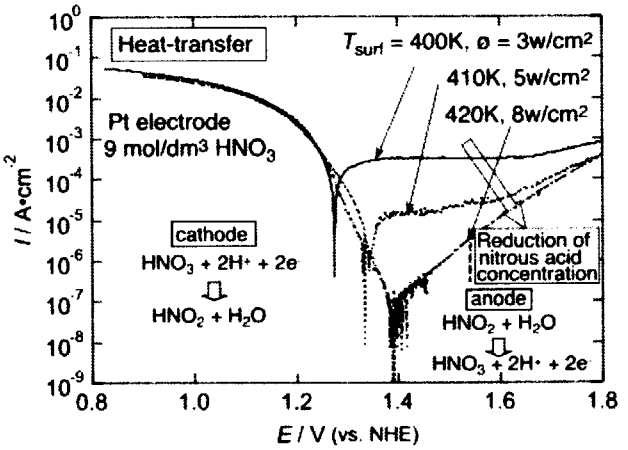

Fig.7.10.4 Effect of surface temperature, T_{surf}, on polarization curves of Pt electrode under heat-transfer conditions in boiling nitric acid solutions.

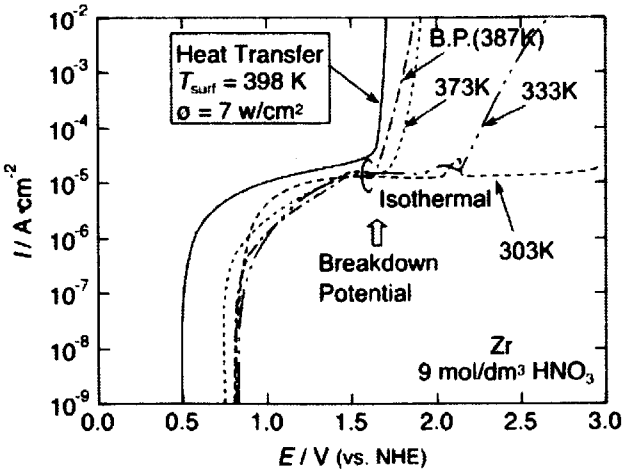

Fig.7.10.5 Effect of surface temperature, T_{surf}, on anode polarization curves of zirconium under heat-transfer and isothermal conditions in nitric acid solutions.

boiling isothermal surface. This conformed to value of corrosion rate on boiling heat transfer surface. A breakdown potential on zirconium related to SCC initiation potential was about 2 V (vs. NHE) at 303K in 9 mol/dm^3 nitric acid solution, and it decrease according to increasing temperature. Figure 7.10.6 shows the relationship between surface temperature and breakdown potential of primary passivity on zirconium under heat-transfer and isothermal conditions in nitric acid solution. The effect of surface temperature to breakdown potential of zirconium was large, however, it was small by increasing concentration of nitric acid.

In a point of view of SCC initiation in unclear reprocessing process, it was possible that SCC of zirconium on boiling heat transfer surface having high potential so that corrosion potential of zirconium was close to the redox potential of nitric acid solution by existence of Pu, Ru and Np. Therefore, we considered the susceptibility of SCC on zirconium in unclear reprocessing process.

Figure 7.10.7 shows the relationship between breakdown potential of zirconium and redox potential of nitric acid under heat-transfer and isothermal conditions in nitric acid with different concentrations. The redox potential of 12 mol/dm^3 nitric acid on a boiling heat-transfer surface was very close to the breakdown potential of primary passivity of zirconium. This suggests the initiation of SCC on a boiling heat-transfer surface in a nuclear fuel reprocessing.

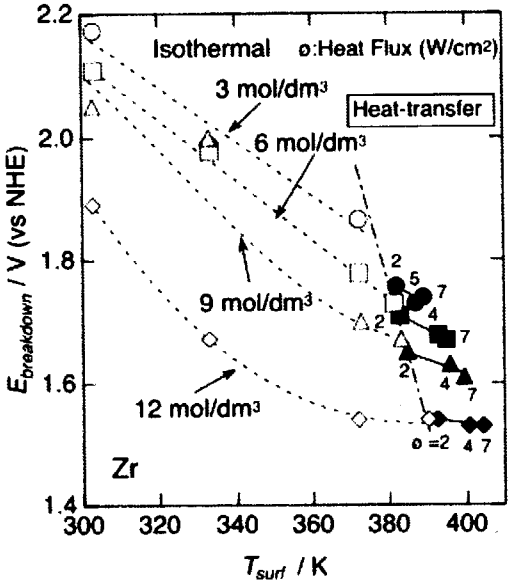

Fig.7.10.6 Relationship between surface temperature, *T*surf, and breakdown potential of primary passivity on zirconium, $E_{breakdown}$, under heat-transfer and isothermal conditions in nitric acid with different concentrations.

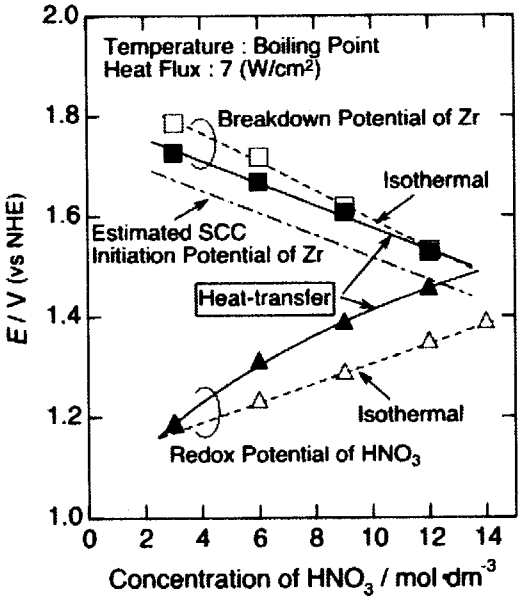

Fig.7.10.7 Relationship between breakdown potential of zirconium and redox potential of nitric acid under heat-transfer and isothermal conditions in nitric acid with different concentrations.

7.11 Thermodynamic Study on Redox Reactions of Boiling Nitric Acid Solutions

C. Kato and K. Kiuchi
(*E-mail* : multi@popsvr.tokai.jaeri.go.jp)

It is required that equipment materials used in the purex type nuclear fuel reprocessing plants have the excellent corrosion resistance in boiling nitric acid solutions with high corrosion potentials caused by oxidizing ions dissolved from spent nuclear fuels. However, it is known that the corrosiveness of material increase so that the oxidizability of nitric acid solution increase on boiling heat transfer surface. In addition, it is reported that oxidizability of boiling nitric acid solution depends on removed NO_x from a system, because the corrosion behaviors of stainless steel in 65% nitric acid depend on the type of cooling condenser. Therefore, in order to understand corrosion of metals in nitric acid solutions, it is necessary to know the generation mechanism of high equilibrium potential in the solutions, especially under boiling conditions. The purpose of this study is to understand the mechanism of redox potential in nitric acid solutions on a boiling heat transfer surface by Raman spectroscopy and thermodynamic calculation.

Existing nitrogen oxides in nitric acid solutions were first analyzed by Raman spectroscopy. It is reported that the nitrogen oxides measured by Raman are NO_3^-, un-dissociated HNO_3 (N-OH bond), HNO_2 and NO_2. Figure 7.11.1 shows the effect of solution temperature on Raman spectrum of nitric acid solutions. The Raman spectroscopic analysis showed that the existing amount of un-dissociated HNO_3 increased with increasing nitric acid concentration and solution temperature and the existing amount of NO_2 also increased by thermal decomposition. The peak of HNO_2 couldn't be observed.

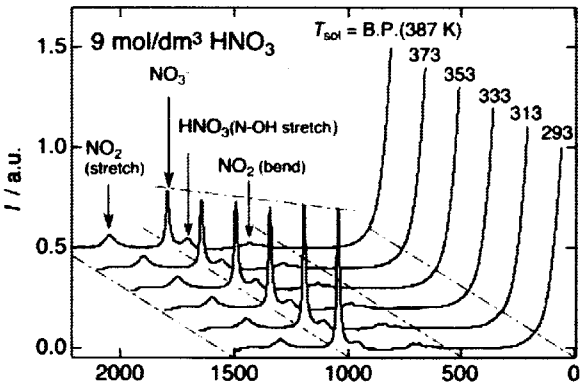

Fig.7.11.1 Effect of solution temperature, T_{sol}, on Raman spectrum of nitric acid solutions with different concentrations.

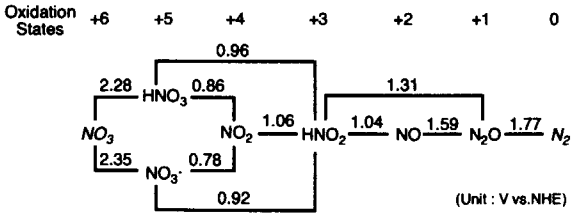

Fig.7.11.2 Standard potential diagram for nitrogen in nitric acid solution at 298K.

In a general way, the redox potential of

nitric acid solution is mixed potential determined by various equilibrium reactions between various nitrogen oxides by thermal decomposition. Figure 7.11.2 shows standard potential diagram for nitrogen in nitric acid solution at 298K. The redox potential of nitric acid solution is mainly determined by HNO_3/HNO_2 equilibrium.

Then existing amount of nitrogen oxides were examined by thermodynamic calculation using the SOLGASMIX software. Table 7.11.1 shows the combinations of nitric oxides for thermodynamic calculation in this study. We categorized combinations from Type1 to Type6 to disregard very few chemical species that could be produced thermodynamically, because the reactions rate of their thermal decomposition was slow. Type6 was the combination to consider oxygen produced by thermal decomposition of nitric acid. (Eq.1)

$$4HNO_3 = 4NO_2 + O_2 + 2H_2O \quad (1)$$

Figure 7.11.3 shows the relationship between temperature and concentration of compounds in 9 mol/dm^3 nitric acid solution (initial HNO_2: $5x10^{-2}$ mol/dm^3) calculated by thermodynamic software SOLGASMIX. The thermodynamic calculation showed that the important nitrogen oxides in nitric acid solutions are HNO_3, NO_3^-, HNO_2, NO_2, and NO (Type5). The thermodynamic calculation also showed that it was possible to produce O_2 by thermal decomposition of nitric acid (Type6). However, it indicated that the

Table 7.11.1 Combinations of nitric oxides for thermodynamic calculation in this study.

	Type1	Type2	Type3	Type4	Type5	Type6
Major Compounds	H_2O H^+ NO_3^- HNO_3 HNO_2 NO_2 NO	H_2O H^+ NO_3^- HNO_3 HNO_2 NO_2 NO	H_2O H^+ NO_3^- HNO_3 HNO_2 NO_2 NO	H_2O H^+ NO_3^- HNO_3 HNO_2 NO_2 NO	H_2O H^+ NO_3^- HNO_3 HNO_2 NO_2 NO	H_2O H^+ NO_3^- HNO_3 HNO_2 NO_2 NO
Minor Compounds	N_2O_4 N_2O_3	N_2O_4 N_2O_3	N_2O_4 N_2O_3	N_2O_4 N_2O_3		
Disregard Compounds	N_2O NO_3 NO_2^- $H_2N_2O_2$ $N_2O_2^{2-}$	N_2O NO_3 NO_2^- $H_2N_2O_2$ $N_2O_2^{2-}$	N_2O			
Final Compounds	N_2					
Final Compounds & Thermal Decomposition	O_2					O_2

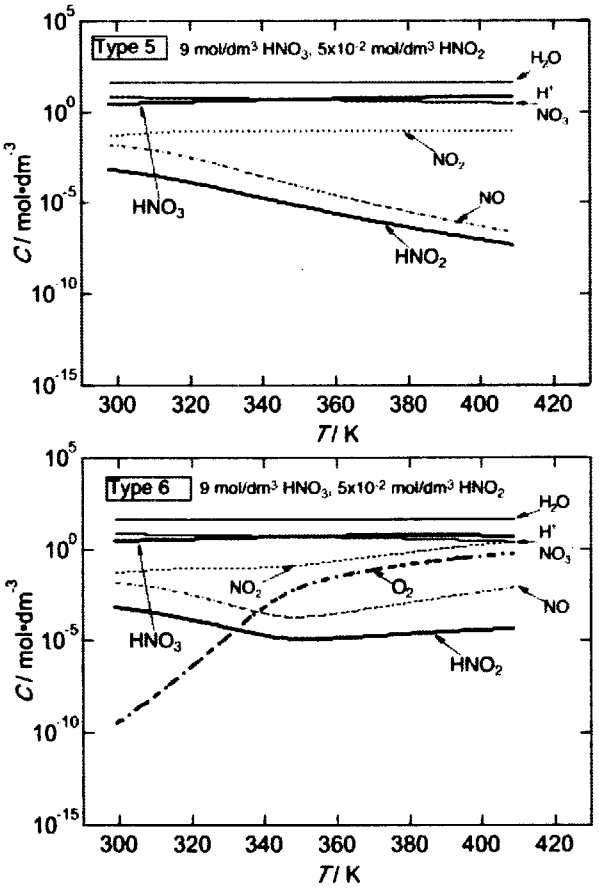

Fig.7.11.3 Relationship between temperature, T, and concentration of compounds, C, in 9 mol/dm^3 nitric acid solution (initial HNO_2 : $5x10^{-2}$ mol/dm^3) calculated by thermodynamic software SOLGASMIX.

influence of temperature on nitrous acid concentration wasn't real behavior. Therefore, it was assumed that it was unnecessary to consider the oxygen by thermal decomposition of HNO_3 so that its reaction rate was extremely slow. It was clear that the combination of important nitrogen oxides, which determined redox potential of nitric acid solution, was Type5 (Fig.7.11.5).

It is reported that boiling heat transfer enhances the oxidizability of nitric acid. Therefore, we considered the bubble gas phase with H_2O, HNO_3, NO_2 and NO by boiling. Figure 7.11.4 shows schematic diagram of thermodynamic model for boiling nitric acid solution. As compared with the model without bubble gas phase, the concentration of nitrous acid was decreased by a formation of bubble gas phase. Figure 7.11.6 shows HNO_3/HNO_2 equilibrium potential calculated by boiling model. The potential calculated accorded closely with measured potential. The increased oxidization potential on a boiling heat-transfer surface was attributed to the reduction of nitrous acid concentration by the thermal decomposition on the surface and the removal of the decomposition product from solution by boiling bubbles.

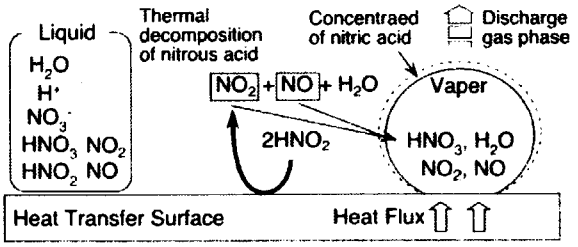

Fig.7.11.4 Schematic diagram of thermodynamic model for boiling nitric acid solution.

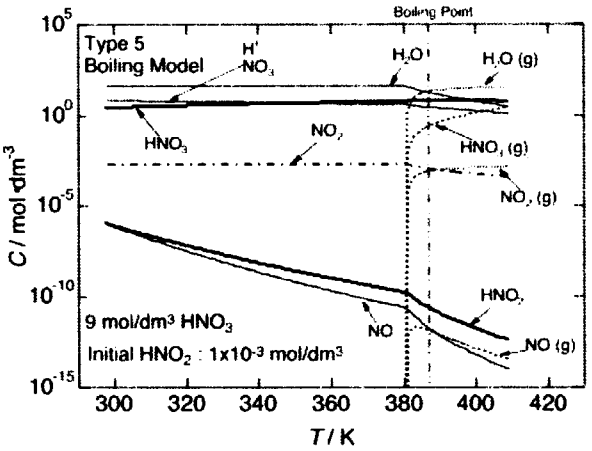

Fig.7.11.5 Relationship between temperature, T, and concentration of compounds, C, in 9 mol/dm3 nitric acid solution calculated by thermodynamic boiling model of Type 5 with different initial concentrations of nitrous acid.

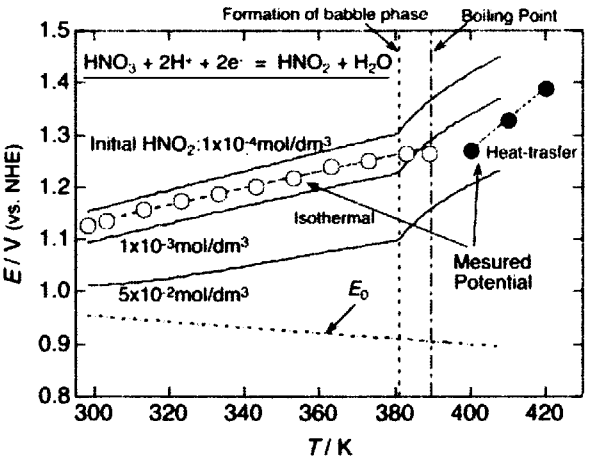

Fig.7.11.6 Relationship between temperature, T, and redox potential, E, of HNO3/HNO2 equilibrium reaction in 9mol/dm3 nitric acid solution calculated by boiling model for Type 5 with different initial concentrations of nitrous acid. Relationship between temperature and redox potential measured on Pt electrode under isothermal and heat-transfer conditions is also given. Under isothermal conditions, solution temperature is equal to temperature of electrode. Under heat-transfer conditions, temperature of electrode is higher than boiling points of solutions.

7.12 Corrosion of Type 304L Stainless Steel in Simulated Acid Recovery Evaporator Solution

Takafumi Motooka and Kiyoshi Kiuchi
(*E-mail*: motooka@popsvr.tokai.jaeri.go.jp)

In a previous investigation,[1] it is possible to artificially simulate the corrosion environment under actual operation conditions by equalizing the redox tendency of the test solution. On the basis of this hypothesis, the mock-up test was conducted under the environment simulating practical environments. For our test, non-radioactive ion, vanadium ion (VO_2^+), is added in nitric acid solutions instead of radioactive ion, neptunium ion (NpO_2^{2+}). The redox potential between VO_2^+ and VO^{2+} is 1.004 V (V *vs.* NHE) and the redox potential between NpO_2^{2+} and NpO_2^+ is 1.149 V. From the fact that redox potential of neptunium is slightly higher than that of vanadium, it imagines that neptunium nitrate causes slightly higher acceleration than vanadium nitrate in the corrosion of 304L SS in nitric acid solution. In this study to verify the corrosiveness of neptunium ions in nitric acid the corrosion of 304L SS under heat-transfer and immersion condition was examined by weight loss and polarization measurements. We have also attempted to establish corrosion mechanism in nitric acid solution containing neptunium.

Test specimens for corrosion tests were cut from a SUS304L plate and finely polished. Test solutions were Solution A (9M HNO_3), Solution B (9M HNO_3 + 3.8mM ^{237}Np) and Solution C (9M HNO_3 + 3.8mM VO_2^+). The specimens were immersed for a total of 930 hours in the above three test solutions. The solutions were newly changed every 310 hours in immersion and heat transfer corrosion tests. The ratio of solution volume to surface area of specimens was about 18 mL/cm^2. Both tests were conducted with a thermostatted glass cell under a boiling condition (at 341K) at a pressure of 160 hPa. The heat-flux in heat-conducting specimens was maintained 60 kW/m^2 during the tests.

Fig.7.12.1 shows the corrosion rate of 304L SS in nitric acid. The corrosion rate was increasing with test time under heat transfer condition. The corrosion rate at 930 hours was about six times higher in the neptunium nitrate solution than in pure 9M HNO_3. Under immersion condition, the corrosion rate at 930 hours was about sixteen times higher in the neptunium nitrate solution than in 9M HNO_3. The corrosiveness of neptunium is slightly weak

compared to vanadium in both conditions.

The redox potential of nitric acid is given as follows:[2)]

$3H^+ + NO_3^- + 2e^- = HNO_2 + H_2O$ (1)

$E = E_0 + (RT/2F) ln(\{[H^+]^3[NO_3^-]/[HNO_2]\})$ (2)

where E_0=0.934 V (V *vs.* NHE). As the redox potential of neptunium NpO_2^{2+}/NpO_2^+ with E_0=1.149 V is low compared with those of the other corrosive ions like Cr(VI), Ru(III) and Ce(IV) [$HCrO_4^-/Cr^{3+}$, E_0=1.350 V; Ru_2O_3/Ru^{2+}, E_0=1.304 V; $Ce(OH)^{3+}/Ce^{3+}$, E_0=1.715 V], it is not likely that neptunium causes an acceleration in corrosion rate of 304L SS. On the other hand, V(V) with the redox potential of VO_2^+/VO^{2+}, E_0=1.004 V, is known to accelerate corrosion rate of stainless steel in boiling nitric acid solution. In the corrosion process, vanadium ion keeps on existing in the highest oxidation state, and is responsible for accelerating the corrosion rate of stainless steel.[2)]

The effect of neptunium on the acceleration of corrosion is able to explain in terms of the decrease of cathodic over-voltage; the cathodic current in the neptunium nitrate solution is higher than that in pure nitric acid solution in polarization curves (Fig.7.12.2). This cathodic current increase suggests that NpO_2^{2+} is reduced to NpO_2^+ on the surface of specimen. NpO_2^+ produced on the surface of specimen is oxidized instantaneously to NpO_2^{2+} in the neptunium nitrate solution and consequently electrons are continuously consumed on the surface of specimen to lead to the acceleration of corrosion. Fig.7.12.3 shows the model for the corrosion mechanism of stainless steels in neptunium nitrate solution.

References:

1) M. Okubo, M. Shintani, H. Ishimaru, *et al.*, "Demonstration tests on corrosion resistance of equipments for spent fuel reprocessing process," SFEN-RECOD 86, p.1181 (1994)

2) A. B. McIntosh and T. E. Evans, *Proc. 2nd Int. Conf. on the Peaceful Uses of Atomic Energy*, P/30 U.K., p.206 (1958)

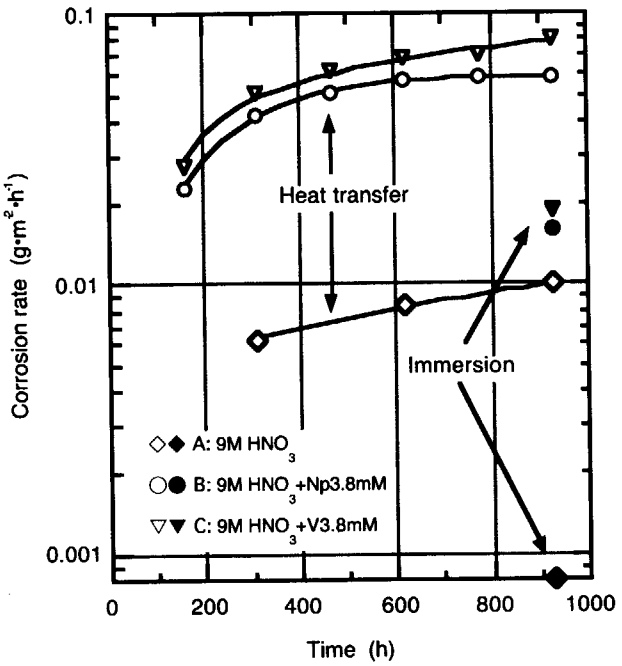

Fig.7.12. 1 Corrosion rates of SUS304L stainless steel.

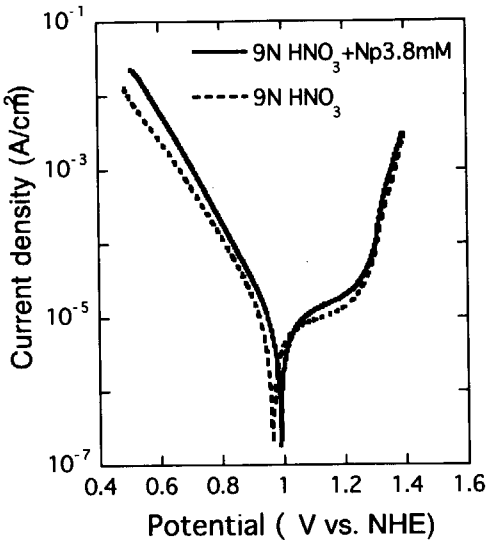

Fig.7.12.2 Polarization curves of SUS304L.

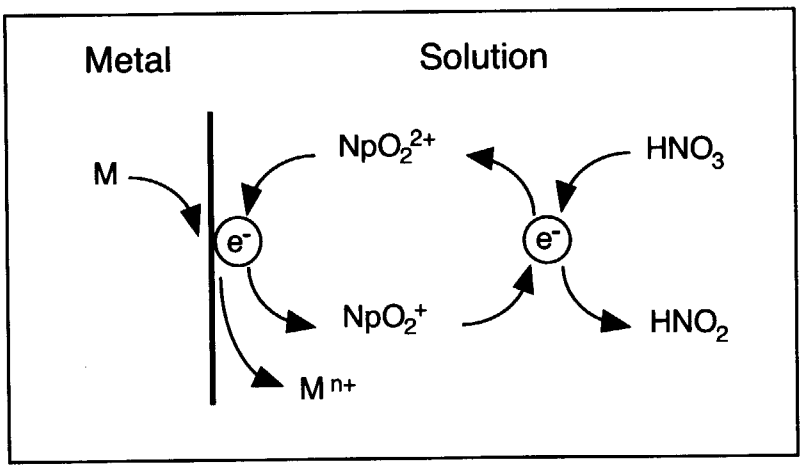

Fig.7.12.3 Schematic model for the corrosion mechanism of stainless steel in neptunium nitrate solution.

7.13 Corrosion Fatigue of Refractory Metals in Boiling Nitric Acid

Takafumi Motooka and Kiyoshi Kiuchi
(*E-mail*: motooka@popsvr.tokai.jaeri.go.jp)

In recent years, Ti-5Ta alloy and zirconium have been adopted as materials for a process dealing with highly corrosive nitric acid, i.e., an acid recovery evaporator or a dissolver for the spent fuel reprocessing. Ti-5Ta alloy and niobium have no stress corrosion cracking (SCC) susceptibility in nitric acid. However, zirconium has the susceptibility to SCC in nitric acid. The purpose of this work is to evaluate the effect of SCC on corrosion fatigue in nitric acid. We have studied corrosion fatigue of Ti-5Ta alloy, niobium and zirconium in boiling 3mol/dm^3 (17%) nitric acid. Results of corrosion fatigue tests through crack propagation rate measurements are presented. The crack growth mechanism under corrosion fatigue was also studied by fractography and polarization measurements.

The materials tested were commercially available zirconium, niobium and Ti-5Ta alloy plates. Fatigue tests were carried out using a closed-loop servohydraulic fatigue machine. Crack propagation was monitored with an optical microscope. Fracture surfaces of test specimens were observed in detail by a scanning electron microscope (SEM). The crystallographic orientation of fracture surface was analyzed by x-ray diffraction (XRD).

Crack propagation rates of zirconium are shown in Figure 7.13.1. In zirconium, a corrosion fatigue phenomenon in nitric acid is noted and this is reflected in an increase in crack propagation rates. The crack propagation rates increased by a factor of 4 at ΔK = 8 MPa$\sqrt{\text{m}}$ compared to in air at room temperature. For niobium, crack propagation rates are shown in Figure 7.13.2. Crack propagation was enhanced in nitric environment. The crack propagation rates increased by a factor of 4 at ΔK=12MPa$\sqrt{\text{m}}$ compared to in air at room temperature. On the other hand, the crack propagation in nitric acid was slightly accelerated compared to in air for Ti-5Ta alloy as shown in Figure 7.13.3. In zirconium, the fracture surface is indicative of the fact that corrosion fatigue crack growth takes place as a grain-to-grain juxtaposition of pseudo-cleavage on a basal plane (0001) and also that plastic deformation leading to the formation of ductile striations is identical to those observed in air. On the other hand, the plastic shear crack growth

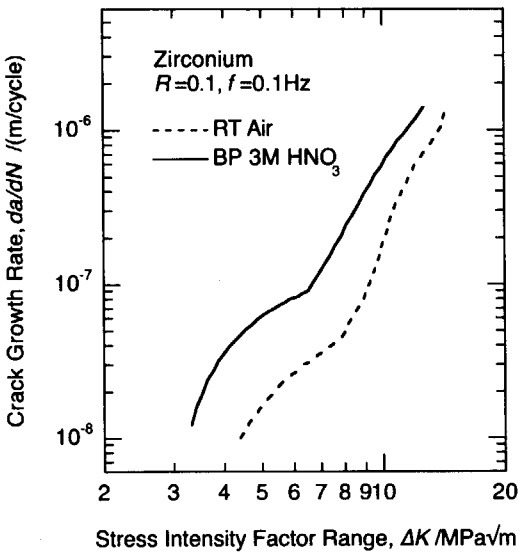

Fig.7.13.1 Crack propagation rates of zirconium.

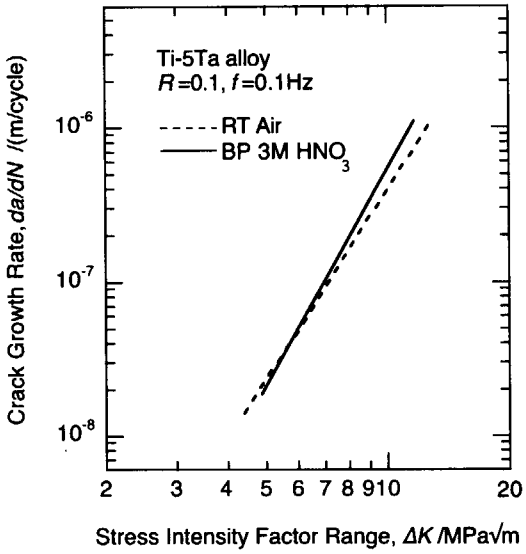

Fig.7.13.2 Crack propagation rates of Ti-5Ta alloy.

mode obtained in air can be linked to the fluting observed in SCC. In both cases, deformation takes place by slip on the same system along the prismatic plane. This fracture feature is characteristic to corrosion fatigue of zirconium. In Ti-5Ta alloy, the fracture surface morphology in air is similar to that in nitric acid. The fracture surface in nitric acid is indicative of the fact that plastic deformation leading to the formation of ductile striations which is identical to that observed in air. In niobium, the fracture surface morphology in air resembles that in nitric acid. The fracture surface in nitric acid presented the fact that plastic deformation and corrosion leading to the formation of brittle striations.

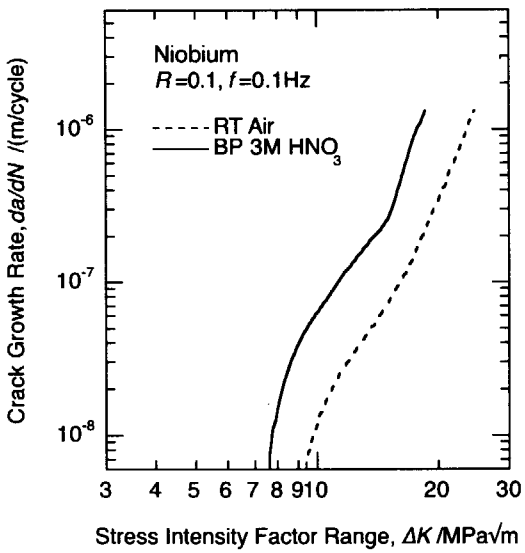

Fig.7.13.3 Crack propagation rates of niobium.

In zirconium, the corrosion fatigue crack growth mechanism is similar to that in

SCC: a brittle fracture by pseudo-cleavage on the basal plane is associated with plastic deformation growth by slip on prismatic planes. In static loading mode, fluting walls interconnects the planes ruptured by pseudo-cleavage. In cyclic loading mode, pure fatigue striations appear on grains of orientation unsuitable for pseudo-cleavage. The two crack growth modes (pseudo-cleavage and plastic slip deformation) are different and are incompatible within a given grain. The juxtaposition of the two mechanisms gives a different role to the crack propagation. In Ti-5Ta alloy, the corrosion fatigue crack growth mechanism is similar to that in air. Ductile fracture is caused by plastic deformation growth on slip planes. In cyclic loading mode, pure fatigue striations appear on grains of orientation suitable for plastic deformation. In niobium, the corrosion fatigue crack growth mechanism resembles to that in air. Brittle striations are caused by plastic deformation and anodic dissolution on slip planes. The SCC of zirconium in nitric acid explains the passive film rupture model (APSCC) model according to results of polarization measurements and optical observations. Zirconium has better general corrosion resistance than Ti-5Ta alloy and niobium. This behavior reflects the stability of passive films or a formation of oxide film. As optical observations, the color on fracture surface of Ti-5Ta is metallic color even in nitric acid. However, one of zirconium in nitric acid changed to yellow or brown. The occurrence of SCC requires some balance between stress and corrosion. Three factors, i.e., the strain rate (R_s), the dissolution rate at slip steps (R_d), and the re-passivation rate of raptured passive films (R_r), are most important in SCC process. SCC occurs when $R_s \approx R_d \approx R_r$ and R_r is slightly $> R_d$. SCC cannot occur when $R_d > R_r$ where general corrosion is predominant. Hence, local anodic dissolution process is responsible for crack propagation. Since Ti-5Ta alloy and niobium have a high corrosion rate, SCC could not occur in nitric acid. In zirconium, ZrO_2 film is formed on its surface in nitric acid. In cyclic loading, the passive film of ZrO_2 was broken at crack tip and many defects were formed, resulting in weakening of the film. Consequently, it is concluded that SCC is initiated in nitric acid under cyclic loading, where weakening of corrosion films occurs on zirconium surface.

8. Research on Advanced Transuranium Bearing Fuels

This study aims at developing advanced fuels containing transuranium element, which could contribut to realize flexible fuel cyscle in future. Rock-like oxide (ROX) fuel has been developed for burning excess plutonium in existing LWRs, followed by direct disposal of spent fuel as a near-term subject. As a long term-subject, nitride fuel has been develoed for ransmutation of long-lived monor actinides and future fast reactors, being coupled with pyrochemical reprocessing by use of molten salt electrorefining. In addition, some basic properties of actinide compounds are investigated in order to contribute to preparation of actinide thermodynamic database.

Destructive post-irradiation examinations of (U,Pu)N and (U,Pu)C fuel pins irradiated at fast test reactor JOYO were carried out at Reactor Fuel Examination Facility (RFEF). From the results of non-destructive and destructive examinations, superior fuel performance of nitride and carbide fuels such as structural stability and retainability of FP gas was demonstrated. With regard to pyrochemical process, electrotransport of U and Pu into liquid cadmium cathode was investigated. It was demonstrated that U and Pu could be co-recovered into liquid cadmium to high concentration when the U/Pu ratio in the salt phase was less than around 1/4. Further, behavior of Am contained as an impurity in Pu was also examined during electrorefining. Formation mechanism of actinide nitrogen chloride which would adversely affect the reprocessing of nitride fuel was investigated and the proper condition free from formation of the compound was found. In addition, thermodynamic properties of UO_3(g) were investigated by high temperature mass-spectrometry.

The joint irradiation test on Pu-ROX fuels was continued in the HFR, NRG-Petten, the Netherlands, without any trouble. Post-irradiation examinations on U-ROX fuels showed that radial swelling of the particle-dispersed type fuels were less than 3%, which will not cause serious problems in practical use as LWR fuels. Leaching tests on these U-ROX fuels were completed, and test procedures were developed to separate and to analyze TRU and long-lived FP elements. By improving the fabrication procedure of the particle-dispersed type fuel, the optimum conditions was established for production of high-density pellets with little gap between YSZ particles and matrix. In the ROX fuel assemblies partial loading core, the power peaking factor of as low as 1.8 was achieved by considering the Pu enrichment and Er content distributions within an assembly, and optimizing the UO_2 and ROX fuel assemblies loading pattern. As a result of, the reactivity initiated accident (RIA) and the loss of coolant accident (LOCA) behaviors of ROX partial loading core were also improved to the comparable level to the conventional UO_2 fuel core.

8.1 Post Irradiation Examination of Nitride and Carbide Fuel Pins for Fast Reactor

T.Iwai and Y.Arai
(*E-mail*: iwait@oarai.jaeri.go.jp)

Based on the JAERI-JNC joint research program, JAERI fabricated uranium-plutonium mixed carbide and nitride fuel pins[1] and carried out the irradiation test at a fast test reactor, JOYO. Non-destructive [2] and destructive [3] post irradiation examination (PIE) has been carried out at JNC.

Carbide fuel and a part of nitride fuels were transferred to JAERI and destructive post irradiation examination of the fuels were performed at JAERI.

The characteristics and irradiation conditions are summarized in Table 8.1.1. The outer diameter of the fuel pins is 8.5 mm. The fuel-clad gap of the nitride fuel I is larger than that of the nitride fuel II to examine the effect of the difference in the gap on the irradiation behavior. The peak linear power is from 734 to 781 W/cm. The burnups of these fuels are about 40 GWd/t (4.6%FIMA).

A series of PIE, density measurement, porosity measurement, metallography, micro gamma scanning, electron probe micro analysis, etc. were carried out.

The macroscopic photograph of fuels are shown in Photo.8.1.1. The maximum temperature of the center of these fuels are estimated about 1490, 1800 and 1570℃. A few large cracks are seen in the photograph. However, remarkable structure change caused by the irradiation was not observed.

Microstructure of carbide fuel is shown in Photo.8.1.2. This carbide fuel included $(U,Pu)_2C_3$ (about 15%) as a second phase. In the outer and the intermediate zones of the fuel, $(U,Pu)_2C_3$ that is observed as a white spot existed after the irradiation. However, $(U,Pu)_2C_3$ was disappeared in the central zone. This is attributed to the transfer of carbon from central zone to outer zone under temperature gradient during irradiation. The grain size of carbide fuel at the central zone was slightly larger than that of the outer zone. In the case of the nitride fuels, the pronounced difference in the grain size was not perceived in the all zones.

Density measurement was performed and the swelling rate, porosity were estimated using the result. The results are shown in Table 8.1.2. The density of the fuels decreased by the irradiation. The swelling rate calculated by the density was about 1.3 to 1.6 %/%FIMA. These values are larger than those of the carbide and the nitride fuels irradiated in JMTR. Open porosity of the fuels was very small, 1.7 to 4.2 % because the fuel pellets were fabricated using pore former. Therefore, the FP gas release rate of the fuels was very small.

Fuel clad chemical interaction (FCCI) was examined by EPMA and the reaction phase

was found in both of the carbide and the nitride fuels. However, the reaction occurred at a limited sphere and the width of the reaction layer was very narrow. Therefore, it was considered that the FCCI does not affect the performance of the fuel pins.

Through the irradiation test and PIE, we confirmed good performance of the carbide and nitride fuels for fast reactor.

References

1) Y.Arai, T.Iwai, T.Sasayama, Y.Okamoto, K.Shiozawa and Y.Suzuki: JAERI-Research 96-009 "Fabrication of uranium-plutonium mixed carbide and nitride fuel pins for the irradiation test in JOYO" (1996) (in Japanese).
2) K.Katsumata, T.Nagamine, K.Maeda and S.Matsumoto: JNC TN9410 2000-009 "Post irradiation examination of (U,Pu)C and (U,Pu)N fuel for fast reactor - Non-destructive examination result of the fuel pin – " (2000) (in Japanese).
3) K.Tanaka, K.Maeda and S.Koyama: JNC TN9400 2002-001 "Post irradiation examination of Uranium-Plutonium Mixed Nitride Fuels for Fast Reactor - Destructive Examination of Nitride Fuel – " (2002) (in Japanese).

Table 8.1.1 Characteristics of fuel pins and irradiation condition

	Carbide fuel	Nitride fuel Ⅰ	Nitride fuel Ⅱ
Outer diameter of fuel pin (mm)	8.5	8.5	8.5
Pellet diameter (mm)	7.42	7.28	7.43
Pellet-clad diameter gap (mm)	0.18	0.32	0.17
Peak linear power rate (W/cm)	734	742	781
Maximum burnup (GWd/t)	40.9	39.5	39.4
(%FIMA)	4.66	4.63	4.62

Table 8.1.2 Density, swelling rate, porosity and FP gas release rate

	Carbide fuel	Nitride fuel Ⅰ	Nitride fuel Ⅱ
Density before irradiation (%TD)	85.0	84.8	86.0
Density before irradiation (%TD)	80.2	79.0	80.6
Swelling rate (%/%FIMA)	1.3	1.6	1.5
Open porosity (%)	1.7	4.2	4.1
Closed porosity (%)	18.1	16.8	15.3
FP gas release rate (%)	2.3	3.3	5.2

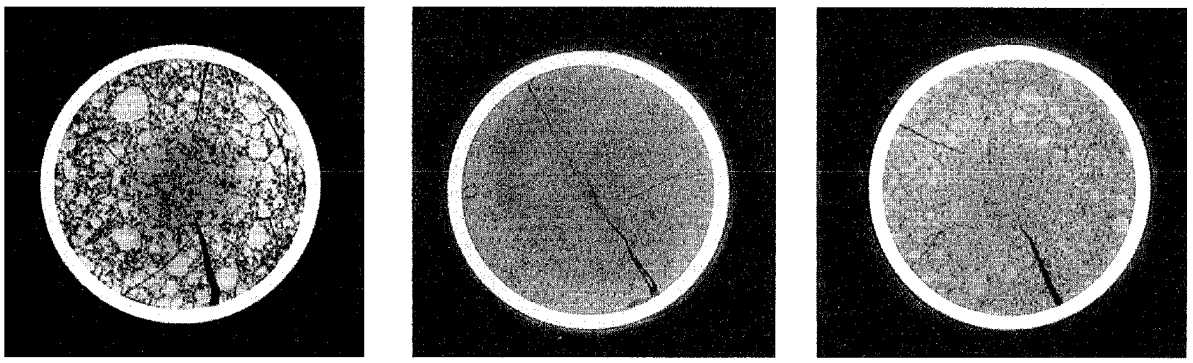

Carbide fuel　　Nitride fuel Ⅰ　　Nitride fuel Ⅱ

Photo. 8.1.1 Macroscopic photograph of fuels irradiated at JOYO

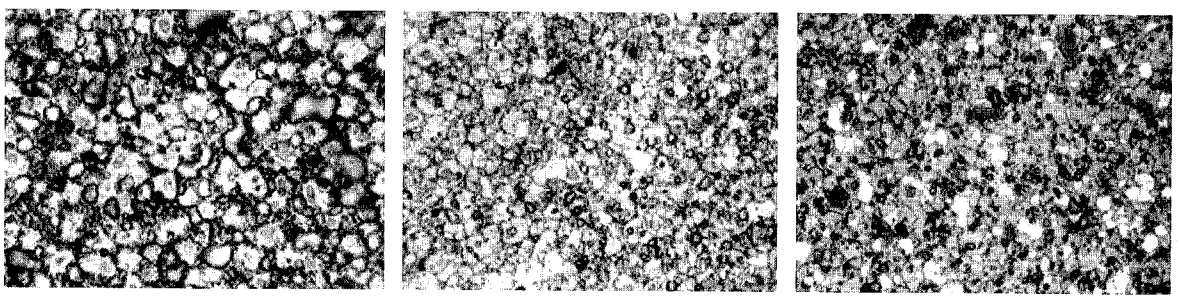

Cenral zone　　Intermediate zone　　Outer zone

Photo. 8.1.2 Microstructure of carbide fuel

8.2 Investigation of Vaporization Behavior of Hyper-stoichiometric Uranium Dioxide by Knudsen Effusion Mass Spectrometry

K. Nakajima and Y. Arai
(E-mail: kuni@popsvr.tokai.jaeri.go.jp)

From the view point of evaluating release behavior of volatile radio nuclides in core disruptive accidents it is essential to know the vaporization behavior of hyper-stoichiometric uranium dioxide, $UO_{2+x}(s)$. The vaporization behavior of uranium-bearing volatile vapor species, or, $UO_3(g)$, are inconsistent among several literature sources[1], where the discrepancies are two orders of magnitude at 1500K and one order of magnitude at 2000K. The reason is possibly due to inaccuracy of Gibbs free energy of formation of $UO_3(g)$, $\Delta G_f(UO_3,g)$. So the mass-spectrometric measurements of pure $UO_{2+x}(s)$ were carried out and $\Delta G_f(UO_3,g)$ was determined from the measured partial pressures of $UO_3(g)$ and $O_2(g)$ over $UO_{2+x}(s)$.

Hyper-stoichiometric uranium dioxides, $UO_{2+x}(s)$, for test specimens were prepared by heating $U_3O_8(s)$ put in a Knudsen cell under a vacuum condition. The samples having the O/U ratios of 2.12 and 2.10 were obtained by heating $U_3O_8(s)$ at 1523K for 4hr and 4.5hr, respectively. The O/U ratio was determined by measuring the weight increase after ignition at 873K in air to $U_3O_8(s)$.

Mass-spectrometric measurements combined with a Knudsen cell were carried out at the prescribed temperatures of 1673, 1773 or 1873K. A quadrupole mass spectrometer (MEXM-1200 ABB EXTREL, USA) was used in this study. Knudsen cell was made of Iridium and its orifice diameter is 1mm. The samples of the O/U ratio of 2.12 were used in the mass-spectrometric measurements at 1673K and 1773K. On the other hand, the samples of the O/U ratio of 2.10 were used in the mass-spectrometric measurements at 1773K and 1873K. The vapor species of $UO_3(g)$ and $O_2(g)$ were ionized at 70 eV, where the ion currents of UO_3^+ become the maximum[2]. Moving a shutter allowed us to distinguish $O_2(g)$ vapor species effusing through an orifice from those of background. The ion currents of UO_3^+ and O_2^+ were measured at the prescribed temperature until the vapor species of $O_2(g)$ effusing through the orifice could not be distinguished from those of background.

The determination of the absolute vapor pressure from its ion current was carried out by the modified integral method[3]. This method requires the total losses of amounts of the vapor species and the ion currents of the vapor species at any time during the mass-spectrometric measurement. The total losses of amounts of $UO_3(g)$ and $O_2(g)$ during the measurement were evaluated from the changes of the weight and the O/U ratio of the sample before and after the mass-spectrometric measurement. If the partial pressures of $UO_3(g)$ and $O_2(g)$ are known, the O/U ratio of the condensed phase during the mass-spectrometric measurement could be evaluated

from Graham's law of effusion.

Fig. 8.2.1 shows the time dependence of the ion currents of a) UO_3^+ and b) O_2^+ observed in the mass-spectrometric measurement at 1673K. This figure also shows the ion currents of UO_3^+ and O_2^+ observed in the case of closed shutter, or the background ion currents. As an example, the determined vapor pressures of $UO_3(g)$ and $O_2(g)$ at 1773K from these ion currents are plotted in Fig.8.2.2. This figure also include the apparent vapor pressures at the temperatures increasing from 1473K to 1773K besides those at 1473K. Furthermore, the experimental and estimated data reported in the past are indicated for comparison. As shown in this figure, the determined $O_2(g)$ pressures almost agree with the experimental values reported in the past. On the other hand, it seems that the determined $UO_3(g)$ vapor pressures are also in good agreement with the recommended value given by Hashizume[4].

In this study, $\Delta_f G°(UO_3,g)$ is evaluated from the following reaction:

$$UO_2(s)+1/2O_2(g)=UO_3(g), \quad (1)$$

and calculated from the following equation utilizing $\Delta_f G°(UO_2,s)$ given by Cordfunke and Konings[5]:

$$\Delta_f G°(UO_3,g)=-RTln[P(UO_3)/P(O_2)1/2a(UO_2)]+\Delta_f G°(UO_2,s). \quad (2)$$

where R is gas constant and $a(UO_2)$ the activity of $UO_2(s)$ in $UO_{2+x}(s)$. According to Olander[1], $a(UO_2)$ is evaluated from the $O_2(g)$ pressure by the following equation utilizing the Gibbs-Duhem equation:

$$\ln a_{UO_2}(x,T)=-\frac{1}{2}\int_0^x x'\frac{d\ln p_{O_2}(x',T)}{dx'}dx'. \quad (3)$$

This activity was calcurated by using the oxygen pressures based on Blackburn's model[1]. The results at 1773K are plotted as function of the O/U ratio in Fig.8.2.3. As shown in these figure, there exists the range where the values of seem to be almost independent of the O/U ratio. In Fig.8.2.4 the temperature dependence of the averaged values of $\Delta_f G°(UO_3,g)$ including the results at 1473K, 1673K and 1873K are shown, together with the reference data. This figure also includes the values of $\Delta_f G°(UO_3,g)$ reported in our previous paper[2]. The values of $\Delta_f G°(UO_3,g)$ obtained in this study almost agree with the recommended value given by Olander.

References:

1) Olander, D.R., J. Nucl. Mater. 270(1999)187.

2) Nakajima, K. and Arai, Y., J. Nucl. Mater. 294(2001)250.

3) Asano, M., et al., Bull. Chem. Soc. Jpn. 45 (1972) 82.

4) Hashizume, K., Wang, W., and Olander, D.R., J. Nucl. Mater. 275(1999)277.

5) Cordfunke, E.H.P., Konings , R.J.M., (Eds.), Thermodynamical Data for Materials and Fission Products, North-Holland, 1990.

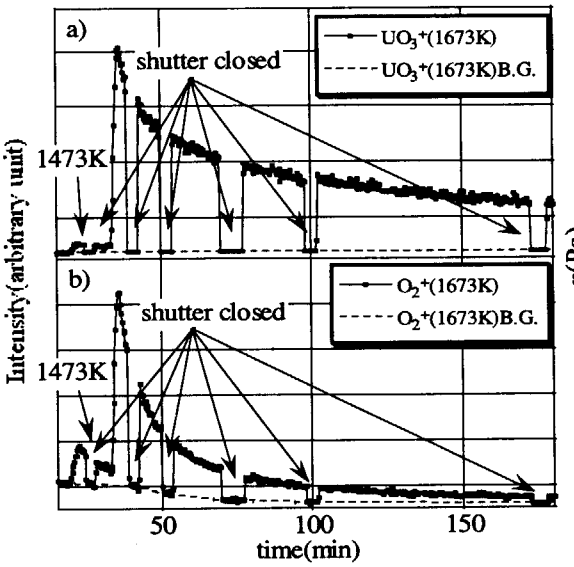

Fig.8.2. 1 Time dependence of the ion currents of (a)UO3+ and (b)O2+ at 1673K

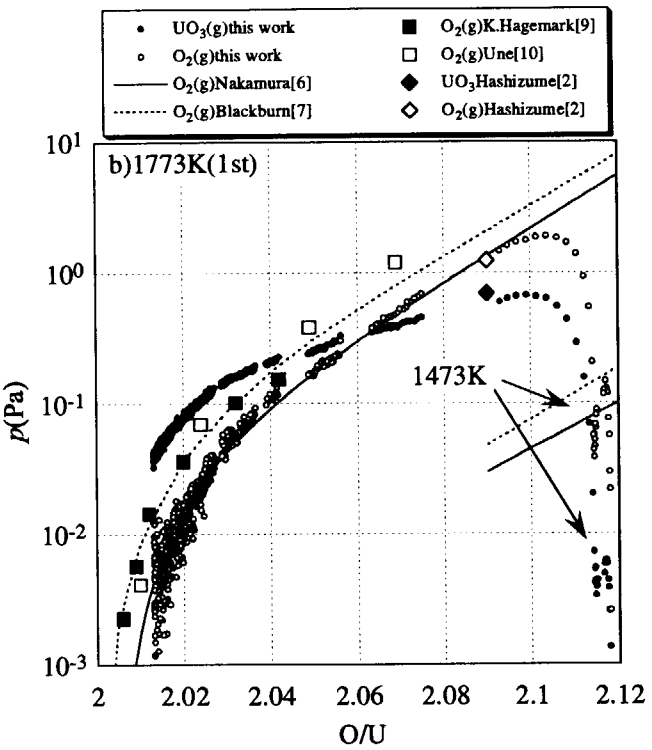

Fig. 8.2.2 Vapor pressures of UO3(g) and O2(g) over UO2+x at 1773K(1st).

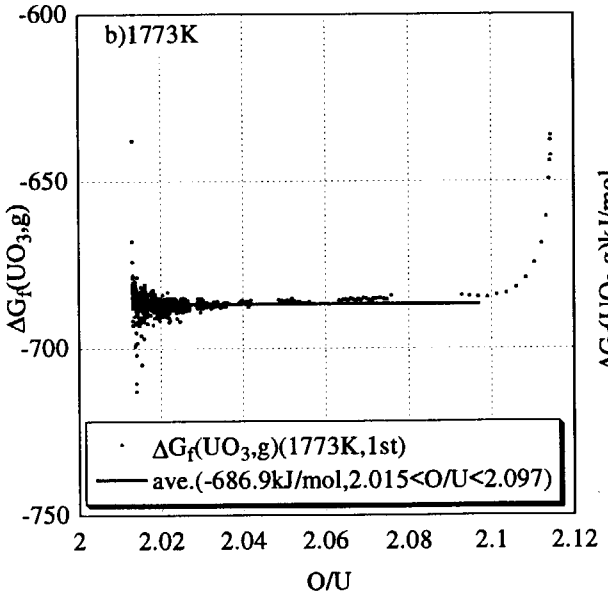

Fig. 8.2.3 Standard Gibbs free energy of formation of UO3(g) at 1773K(1st) plotted as function of the O/U ratio.

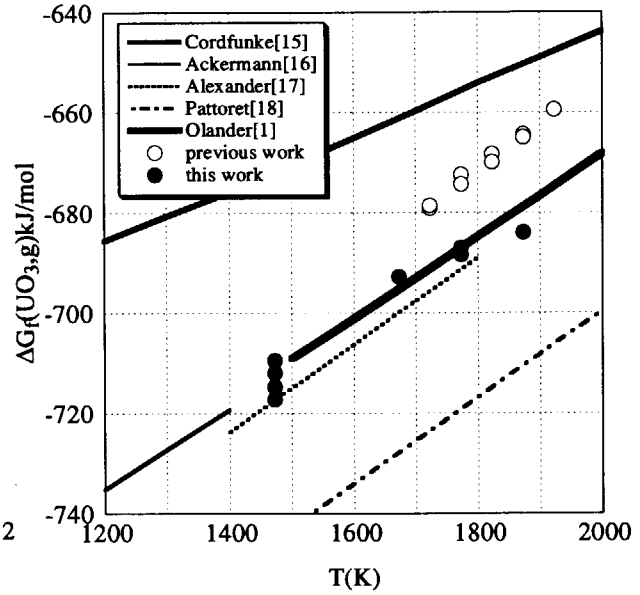

Fig. 8.2.4 Comparison of Standard Gibbs free energy of formation of UO3(g)

8.3 Anodic Dissolution of UN in LiCl-KCl Eutectic Melts

Osamu Shirai, Koichi Uozumi*, Takashi Iwai and Yasuo Arai
(*E - mail*: shirai@popsvr.tokai.jaeri.go.jp)

The information regarding the electrochemical behavior of various actinide nitrides is important to control the electrolysis of spent nitride fuel in the pyrochemical reprocessing. In the case of UN, its electrochemical behavior was elucidated by several groups.[1,2] The information on formation of U_2N_3 and uranium nitride chloride, UNCl, during the anodic dissolution of UN was reported by Kobayashi et al.[3] However, the formation mechanism of U_2N_3 and UNCl and the condition of the electrolysis by using UN as an anode have not been optimized for the recovery of U yet.

In the present work, the electrochemical behavior of UN in the LiCl-KCl melt containing UCl_3 was investigated, and it was demonstrated that U metal was successfully be recovered at the cathode when more negative potential than the redox potential of the U^{4+}/U^{3+} couple was applied to the anode.

The equilibrium potential of UN at 773 K was -0.71 ± 0.1 V vs. the Ag/AgCl reference electrode, when the salt phase contained 0.30 wt.% UCl_3 and partial pressure of N_2 gas in the atmosphere was 10^{-4} – 10^{-5} atm. This potential is considered to correspond to the equilibrium on the following reaction:

$$UN = U^{3+} + 3e^- + 1/2N_2. \quad (1)$$

The equilibrium potential against the Ag/AgCl reference electrode, $E_{UN\text{-}Ag/AgCl}$, is described as eqn. (2).

$$E_{UN\text{-}Ag/AgCl} = \Delta G_{UCl_3}^0/3F - \Delta G_{UN}^0/3F - \Delta G_{AgCl}^0/F + (RT)/(3F) \ln \gamma_{UCl_3} c_{UCl_3} + (RT)/(6F) \ln p_{N_2} - (RT)/F \ln \gamma_{AgCl} c_{AgCl}, \quad (2)$$

where F is the Faraday constant. The standard Gibbs energy for formation of UN at 773 K, ΔG_{UN}^0, is -225.9 kJ·mol^{-1}, and that of AgCl, ΔG_{AgCl}^0, -86.22 kJ·mol^{-1}. The concentration of UCl_3 in the melt and that of AgCl in the reference electrode, c_{UCl_3} and c_{AgCl}, were 0.30 wt.% (0.049 mol%) and 1.00 wt.% (0.390 mol%), respectively. The activity coefficient of AgCl in the reference electrode, γ_{AgCl}, is assumed to be unity. The standard Gibbs free energy for formation of UCl_3 in the LiCl-KCl eutectic melt phase at 773 K, $\Delta G_{UCl_3 \text{ in LiCl-KCl}}^0$, is evaluated as -713.5 J·mol^{-1}. $\Delta G_{UCl_3 \text{ in LiCl-KCl}}^0$ is made up by the sum of the standard Gibbs free energy for formation of UCl_3, $\Delta G_{UCl_3}^0$, and the solvation energy of UCl_3 in the LiCl-KCl eutectic melt. The solvation energy is expressed by RT $\ln \gamma_{UCl_3}$, where γ_{UCl_3} is the activity coefficient of UCl_3 in the LiCl-KCl eutectic melt. Therefore, the equilibrium potential at 773 K derived from eqn. (2) is expressed as follows:

$$E_{UN\text{-}Ag/AgCl} = -0.4231 + 0.02221 \times \ln c_{UCl_3} + 0.0111 \times \ln p_{N_2} \quad (3)$$

---

*A Guest researcher from the Central Research Institute of Electric Power Industry, during October, 1999 ~ December, 2002

Therefore, the equilibrium potential at 773 K under the present experimental condition is expected as -0.695 ― -0.720 V. The above value is comparable with the observed value.

The typical voltammogram for dissolution of UN obtained in the LiCl-KCl eutectic salt containing with 0.55 wt.% UCl_3 at 773 K is indicated in Fig. 8.3.1. Anodic current, which was caused from the reaction (1), was observed, and cathodic current was also observed in the reverse potential sweep. The reaction (1) was irreversible because partial pressure of N_2 in the salt was considered to be much less than atmospheric pressure (1 atm) and it might be very slow in analogy with the cases of PuN and NpN.[4, 5] Figure 8.3.2 shows voltammograms for the dissolution of UN and for the redox reaction of the U^{4+}/U^{3+} couple in the LiCl-KCl eutectic salt containing 0.55 wt.% of UCl_3 at 773 K. The anodic current increased drastically around –0.4 V. Kobayashi et al. reported this anodic reaction was attributable to the reaction (1). However, the redox reaction of the U^{4+}/U^{3+} couple was observed, as shown in Fig. 8.3.2. Consequently, we consider the anodic current results from the composite wave of dissolution of UN to U^{3+}, the redox reaction of the U^{4+}/U^{3+} couple and the directly formation of UNCl from UN described as eqn. (4).

$$UN = UN^{+} + e^{-} \{\text{and } UN^{+} + Cl^{-} = UNCl(\downarrow)\} \quad (4)$$

Here, UN^{+} is considered to be obtained by oxidation of UN, since U behaves trivalent ion in UN. Therefore, the electrolysis using UN as an anode by applying more negative potential than -0.4 V should be performed for the reasonable.

When the constant potential of -0.55 V versus the reference electrode was applied to the working electrode, in which UN was placed, U metal was recovered at the Mo counter electrode. The current was about 0.02 A at the beginning of electrolysis and increased slightly to 0.025A. When the electrolysis was initiated, potential of the Mo counter electrode changed from -1.0 ± 0.1 V to -1.6 V. Few minutes later, the Mo counter showed almost constant value, -1.45 V. This potential shift during the electrolysis might be caused by the increase of surface area of the counter electrode. After the electrolysis had been performed for 7.2 kilo seconds, the cathode and the anode were picked up from the salt. By using an X-ray diffractometer, U metal was identified in the electrodeposit. The results of ICP-AES indicates that the concentration of UCl_3 in the melt was kept approximately constant throughout the electrolysis (0.29－0.31 wt%). During the electrolysis, production of N_2 gas was identified by gas chromatography. Accordingly, the recovery of U by the controlled-potential electrolysis using UN as the anode was successful in this condition.

Similarly, under the controlled-potential electrolysis by applying -0.3 V to the anode, U metal was recovered at the Mo electrode. The current was about 0.2 A at the beginning of electrolysis, but quickly fell down to about 0.05 A. The potential of Mo counter electrode behaved the same as the electrolysis by applying -0.55 V to the anode. After the accumulated electric charge reached at about 90 coulombs, which corresponded to 0.074g of U metal, the electrodeposit on the Mo wire was taken out from the salt. During the electrolysis, only slight amount of N_2 gas was identified by gas

chromatography. The concentration of UCl_3 in the salt changed from 0.30 wt.% to 0.22 wt.%, corresponding to loss of 0.056 g of U. Therefore, only 24 % of the UN in the anode was dissolved as U^{3+} into the salt phase and the majority of the UN must be transformed into insoluble compounds such as UNCl. Taking into account the above understandings, the electrolysis of UN should be performed by applying more negative potential than -0.4 V versus the reference electrode in order to prevent the loss of U due to the formation of UNCl.

References

1) F. Kobayashi, et al., J. Am. Ceram. Soc., **78**[8], 2279 (1995).
2) B. D. Rogozkin, et al., Proc. of ARS'94 Int. Topical Meeting on Advanced Reactors Safety, Vol. 1, Pittsburgh, Pennsylvania, Apr. 17-21, 1994, p.382 (1994).
3) F. Kobayashi, et al., J. Alloys and Compounds, **271-273**, 374 (1998).
4) O. Shirai, et al., J. Nucl. Mater., **277**, 226 (2000).
5) O. Shirai, et al., J. Nucl. Sci. Technol., 37, 676 (2000).

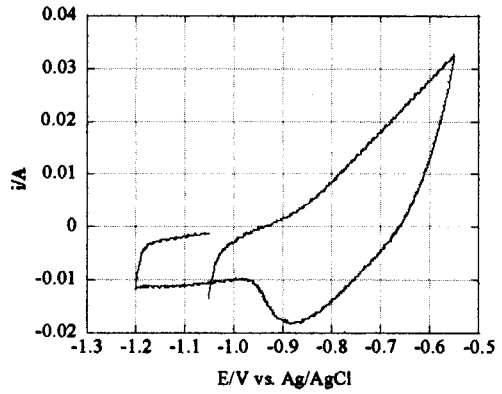

Fig. 8.3.1 Cyclic voltammogram in the UCl_3-LiCl-KCl melt. Working electrode: UN (surface area: 1.80 cm^2), UCl_3 concentration: 0.55 wt.%, Potential scanning rate: 0.001 $V \cdot s^{-1}$.

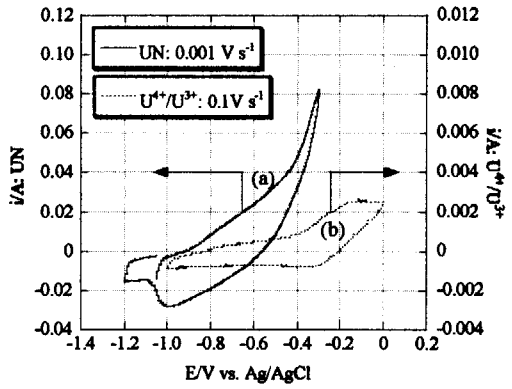

Fig. 8.3.2 Cyclic voltammograms in the UCl_3-LiCl-KCl melt. Working electrode: (a)UN (surface area: 1.80 cm^2), (b)Mo (surface area: 0.322 cm^2), UCl_3 concentration: 0.55 wt.%, Potential scanning rate: (a) 0.001 $V \cdot s^{-1}$, (b) 0.1 $V \cdot s^{-1}$.

8.4 Behaviors of Uranium and Plutonium at Simultaneous Recoveries into Liquid Cadmium Cathodes

K. Uozumi*, T. Kato**, O. Shirai and T. Iwai

(*E-mail:* uozumi@criepi.denken.or.jp)

Four experiments were conducted on recovering uranium and plutonium simultaneously into 120g LCCs at different U/Pu ratios in the salt phase, and the influence of the salt composition on the recovery of both elements and their deposited forms was studied. Additionally, the behavior of americium was also examined.

We used the same apparatus as described in the previous report[1]. The starting compositions of the molten salt for all experiments are listed in Table 10.4.1. The U/Pu weight ratios in the salt phase ranged between 1/8.0 and 1/1.73. Each electrotransport was conducted at a constant current with the cathode current density of 23.4mA/cm^2 in principal. The total electric charge passed in each experiment was 1.85×10^4-1.91×10^4 coulombs, which corresponded to 11.3-11.6wt% of actinides in the LCC, assuming a current efficiency of 100%.

After each electrotransport, the solidified cathode cadmium ingot was removed from the cathode crucible. In the case of LCC-25, which was conducted without cathode stirrer rotation to confirm the effect of cathode mixing, the cathode showed a smooth surface. However, about 30g of deposit was found on the stirrer. On the other hand, the cathode ingots of LCC-28, LCC-30, and LCC-34 showed smooth surfaces and little deposit on stirrers. Accordingly, the cathode stirring seems to be effective for collecting the actinides smoothly.

Except for LCC-25, it was estimated from the cathode weight gains, that 14.17-15.33g of uranium plus plutonium were recovered in cathodes. According to these values, uranium plus plutonium weight ratios in cathodes reached 10.9-11.3wt%, exceeding 10wt%, which is the tentative target. Separation factors of uranium to plutonium (=SF(U/Pu)) before the saturation of cathodes, which were defined as (U/Pu ratio in the samples taken from the saturated cathode)/(U/Pu ratio in the salt), were calculated to be 1.5-2.0. These values roughly agreed with the SF(U/Pu) in LiCl-KCl eutectic salt/unsaturated liquid cadmium system, that is 1.88.

---

*A guest researcher from the Central Research Institute of Electric Power Industry, during October, 1999～December, 2001

**A guest researcher from the Central Research Institute of Electric Power Industry, since April 2002

The uranium and plutonium content profiles in the LCC-28 and LCC-34 cathodes are shown in Figs. 10.4.1 and 10.4.2. According to the mass balances in the system, the current efficiencies for all experiments were higher than 80%. The total SF(U/Pu), defined as (U/Pu ratios in the cathode products)/(U/Pu ratio in the salt), ranged between 1.2 and 2.0 except for LCC-34. In contrast, weight ratio of plutonium in the LCC-34 cathode estimated from the mass balance was close to the values in the samples taken from the cathode after saturation. This means that only uranium was recovered after the cathode saturation in the case of LCC-34. From these results, it is concluded that under the conditions that U/Pu ratio in the salt phase is less than around 1/4, uranium and plutonium can be recovered into LCCs up to 10wt% with SF(U/Pu) ranging between 1.2 and 2.0. However, under the conditions that U/Pu ratio in the salt phase is around 1/2, only uranium is collected into the cathode after the saturation. Accordingly, it was indicated that there is a threshold in the U/Pu ratio in the salt phase between 1/4 and 1/2 for the simultaneous recovery of uranium and plutonium.

Cross sections of LCC-28 and LCC-34 cathodes were analyzed by EPMA to investigate the chemical forms of uranium and plutonium in the cathodes. The LCC-28 cathode consisted of three phases: a pure cadmium phase and MCd_6 and MCd_{11} (M: U, Pu) type ternary intermetallic compounds. In LCC-34, besides pure cadmium and MCd_{11} type ternary intermetallic compound phases, uranium phase containing little amount of cadmium or plutonium was found.

In the cases of LCC-28 and LCC-34, behavior of americium during the electrotransport was studied. In both runs, the concentrations of americium in the samples drawn from the LCCs became constant during electrotransport, as shown in Figs. 10.4.3 and 10.4.4. In contrast, the weight ratio of americium in the final cathode cadmium of LCC-28, estimated by analyzing the solidified ingot, was much higher than in the samples drawn from the cathode cadmium. The weight ratios of americium estimated by the ingot analysis method agreed well with the extrapolated concentrations of americium in the samples drawn directly from the LCC-28 cathode before the saturation of LCC. This indicates that the electrotransport of americium was not affected by the saturation of uranium and plutonium in the cathode cadmium. In the case of LCC-34, the weight ratios of americium estimated by analyzing the solidified ingot agreed with the concentrations of americium in the samples drawn directly from the LCC-34 cathode after the saturation of LCC. This means that americium behaved like plutonium and was not collected into the LCC-34 cathode after the saturation.

The separation factors of americium to plutonium (=SF(Am/Pu)) before the saturation of cathodes, which were defined as (Am/Pu ratio in the samples taken from the saturated cathode)/(Am/Pu ratio in the salt), were calculated to be 0.70 for LCC-28 and 0.66 for LCC-34. These values roughly agreed with the separation factor of 0.61 for americium to

plutonium in LiCl-KCl/unsaturated liquid cadmium system. The total SF(Am/Pu), defined as (Am/Pu ratio in the cathode product)/(Am/Pu ratio in the salt), was 0.78 for LCC-28.

References

1) Uozumi, K., Shirai, O. and Iwai, T.: iPlutonium and Uranium Recovery Experiments into Liquid Cadmium Cathodesî, JAERI-Review 2002-005, pp. 209-211(2002).

Table 10.4.1 Initial salt compositions in weight

Run#	Pu	U	U/Pu ratio
LCC-25	5.0%	0.62%	1/8.0
LCC-28	4.7%	1.07%	1/4.4
LCC-30	4.8%	1.11%	1/4.3
LCC-34	4.5%	2.6%	1/1.73

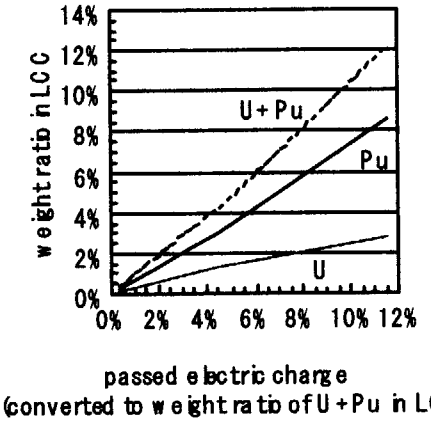

Fig. 10.4.1 Weight ratio profiles in LCC-28 cathode

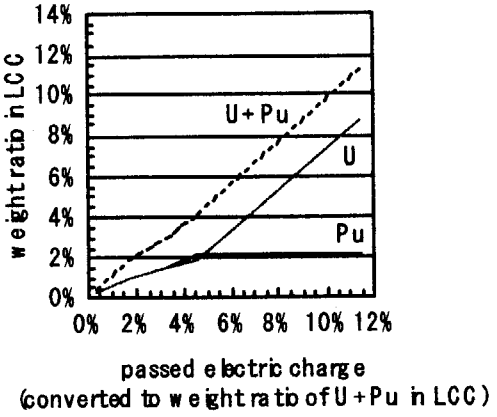

Fig. 10.4.2 Weight ratio profiles in LCC-34 cathode

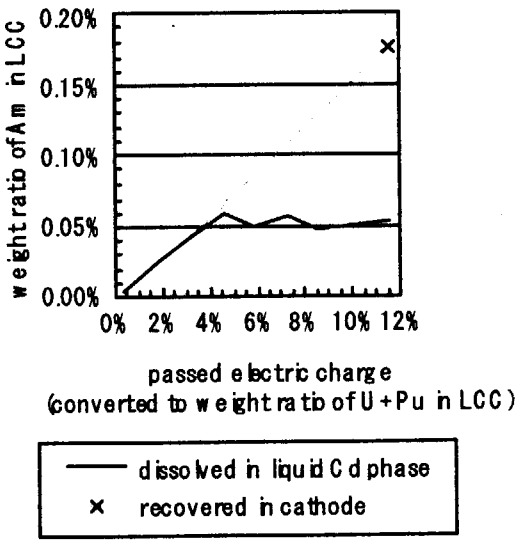

Fig. 10.4.3 Weight ratio profile of Am in LCC-28 cathode

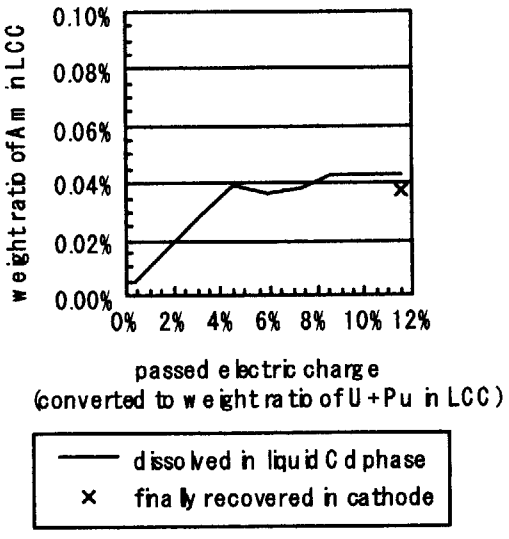

Fig. 10.4.4 Weight ratio profile of Am in LCC-34 cathode

8.5 Post-Irradiation Examination of Rock-like Oxide Fuels (4) -Ceramography and EPMA

N. Nitani, K. Kuramoto, T. Yamashita, Y. Nihei and Y. Kimura
(E-mail: noriko@popsvr.tokai.jaeri.go.jp)

On the rock-like oxide fuel, we have carried out an irradiation test to clarify the irradiation behavior. Five kinds of ROX fuels were prepared; a single phase fuel of yttria-stabilized zirconia, YSZ (Z), two particle-dispersed type fuels of YSZ particles in spinel or corundum matrix (SD or CD), two homogeneously-blended type fuels of YSZ and spinel or corundum (SH or CH). Estimated irradiation conditions and burn-up of ROX fuels are listed in Table 8.5.1. It must be mentioned that the temperature of each fuel is remarkably higher than that of UO_2 in LWRs. Microstructure analyses for irradiated fuel pellets were carried out by ceramography and electron probe micro-analysis (EPMA), and FPs distributions in fuel pellets were obtained.

The aspect of the Z fuel pellet was analogous to LWR UO_2 fuels, and showed uniform structure throughout the pellet surface. However, the decomposition of spinel and vaporization of MgO occurred in SD and SH fuels, caused by high temperature irradiation. It is expected that the spinel decomposition and phase restructuring is avoided by lowering the irradiation temperature less than 1700K. For CD and CH fuels, because of sufficiently high irradiation temperature to anneal the amorphous corundum, significant appearance changes such as swelling and heterogeneity of fuel structures were not observed.

The SEM image of the outer region of SD fuel pellet is shown in Fig. 8.5.1 (a). That is the region where the vaporization of MgO did not occur. Gray layer of about 10μm thickness was observed at the surface of the particle. The layer was composed of fine grains of spinel and U-YSZ. The thickness of the layer was comparable to mean range of fission fragments. In irradiation field, the spinel decomposed and segmented to fine grain by heavy fission fragments, and the YSZ grains also grained finely. The layer probably indicates the radiation damaged region. Figures 8.5.1 (b) ~ (e) are the distributions of matrices and U. All matrix elements existed in the reaction layer. The distributions of Al and Mg are ununiform, it was appeared that the phase restructuring occurred for spinel. FP distributions of SD fuel were also shown in Fig. 8.5.1 (f) ~ (j). The distribution of Nd and Ba was similar

to those of U and Zr, and it is confirmed that Nd and Ba were immobilized in U-YSZ phase. A part of Cs and Xe concentrated to pores in YSZ. The Cs and Xe aggregation to the boundary region between U-YSZ particle and spinel was also observed. Those elements could migrate more easily due to generation of the reaction layer. Even though the aggregations to the periphery of YSZ particles occur, the influence of the aggregation on fission gas release and leaching behavior is negligible in the case the crack generation is prevented.

SEM image and element distributions on middle region of SD fuel were shown in Fig. 8.5.2. In this region, vaporization of MgO and subsequent restructuring occurred, and the fuel particle deformation proceeded. The boundary between matrix and fuel particle was extremely complicated, the pores in the fuel particles grew to a few micrometers in diameter. Magnesium was detected only trace amount (Fig. 8.5.2 (e)). Some amounts of Xe and Cs remained in YSZ. Although the aspects of fuel were changed extremely, the changes of FP distribution were little and large amounts of FPs were remained in YSZ phase. In this region, a new hibonite formation was found. The plate-like grains seen in Fig. 8.5.2 (a) are the hibonite phases. It is confirmed that the hibonite was consist of Ba ($BaAl_{12}O_{19}$) or Nd ($NdAl_{11}O_{18}$, $NdMgAl_{11}O_{19}$). Almost of magnesium existed in this region formed hibonite, not spinel. The hibonite might be the host phase of trivalent actinide element such as Pu and Am. In practice, the hibonite formation with Pu ($PuMgAl_{11}O_{19}$) was observed in previous study. Though the many properties of hibonite are unknown, it is reported that the hibonite has sufficient chemical durability from the geological safety point of view. So the formation of hibonite is not necessarily unsuitable.

For CD fuel, no reaction layer was observed. Distribution of Nd was similar to those of U and Zr. Ruthenium and Mo were found as fine inclusions in U-YSZ phase, and a part of Cs and Xe migrated to pores in YSZ and escaped through cracks of matrix. The FP distribution states of CD fuel were analogous to those of SD fuel. For CD fuel, the FP distributions at center region were almost similar to that at outer region. At the most, the difference was that the size of fine inclusions of Mo and Ru became larger, because of higher irradiation temperature at center region.

Table 8.5.1. Estimated irradiation condition and burn-up of ROX fuels

Fuels	Z	SD	CD	SH	CH
Linear power / $kW \cdot m^{-1}$	13.9	23.0	24.9	23.4	20.7
Temperature at					
Surface of pellet / K	990	1250	1300	1440	1290
Center of pellet / K	1490	1740	1820	1940	1730
Burn-up					
^{235}U / %	21.01	23.28	23.89	24.15	20.87
/ $GWD \cdot m^{-3}$	59	100	105	103	88

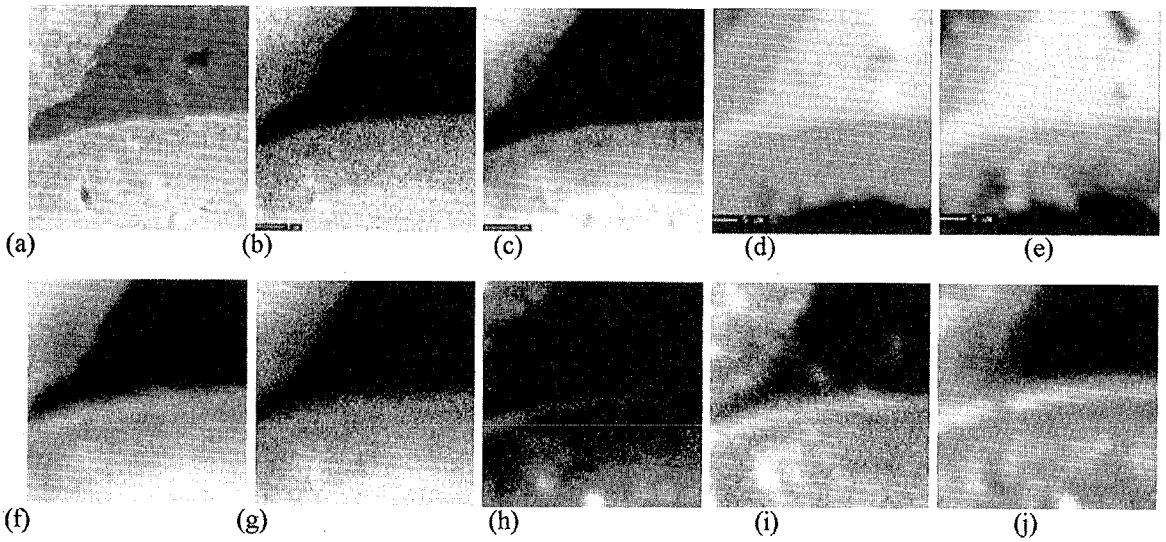

Fig. 8.5.1. Typical SEM image and characteristic X-ray picture on the outer region of SD fuel
(a) SEM, (b) Zr, (c) U, (d) Al, (e) Mg, (f) Ba, (g) Nd, (h) Ru, (i) Cs and (j) Xe.

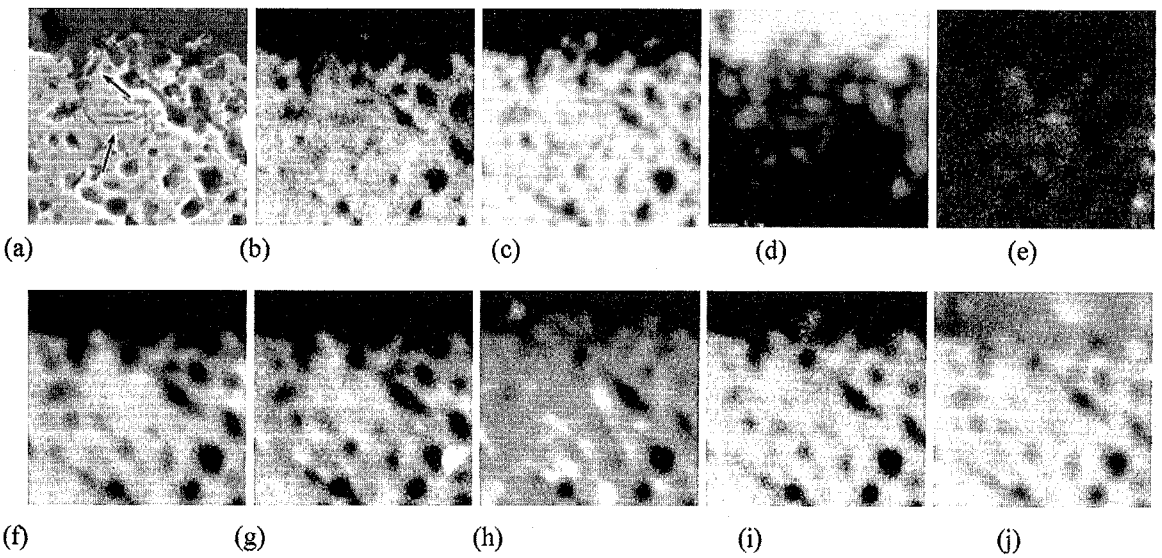

Fig. 8.5.2. Typical SEM image and characteristic X-ray picture on the middle region of SD fuel
(a) SEM, (b) Zr, (c) U, (d) Al, (e) Mg, (f) Ba, (g) Nd, (h) Ru, (i) Cs and (j) Xe.

8.6 Fabrication of Macro Grain Dispersed Type Rock-like Oxide Fuels

N. Nitani, K. Kuramoto, Y. Nakano and T. Yamashita
(*E-mail: noriko@popsvr.tokai.jaeri.go.jp*)

On the development of rock-like oxide fuel, we have proposed a particle-dispersed type fuel for the improvement of swelling behavior. In the case that appropriate size of YSZ particles are dispersed homogeneously in the spinel or corundum matrix, damaged area by fission fragments of the matrix is limited to thin layers surrounding the particles. However, special apparatus and technique are necessary to fabricate of particle-dispersed fuel. So, we proposed a new type fuel, or macro grain dispersed type fuel that can be fabricated by use of current facilities. The macro grain dispersed type fuel is fabricated by sintering the mixture of YSZ macro grains and fine powder of matrix. The macro grain dispersed type fuel as well as particle dispersed type fuels will be able to restrain the amounts of matrix fission damage, and they have the advantage against micro-dispersed and homogeneously-blended type fuels for matrix fission damage. In this study, $MgAl_2O_4$, spinel, and Al_2O_3, corundum, were selected as inert matrix (S and C fuel).

Before we start the fuel preparation, we had carried out some cold trial experiment to find the optimum conditions for the fuel fabrication; temperature of calcination, pelletizing pressure, blending methods and so on. Those factors were examined systematically, and the fuel fabrication methods were established. Designed amounts of YSZ and UO_2 powders were mixed and calcined at 1550 °C for 24 hours in a stream of 4% H_2 + He, and then grained by a zirconia ball mill to obtain fine powdered solid solution with U and YSZ. The amount of fissile element was determined by burnup calculation to control the irradiation temperature. The powder was pressed uniaxially and calcined at 1300 °C for 24 hours. The density of the resultant calcined pellet was about 65%TD. It is required that shrinkage ratio of the calcined grain and matrix at the sintering temperature must be controlled as same grade by adjusting the calcined grain density. The density of fuel pellet prepared with 95%TD YSZ grains and fine powder of matrix was 85% at the best. For the pellets made of high dense sintered grains and matrix powder, many cracks and considerable gaps between grain and matrix were observed.

The calcined pellets were crushed into pieces, and the grains whose size was 125 –

250 μm were sifted out. And then the grains and a matrix were mixed uniformly, pressed at 370 MPa uniaxially, and sintered at 1550 °C for 24 hours in the stream of 4% H_2 + He. The size and density of resultant pellets for S and C fuels are listed in Table 8.6.1. The fabricated pellets showed high densities (>92%). Fig. 8.6.1 shows the appearances and the aspects of ROX fuels. The homogeneous distribution of the YSZ grains in the matrix was confirmed by the ceramography. The grains showed appropriate sizes, about 100 – 200μm. Although some gaps were observed between YSZ grain and matrix, it does not matter because the thermal expansion of YSZ particle is higher than that of the matrix.

Table 8.6.1 Size and relative density of ROX fuels

(a) S [macro grain dispersed type and spinel matrix] fuel

No.	Weight(g)	Diameter (mm)	Height (mm)	Density (g/cm^3)	App. density (%TD)	^{235}U density ($10^{20}/cm^3$)
1	0.6818	5.19	5.74	5.63	93.8	11.44
2	0.6715	5.19	5.69	5.58	93.0	11.34
3	0.6641	5.19	5.62	5.59	93.1	11.36
4	0.6722	5.20	5.67	5.58	93.1	11.35
5	0.6598	5.21	5.55	5.59	93.2	11.36
6	0.6655	5.19	5.62	5.60	93.3	11.38
7	0.6652	5.20	5.65	5.54	92.4	11.27
8	0.6780	5.20	5.71	5.59	93.2	11.37
9	0.6600	5.19	5.57	5.60	93.4	11.39
10	0.6769	5.20	5.70	5.59	93.2	11.37
Av.				5.59	93.2	11.36

Theoretical density of Z fuel is 6.00 g/cm^3.

(b) C [macro grain dispersed type and corundum matrix] fuel

No.	Weight(g)	Diameter (mm)	Height (mm)	Density (g/cm^3)	App. density (%TD)	^{235}U density ($10^{20}/cm^3$)
1	0.6934	5.18	5.63	5.86	94.4	11.52
2	0.7073	5.20	5.78	5.77	93.1	11.35
3	0.6881	5.19	5.61	5.80	93.5	11.40
4	0.7098	5.19	5.78	5.80	93.6	11.42
5	0.7039	5.20	5.76	5.75	92.8	11.32
6	0.6941	5.20	5.71	5.73	92.5	11.28
7	0.6980	5.21	5.75	5.71	92.0	11.22
8	0.6946	5.21	5.68	5.74	92.5	11.28
9	0.6885	5.22	5.61	5.73	92.5	11.28
10	0.7008	5.21	5.74	5.74	92.5	11.28
Av.				5.76	92.9	11.33

Theoretical density of Z fuel is 6.20 g/cm^3.

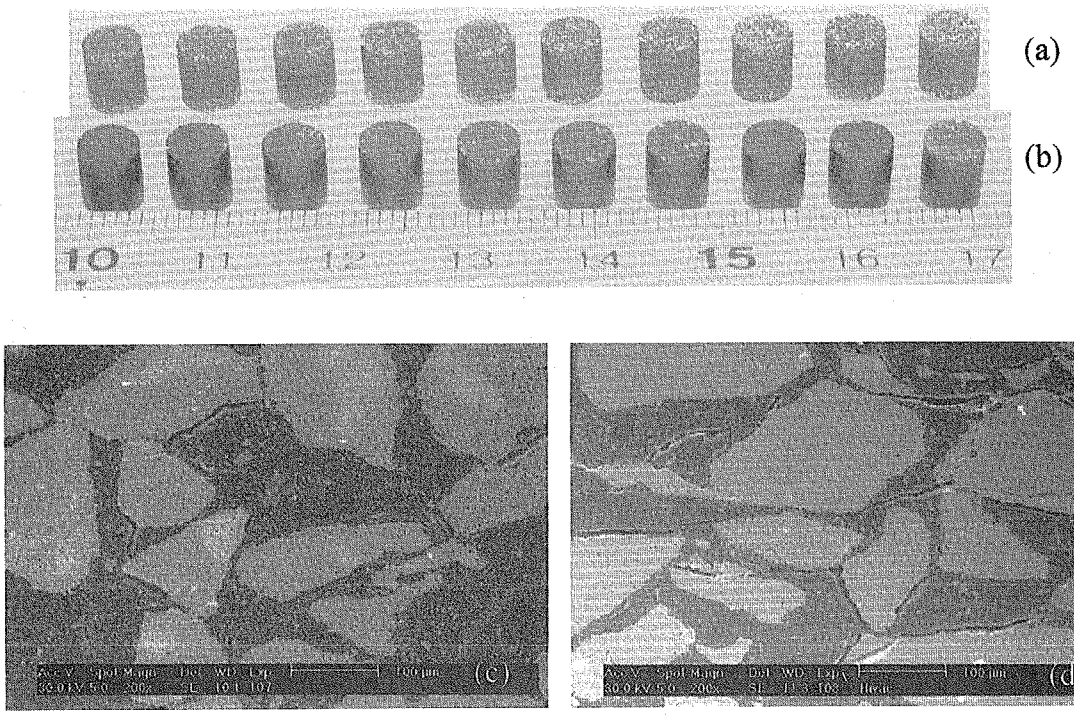

Fig. 8.6.1
Appearances and aspects of ROX fuels submitted to the irradiation test
Appearance of (a) S fuel and (b) C fuel, and
Aspects of (c) S fuel and (d) C fuel

8.7 Experimental Procedure of Leach Test for Irradiated Rock-Like Oxide (ROX) Fuels

K. Kuramoto, N. Nitani and T. Yamashita
(E-mail: kura1@nucef.tokai.jaeri.go.jp)

The ROX-LWR concept consists of fabrication of stable ROX fuels in conventional fuel facilities, almost complete Pu burning in LWR and disposal of chemically stable spent fuels without further processing. In our previous works we have showed that ROX could be fabricated simply, transmute Pu twice as much as MOX fuel for reactor-grade Pu in LWR and be irradiated in LWR with comparable safety to UO_2 fuels. The ROX concept can be completed successfully by establishing good performance of spent ROX fuels after geological disposal. The important radiotoxic nuclides are TRU (Np-237 and Am-243) and β-emitters with long half-lives such as Cs-135, Tc-99, Se-79, I-129, Kr-81, Sn-126. These elements as well as matrix elements leached from the irradiated ROX fuel would exist as ions and/or colloidal species in leachate and/or as precipitates on a vessel and a sample holder. Thus, the leach rate of the important nuclides and elements must be estimated by total amount existing in leachate and precipitates. In addition, the amount of colloids must be estimated quantitatively, because the colloidal species will influence the equilibrium in the solution and migration of the nuclides and the elements.

Five kinds of irradiated fuels (Z, SD, SH, CD and CH) were used for the present leach tests. Six disk specimens with 2 mm height were cut out from each irradiated ROX pin including stainless steel cladding. The surface area of each specimen is ~ 0.45 cm^2. Leachate is 50 ml of deionized water and temperature is controlled at 90 °C. Leaching period is 8, 24, 60, 115 and 173 days. One specimen is submitted to each leaching periods of 8, 24, 60 and 115 days, and two specimens to leaching period of 173 days. Vessels used in the tests are made from stainless steel and inside surfaces were coated with 20 μm-thick Au. The packing is made from ethylene propylene diene monomer. For a specimen holder, vinyl chloride frame and Pt wire were used.

Leach tests were performed at the No.4 hot cell of Waste Safety Testing Facility in JAERI. Weight of the vessel including a specimen, leachate and a sample holder was measured every 2 weeks to check the leakage amount of leachate. Weight loss of every leachate was less than 2 % of the initial weight even after 173 days, which is within the MCC-1 regulation. Figure

8.7.1 shows the sampling flow after leach tests. After the given leaching period, vessels were pull out from an oven and pH measurements were made. The leachate was passed through a 0.20 μm-filter to remove small amounts of fuel fragments. The filtrated leachate was transferred to a glove box and was distributed evenly into two bottles. A designed amount of nitric acid was added to one bottle to adjust its nitric acid concentration of the leachate to 0.1 mol/l (Leachate A: LA). The other half leachate was passed through a 1.8 nm-ultrafilter, and then a designed amount of nitric acid was also added to the leachate (Leachate B: LB). To investigate the amount of precipitation on the vessel and sample holder quantitatively, 0.1 mol/l of nitric acid was added to a used vessel including a used sample holder, heated up at 90 °C for 1 week and the solution was passed though a 0.20 μm-filter (Leachate C: LC). The total amounts leached from the irradiated ROX fuels were obtained by concentration measurements in LA and LC. Colloids of the important elements and nuclides were obtained quantitatively by comparing the concentration in LA and LB. Additionally, a distribution factor between the precipitate and the solution could be estimated by concentration comparison in LA and LC.

To remove Cs from LA, LB and LC, 0.020 g of ammonium phosphomolybdate ($(NH_4)_3PO_4/12MoO_3/nH_2O$: AMP) was added to every leachate. The mixture was shaken and settled for 10 minutes, and shaken again. After 10 minutes settlement, the mixture was 0.20 μm-suction filtrated. More than 99.9 % of Cs could be removed from the leachate by these operations.

After Cs separation by AMP, the concentration of matrix elements, TRU and the β-emitters with long half-lives except for Cs in LA, LB and LC were determined by inductively-coupled plasma-mass spectroscopy (ICP-MS). Mass numbers from 24 to 27, 50-172, 192-198 and 204-260 were measured using a standard solution by calibration curve method. The normalized leach rate of element k (NL_k, in g/cm^2/day) is given by the following equation (1).

$$NL_k = (C_{k\text{-}LA} + C_{k\text{-}LC})*V/SA/F_k/T, \qquad (1)$$

where, $C_{k\text{-}LA}$ and $C_{k\text{-}LC}$ are concentration in g/ml of element k in LA and LC, respectively, V is leachate or solution volume in ml, SA is the initial surface area of specimen in cm^2, F_k is the mass fraction of element k in a specimen and T is the leaching period in day. Additionally, normalized total leached amount of element k (NLA_k, in g/cm^2) and normalized leach amount of element k ($NLA_{k\text{-}LA}$, $NLA_{k\text{-}LB}$ and $NLA_{k\text{-}LC}$, in g/cm^2) in LA, LB or LC are presented as the following equations (2), (3), (4) and (5), respectively.

$$NLA_k = (C_{LA} + C_{LC})*V/SA/F_k, \qquad (2)$$

$$NLA_{k\text{-}LA} = C_{k\text{-}LA}*V/SA/F_k, \qquad (3)$$

$$NLA_{k\text{-}LB} = C_{k\text{-}LB}*V/SA/F_k, \quad (4)$$

$$NLA_{k\text{-}LC} = C_{k\text{-}LC}*V/SA/F_k, \quad (5)$$

Meaningful counts of Mg and Sn were not detected by ICP-MS because of contamination from AMP, the equipment, the hot-cell and the glove box. Because only stable elements of I-127 and Se-82 were detected by ICP-MS, these data were corrected by the ratio of mass fraction $F_{I\text{-}129}/F_{I\text{-}127} = 4.24$ and $F_{Se\text{-}79}/F_{Se\text{-}82} = 0.16$ to obtain leach rate and leach amounts of I-129 and Se-79. Measurement of Kr was not carried out because Kr is inert gas and may volatilize quickly during the procedure and Kr standard solution was not available.

Leach rate and leach amount of Cs-135 were estimated by γ-ray measurement of the leachate before Cs separation using Li-drifted type Ge semiconductor detector. Cs-137 with the γ-ray at 661.64 keV were detected in the LA, LB and LC solutions. The counting time was 3600 seconds. Normalized leach rate and normalized leach amount of Cs-135 is given to the following equations (6) and (7), respectively.

$$NL_{Cs\text{-}135} = ((A_{Cs\text{-}137\text{-}LA}+A_{Cs\text{-}137\text{-}LC})/10/\lambda)*(137/N)*V/SA/F_{Cs\text{-}135}/T, \quad (6)$$

$$NLA_{Cs\text{-}135} = ((A_{Cs\text{-}137\text{-}LA}+A_{Cs\text{-}137\text{-}LC})/10/\lambda)*(137/N)*V/SA/F_{Cs\text{-}135}, \quad (7)$$

where, $A_{Cs\text{-}137\text{-}LA}$ and $A_{Cs\text{-}137\text{-}LC}$ is radioactivity of Cs-137 in LA and LC in 10.0 ml, λ is decay constant of Cs-137 in second, and N is Avogadro's constant.

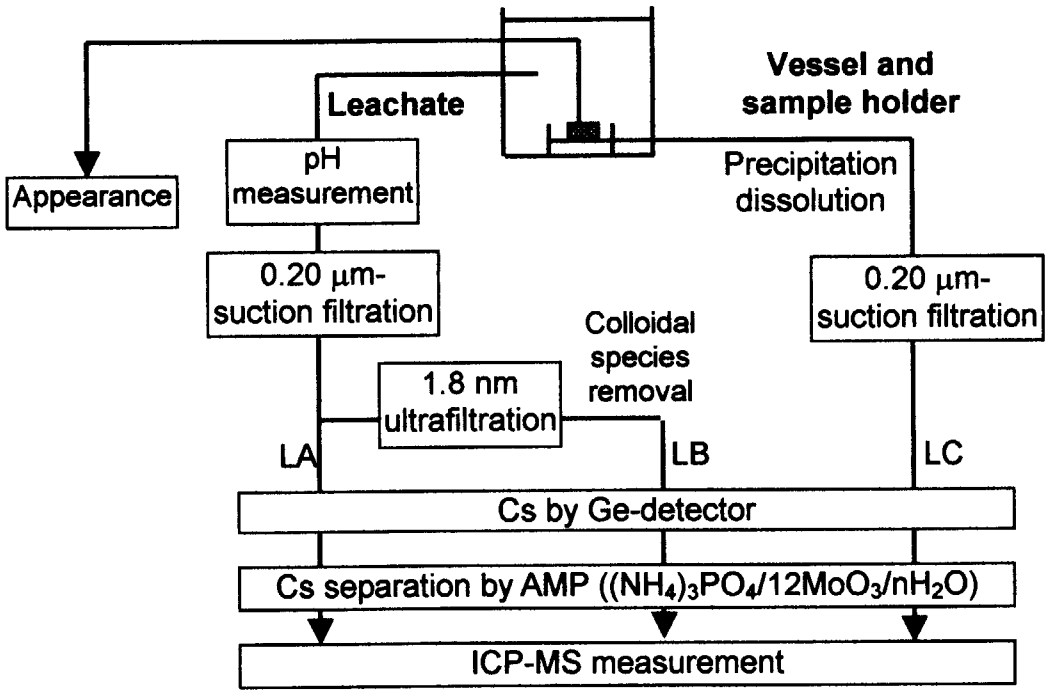

Figure 8.7.1 Sampling flow after leach test.

8.8 Improvement of Power Distribution of Plutonium Rock-like Oxide Fuel Partial Loading PWR Core

H. Akie, Y. Sugo*, R. Okawa**
(*E-mail*: akie@mike.tokai.jaeri.go.jp)

Plutonium rock-like oxide (ROX) fuel (PuO_2-$(Zr,Y,Gd)O_2$-$MgAl_2O_40$ in a LWR burning system has been studied for its potential of high plutonium transmutation rate. This type of U-free matrix fuel, however, has smaller negative reactivity coefficients and severer transient behaviors in comparison with UO_2 fuel core [1]. In order for the improvement of these ROX-LWR core behaviors, a partial loading core concept was studied, where the ROX fuel assemblies are partially loaded in a UO_2 fuel core. Although it was found effective to improve the reactivity coefficients and accident behaviors of ROX fueled core, the ROX partial loading core still has large power peaking factor, and further improvement seemed necessary [1].

Without containing any fertile nuclides, ROX fuel tends to have large burnup reactivity swing. In order to suppress this excess reactivity, Gd_2O_3 burnable poison was used in the original ROX fuel. The Gd burnable poison efficiently reduce the excess reactivity at BOL, and loses its effect very quickly with burnup. As a result in a batch loading core, this burnup reactivity swing causes a large power level mismatch between fuel assemblies at different burnup stages [1]. To avoid this, Er_2O_3 burnable poison is chosen instead of Gd_2O_3 in ROX fuel. The Er poison has not such large effect on reactivity as Gd in LWR, and gradually decreases with burnup.

Local power peaking within an assembly in the ROX and UO_2 assemblies partial loading system takes place near the gap between ROX and UO_2 assemblies because of the neutron spectrum difference. For example in the 4-assembly model of a ROX assembly and 3 UO_2 assemblies based on 17×17 type PWR assembly as shown in Fig. 8.8.1, the power peak appears at pin "A" at BOL, and at pin "B" at EOL. For the power peaking reduction, the Pu enrichment at the corner part of ROX fuel assembly is reduced at the same time of increasing Er content. For the reduction of the power peak at pin B in UO_2 assembly at EOL, the Pu enrichment and Er content are increased in the several ROX pins along ROX-UO_2 assembly

* Information Technologies Japan Inc. **The Japan Research Institute, Limited

gap on the other side of pin B. As a result of the assembly burnup calculations by using the SRAC95 system [2] in the weapons-grade Pu (W-Pu) ROX fuel assembly system, it is possible to reduce the local peaking factor to less than 1.2 at BOL, and to less than 1.3 at EOL. The power peaking factor also becomes less than 1.2 in the reactor-grade Pu (R-Pu) system.

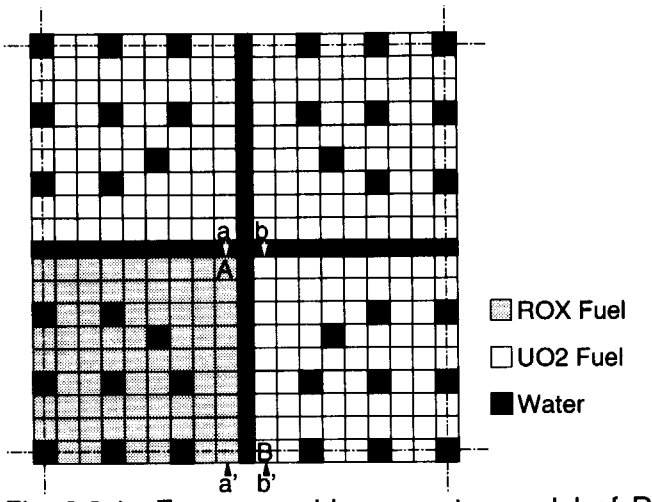

Fig. 8.8.1 Four assembly geometry model of ROX and UO_2 fuels based on 17x17 type PWR.

Axial power distribution flattening is also aimed by considering Er content distribution in the axial direction of fuel pin. By increasing the Er content at the core center, and decreasing at the core bottom and top, it is estimated possible in the one-dimensional core burnup calculations to reduce the axial power peaking factor to be as low as 1.2.

Core radial power peaking is then estimated by the two-dimensional X-Y core burnup calculations on a core model based on 17×17 type 1100 MWe class PWR with the assumption of 3-batch refueling. The loading and refueling pattern is surveyed for ROX and UO_2 assemblies at 1st, 2nd and 3rd burnup cycles, and the core radial power peaking factor of 1.2 is obtained both for W-Pu and R-Pu ROX partial loading cores. The total power peaking of radial × axial × local peaking factors is 1.7 for W-Pu core, and 1.8 for R-Pu core. The estimated core characteristics are summarized in Table 8.8.1.

By using these core characteristics, reactivity initiated accident (RIA) and loss of coolant accident (LOCA) behaviors are analyzed with EUREKA-2 [3] and RETRAN2 [4] codes, respectively. The results are shown in Table 8.8.2. In the original ROX partial loading

Table 8.8.1 Doppler reactivity (%$\Delta k/k$) and power peaking factor of ROX fuel partial loading cores at BOC

	Doppler reac. (900→1200K)	Peaking factor
Weapons-Pu 1/3ROX+2/3UO_2 (original)	-0.48	2.8
(modified)	-0.53	1.7
Reactor-Pu 1/3ROX+2/3UO_2 (modified)	-0.48	1.8
UO_2	-0.75	2.0

core, the maximum fuel enthalpy in RIA event is larger than 0.96 MJ/kg, which is the current UO_2 pin failure condition in RIA. In the pulse irradiation experiments of ROX fuels at Nuclear Safety Research Reactor (NSRR) of JAERI, the failure condition of ROX fuel pin was shown to be almost the same as that of UO_2 fuel pin in terms of volumetric enthalpy [5]. The volumetric enthalpy values are also shown in this table. The pin failure condition in this unit will be about 10 GJ/m^3. In the original ROX partial loading core, the enthalpy value is still larger than that in the UO_2 core, even though there is a margin to the pin failure condition. In the LOCA analysis, the cladding temperature is less than the limitation value of 1470 K (1200 °C) in the original ROX partial loading core, and is also still larger than that in the UO_2 core. It is worth further improving the accident behaviors to the comparable level to UO_2 core.

With the improved power distribution and reactivity coefficients evaluated in Table 8.8.1, the fuel enthalpy in RIA and cladding temperature in LOCA are both well improved as low as those of UO_2 core, both for W-Pu and R-Pu ROX partial loading cores.

Table 8.8.2 Maximum fuel enthalpy (H) in RIA and peak cladding temperature (T_{PC}) in LOCA of ROX fuel partial loading cores

	RIA		LOCA
	H (MJ/kg)	H (GJ/m^3)	T_{PC} (K)
Weapons-Pu 1/3ROX+2/3UO_2 (original)	1.02	5.7	1240
(modified)	0.75	4.2	1080
Reactor-Pu 1/3ROX+2/3UO_2 (modified)	0.79	4.4	1070
UO_2	0.39	4.3	1080

References

1) H. Akie, H. Takano, and Y.Anoda : J. Nucl. Mater. 274, 139-145 (1999).

2) K. Okumura, K. Kaneko and K. Tsuchihashi : JAERI-Data/Code 96-015 "SRAC95; General Purpose Neutronics Code System" (1996) (in Japanese).

3) N. Ohnishi, T. Harami, H. Hirose and M. Uemura : JAERI-M 84-074 "EUREKA-2 : A Computer Code for the Reactivity Accident Analysis in a Water Cooled Reactor" (1984) (in Japanese).

4) C.E. Peterson, J.H. McFadden, M.P. Paulsen and G.C. Gose : EPRI NP-1850 CCM (1981).

5) T. Nakamura, K. Kusagaya, M. Yoshinaga, H. Uetsuka, T. Yamashita : Prog. Nucl. Energy, 38, 379-382 (2001).

9. Research on Small Reactor for Dispersive Energy Supply System

Concept designs of two small-scale reactors for dispersive energy supply systems, which will be sited close to demand areas, have been studied by taking over the results of the nuclear ship research activities. Enhancements of safety and economy are focused on the design study. The one of the reactors is the MR-100G with thermal output of 100 MW exclusive for district heat supply, which has been studied from 2000, and the other is a PSRD-100E with thermal output of 100 MW for small grid electricity supply, which has commenced in 2001.

Regarding the district heat supply system with the MR-100G, the reactor is designed to be sited at a deep underground in depth of about 50m. Feasibility studies on construction of reactor system at the deep underground and economics of the system have been conducted. A cave to install the reactor at the deep underground should stand up to the ground pressure and the stress caused by an earthquake. The static and dynamic stabilities of the underground cave have been confirmed analytically. A construction method for the cave also has been studied. Construction and operation costs of the heat supply system with MR-100G have been evaluated by comparing with the costs by the LNG boiler.

In design of PSRD-100E, the major parameters such as the dimensions of reactor vessel, and the operation pressure, temperature, core flow rate, etc., have been determined. The reactor core has been designed for a long life cycle –about 10 years– of operation until refueling, after analyzing using the neutronics code system, SRAC95.

To enhance safety of the reactors, a passive reactor shut down system for in case of an anomaly is adopted together with the in-vessel type control rod driving mechanism (CRDM), which has been already developed. A concept of passive reactor shut down has been studied.

9.1 Study on Very Small Reactor for Heat Supply -Possibility of Deep Underground Siting: Examination of Static Stability for a Cave-

N. Nakajima, T. Kusunoki and H. Takahashi
(*E-mail*: nakajima@popsvr.tokai.jeari.go.jp)

Japan Atomic Energy Research Institute has been studying the possibility of installing a reactor system in energy demand areas, such as a big city, to expand nuclear energy utilization in various civilian applications[1]. A nuclear heat supply system is one of the promising applications, while the reactor should be sited close to demand area due to loss of heat transfer within about 5km. Office buildings, apartments and other concrete structures already exist in a big city. Several kinds of transportation networks such as automobile road systems and rapid transit railway network have been also developed recently. Therefore, there are many restrictions for installing in a big city. The underground, however, has a possibility of a strong candidate for the reactor installation place.

The deep underground that implies the place (deeper than 50m below the ground revel) recently can be used only for public interests by urban regulations such as Tokyo or Yokohama. Since the areas where these big cities exist are once to be big rivers, the ground are not always firm. It is difficult to find out the Tertiary system in these areas, so that the reactor is taken to be sited underground in Quaternary system. The dimensions of cave to install the reactor system of about 100 MW of thermal powers are 8.5m in the diameter, and 22m height. Since there is no experience, which built such a large cave in the Quaternary system in deep underground, the static analysis is necessary to examine the possibility of cave construction.

In order to build the cave in the weak foundations of the Quaternary system, a special construction method is required to prevent subsidence of the ground surface, collapse of a ground, and flood of ground water die to its construction. In the present study, the construction method which refers to the existing construction approach is adopted as shown in Fig. 9.1.1 with that for the case of the Tertiary system. Since the base rock is firm in the case of the Tertiary system, it is not necessary to adopt a special construction method. In the case of the Quaternary system, the upper part of cave is reinforced to prevent various kinds of hindrance with a temporary structure of an upper advancing tunnel (inside diameter: 7m) and a pipe roofing (diameter: 0.9m). At the side part of cave, diaphragm walls as a temporary

structure are built.

Technical feasibility of the cave depends on the amount of subsidence of ground surface and the local stress concentration of the temporary structure due to the cave construction. The permissible subsidence is 2-3cm in the case of a general reinforced-concrete building and 4-7mm in the case of a railroad orbital and 4mm in the case of a rapid railway. The subsidence and stress profile of the cave were analyzed by SIGNAS code. The ground properties used in the analysis are shown in Table 9.1.1. The detail of the mesh configuration, the number of node, and the number of plane element are shown in Fig.9.1.2.

As a result of analysis, it became clear that the stress concentration of the junction part of the pipe roofing and the upper advancing tunnel is large, so some cases are examined to see the effect of improvements construction method. Consequently, the amount of subsidence ground surface can be about 4.5mm by reinforcing the junctions, and it is possible to build such a big cave to in the underground of the Quaternary system. The amount of subsidence in the case of the Tertiary system is very small, about 0.06mm.

It is planning on about the behavior in the dynamic analysis of this underground cave, i.e., a great earthquake, and synthetic underground cave formation is examined including the stability not only under construction but after construction.

Reference

1) N. Nakajima et al: JAERI-Review 2002-005 (2002) 244-246

Table 9.1.1 Lists of ground mechanical properties

	Quaternary system	Tertiary system
Density g/cm^3	1.90	1.85
Elastic constant MPa	100	300
Poisson's ratio	0.350	0.300
Shear strength MPa	0.100	1.00
Angle of internal friction °	35.0	15.0

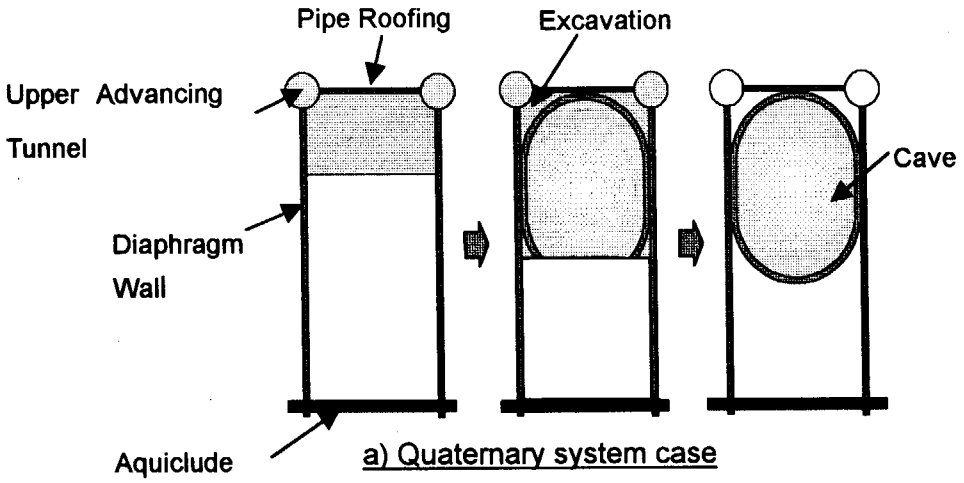

Fig.9.1.1 Construction procedure of the cave

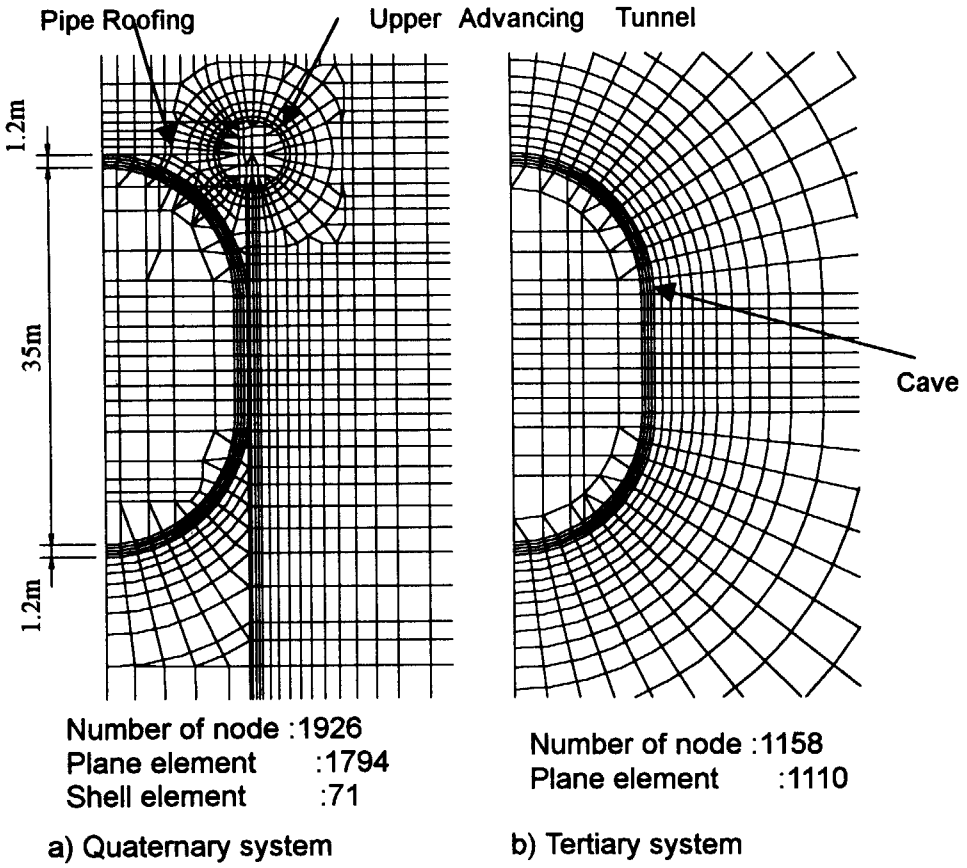

Fig.9.1.2 Static analysis method of the underground cave

9.2 Study on Very Small Reactor for Heat Supply - Evaluation of Economy -

H. Takahashi, N. Nakajima and T. Kusu-noki
(*E-mail:* htaka@popsvr.tokai.jaeri.go.jp)

JAERI has been studying a concept of "MR-100G" which is a very small reactor exclusive for heat supply, with thermal-power of 100MW. The heat supply system with the MR-100G is designed to be sited at depth underground[1]. Influences of the reactor power scale of the hear-source unit on construction and operation costs were surveyed by considering system optimization.

A heat-source unit consists of some main cavities and an auxiliary cavity. One MR-100G is installed in one main cavity. Because, the reactor is installed inside a deep underground cavity, the maximum reactor size is limited from the viewpoints of cavity stability etc. The MR-100G is the limit size that can be installed in the cavity. The auxiliary facilities, the spent fuel storage facility, etc., are installed in an auxiliary cavity.

Introduction of the heat supply system to areas of high population density is effective. In the present study, the heat supply system with MR-100G was assumed to supply the heat to a virtual city of 100,000 populations. The data of this virtual city is shown in Table 9.2.1. The amount of required energy for the district heat and cooling, the air conditioning and the hot-water supply, except the electricity was estimated as 200MW, that is, two MR-100Gs for the heat supply system of this city[2), 3)]. Therefore, two main cavities with the MR-100G are necessary for the virtual city. For larger city than this virtual city, more main cavities for the MR-100Gs are necessary.

The cost of heat-source unit construction was estimated for the case of two to eight MR-100Gs. Taking account of the population density in a city, the number of people population living in the area where heat supply is available, that is, inside the circle radii of 5 km will not exceed 400,000 person.

In this paper, MR-100Gs were taken as the heat source for 400,000 person in that area. The construction cost of heat-source unit per MR-100G is found to be

Table 9.2.1 Data of a virtual city

City feature	Most of apartment houses and office buildings are very close
Area	Less than 50km^2 (inside the circle radii of 5km)
Population	100,000 persons (he has no population outflow close)
A birth ratio, mortality rate	from Japanese 1999 data
Number of households	40,000
Household average population	2.5 persons
Climate	about the same as Tokyo

smaller with MR-100G to increase (Fig.9.2.1).

To evaluate economy, the costs of construction and fuel were compared between the MR-100G heat-source unit and a natural gas (LNG) boiler unit. The cost comparison is shown in Fig.9.2.2 for the case of heat capacity of 400MWt, by neglecting the construction costs of the common heat supply system such as the air-conditioning pipe, the heat utilities and so on. It is shown that the MR-100G heat supply system is advantageous after 32 years operation.

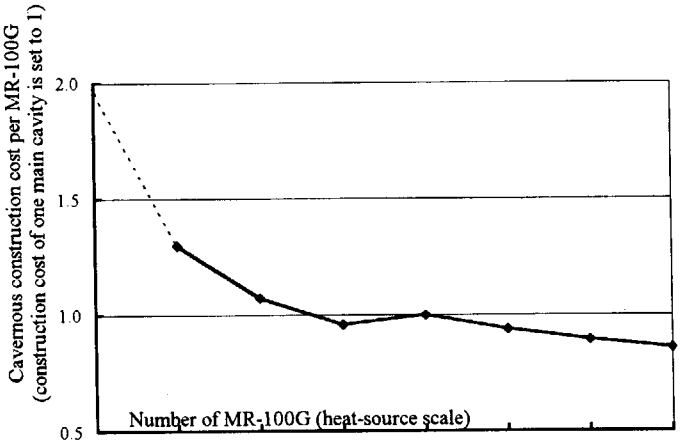

Fig.9.2.1 The relation between cavernous construction cost and the number of MR-100G

As a reference case where the construction cost of MR-100G is half, the costs were compared similarly. The result is shown in Fig.9.2.3, which shows the MR-100G heat-source unit competes from the beginning of operation. Therefore, in order to enhance economy, the reduction of a reactor cost is very effective.

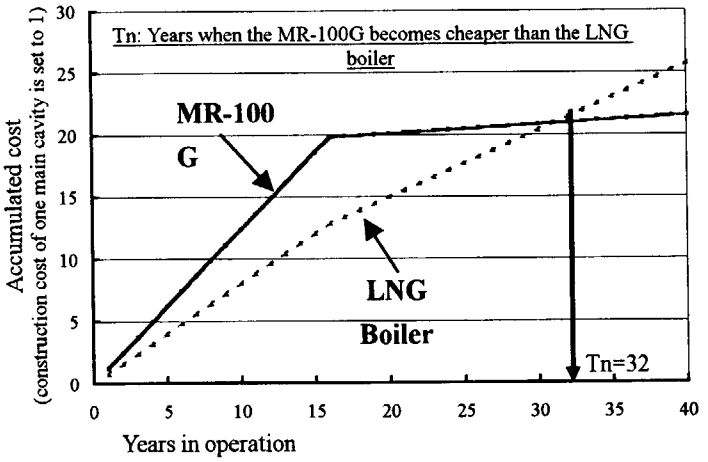

Fig.9.2.2 Cost comparison

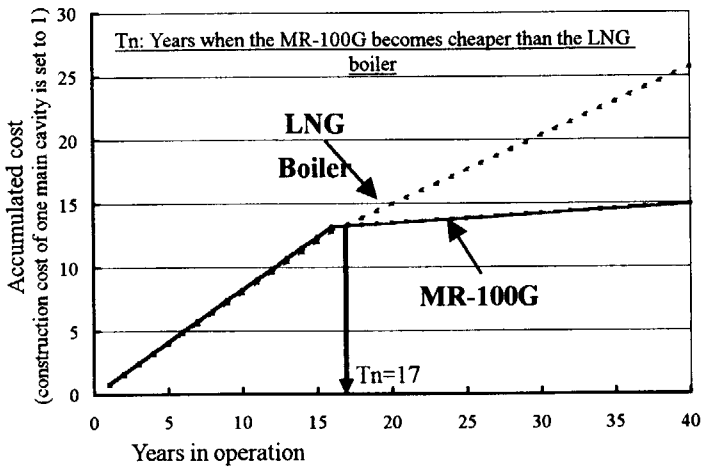

Fig.9.2.3 Cost comparison (In the reference case)

References

1) N.Nakajima et al : JAERI-Review 2002-005 (2002) 244-246

2) H.Takahashi et al : "Study on Very Small Reactor for Heat Supply (6)" *2001 Annual Meeting of the Atomic Energy Society of Japan*, J5 (2000)

3) N.Nakajima et al : "Study on Very Small Reactor for Heat Supply (8)" *2001 Annual Meeting of the Atomic Energy Society of Japan*, J7 (2000)

9.3 Design Study on a Very Small Reactor for Small Grid Electricity Supply

K. Sawada, T. Ishida, T. Yoritsune and S. Kuga
(*E-mail*: sawa@koala.tokai.jaeri.go.jp)

Japan Atomic Energy Research Institute has carried out a conceptual design study of a passive safe small reactor for distributed energy system, PSRD-E100. The reactor of PSRD-E100 is the energy source with thermal output of 100MW for small grid electricity supply. The PSRD-E100 has been designed on the base of design technologies of the advanced marine reactor, MRX and current light water reactors.

The schematic concept of pressure vessel is shown in Fig.9.3.1. The PSRD-E100 is an integral type reactor: installing major primary components inside the reactor pressure vessel, and adopting self-pressurization and natural circulation cooling in the primary coolant system. The core reactivity is controlled by only using the control rod without the soluble boron, because the chemical volume control system is not operated during operation besides refueling or uncovering the reactor pressure vessel. These make the reactor plant to be compact and the frequency of LOCA occurrence greatly to be reduced. The in-vessel type control rod driving mechanism (INV-CRDM) is used to eliminate the possibility of occurrence of a rod ejection accident. Since the INV-CRDMs are set for all fuel assemblies, the area of primary coolant flow can not help being small. In order to ensure the flow area, layout of the control rods and fuel rods in the fuel assembly is suitably arranged. The two phase natural circulation flow in primary system is adopted to generate large driving force. The steam generator is the type of helical coil tube suitable to the integral type reactor. The upper side of steam generator is designed to be exposed to vapor phase. This means that both of the vapor phase and the liquid phase of the primary coolant can be cooled by the steam generator. The void fraction of the core outlet is 10 %, which assures change of the water level in the pressure vessel between in the states of the cold and the normal operation to be a permissible range. As the results, the dimensions of the pressure vessel are four meters in diameter and 9.6 meters in height.

One of core design goals is to achieve long core life term which is for 10 years with the load factor of 50 %, in order to improve economy. The zyrcaloy-4 cladding UO_2 fuel rods with U-235 enrichment of below 5 % are used for the PSRD core. Major parameters of the core are shown in Table 9.3.1. The pitch of fuel rods 13.9 mm is larger than that of the current

PWRs, 12.9 mm. The large pitch contributes to reduce the core flow resistance make the core burnup to be longer. To reduce the excessive reactivity at the beginning of core life, the fuel rods include Gd_2O_3 with weight of 6 wt% as burnable absorber. The reactor power is controlled by only the control rods. Number of the control rod drive mechanisms is 37, 21 for control-shutdown system and 16 for backup shutdown system. Nuclear characteristics have been evaluated by the neutronics code system, SRAC95 [1]. Fig.9.3.2 shows the typical result of burnup calculation. The calculation shows that the core life can be 9.8 years considering with condition of having the margin of 2 %Δk/k reactivity for being capable of restarting of reactor any time in the life. The shutdown capacity for both control-shutdown system and backup shutdown system has enough safety margins for the cold shutdown of reactor.

Reference

1) K. Okumura, K. Kaneko and K. Tsuchihashi: "SRAC95; General Purpose Neutronics Code System", JAERI-Data/Code 96-15

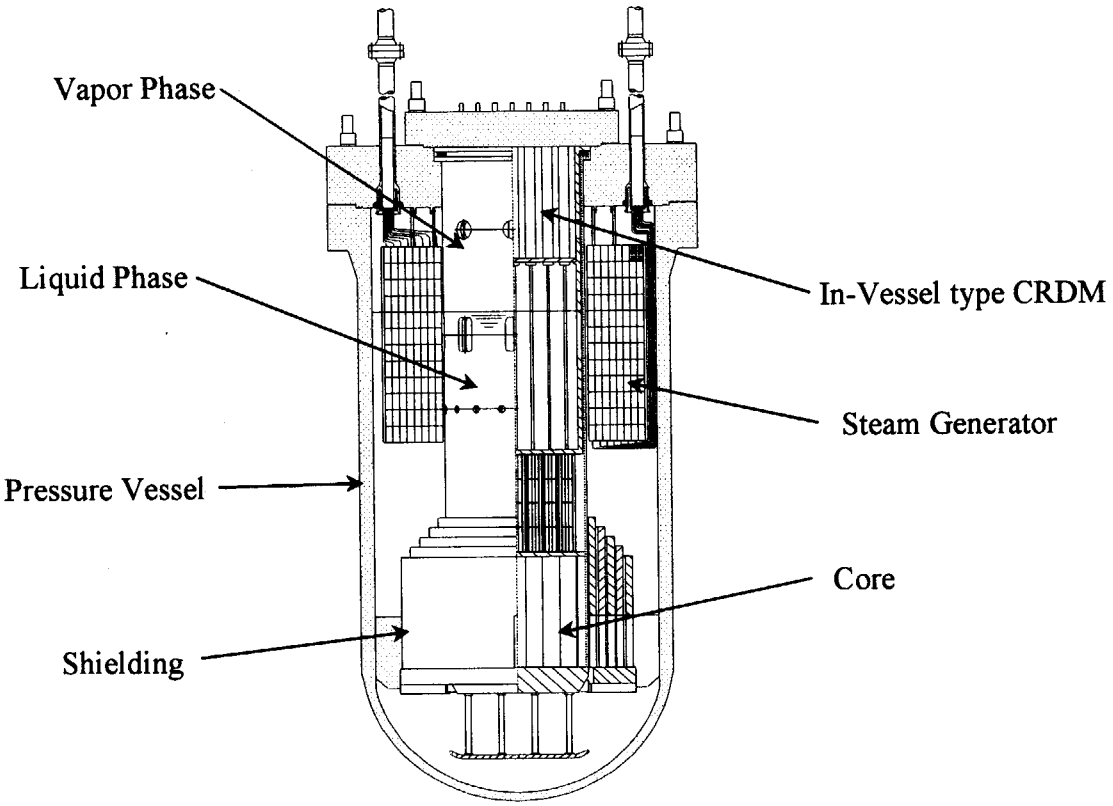

Fig. 9.3.1 Schematic of the Pressure Vessel

Table 9.3.1 Major specifications of the PSRD-E100

Thermal power	100 MWt
The primary system	
Pressure	8.3 MPa
Temperature of core outlet	297.5 ℃
Void fraction	10%
Core	
Equivalent diameter	162 cm
Effective height	140 cm
Average liner heat rate	7.3 kW/m
No. of fuel assembly	37
Outer diamitere of fuel rod	9.5 mm
Pitch of fuel rod	13.9 mm
Enrichment of U-235	4.9 wt%
Burnable poison	6 wt% of Gd_2O_3
Core life	9.8 years
Control rod	
No. of CRDM	37
No. of control rod (per CRDM)	24
Absorber	B_4C

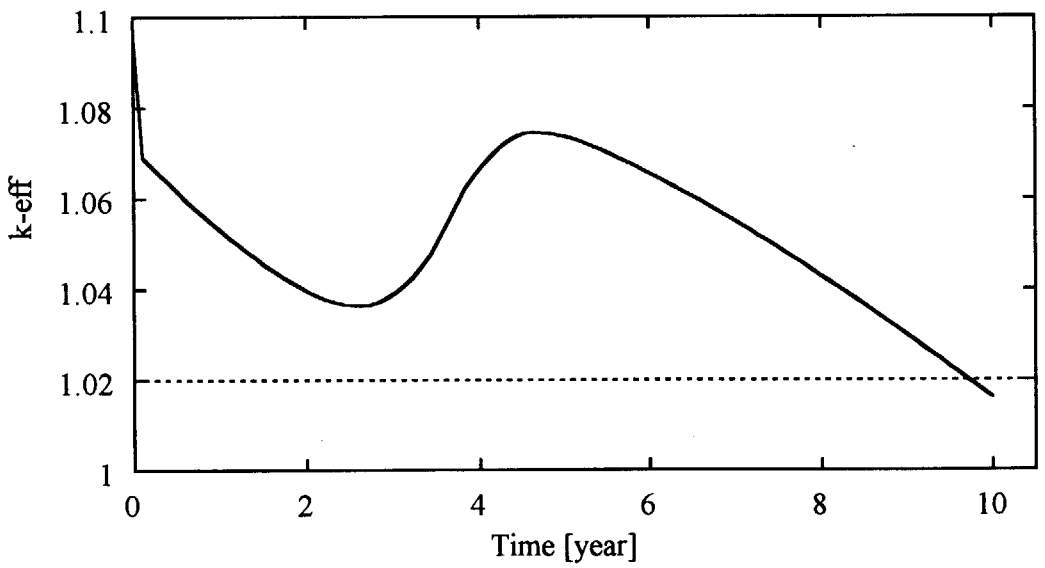

Fig. 9.3.2 Transition of reactivity accompanies by burnup

9.4 Development of Control Rod Drive Mechanism for Very Small Reactor -Back-up Mechanism with Passive Reactor Shut-down System-

T. Yoritsune and T. Ishida
(*E-mail*: tyori@popsvr.tokai.jaeri.go.jp)

In general, the reactor power of a very small reactor is controlled by the reactor control system using only the control rods, without a chemical shim, to avoid a complex chemical processing system. An in-vessel type control rod drive mechanism (INV-CRDM) [1), 2)], which is installed inside the reactor vessel, can help to achieve a highly compact and simple reactor system, and eliminate the possibility of a rod ejection accident. JAERI has developed this type of CRDM driven by an electric motor as a part of a Passive Safe Reactor for Distributed energy system (PSRD) design. Since the back-up system for reactor shut-down is required in general, an other INV-CRDM with a new type of latch mechanism using an electromagnetic force to directly connect both of the shafts, one of which is the motor driven shaft and the other the control rod driving shaft, is applied so as to make the INV-CRDM very compact.

The motion of the latch mechanism is illustrated in Fig.9.4.1. The latch mechanism is composed of an electric magnet coil, a magnet enclosure for the magnetic field, and the shaft. These shafts are apart from each other during non-operation. When the electric magnet is energized, a magnetic flux passes through the magnet enclosure and these shafts, and both shafts are attracted by the magnetic force. After de-energizing the electric magnet, both shafts

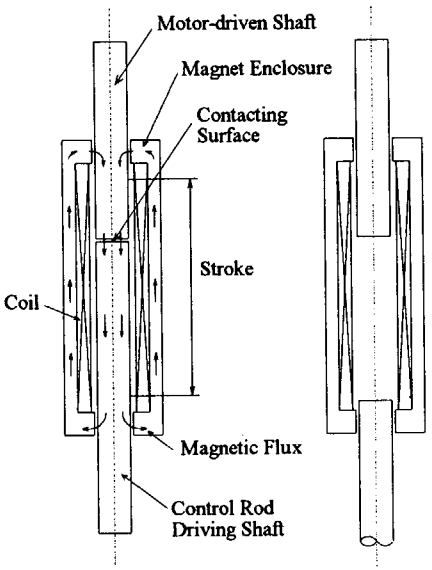

Fig.9.4.1 Motion of latch mechanism

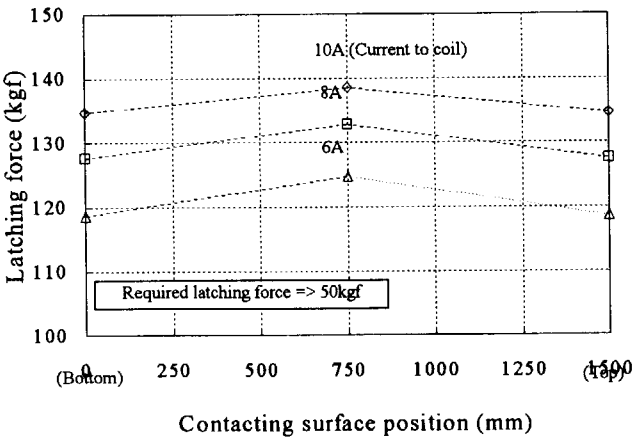

Fig.9.4.2 Result of magnetic flux analysis

can be separated with the assistance of the self-weight or a spring force.

The magnetic flux analysis was conducted to clarify to ensure required latching force. A finite element analysis code, MAGNA/FIM, was used with the axial symmetry two-dimensional vector potential method. The ampere to the magnet is varied in three cases; 6A, 8A, 10A respectively. The analysis result of the latching force in the range of the stroke is shown in Fig.9.4.2. As shown in the figure, it confirmed that required latching force was acquired in these cases.

Furthermore, the concepts of temperature and water level sensing type passive reactor shut-down mechanisms were created to improve the passive safety in reactor system. Both types of passive reactor shut-down mechanism are shown in Fig.9.4.3 and Fig.9.4.4. The temperature sensing type passive reactor shut-sown mechanism consists of a permanent magnet and a latching board using the temperature sensing metal (e.g. Ni). If the temperature of the latching board raises, magnetic saturation value of the latching board decreases. Therefore, even if the reactor cannot be scrammed by the CRDM in an abnormal condition, the temperature raise in the reactor vessel will induce, the magnetic saturation value of the latching board, to lower and the latching force to decrease, so that a control rod cluster can be inserted into the core.

The water level sensing type passive reactor shut-down mechanism are composed of

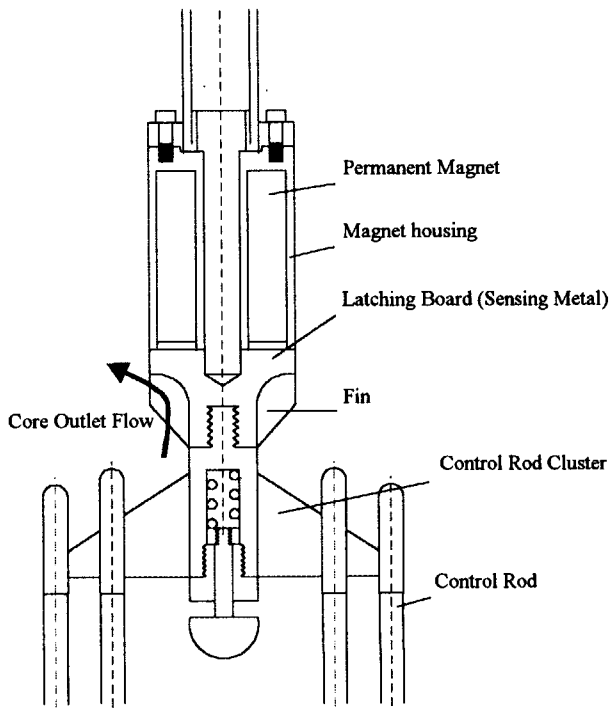

Fig.9.4.3 Concept of temperature sensing type passive reactor shut-down system

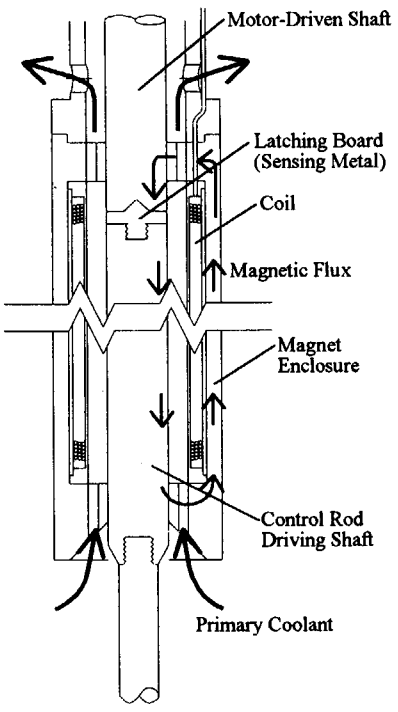

Fig.9.4.4 Concept of water level sensing type passive reactor shut-down system

an electric magnet coil, a magnet enclosure for the magnetic field, a latching board and the shafts. In a normal operation, a magnetic flux passes through the magnet enclosure and these shafts, and both shafts are attracted through the latching board. This mechanism is cooled by the primary coolant, which flows the cooling path of the magnet enclosure. When the water level in the reactor vessel decreases, the cooling of this mechanism is weakened by the primary coolant steam, and the temperature of the latching board increases, so that latching force also decrease to separate passively.

References

1) T. Ishida, et al., "Development of In-vessel Type Control Rod Drive Mechanism for Marine Reactor", Nuclear Science and Technology, Vol.38, No.7, pp. 557-570 (2001).

2) T. Yoritsune, et al., "In-vessel Type Control Rod Drive Mechanism Using Magnetic Force Latching for a Very Small Reactor", Nuclear Science and Technology, Vol.39, No.8, pp. 913-922 (2002).

10. Facility Operation and Techniques Development

There are four reactor-engineering facilities such as Heat Transfer Fluid Flow Test Facility, Fast Critical Assembly (FCA), Tank-type Critical Assembly (TCA) and Very High Temperature Reactor Critical Assembly (VHTRC). Maintenance work for VHTRC and operations of other facilities were carried out as scheduled. Major activities of each facility of this fiscal year are summarized briefly below.

(1) The Heat Transfer Fluid Flow Test Facility was operated for various experiments such as Departure from Nucleate Boiling Test for Advanced Reactor, Measurement Test of Void Fraetion Distribution by Neutron Radiography etc. And Thermal Fluid Safety Test (Ingress of Coolant Event/Loss of Vacuum event) for Fusion Reactor was carried out.

(2) The FCA was operated according to various purposes of experiments and recorded the operation time of 558.4 hours. Maintenance activities, fuel management and physical protection were done, i.e., renewal of the exhaust equipment for the reactor room, repair for defects of coating on fuels etc. And the Physical Inventory Verification (PIV) of nuclear fuel materials was carried out.

(3) The TCA was operated for the nuclear constant experiments and the training courses of the Nuclear Technology and Education Center (NuTEC). And it was recorded 223 times operation in 77 days. Fuel management, Physical Protection and PIV were also carried out.

(4) Maintenance works were done for VHTRC such as the monthly and annual inspections according to the safety regulation. The PIT and PIV for VHTRC were also carried out.

The decommissioning of VHTRC reactor assembly and control panel was performed from Sep.2000 to Mar.2001.

10.1 Operation Report of Heat Transfer Fluid Flow Test Facility

T. Satoh、H. Watanabe、M. Shibata、and K. Nakajima

(*E-mail* : takasato@popsvr.tokai.jaeri.go.jp)

In Fy-2001, operation and maintenance of Heat Transfer and Fluid Flow Test Facilities were carried out as scheduled.

As for the maintenance of test facilities, annual official inspections of the pressure vessels and the steam generator located at both Chemical/Mechanical Engineering Building and Thermal Engineering Test Facilities were carried out.

As for the operation of test Facilities, the following three tests were performed.

1) DNB test for Reduced-Moderation Water Reactors

2) Two-Phase Flow Visualization Test by NRG

3) Thermal Fluid Safety Test (Integrated ICE/LOVA Test Facility) for Fusion Reactor

As for the design and construction of test Facilities, the following two test Facilities were newly constructed.

1) Reduced-Moderation Water Reactors with a double flat core test Section

2) Low Pressure Thermal-Hydraulic Test Facility

As for the representative R&D, void fraction measurement system(Ⅲ) was developed.

10.2 Operation Report of FCA

K. Hayasaka, K. Satoh, K. Kurosawa, H. Sodeyama, M. Saitoh and T. Ono

(*E-mail*:hayasaka@fca001.tokai.jaeri.go.jp)

Operation of Fast Critical Assembly (FCA) was carried out in accordance with the experimental schedule on the FCA XXI-1 assembly. Operation of 119 times was carried out in 93 days. No scram was recorded during the operation. The total operation time was 558.4 hours and the integrated power was 0.59 kWh. A total number of 5557 criticality operations have been recorded at the end of this fiscal year since the first achievement of criticality on the 29 of April 1967. For the safety regulation of operation, two days were devoted to the monthly inspection and about 10 weeks from October 2001 to the annual inspection. Routine maintenance activities were done during the inspection to provide maximum operation days for the experiments.

As for the physical protection (P/P), security control of the gate was done restrictively and the system was maintained properly.

In connection with safeguard, IAEA and JSGO* carried out monthly inspection under the international treaty. They made the PIV (Physical Inventory Taking) from the 25th to the 28th of June. Prior to the PIV we performed item counting, weighing and non-destructive assay of the fuel from the 18th to the 22th of June.

* JSGO: Japan Safeguards Office

10.3 Operation Report of TCA

K. Murakami and Y. Hoshi

(*E-mail*:murakami@nucef.tokai.jaeri.go.jp)

Operation of Tank-type Critical Assembly (TCA) was carried out in accordance with the schedule on the experiments (the neutron multiplication experiment on the core, the measurement of reactivity worth of the safety sheet, the measurement of sub-criticality on the core) for the Research Group for Reactor Physics and on the experiments for the training courses of NuTEC(Nuclear Technology and Education Center) and on the experiments (Evaluation for sub-criticality measurement) for the Critical Safety Laboratory. The total operation time was 233 hours and integrated power was 52.8Wh during 223 times operation in 77 days. A total number of 11,249 criticality operations had been recorded at the end of this fiscal year since the first achievement of criticality on the 23rd of August 1962.

As for the nuclear material physical protection(P/P), the management of the entrance and exit was done restrictively and the system was maintained properly.

In connection with safeguard the inspection of nuclear material, stored at TCA, was carried out by IAEA and NSB* under the international treaty. The Physical Inventory Taking (PIT) of the fuels was performed on the 14nd of June and IAEA and NSB made the Physical Inventory Verification (PIV)on the 19rd of June by means of item counting, and non-destructive assay

* NSB : Nuclear Safety Bureau

10.4 Maintenance Work Report of VHTRC

M. Kyoya, M. Takeuchi, N. Yabuuchi, N. Ohzeki, T. Ouchi and K. Nakajima

(*E-mail* : kmasa@popsver.tokai.jaeri.go.jp)

The decommissioning of reactor assembly and control panel which is the first step of the decommission construction of the VHTRC started from September 2000 and it was finished in March 2001.

The other reactor equipment facilities such as reactor building and fuel storage room of the VHTRC continue from now on maintenance and management in future.

According to the safety regulation for maintenance, the 16 weeks were devoted to the annual inspection from July to October in 2000.

As for management, Physical Inventory Taking (PIT) was carried out from May 11 to 12 by means of item counting for fuel compact and fuel disk. IAEA and STA made the Physical Inventory Verification (PIV) under the international treaty on May 12. No anomaly was confirmed. The maintenance activity was also taken on the physical protection (P/P) system.

The sensitivity and function of the system were examined and calibrated.

11. Activities of the Research Committee

The department of Nuclear Energy System serves as a secretariat of the following two research committees organized by JAERI: Japanese Nuclear Data Committee and Research Committee on Reactor Physics. The purpose and the expected task of each research committee are summarized here. The detailed activities of each committee are presented in the following sections.

Japanese Nuclear Data Committee

The committee is organized to promote the evaluation of nuclear data and the production of group constants for application fields. There are three subcommittees, six standing groups and a steering committee under the Committees. The Committee also takes a task of compiling the activities of the International Nuclear Data Committee and the Work Party on International Evaluation Cooperation under OECD/NEA/NSC.

Research Committee on Reactor Physics

The committee reviews the research activities related to reactor physics in Japan and supports the activities of Nuclear Science Committee (NSC) of OECD/NEA. The committee consists of three working parties: reactor physics of sub-critical systems; reactor physics of LWRs loaded with next generation fuels; and code systems for common usage of reactor physics calculations.

11.1 Activities of Japanese Nuclear Data Committee

A. Hasegawa

The Japanese Nuclear Data Committee (JNDC) consists of three subcommittees, six standing groups and a steering committee. Each subcommittee consists of several working groups (WG). The Committee Meeting of JNDC was held on July 2001 to discuss the nuclear data activity in the previous fiscal year and plans for the fiscal year 2001. Discussions were made on several topics including final preparation status of ND2001 (International Conference on Nuclear Data for Science and Technology) to be held in TSUKUBA as well as domestic and international collaboration on nuclear data.

The ND2001 was held on 7-12th October 2001 at the EPOCHAL Tsukuba International Congress Center in Tsukuba, Ibaraki, Japan. As a side effects both of the 2001 Symposium on Nuclear Data, which is held every year in November, and a specialists' meeting on some special topics, which is a topical meeting held every year on the selected hottest topics in that period, were cancelled.

The activities of subcommittees and standing groups are briefly summarized below.

Subcommittee on Nuclear Data

1) High Energy Nuclear Data Evaluation WG :

The evaluation is progressing in parallel in two phases. In the phase-I, the data up to 50 MeV for IFMIF(International Fusion Material Irradiation Facility) project are targeted for neutron and proton induced reactions. In the phase-II, evaluations for high-energy neutron/proton induced reactions up to 3GeV are on going. Data requests are very keen by the joint projects for High Intensity Proton Accelerator of Center for Neutron Research in JAERI and KEK (High Energy Accelerator Research Organizations). Following is the status of each Sub Working Group (SWG).

- IFMIF Neutron File Compilation SWG: Neutron file compilation is the main task of this SWG. Up to now, evaluation of 43 nuclides has been finished. The files are in the final reviewing stage after the FORMAT check.
- MeV and GeV File compilation SWG: Compilation and evaluation of phase-II data is the main mission. Evaluations for the priority 2 nuclides (about 40 nuclides) has been performed together with the code preparation inevitable as a fundamental calculation tools in this energy range(Quick-Gnash, QMD, JAM). Evaluation has started for the priority 3 nuclides.
- Other Sub-Groups like Photonuclear Data, PKA/KERMA, High Energy Activation Cross-sections, and Guideline discussion group for differential data checking also have been progressed.

2) Evaluation and Calculation System WG :
Recommended parameters required in the nuclear model calculations such as OMP, level density, gamma strength functions, as well as advanced methodologies like multi-modal fission, essence from the latest frontiers of theoretical calculations are discussed. The results will be reflected to RIPL-2(Reference Input Parameter Library Version 2).
3) Charged Particle Nuclear Data WG : This WG is responsible for the JENDL (alpha,n) Reaction File. Evaluation has been finished and a file will be produced within a year. This group was dissolved at the end of March 2002 due to the completion of the missions..
4) Delayed Neutron Data Evaluation WG: This group was set up due to the follow up work of OECD/NEA/WPEC(Working Party on Evaluation Cooperation) subgroup 13 to investigate the delayed neutron data related problems. Evaluations of delayed neutron yields and spectra for main actinides of JENDL 3.3(U-235,-238, Pu-239) are also the mission of this group. Data evaluation in 6 group time dependent scheme has been made.
5) Evaluation WG on Intermediate Mass Nuclides: This WG was set up due to a revision work for JENDL-3.3. Re-evaluation work and relevant checking has been finished for Na-23, V-51, Co-59, Cr, Ti, Ni, W, Nb and Er (total of 32 nuclides). Some follow ups from the results of benchmark tests were made. This group has been dissolved by the end of March 2002 due to the completion of JENDL-3.3.
6) Evaluation WG on Heavy Mass Nuclides: This WG was set up due to the revision work for JENDL-3.3. Re-evaluation work has been made for U-233, -235,-236,-238, and Pu-236,-239,-240,-241,-242. Working group has been watching the feedback information from benchmark tests made by subcommittee of reactor constants. This group has been dissolved by the end of March 2002 due to the completion of the mission.

Subcommittee of Reactor Constants

1) Reactor Integral Test WG : Benchmark test of JENDL-3.3 tentative version for fast and thermal reactors has been made. Although over all agreements (C/E values) in Keff for thermal system as well as fast system revealed superior than JENDL 3.2 data. Problems for over estimation on Keff for SUS reflected cores are dissolved by the reevaluation of Cr data. No major problems are found for the revised file.
2) Shielding Integral Test WG :
For the tentative version of JENDL-3.3, benchmark test were made for main shielding materials such as Al, Si, Na, Ti, V, Cr, Fe, Co, Ni, Cu, Nb, W. All the results were fed back to the evaluation WG on intermediate mass nuclides. Much effort has been given to Na, Fe, Cr and Ni data reevaluation.
3) Standard Group Constants WG : Revision work for JSSTDL library has been progressed. Report of the JSSTDL-300 are being prepared. Direction of group constants preparation for

JENDL-3.3 has been discussed.

Subcommittee on Nuclear Fuel Cycle

The subcommittee on nuclear fuel cycle consists of three WGs, i.e., Decay Heat Evaluation WG, WG on Evaluation of Nuclide Generation and Depletion, and FP Mass Yield Evaluation WG.

For the first WG, FP Decay Data File has been completed and released as JENDL FP Decay Data File 2000. A plan for new measurement of strength function of beta decay at Valencia University(TAGS) was presented and discussions were made how to contribute this project by JNDC. For the second WG, new entry for PWR and BWR-MOX has been added to ORIGEN-2 Library and published a report. Methodology for the evaluation of sensitivity in one group cross section is discussed. To pole for questionnaire of ORIGEN Calculation Needs has been decided and preparation work has been made. For the last WG, this group was organized so as to work with IAEA CRP(Coordinated Research Project). To give precise mass yields data for minor actinides as well as major actinides covering wide range of incident neutron/proton energies is the main mission. Collection work for mass yields data evaluated/measured in Japan was made. The systematics made by Moriyama and Ohnishi was applied and analyzed and found that for Cm-248(p,f) case typical two peak cannot produced. A possibility for updating of recent Benllinure's semi-empirical model was investigated. Measurements of mass yields for Np-237, Am-241 and 243, Cm-248 by proton bombardment at 25 and 30Mev were made.

Standing Groups

1) CINDA Group : Papers on neutron induced reaction data published in Japanese journals and reports are surveyed. Total of 289 entries (without ND2001 presentations) were sent to the NEA Data Bank in the last one year to update the CINDA master database.

2) ENSDF Group : The evaluation of nuclear structure data is a duty of this group. Nuclei with mass numbers from 118 to 129 are assigned as duties to Japan. Re-evaluation work has been made for A= 118 and 124.

3) Group on Atomic, Molecular and Nuclear Data for Medical Use : Survey work has been made for the radiopharmaceutical data needed in the field of nuclear medicine. Home page of this group was opened to promote and encourage WG missions.

4) JENDL Compilation Group : File compilation and editing were made for the JENDL-3.3.

5) Editorial Group of "Nuclear Data News" : Three issues of "Nuclear Data News" (No.69-71) which is a periodic informal journal circulated in nuclear data communities of Japan (written in Japanese) were published. Some 450 copies were distributed among the

nuclear data communities in Japan without fee.

6) High Priority Request List (HPRL) Group: A revision was made (new entry:3, remove/merge:35, others:71) for the latest version of HPRL, this is mainly from ADS (Accelerator Driven System) application's requests. This group is a coordination group to set up a Japanese Requests Lists from domestic data users and a world-wide request list HPRL that is maintained at OECD/NEA/WPEC (Working Party on Evaluation Cooperation).

ND2001: International Conference on Nuclear Data for Science and Technology

The International Conference on Nuclear Data for Science and Technology (ND2001) was held 7-12th October 2001 at the EPOCHAL Tsukuba International Congress Center in Tsukuba, Ibaraki, Japan. The Japan Atomic Energy Research Institute (JAERI) sponsored and organized in collaboration with OECD Nuclear Energy Agency – Nuclear Science Committee (NEA/NSC) and Atomic Energy Society of Japan (AESJ) as the co-sponsors. Total of 375 scientists from 41countries and 4 international organizations participated in the conference, of which 207 persons come from abroad. Total of 375 papers were presented including 4 key notes and 3 summary talks in the 40 sessions; i.e., 50 invited talks, 116 oral and 202 poster contributed papers. One third of the presented papers are in the topics of Nuclear Reaction Data and Evaluated data Libraries. The other one third is devoted to the applications in energy production including ADS applications and Industry or Medical applications. The rest one third is devoted for forefront of Nuclear Reaction Theory, Astrophysics, Facilities available in new century, and steady progress in International Collaborations. An emphasis was laid down on the application of the Nuclear Data to ADS due to the increased interests in the world-wide environmental concern on nuclear high level waste. And data applications in the Astrophysics are also enthusiastically debated in connection with nuclear synthesis of the universe.

The proceedings was published on August 2002 as a supplement to Journal of Nuclear Science and Technology, i.e., a publication of Japan Atomic Energy Society, including all invited and contributed papers after critical reviews.

11.2 Activities of the Research Committee on Reactor Physics

M. Nakagawa and T. Osugi

The committee reviews research activities related to reactor physics in Japan and supports the activities of Nuclear Science Committee (NSC) of OECD/NEA. The committee consists of three working parties and a steering committee.

The 71st meeting of the Research Committee on Reactor Physics (RCRP) was held on June 29th, 2001. Documents discussed at the 12th meeting of NEA/NSC held at OECD Headquarters, Paris, June 11 - 13 2001 were distributed. The three-working parties were closed in FY-2000 since the interval of their activities was limited in two years. The summaries of their activities were introduced by a leader of each working party. The meeting was devoted to discussing the establishment of new working parties for next two years (FY-2001 and -2002). The six topics as the special tasks were nominated and the scopes and action plans of each topic were discussed. Three working parties were finally established and their activities were started up in FY-2001. The meetings were held twice in each working party.

1) Working Party on Reactor Physics of Sub-critical Systems,

Scope of activities:

- Review of definition of the sub-criticality practically used in Accelerator Driven Systems (ADS),
- Proposal of Benchmark problems for sub-critical system such as ADS,
- Discussion of sub-critical condition in design study of ADS,

2) Working Party on Reactor Physics of LWRs Loaded with Next Generation Fuels,

Scope of activities:

- Benchmark Problems for Calculation Accuracy Evaluation on LWRs Loaded with Next Generation Fuels,

3) Working Party on Code Systems for Common Usage of Reactor Physics Calculations,

Scope of activities:

- Discussion of Scope of Common Code Systems,
- Review of Code Systems used in Japan.

Publication List

1. Nuclear Data

1) T. Fukahori, S. Chiba, K. Shibata, Y. Ikeda, T. Aruga, Y. Watanabe, T. Murata, N. Yamano and M. Kawai: "JENDL PKA/KERMA File for IFMIF Project", Proc. the Tenth International Symposium on Reactor Dosimetry, Sep.12-17, 1999, Osaka, Japan, Reactor Dosimetry: Radiation Metrology and Assessment, ASTM STP 1398, pp.591, Jhon G. Williams, David W. Vehar, Frank H. Ruddy, and David M Gilliam, Eds., American Society for Testing and Materials, West Conshohocken, PA, 2001.

2) H. Sakane, Y. Kasugai, M. Shibata, T. Iida, A. Takahashi, T. Fukahori and K. Kawade: "Measurement of Activation Cross Sections for (n, 2n) Reactions Producing Short-lived Nuclei in the Energy Range between 13.4 and 14.9 MeV", Ann. Nucl. Energy, 28, 1175 (2001).

3) H. Sakane, Y. Kasugai, M. Shibata, T. Iida, A. Takahashi, T. Fukahori and K. Kawade: "Measurement of Activation Cross Sections of (n,np+d) Reactions Producing Short-lived Nuclei in the Energy Range between 13.4 and 14.9 MeV Using an Intense Neutron Source OKTAVIAN", Ann. Nucl. Energy, 29, 53 (2001).

4) S. Chiba, T. Fukahori, K. Shibata, B. Yu, K. Kosako and N. Yamamuro: "JENDL Fusion File 99", J. Nucl. Sci Technol., 39[2], 187 (2002).

5) A.Y. Donets, A.V. Evdokinov, A.V. Fomichev, T. Fukahori, A. Hasegawa, A.B. Laptev, V.M. Maslov, G.A. Petrov, O.A. Shcherbakov, Yu.V. Tuboltsev and A.S. Vorobyev: "Neutron-induced Fission Cross Sections of U-233, 238, Th-232, Pu-239 and Np-237 in the Energy Range 1-200 MeV", Proc. XI International Seminar on Interaction of Neutrons with Nuclei (ISINN-9), May 23-26, 2001, Dubna, Russia (2001).

2) A. Y. Donets, A.V. Evdokinov, A.V. Fomichev, T. Fukahori, A. Hasegawa, A.B. Laptev, O.A. Shcherbakov, Yu.V. Tuboltsev and A.S. Vorobyev: "Neutron-induced Fission Cross Sections of Pb-nat and Bi-209 Relative to U-235 in the Energy Range 1-200 MeV", Proc. XI International Seminar on Interaction of Neutrons with Nuclei (ISINN-9), May 23-26, 2001, Dubna, Russia (2001).

7) T. Fukahori: "Necessity of Long Term Nuclear Data Development for Various Applications Needing Nuclear Data", Texts of Papers Presented at the Advisory Group Meeting on Long Term Needs for Nuclear Data Development, Nov. 28-Dec. 1, 2000, Vienna, Austria, INDC(NDS)-428 (2001) pp.199.

8) T. Fukahori: "Status of Japanese Contribution to RIPL-2", Summary Report of the 3rd Research Coordination Meeting on Nuclear Model Parameter Testing for Nuclear Data Evaluation (Reference Input Parameter Library: Phase II), Dec. 3-7, 2001, IAEA

Headquarters, Vienna, Austria, INDC(NDS)-431 (2002) pp.53.

9) A. Ichihara and J. Eichler: "Angle-differential cross sections for radiative recombination and the photoelectric effect in the K, L, and M shells of one-electron systems calculated within an exact relativistic description", At. Data Nucl. Data Table 79, 187 (2001).

10) J. Katakura: "FP Decay Heat Calculation using JENDL FP Decay Data File", Trans.Am.Nucl.Soc. 85, 318 (2001).

11) J. Katakura, T. Yoshida, K. Oyamatsu and T. Tachibana: "Estimation of Beta- and Gamma-Ray Spectra for JENDL FP Decay Data File", J. Nucl. Sci. Technol. 38[7], 470 (2001).

12) K. Suyama, J. Katakura, T. Kiyosumi, T. Kaneko and Y. Nomura: "Comparison of Burnup Calculation Results Using Several Evaluated Nuclear Data Files", J. Nucl. Sci. Technol. 39[1], 82 (2002).

13) M. Kawai, T. Nakagawa, T. Watanaba, Y. Nakajima, A. Zukeran, H. Matsunobu, T. Sugi and S.Chiba: "Re-evaluation of Nuclear Data of Fission Product Nuclides for JENDL-3.2", J. Nucl. Sci. Technol. 38[4], 261 (2001).

14) J. Katakura, T. Yoshida, K. Oyamatsu, and T. Tachibana: "JENDL FP Decay Data File 2000", JAERI 1343 (2001).

15) K. Kobayashi, T. Iguchi, S. Iwasaki, T. Aoyama, S. Shimakawa, Y. Ikeda, N. Odano, K. Sakurai, K. Shibata, T. Nakagawa and M. Nakazawa: "JENDL Dosimetry File (JENDL/D-99)", JAERI 1344 (2002).

16) V. Manokhin, N. Odano and A. Hasegawa: "Comparison of (n, 2n) and (n,3n) Reaction Cross Sections for Fission Products in JENDL-3.2 with Available Experimental and other Evaluated Cross Section Data", JAERI-Data/Code 2001-019 (2001).

17) J. Katakura(Ed.): "Proceedings of the Specialists' Meeting on Reactor Group Constants", JAERI-Conf 2001-009 (2001).

18) T. Kawano, A. Carlson, H. Matsunobu, T. Nakagawa, K. Shibata, P. Talou, P. Young, and M. Chadwick: "Comparison of ^{235}U Fission Cross Sections in JENDL-3.3 and ENDF/B-VI", JAERI-Research 2001-058 (2002).

19) T. Nakagawa, O. Iwamoto and A. Hasegawa: "Improvement of Evaluated Neutron Nuclear Data for ^{237}Np and ^{241}Am", JAERI-Research 2001-059 (2002).

2. Reactor Physics

1) K. Okumura, H. Unesaki, T. Kitada and E. Saji: "Benchmark Results of Burn-up Calculation for LWR Next Generation Fuels", Proc. of Int. Conf. on the New Frontiers of Nuclear Technology : Reactor Physics, Safety and High-Performance Computing

(PHYSOR 2002), 9A-03 (paper index number in CD), Seoul, Korea, 7-10 October, (2002).

2) Y. Nagaya, K. Okumura and T. Mori: "Analysis of VENUS-2 MOX Core Measurements with A Monte Carlo Code MVP" Proc. of Int. Conf. on the New Frontiers of Nuclear Technology : Reactor Physics, Safety and High-Performance Computing (PHYSOR 2002), 4A-04 (paper index number in CD), Seoul, Korea, 7-10 October, (2002).

3) T. Sakurai and S. Okajima: "Adjustment of Total Delayed Neutron Yields of 235U, 238U and 239Pu in JENDL-3.2 Using Benchmark Experiments on Effective Delayed Neutron Fraction β eff", J. Nucl. Sci. and Technol., Vol.39, No.1, pp.19 - 30(2002).

4) T. Yoshida, S. Okajima, T. Sakurai, K. Nakajima, T. Yamane, J. Katakura, Y. Tahara, A. Zukeran, K. Oyamatsu, T. Ohsawa, T. Nakagawa and T. Tachibana: "Evaluation of Delayed Neutron Data for JENDL-3.3", Proc. Int. Conf. on Nuclear Data for Science and Technology, Tsukuba, Japan, (2001) [in print].

5) K. Nishihara, K. Iwanaga, T. Yamane and S. Okajima: "Determination of Reactivity and Source Intensity Based on the Maximum Likelihood Method", JAERI-Research 2002-030, (2002) [in print].

6) Y. Nauchi, T. Kameyama, T.Matsumura, T. Suzaki and Y.Miyoshi, "Measurement and Analysis of High Energy Gamma Ray and Neutron in MOX Fuel Lattices For Subcriticality Estimation", PHYSOR 2002, Seoul, Korea, (2002).

7) M. Rahman, T. Suzaki and T. Mori, "Analytical Study of Two-Region TCA Critical Experiments with PWR-Type MOX Fuel by Using Monte Carlo Code MVP", JAERI-Research, to be submitted, (2002).

3. Advanced Reactor System Studies

1) T. Okubo, et al.: "Advanced Concept of Reduced-Moderation Water Reactor(RMWR) for Plutonium Multiple Recycling", Proc. of International Conference on Back-End of the Fuel Cycle(GLOBAL2001), Paris, Japan (2001).

2) H. Akie, et al.: "Core Design Study on Reduced-moderation Water Reactors", Proc. of Workshop on Advanced Reactors with Innovative Fuels, Chester, UK(2001).

3) T. Iwamura and M. Ochiai: "Activities of Design Studies on Innovative Small and Medium LWRs in JAERI", Proc. of 1st Asian Specialist Meeting on Future Small-Sized LWR Development, Bangkok, Thailand (2001).

4) (Eds.) T. Nakatsuka, et al.: "Summary of the 4th Workshop on the Reduced-Moderation Water Reactor", JAERI-Conf 2001-013 (2001) [in Japanese].

5) T. Nakatsuka, Y. Oka and S. Koshizuka: "Startup Thermal Considerations for Supercritical-Pressure Light Water-Cooled Reactors", Nuclear Technology, Vol. 134, No. 3 (2001).

6) K. Hibi, et al.: "Conceptual Designing of Reduced-moderation Water Reactor with Heavy Water Coolant", Nucl. Eng. Design, Vol. 210 (2001).

7) Y. Asahi: "THYDE-NEU: Nuclear Reactor System Analysis Code", JAERI-Data/Code 2002-002 (2002).

8) N. Ishikawa and K. Suzuki: "A Mobile Robot System Executing a Task under Human Assistance", Journal of the Robotics Society of Japan, Vol.20, No.2 (2002) [in Japanese].

9) K. Nabeshima, et al.: "Neuro-Expert Monitoring System for Nuclear Power Plant", Proc. of 5th International Conference on Knowledge-Based Intelligent Information Engineering Systems, Osaka, Japan (2001).

10) K. Nabeshima, et al.: "Nuclear Reactor Monitoring with the Combination of Neural Network and Expert System", Proc. of European Workshop on Intelligent Forecasting, Diagnosis and Control (IFDICON'2001), Santorini, Greece (2001).

11) T. Kaizouji and T. Suzudo : "Evolutionary Model of Opinion Formation", Proc. of 4th International Conference on Computational Intelligence and Multimedia Applications, Yokosuka, Japan (2001).

4. Thermal and Fluid Engineering

1) M. Kureta and H. Akimoto: "Critical Heat Flux of Subcooled Boiling in High-Heat-Load Narrow Channels", Trans. of the JSME, B, Vol. 67[662], 162-169, (2001) [in Japanese].

2) M. Kureta and H. Akimoto: "Critical Heat Flux Correlation for Subcooled Boiling Flow in Narrow Channels", Int. J. of Heat and Mass Transfer, Vol. 45,4107-4115, (2002).

3) M. Kureta, H. Akimoto, T. Hibiki, and K. Mishima: "Void Fraction Measurement in Subcooled-Boiling Flow Using High-Frame-Rate Neutron Radiography", Nuclear Technology, Vol.136, 241-254, (2001).

4) M. Kureta, T. Hibiki, K. Mishima and H. Akimoto: "Measurement of Boiling Flow by High-Frame-Rate Neutron Radiography (2nd Report, Point of Net Vapor Generation of Flow-Boiling in Rectangular Channels with Short Heated Length)", Trans. of the JSME, B, Vol. 67[661], 2295-2303, (2001) [in Japanese].

5) A. Ohnuki et al.: "ACE-3D Code Analyses of Multi-dimensional Boiling Flow in Horizontal PCCS Water Pool", Proc. of Ninth Int. Conf. on Nuclear Engineering

(ICONE-9), Nice, France, April (2001).

6) A. Ohnuki, M. Akamatsu and H. Akimoto: "Numerical Analysis of Air-Water Two-Phase Flow around a Circular Cylinder", Proc. of the 5th Organized Multiphase Flow Forum, Fukushima, Japan, September (2001).

7) A. Ohnuki et al.: "Analysis of Multi-Dimensional Boiling Flow in Secondary Water Pool of Horizontal PCCS -Effect of Pool Size-", Proc. of Thermal Engineering Conference '01, Okayama, Japan, November (2001).

8) A. Ohnuki and H. Akimoto: "Model Development for Bubble Turbulent Diffusion and Bubble Diameter in Large Vertical Pipes", J. Nucl. Sci. Technol., 38[12], pp.1074-1080 (2001).

9) A. Ohnuki and H. Akimoto: "Verification of Models for Bubble Turbulent Diffusion and Bubble Diameter in Multi-dimensional Two-fluid Model", Proc. of 8th Int. Symposium on Flow Modeling and Turbulent Measurements (FMTM2001), Tokyo, Japan, December (2001).

10) K. Takase: "Three-Dimensional Numerical Simulations of Dust Mobilization and Air Ingress Characteristics in a Fusion Reactor during a LOVA Event", Fusion Engineering and Design, 54, pp.605-615 (2001).

11) K. Takase, H. Akimoto, L. Topilski: "Results of Two-Phase Flow Experiments with an Integrated Ingress-of-Coolant Event (ICE) Test Facility for ITER Safety", Fusion Engineering and Design, 54, pp.593-603 (2001).

12) K. Takase: "Numerical Simulations on Dust-Air Two-Phase Flows in Fusion Experimental Reactors during Loss-of-Vacuum Accident Events", Fusion Technology, 39, pp.1043-1049 (2001).

13) K. Takase, Y. Ose, H. Akimoto: "Analysis of Pressure Rise in an ITER-Like Fusion Reactor during In-Vessel LOCA by a Modified TRAC-PF1 Code", Fusion Technology, 39, pp.1050-1055 (2001).

14) K. Takase: "A Preliminary Study on Direct-Contact Condensation Between Water and Vapor in a Suppression Tank for Fusion Reactor Safety", Fusion Technology, 39, pp.1056-1060 (2001).

15) K. Takase and H. Akimoto: "Experimental Verification of Effectiveness of Integrated Pressure Suppression Systems in Fusion Reactors during In-Vessel Loss of Coolant Events", Nuclear Fusion, 41, No.12, pp.1873-1883 (2001).

16) K. Takase and H. Akimoto: "Depressurization Effects of Vacuum Vessel Pressure Suppression Systems in Fusion Reactors at Multiple First Wall Pipe Break Events", 10th International Symposium on Applied Electromagnetics and Mechanics, Tokyo,

May, pp. 177-178 (2001).

17) K. Takase, Y. Ose and H. Akimoto: "Three-Dimensional Computations of Two-Phase Flow Behavior in a Simulated Fusion Reactor under Water Ingress", 1st International Symposium on Advanced Fluid Information, pp.227-232 (2001).

18) K. Takase: "Analysis on Mobilization of Activated Dust with Different Densities in Fusion Reactors", 1st International Symposium on Advanced Fluid Information, pp.370-375 (2001).

19) K. Takase: "Effect of Turbulence Models on Thermal-Hydraulics in Targets of Accelerator Driven Systems", 1st International Symposium on Advanced Fluid Information, pp.376-381 (2001).

20) K. Takase, Y. Ose, M. Shibata and H. Akimoto: "Boiling and Condensation of Water Discharged into a Vacuum Vessel of a Fusion Reactor", 38th National Heat Transfer Symposium of Japan, I215, pp. 641-642 (2001) [in Japanese].

21) K. Takase, Y. Ose and H. Akimoto: "Water Ingress Behavior into Fusion Reactors and Pressure Drop Characteristics at Divertor", Fluids Engineering Conference, JSME, No.01-3, G701 (2001) [in Japanese].

22) K. Takase, Y. Ose and H. Akimoto: "Experimental and Analytical Studies on Water Evaporation and Condensation under Atmospheric Pressure", Yamaguchi Visualization Symposium, J. Visualization Society of Japan, B201 pp.115-118 (2001) [in Japanese].

23) K. Takase, Y. Ose, T. Suzuki and T. Kunugi: "Analysis on Direct-Contact Condensation of Vapor into a Pressure Suppression Tank", Yamanashi District Conference, JSME, No.010-4, pp.198-199 (2001) [in Japanese].

5. Energy System Analysis and Assessment

1) O. Sato, K. Tatematsu, Y. Tanaka: "Toward Very Long-term Utilization of Nuclear Energy -Prospects and Problems of Water-cooled Breeder "Reduced Moderation Water Reactor"- ", Genshiryoku eye, Vol.47, No.7, 60 (2001) [in Japanese].

6. Reactor Structural Materials

1) T. Tsukada and N. Ebine: "Aging degradation of light water reactor materials – Reactor internal and pressure vessel materials", Journal of the Japan Society of Applied Electromagnetics and Mechanics (2001) [in Japanese].

2) T. Tsukada, Y. Komori, H. Tsuji, H. Nakajima and H. Itoh: "In-pile high temperature water loop system at JMTR for IASCC studies", Proceedings of the seminar on water chemistry of nuclear reactor systems 2001.

3) H. Tsuji: "Report of Examinxation of the Ruptured Pipe at the Hamaoka Nuclear Power Station Unit-1", JAERI-Tech 2001-094 (2001) [in Japanese].

4) T. Tsukada: "The state and trend of IASCC study", Text book of weldment [in Japanese].

5) S. Jitsukawa, Y. Miwa and T. Tsukada, ITER task report, G17TT63FJ (2001)

6) H. Ugachi, T. Tsukada, Y. Kaji, Y. Matsui, M. Kikuchi, F. Takada and H. Tsuji: "In-pile SCC Test Technique using Bent-Beam Method in High Temperature Water", Proc. of 10th International Conference on Environmental Degradation of Materials in Nuclear Power Systems - Water Reactors -, No.59, August 5-9, Lake Tahoe, NEVADA, USA (2001).

7) Y. Nemoto, Y. Miwa, T. Tsukada, M. Kikuchi and H. Tsuji: "Development of analytical method for microstructure observation of oxide film on stainless steel", JAERI-Tech 2001-079 (2001) [in Japanese].

8) Y. Kaji, Y. Matsui, S. Kita, K. Ide, T. Tsukada and H. Tsuji: "Application of A Fiber Optic Grating Stain Sensor for The Measurement of Strain under Irradiation Environment", Nuclear Engineering and Design Vol.43, 160-16 (2001).

9) Y. Kaji, W. Gu, M. Ishihara, T. Arai and H. Nakamura: "Development of Structural Analysis Program for Non-Linear Elasticity by Continuum Damage Mechanics", Nuclear Engineering and Design, 206, 1-12 (2001).

10) Y. Kaji, K. Kikuchi and H. J. Penkalla: "Inelastic Constitutive Equation in Alloy 800H", Proc. of 7th Int. Conf. on Creep and Fatigue at Elevated Temperatures, 179-183 (2001).

11) H. Tsuji, H. Nishi, Y. Kaji, Y. Muto, H. J. Penkalla and F. Schubert: "Multiaxial Creep Behavior of Nickel-Base Heat-Resistant Alloys Hastelloy-XR and Ni-Cr-W Superalloy at Elevated Temperatures", Proc. of 7th Int. Conf. on Creep and Fatigue at Elevated Temperatures, 101-106 (2001).

12) A. T. Yokobori, Y. Kaji and T. Kuriyama: "Damage Progression Behavior under High Temperature Creep and Fatigue Conditions", Advances in Fracture, Proc. of 10th Int. Conf. of Fracture, Special Lecture (2001).

13) Y. Kaji, T. Sakino and H. Tsuji: "Additional Function of JAERI Material Performance Database (JMPD) ", Proc. 10th German-Japanese Workshop on Chemical Information, 67-70 (2001).

14) H. Tsuji, Y. Kaji, M. Fujita, J. Kinugawa and K. Yoshida, et al.: "Obtainable Knowledge for Materials from Data-Free-Way -Description Method of Knowledge Extracted from Fact Database -", Proc. 10th German-Japanese Workshop on Chemical Information, 131-133 (2001).

7. Research on Advanced Materials for Light Water Reactors and Reprocessing Plants

1) K. Kiuchi, I. Ioka, M. Tachibana et.al.: "Study on High-performance Fuel Cladding Materials- Joint Research in FY 1999-2000 (Phase 1)", JAERI-Research 2002-8 (2002) [In Japanese].

2) I. Ioka, M. Futakawa, Y. Nanjyo et.al.: "Effect of Triple Ion-Beam Irradiation on Mechanichal Properties of High Chromium Austenitic Stainless Steel", Proc. of Int. Symp. on Material Chemistry in Nuclear Environment, Tsukuba, Japan , March (2002).

3) C. Kato and K. Kiuchi: "Effect of Heat Flux on Stress Corrosion Cracking of Zirconium in Nitric Acid Environments", Proc. of Int. Symp. on Material Chemistry in Nuclear Environment, Tsukuba, Japan , March (2002).

4) T. Motooka and K. Kiuchi: "Corrosion of Type 304L Stainless Steel in Boiling Dilute Neptunium Nitrate Solution", Proc. of Int. Symp. on Material Chemistry in Nuclear Environment, Tsukuba, Japan , March (2002).

5) T. Motooka and K. Kiuchi: "Corrosion Fatigue of Refractory Metals with Corrosion Resistance to Boiling Nitric Acid", Proc. of Second Int. National Conf. on Environmental Sensitive Cracking and Corrosion Damage, Hiroshima, Japan, November (2001).

6) T. Motooka, S. Terakado, T. Kohya et.al.: "Development of Corrosion Testing Equipment to Evaluate Corrosion Resistance in Fuel Dissolved Solution (Contract Research), JAERI-Tech 2001-089 (2001) [In Japanese].

7) T. Motooka, M. Numata and K. Kiuchi: "Development of Corrosion Testing Equipment under Heat Transfer and Irradiation Conditions to Evaluate Corrosion Resistance of Materials used in Acid Recovery Evaporator (Contract Research)", JAERI-Tech 2001-088 (2001) [In Japanese].

8) T. Motooka and K. Kiuchi: "Effect of Neptunium Ions on Corrosion of Stainless Steel in Nitric Acid", Proc. of ACTINIDES-2001, Hayama, Japan, November (2001).

9) M. Futakawa, T. Wakui, Y. Tanabe and I. Ioka: "Identification of the Constitutive Equation by the Indentation Technique using Plural Indenters with Different Apex Angles", J. Mater. Res., 18(8), 2283-2292.

10) T. Wakui, M. Futakawa, Y. Tanabe and I. Ioka: "Identification of Material Constants in Constitutive Equation by Indentation Test with Different Indenters", Zairyo, 51(6) [In Japanese].

11) S. Hamada, K. Fukaya, C. Kato et.al.: "Inspection of the Heat Transfer Tubes after Mock-up Tests of Minituarized Apparatus for the Acid Recovery Evaporator (Contract Research)", JAERI-Tech 2001-063 (2001) [In Japanese].

12) M. Futakawa, T. Wakui, Y. Tanabe and I. Ioka: "Stress-strain relationship evaluated by Inverse analysis on Indentation Load-depth Curve", Proc. of 10th Asia-Pacific Conf. on Non-Destructive Testing, Australia, September (2001).

13) T. Ohba, T. Yanagihara, C. Kato and S. Hamada: "Manufacture of Ultrasonic Thickness Measurement Apparatus (Contract Research)", JAERI-Tech 2001-59 (2001) [In Japanese].

14) H. Nishi, M. Etoh and K. Tachibana: "Fatigue Strength Reduction Factor of Partial Penetration Weldments for ITER Vacuum Vessel", Proc. of Int. Conf. on Structural Mechanics in Reactor Technolgy", Washinton D.C., USA, August (2001).

8. Research on Advanced Transuranium Bearing Fuels

1) H. Serizawa, Y. Arai and K. Nakajima: "The Estimation of the Specific Heat of NpO_2", J. Chem. Thermodynamics, 33, 615 (2001).

2) T. Fujino, N. Sato, K. Yamada, M. Okazaki, K. Fukuda, H. Serizawa and T. Shiratori: "Oxygen potential and defect structure of the solid solution, Mg-Gd-UO_2", Journal of Nuclear Materials 289 (3), 270 (2001).

3) K. Nakajima and Y. Arai: "Mass-spectrometric investigation of UO_3(g)", Journal of Nuclear Materials 294 (3), 250 (2001).

4) Y. Sakamura, O. Shirai, T. Iwai and Y. Suzuki: "Distribution behavior of plutonium and americium in LiCl-KCl eutectic/liquid cadmium systems", J. Alloys and Compd. 321, 76 (2001).

5) Y. Arai and T. Ogawa: "Research on Nitride Fuel and Pyrochemical Process for MA Transmutation", Proc. 6th OECD/NEA Information Exchange Meeting on Actinide and Fission Product Partitioning and Transmutation, 11-13 December 2000, Madrid , 445(2001) (CD-ROM).

6) M. Iizuka, K. Uozumi, T. Inoue, T. Iwai, O. Shirai and Y. Arai: "Development of Plutonium Recovery Process by Molten Salt Electrorefining with Liquid Cadmium Cathode", Proc. 6th OECD/NEA Information Exchange Meeting on Actinide and Fission Product Partitioning and Transmutation, 11-13 December 2000, Madrid, 327(2001) (CD-ROM).

7) T. Osugi, H. Takano, T. Takizuka, Y. Arai, T. Ogawa, S. Tachimori and Y. Morita: "Recent Topics in R&D for OMEGA Program in JAERI", Proc. 6th OECD/NEA Information Exchange Meeting on Actinide and Fission Product Partitioning and Transmutation, 11-13 December 2000, Madrid, 197 (2001) (CD-ROM).

8) Y. Arai: "Advanced recycle technology based on electrarefining of nitride

fuel"Advances in Nuclear fuel Technology-Present and future, Atomic Energy Society of Japan, 9,9.3, 451(2001).

9) K. Minato, T. Shiratori, H. Serizawa, K. Hayashi, K. Une, K. Nogita, M. Hirai and M. Amagai,: "Thermal conductivities of irradiated UO_2 and $(U,Gd)O_2$", J. Nucl. Mater., 288 (1), 57 (2001).

10) M. Iizuka, T. Inoue, O. Shirai, T. Iwai and Y. Arai: "Application of normal pulse voltammetry to on-line monitoring of actinide concentrations in molten salt electrolyte", J. Nucl. Mater., 297 (1), 43(2001).

11) M. Iizuka, K. Uozumi, T. Inoue, T. Iwai, O. Shirai and Y. Arai: "Behavior of Plutonium and Americium at Liquid Cadmium Cathode in Molten LiCl-KCl Electrolyte", J. Nucl. Mater., 299 (1), 32 (2001).

12) T. Fujino, N. Sato, K. Yamada, K. Fukuda, H. Serizawa and T. Shiratori: "Thermodynamics of the UO_2 solid solutions with magnesium and europium oxide", Journal of Nuclear Materials 297 (3), 332(2001).

13) T. Albiol and Y. Arai: "Review of actinide nitride properties with focus on safety aspects", JAERI-Review 2001-040 (2001).

14) O. Shirai, M. Iizuka, T. Iwai and Y. Arai: "Electrode reaction of the Np^{3+}/Np couple in LiCl-KCl eutectic melts", J. Applied Electrochemistry 31 1055(2001).

15) H. Sawa、T. Tobita, M. Takahashi, T. Saito, K. Iimura, Y. Iichiro, H. Serizawa, T. Sekino and A. Ishikawa: "Irradiation test of high burnup coated fuel particles for high temperature gas-cooled reactor (91F-1A Sweep gas capsule Irradiation test), JAERI-Research 2001-043 (2001).

16) Y. Sakamura, T. Inoue, T. Iwai and H. Moriyama: "Chlorination of UO_2, PuO_2 and rare-earth oxides using $ZrCl_4$, Komae Research Laboratory Rep. No. T00054 .

17) R.P.C. Schram, K. Bakker, H. Hein, J.G. Boshoven, R.R. van der Laan, C.M. Sciolla, T. Yamashita, Ch. Hellwig, F. Ingold, R. Conrad and S. Casalta: "Design and fabrication aspects of a plutonium-incineration experiment using inert matrices in a "Once-Through-Then-Out" mode", Progress in Nuclear Energy, 38 (3-4), 259 (2001).

18) J.M. Paratte, R. Chawla, H. Akie, P.M.G. Damen, H.K. Joo, P. Mikolas, E. Padovani, Y. Peneliau and G. Youinou: "A numerical neutronics benchmark study for inert matrix plutonium fuels in uranium dioxide and mixed plutonium-uranium dioxide environments", Progress in Nuclear Energy, 38 (3-4), 335 (2001).

19) T. Yamashita: "Rock-like and inertmatrix fuels", Advances in Nuclear fuel Technology-Present and future, Atomic Energy Society of Japan, 9,9.3, 467 (2001).

20) N. Nitani, K. Kuramoto, T. Yamashita, Y. Nakano and H. Akie: "In-pile irradiation of

rock-like oxide fuels", Proc. Int. Conf. on Back-end of the Fuel Cycle: from Research to Solutions (Global-2001), 9-13 September, Paris, France, 2001, Paper No. 018 (2001) (CD-ROM).

21) T. Yamashita, K. Kuramoto, H. Akie, Y. Nakano, N. Nitani, T. Nakamura and K. Kusagaya: "Rock-like oxide fuels for burning excess plutonium in LWRs", Proc. Advanced Reactors with Innovative Fuels (ARWIF-2001), 22-24 October 2001, Chester, UK, Paper No. 15 (2001) (CD-ROM).

9. Research on Small Reactor for Dispersive Energy Supply System

1) K. Saito, T. Kusunoki and T. Ishida: "Design Study for Thermal Insulation Method of Submerged Piping", JAERI-Tech 2001-038 (2001) [in Japanese].

2) K. Saito and T. Ishida: "Simple Evaluations of Fluid-induced Vibrations for Steam Generator Tube Arrays in Advanced Marine Reactors (MRX, DRX)", JAERI-Tech 2001-039 (2001) [in Japanese].

3) H. Nunokawa, T. Yoritsune, S. Imayoshi, Y. Kasahara, M. Ochiai and T. Ishida: "Development of Ball Bearing in High Temperature Water for In-vessel Type Control Rod Drive Mechanism of Advanced Marine Reactor", JAERI-Tech 2001-040 [in Japanese].

4) T. Ishida, S. Imayoshi, T. Yoritsune, H. Nunokawa, M. Ochiai and Y. Ishizaka: "Development of in-vessel type control rod drive mechanism for marine reactor", Journal of Nuclear Science and Technology, 38(7), p.557-570 (2001).

5) T. Kusunoki, T. Takahashi, H. Nishimura, S. Tokunaga, N. Odano, T. Yoritsune and T. Ishida: "Concept of a Nuclear Powered Submersible Research Vessel and a Compact Reactor", JAERI-Tech 2001-045 (2001) [in Japanese].

6) T. Ura, T. Takamasa, H. Nishimura, T. Aoki, M. Ueno, T. Maeda, M. Nakamura, S. Shimazu, S. Tokunaga, Y. Shibata, O. Togawa, T. Ishida, J. Shimazaki, N. Odano, T. Takahashi, T. Kusunoki and T. Yoritsune: "Study on Operation Conditions and an Operation System of a Nuclear Powered Submersible Research Vessel, Report of Working Group on Application of a Very Small Nuclear Reactor to an Ocean Research", JAERI-Tech 2001-049 (2001) [in Japanese].

7) N. Odano, T. Ishida, K. Wada and H. Imai: "Neutronic Study of SCR Core for Under-sea Scientific Research Vessel", JAERI-Research 2001-39 (2001) [in Japanease].

8) H. Takahashi, T. Kano, T. Takahashi, M. Kyoya and J. Shimazaki: "Improvement of Nuclear Ship Engineering Simulation System –Hardware Renewal and Interface Improvement of the Integral Type Reactor-", JAERI-Tech 2001-068 (2001) [in

Japanese].

9) N. Odano, T. Ishida and M. Ochiai: "Neutronic Study of a Very Small Reactor MR-1G Core for Excusive Use of Heat Supply", JAERI-Research 2001-044 (2001) [in Japanese].

10) T. Yoritsune and T. Ishida: "Effect of Ship Motions and Flow Stability in a small Marine Reactor Driven by Natural Circulation", JAERI-Research 2001-053 (2001) [in Japanese].

Appendix I

March 2002

Department of Nuclear Energy System Organization Chart

Department of Nuclear Energy System

Director : M. Ochiai

Deputy Director : T. Osugi H. Nakajima

K. Fukuda H. Fujisaki T. Fujimura S. Hamada
Y. Anoda(1) H. Oigawa(2)

Administrative Service

S. Akaosugi (Administrative Manager)
T. Nogami C. Kawawa S. Toida T. Ikejima

Reactor Engineering Facility Operation Division

K. Nakajima (Head)

K. Satoh	N. Yabuuchi	K. Kurosawa	K. Murakami
M. Takeuchi	H. Watanabe	M. Kyoya	T. Satoh
T. Ono	M. Shibata	K. Hayasaka	H. Sodeyama
M. Ozeki	T. Ouchi	M. Saitoh	Y. Hoshi
Y. Miyoshi(3)	K. Nakajima(3)	T. Yamamoto(3)	K. Tonoike(3)
Y. Yamane(3)	T. Nakamura(3)	H. Shitobe(4)	Y. Funayama(5)
M. Fumisawa(4)			

Nuclear Data Center

A. Hasegawa (Head)

T. Nakagawa	J. Katakura	K. Shibata	T. Fukahori
A. Ichihara	O. Iwamoto	M. Kataoka	A. Y. Konobeyev
S. Chiba(6)	H. Iimura(7)		

Research Group for Energy System Assessment

O. Sato (Head)

M. Yamaguchi	Y. Tanaka	K. Kunii	K. Tatematsu

Research Group for Advanced Reactor Systems

T. Iwamura (Head)

Y. Asahi	T. Okubo	T. Suzudo	S. Fujiwara
H. Akie	K. Nabeshima	Y. Nakano	N. Ishikawa
T. Nakatsuka	T. Kakuta	A. Shelley	M. Katagiri(6)
M. Suzuki(8)	T. Yonomoto(8)	H. Mineo(3)	

Research Group for Reactor Physics

T. Mori (Head)

S. Iijima	S. Okajima	K. Okumura	T. Yamane
T. Suzaki	M. Haruyama	M. Kurosawa	T. Sakurai
M. Andoh	Y. Nagaya	M. Takase	Y. Uno
Y. Seki	K. Nishihara(2)		

Research Group for Thermal and Fluid Engineering

H. Akimoto (Head)

A. Ohnuki	K. Takase	H. Yoshida	M. Kureta

Research Group for Reactor Structural Materials

H. Tsuji (Head)

T. Tsukada	Y. Kaji	M. Kikuchi	H. Ugachi
J. Nakano	Y. Miwa	Y. Nemoto	Y. Sawai(7)
M. Omi(9)	Y. Matsui(9)		

Research Group for Compatible Materials

K. Kiuchi (Head)

M. Futakawa	T. Saito	I. Ioka	H. Nishi
K. Tachibana	T. Suzuki	R. Onishi	T. Motooka
N. Maruyama	T. Yanagihara	M. Tanabe	M.Ichiba
C. Kato	Y. Kurata(2)	S. Ishiyama(10)	S. Baba(10)
T. Ishiyama(11)	A. Naito(7)		

Research Group for Advanced Fuel

Y. Arai (Head)

T. Yamashita	H. Serizawa	K. Kikuchi	A. Inoue
T. Iwai	K. Kuramoto	O. Shirai	N. Shirasu
K. Nakajima	K. Shiozawa	T. Sasayama	H. Kimura(3)
H. Otsuka(7)			

Research Group of Small Reactor for Dispersive Energy Supply System

T. Ishida (Head)

N. Nakajima	M. Kuga	T. Kusunoki	S. Kakisaki
T. Yoritsune	H. Takahashi	K. Sawada	

Research Committee

Japanese Nuclear Data Committee

Research Committee on Reactor Physics

Research Committee on Marine Reactors

(No.) Original Organization of the Shared-Time Members
(1) Nuclear Safety Research Center
(2) Center for Proton Accelerator Facilities
(3) Dept. of Fuel Cycle Safety Research
(4) Nuclear Technology and Education Center
(5) Dept. of Research Reactor
(6) Advanced Science Research Center
(7) Dept. of Materials Science
(8) Dept. of Reactor Safety Research
(9) Dept. of JMTR
(10) Dept. of Advanced Nuclear Heat Technology
(11) Dept. of Environmental Science

Appendix Ⅱ Engineering Facilities Related to the Department

FCA : Fast Critical Assembly

The FCA is a split-table type facility of horizontal matrix structure designed for studying nuclear characteristics of fast reactor. The construction of the FCA was started in 1965 and the first core went critical on 29th April 1967. The main features of facility are Summarized as follows:

Type:	Split-table type of horizontal matrix structure
Size:	2.8m×2.8m×1.3m (each half assembly)
Fuel:	Enriched uranium and plutonium (Plate type)
Other material:	Sodium, stainless steel, aluminum oxide, polystyrene etc. (Plate type)
Maximum power:	2kW
Assembly name:	FCA-1～FCA-XXI

Critical experiment using enriched uranium cores were made in 1 960s investing basic characteristics of fast reactor cores. Mock-up experiments were extensively made in 1 970s for the Fast Experimental Reactor JOYO and the Prototype Fast Breeder Reactor MONJU. In 1980s, the main subjects of experiments were the investigation of the core characteristics of an axially heterogeneous large fast breeder reactor and the core physics study on a high conversion light water reactor. In early 1990s, the reactor physics experiment of metallic-fueled LMFBR was carried out. Since 1995, international benchmark experiments for β eff was carried out. Since 2000, the reactor physics experiments for ADS have been condacted by using uranium fueled core.

VHTRC : Very High Temperature Reactor Critical Assembly

The VHTRC is a low-enriched uranium fueled and graphite moderated / reflected critical assembly. At VHTRC, reactor physics experiments have been carried out mainly for the verification of the neutronics design of the HTTR.

Main features of VHTRC

Type:	Split table of hexagonal prism (prismatic block structure)
Size:	2.4m across the flats and 2.4m long
Fuel:	2,4 and 6wt% enriched UO_2 Coated particle fuel compact, Pin-in-block type
Moderator/reflector:	Graphite
Core temperature:	Room temperature to 210℃ by electric heaters
Maximum power:	10W
Auxiliary equipments:	① Sample heating device (up to 800℃) ② pulsed neutron source

TCA: Tank-type Critical Assembly

The TCA is a light-water-moderated critical facility to provide the experimental data on light water reactor physics. The construction of the TCA was started in 1961 and the first criticality was attained on 23rd August 1962.

Main features of TCA

Type:	Light water moderated Tank-type
Size:	Typically 0.5m×0.5m×1m
	(Core Tank 1.8m diam.×2.1m height)
Fuel:	Low-enriched U02 and Pu02- U02 fuel rod
Moderator:	Light Water
Maximum Power:	200W
Auxiliary equipments:	Pulsed neutron source
	Neutron absorbing materials (soluble or solid state)

国際単位系 (SI) と換算表

表1　SI基本単位および補助単位

量	名称	記号
長さ	メートル	m
質量	キログラム	kg
時間	秒	s
電流	アンペア	A
熱力学温度	ケルビン	K
物質量	モル	mol
光度	カンデラ	cd
平面角	ラジアン	rad
立体角	ステラジアン	sr

表2　SIと併用される単位

名称	記号
分，時，日	min，h，d
度，分，秒	°，′，″
リットル	l，L
トン	t
電子ボルト	eV
原子質量単位	u

1 eV = 1.60218 × 10^{-19} J

1 u = 1.66054 × 10^{-27} kg

表3　固有の名称をもつSI組立単位

量	名称	記号	他のSI単位による表現
周波数	ヘルツ	Hz	s^{-1}
力	ニュートン	N	m·kg/s^2
圧力，応力	パスカル	Pa	N/m^2
エネルギー，仕事，熱量	ジュール	J	N·m
工率，放射束	ワット	W	J/s
電気量，電荷	クーロン	C	A·s
電位，電圧，起電力	ボルト	V	W/A
静電容量	ファラド	F	C/V
電気抵抗	オーム	Ω	V/A
コンダクタンス	ジーメンス	S	A/V
磁束	ウェーバ	Wb	V·s
磁束密度	テスラ	T	Wb/m^2
インダクタンス	ヘンリー	H	Wb/A
セルシウス温度	セルシウス度	℃	
光束	ルーメン	lm	cd·sr
照度	ルクス	lx	lm/m^2
放射能	ベクレル	Bq	s^{-1}
吸収線量	グレイ	Gy	J/kg
線量当量	シーベルト	Sv	J/kg

表4　SIと共に暫定的に維持される単位

名称	記号
オングストローム	Å
バーン	b
バール	bar
ガル	Gal
キュリー	Ci
レントゲン	R
ラド	rad
レム	rem

1 Å = 0.1 nm = 10^{-10} m

1 b = 100 fm^2 = 10^{-28} m^2

1 bar = 0.1 MPa = 10^5 Pa

1 Gal = 1 cm/s^2 = 10^{-2} m/s^2

1 Ci = 3.7 × 10^{10} Bq

1 R = 2.58 × 10^{-4} C/kg

1 rad = 1 cGy = 10^{-2} Gy

1 rem = 1 cSv = 10^{-2} Sv

表5　SI接頭語

倍数	接頭語	記号
10^{18}	エクサ	E
10^{15}	ペタ	P
10^{12}	テラ	T
10^{9}	ギガ	G
10^{6}	メガ	M
10^{3}	キロ	k
10^{2}	ヘクト	h
10^{1}	デカ	da
10^{-1}	デシ	d
10^{-2}	センチ	c
10^{-3}	ミリ	m
10^{-6}	マイクロ	μ
10^{-9}	ナノ	n
10^{-12}	ピコ	p
10^{-15}	フェムト	f
10^{-18}	アト	a

（注）

1. 表1－5は「国際単位系」第5版，国際度量衡局 1985年刊行による。ただし，1 eVおよび1 uの値はCODATAの1986年推奨値によった。
2. 表4には海里，ノット，アール，ヘクタールも含まれているが日常の単位なのでここでは省略した。
3. barは，JISでは流体の圧力を表わす場合に限り表2のカテゴリーに分類されている。
4. EC閣僚理事会指令ではbar，barnおよび「血圧の単位」mmHgを表2のカテゴリーに入れている。

換算表

力	N(=10^5 dyn)	kgf	lbf
	1	0.101972	0.224809
	9.80665	1	2.20462
	4.44822	0.453592	1

粘度　1 Pa·s(N·s/m^2) = 10 P(ポアズ)(g/(cm·s))

動粘度　1 m^2/s = 10^4 St(ストークス)(cm^2/s)

圧力	MPa(=10 bar)	kgf/cm^2	atm	mmHg(Torr)	lbf/in^2(psi)
	1	10.1972	9.86923	7.50062 × 10^3	145.038
	0.0980665	1	0.967841	735.559	14.2233
	0.101325	1.03323	1	760	14.6959
	1.33322 × 10^{-4}	1.35951 × 10^{-3}	1.31579 × 10^{-3}	1	1.93368 × 10^{-2}
	6.89476 × 10^{-3}	7.03070 × 10^{-2}	6.80460 × 10^{-2}	51.7149	1

エネルギー・仕事・熱量	J(=10^7 erg)	kgf·m	kW·h	cal(計量法)	Btu	ft·lbf	eV
	1	0.101972	2.77778 × 10^{-7}	0.238889	9.47813 × 10^{-4}	0.737562	6.24150 × 10^{18}
	9.80665	1	2.72407 × 10^{-6}	2.34270	9.29487 × 10^{-3}	7.23301	6.12082 × 10^{19}
	3.6 × 10^6	3.67098 × 10^5	1	8.59999 × 10^5	3412.13	2.65522 × 10^6	2.24694 × 10^{25}
	4.18605	0.426858	1.16279 × 10^{-6}	1	3.96759 × 10^{-3}	3.08747	2.61272 × 10^{19}
	1055.06	107.586	2.93072 × 10^{-4}	252.042	1	778.172	6.58515 × 10^{21}
	1.35582	0.138255	3.76616 × 10^{-7}	0.323890	1.28506 × 10^{-3}	1	8.46233 × 10^{18}
	1.60218 × 10^{-19}	1.63377 × 10^{-20}	4.45050 × 10^{-26}	3.82743 × 10^{-20}	1.51857 × 10^{-22}	1.18171 × 10^{-19}	1

1 cal = 4.18605 J (計量法)

= 4.184 J (熱化学)

= 4.1855 J (15 °C)

= 4.1868 J (国際蒸気表)

仕事率　1 PS (仏馬力)

= 75 kgf·m/s

= 735.499 W

放射能	Bq	Ci
	1	2.70270 × 10^{-11}
	3.7 × 10^{10}	1

吸収線量	Gy	rad
	1	100
	0.01	1

照射線量	C/kg	R
	1	3876
	2.58 × 10^{-4}	1

線量当量	Sv	rem
	1	100
	0.01	1

(86年12月26日現在)

Nuclear Energy System Department Annual Report (April 1, 2001- March 31,2002)